Investigation of deposition conditions and annealing treatments on sputtered ZnO:Al thin films: Material properties and application to microcristalline silicon solar cells

Coralie Charpentier

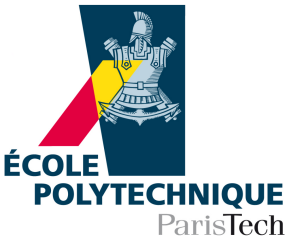

Thèse

présentée en vue d'obtenir le grade de

Docteur de l'Ecole Polytechnique

Spécialité Science des Matériaux

par

Coralie Charpentier

coralie.charpentier@polytechnique.edu

Investigation of deposition conditions and annealing treatments on sputtered ZnO:Al thin films: Material properties and application to μc-Si:H solar cells

Thèse soutenue le 20 Décembre 2012 devant le jury composé de:

Prof.	Farzaneh Arefi-Khonsari	Présidente du jury
Dr.	Angélique Bousquet	Rapporteur
Prof.	Daniel Bellet	Rapporteur
Prof.	Daniel Lincot	Examinateur
Dr.	Fabien Paumier	Examinateur
Dr.	Bruno Delahaye	Examinateur
Dr.	Thierry Emeraud	Invité
Dr.	Patricia Prod'homme	Co-encadrante
Prof.	Pere Roca i Cabarrocas	Directeur de thèse

Contents

List of Figures

List of Tables

Abbreviations and symbols

Abbreviations

AFM Atomic Force Microscope
AM 1.5 Solar spectrum at an air mass of 1.5
AP-CVD Atmospheric pressure - Chemical Vapor Deposition
ARS Angular Resolved Scattering
ARTA Angular Resolved Transmittance Analyser
AZO Aluminium-doped Zinc Oxide
BG Band Gap
CVD Chemical Vapor Deposition
DC Direct Current
ELA Excimer Laser Annealing
EQE External Quantum Efficiency
FESEM Field Emission Scanning Electron Microscope
FIB Focused Ion Beam
FTO Fluorine-doped Tin Oxide
FWHM Full Width at Half Maximum
i-type Intrinsic
IR Infrared
ITO Tin-doped Indium Oxide
LO Longitudinal
LP-CVD Low Pressure - Chemical Vapor Deposition
MPP Maximum Power Point
n-type Negatively doped
NIR Near Infrared
p-type Positively doped
PE-CVD Plasma Enhanced - Chemical Vapor Deposition
PMT Photomultipiler tuber
PSA Polarization State Analyzer
PSG Polarization State Generator
PV Photovoltaic(s)
PVD Physical Vapor Deposition
RF Radio Frequency (13.56 MHz)
RMS Root Mean Square
RT Room Temperature

sccm Standard Cubic Centimeters per Minute
SE Spectroscopic Ellipsometry
SR Spectral Response
SEM Scanning Electron Microscope
TA Transverse acoustic mode
TCO Transparent Conductive Oxide
TCM Transparent Condutive Material
TEM Transmission Electron Microscope
TO Transverse optical mode
UV Ultraviolet
VIS Visible
XRD X-Ray Diffraction

Symbols

β Full Width at Half Maximum of the diffraction
δ_{RMS} Root Mean Square roughness
ε Weighted average strain
$\varepsilon\varepsilon_0$ Static dielectric constant
ζ_d Parameter which describes the non-parabolicity of the conduction band
η Efficiency
θ_{hkl} Angle of incidence onto Miller indices (hkl) planes
λ Wavelength of the light
μ_{a-ph} Acoustical phonon mobility
μ_{bulk} Mobility from the bulk
μ_{gb} grain boundaries mobility
μ Hall mobility
μ_{ii} ionized impurities mobility
μ_{opt} Optical mobility
ρ Resistivity
σ Conductivity
τ Relaxation time between two scattering events
ω Frequency
ω_p Plasma frequency
Γ_d Damping term
ΔE^{BM} Band gap broadening from the Burstein-Moss band filling effect
ΔE^{EX} Band gap narrowing from the exchange energy
Φ Work function
Φ_b Energetic barrier height at grain boundaries
A Absorption
Al_{Zn} Aluminium at the substitutional zinc site
c_l Averaged longitudinal elastic constant
d_{hkl} Lattice parameter along the [hkl] orientation
D Thickness of the coherent diffracting domain
E_C Conduction band minimum
E_F Fermi level
E_{g0} Intrinsic band gap

E_1	Deformation potential
E_V	Valence band maximum
E_{vac}	Vacuum level
FF	Fill Factor
F_{ii}	Screening function
Ga_{Zn}	Gallium at the substitutional zinc site
H_i	Hydrogen interstitial
In_{Zn}	Indium at the substitutional zinc site
I_p	Ionization potential
J_{SC}	Short circuit current density
$J(V)$	Illuminated current density-voltage
k	Extinction coefficient
L	Grain length
Li_{Zn}	Lithium at the substitutional zinc site
m^*	Effective mass of an electron from the conduction band
m_0^*	Effective mass of an electron at the conduction band edge
n	Refractive index
N	Free carrier density
N_{opt}	Optically active free electron density
N_O	Nitrogen at the substitutional oxygen site
Na_{Zn}	Sodium at the substitutional zinc site
N_t	Charge carrier trap density at the grain boundaries
P_W	RF power
q_z	Scattering vector
r	Hall coefficient factor for acoustical phonon
R	Reflectance
R_{sh}	sheet resistance
T	Transmittance
T_{diff}	Diffuse transmittance
T_{dir}	Direct transmittance
T_{sub}	Substrate temperature
T_{total}	Total transmittance
V_O	Oxygen vacancies
V_{OC}	Open circuit voltage
Zn_i	Zinc interstitial

Introduction

In 2011, the primary energy consumption in the world has increased by 2.2% after a strong growth in 2010 of 4.9%. Countries from the Organisation for Economic Co-operation and Development (OECD) were impacted again by the economic crisis and their energy consumption fell by 1.3% (-3.2% in the European Union, -0.7% in USA), while in China and India, energy consumption continued to grow steadily (+7.7% and +6.2% respectively) [1].

The global warming emissions resulting from this increase of energy consumption have achieved unprecedented levels. The main sources of greenhouse gases due to human activity are burning of fossil fuels, corresponding to 80.6% of the energy consumption in 2010 (Figure 1). While global oil products consumption increased by 0.6% only in 2011, solid fuel consumption continued to soar with a increase of 5.4%, in particular for electricity generation, driven by the dynamism in Chinese demand, which corresponds of 45% of total consumption [6].

With climate change concerns, coupled with high oil prices and peak oil scenario, the need for renewable energy sources has become a evidence for future generations.

Renewable energies

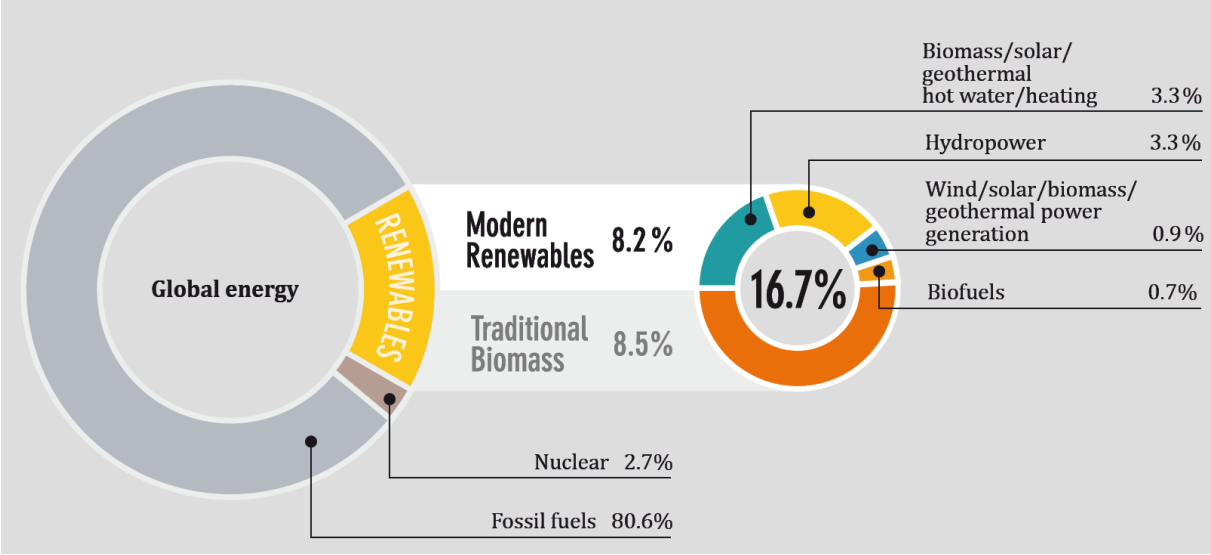

Figure 1: Renewable energy share of global final energy consumption in 2010 [7].

Renewable energy in 2010 supplied an estimated 16.7% of global final energy consumption as shown in Figure 1. Of this total, an estimated 8.2% came from modern renewable energy counting hydropower, wind, solar, geothermal, biofuels, and modern biomass [7].

In the power sector, renewable energy accounted for almost half of the estimated 208 gigawatts (GW) of electric capacity added globally during 2011. Wind and solar photovoltaics (PV) accounted for almost 40% and 30% of new renewable capacity, respectively, followed by hydropower with nearly 25%. By the end of 2011, total renewable power capacity worldwide exceeded 1,360 GW, (390 GW except hydropower as shown in Figure 2) [2]. In the European Union, renewables accounted for more than 71% of total electric capacity additions in 2011, bringing renewable energy's share of total electric capacity to 31.1%. Solar PV alone represented almost 47% of new capacity that came into operation.

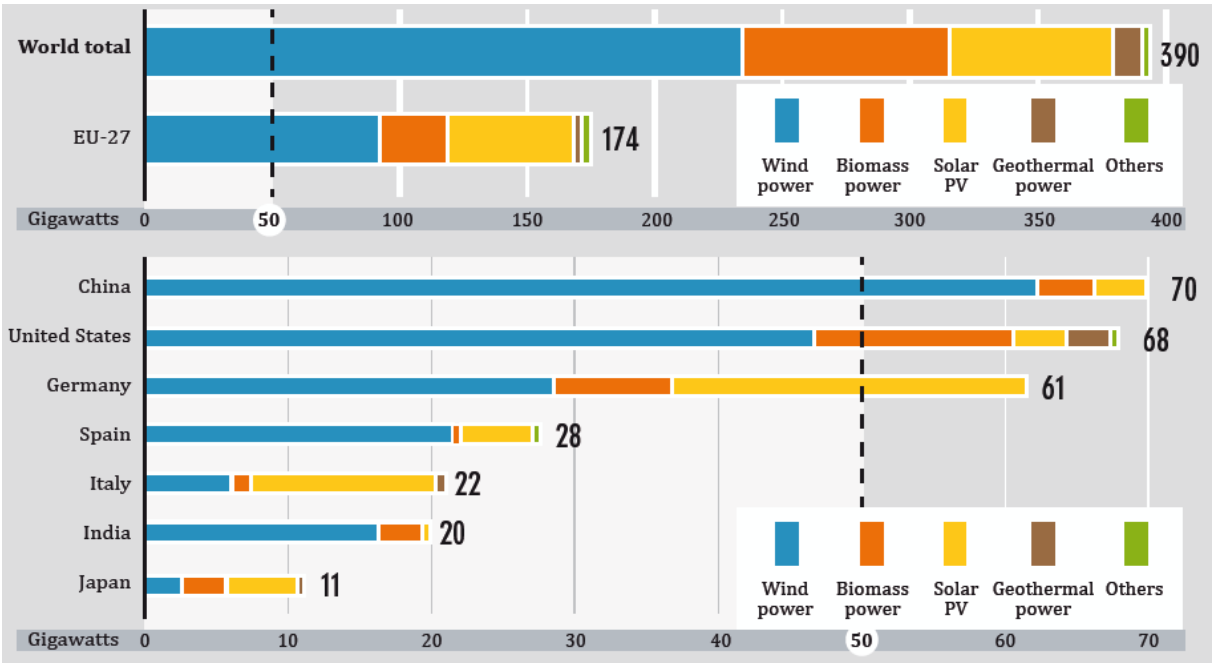

Figure 2: Renewable power capacities (except hydropower) for European Union and the top seven countries in 2011 [7].

A lot of countries have now renewable energy targets, at least 118 by early 2012. These support policies are a driving force behind increasing markets for renewable energy.

Solar photovoltaics

Solar PV grew the fastest of all renewable technologies during the period from 2006 through 2011, with operating capacity increasing by an average of 58% annually.

The solar PV market saw another year of extraordinary growth as presented in Figure 3. Almost 30 GW of new solar PV capacity came into operation worldwide in 2011, increasing the global total by 74% to almost 70 GW [7]. The aggregate size of the global PV industry now exceeds USD 100 billion per year.

The top 15 solar PV module manufacturers accounted for 49% of the 34.8 GW produced globally. Suntech of China remained in first place, having surpassed First Solar in 2009. First Solar is still the dominant firm for CdTe thin film production (Figure 4).

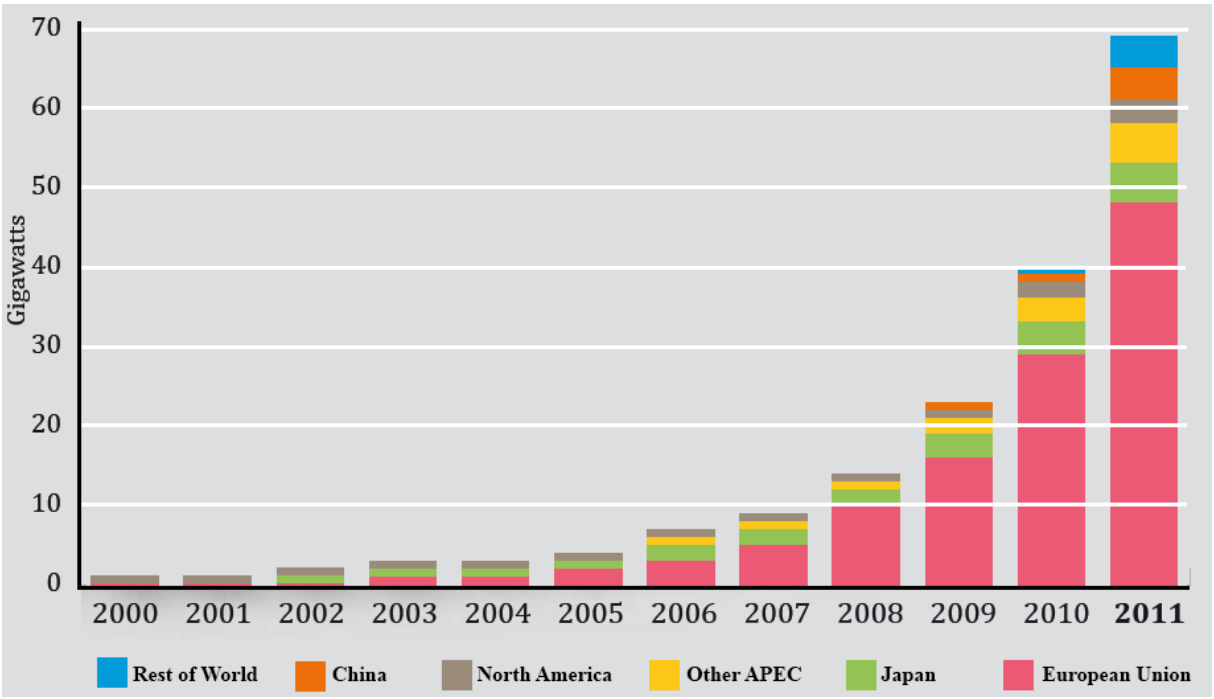

Figure 3: Solar PV total world installed capacities between 2000 and 2011 [3].

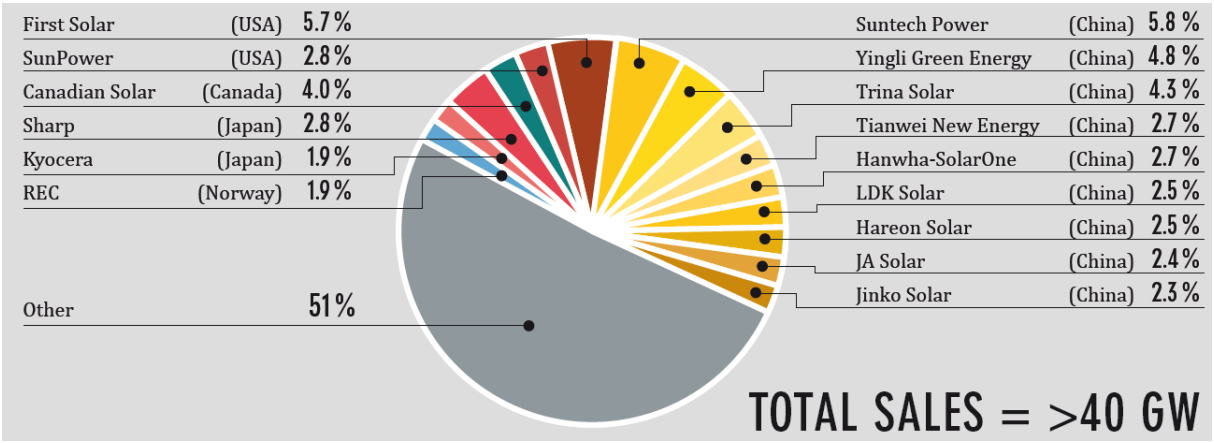

Figure 4: Market shares of top 15 solar PV module Manufacturers in 2011 [7].

Solar photovoltaic technologies

There is a wide range of PV cell technologies on the market today, using different types of materials, and an even larger number will be available in the future. PV cell technologies are usually classified into three generations, depending on the basic material used and the level of commercial maturity:

* First-generation PV systems are the mainstream PV technology with 89% of the market [3]. They use the wafer-based crystalline silicon (c-Si) technology, either mono-crystalline or multi-crystalline and ribbon silicon.

* Second-generation PV systems, in an early market deployment with 11% of the market share [3], are based on thin-film PV technologies and generally include amorphous silicon (a-Si:H) and tandem solar cells (a-Si:H/μc-Si:H), also refered

as micromorph, Cadmium-Telluride (CdTe), Copper-Indium-Diselenide ($CuInSe_2$) and Copper-Indium-Gallium-Diselenide ($CuIn_{1-x}Ga_xSe_2$).

* Third-generation PV systems are based on low cost materials for higher efficiencies and include technologies that are still under demonstration or have not yet been widely commercialised, as well as novel concepts under development.

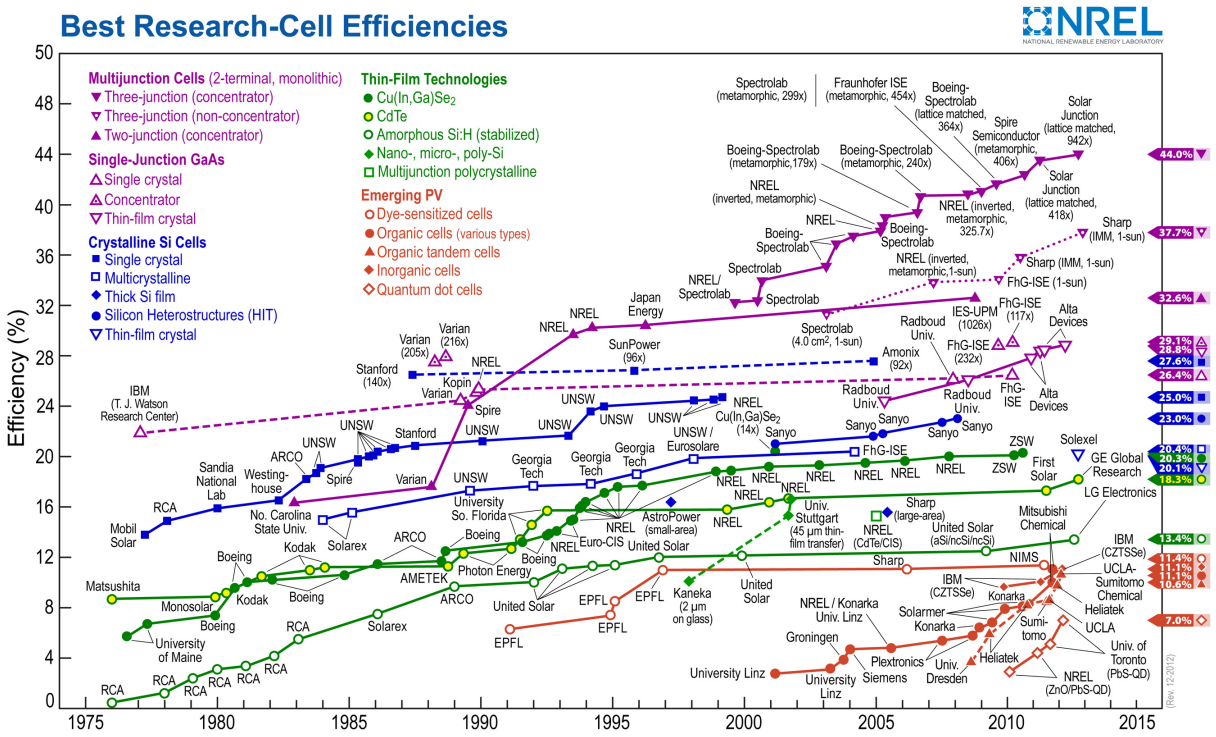

Figure 5: Evolution of the best research cell efficiencies for the different technologies (NREL, revised in December 2012)

The best research solar cell efficiencies under AM1.5 standard testing conditions (temperature 25 °C, light intensity 1000 W/m^2, air mass 1.5) are presented in Figure 5. Second-generation thin-film PV technologies are attractive because of their low material and manufacturing costs.

Silicon thin film solar cells

Silicon thin film solar cells, which are part of the 2nd generation in PV technologies, offer several promising advantages. This technology is silicon based, one of the most abundant elements in the earth's crust, with practically no ecological risk during manufacturing, operation and disposal. Compared to c-Si, thin-film solar cells can provide lower cost electricity, thanks to a lower quantity of material required for their manufacturing, and fewer waste. Their deposition is based on continuous low temperature processes, which enable the use of low-cost and large (up to 5.7 m^2) substrates, which leads to a substantial manufacturing cost reduction, or also flexible substrates for an easier integration into building components or others markets.

The thin film silicon solar cells are either amorphous, microcrystalline or both. Hydrogenated amorphous silicon exhibits a lack of long-range order and a high content of bonded hydrogen, which passivates most of unsaturated silicon dangling bonds. This material presents a band gap of 1.7 - 1.8 eV, therefore light at wavelengths above 730 nm cannot be absorbed. Moreover, amorphous silicon suffers from a light-induced degradation, the Staebler-Wronski effect, which causes efficiency reduction of the solar cells [4].

The crystallinity of the material depends on the gas mixture used for the deposition. With the decrease of the silane concentration in the H_2-SiH_4 gas mixture, the material structure shifts from amorphous to crystalline. Hydrogenated microcrystalline silicon is generally obtained at high hydrogen dilution, the silicon structure consisting of crystalline regions within an amorphous matrix. μc-Si:H was introduced in 1968 [8] and the first μc-Si:H based solar cells were made by J. Meier *et al.* in 1994 [5]. The material presents a band gap of 1.1 eV, which extends the wavelength range of absorption up to 1100 nm. However the indirect band gap, due to the crystalline nature of the material, decreases the absorption coefficient in the visible range, thus requiring the use of thicker i-layers (1 μm or more) compared to a-Si:H (0.3 μm). Moreover, μc-Si:H presents the advantage to be stable against light induced degradation, contrary to a-Si:H.

The best way to use μc-Si:H solar cells is in a tandem configuration, as a bottom cell together with an a-Si:H top cell, structure called micromorph tandem solar cell.

Hydrogenated microcrystalline silicon solar cells in pin structure

Silicon based solar cells can have two different configurations: pin or nip structures, depending on the deposition sequence of positive (p) or negative (n) doped layers and intrinsic (i) layer. In our case, the solar cell studied is hydrogenated microcrystalline solar cells in pin structure, as presented in Figure 6.

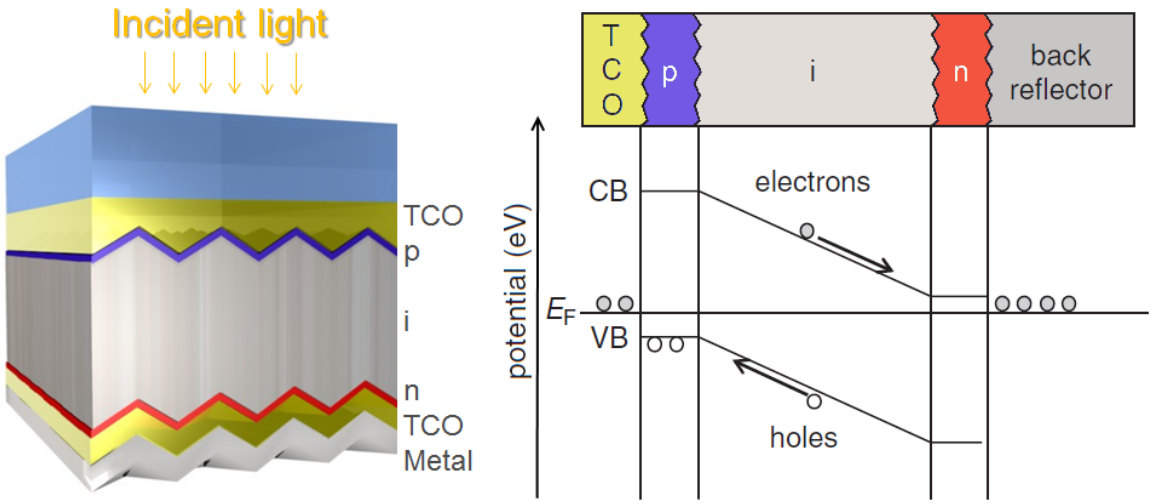

Figure 6: pin configuration and corresponding schematic energy band diagram, with E_F the Fermi level, CB the conduction band, and VB the valence band.

The doped and intrinsic layers are packed between a TCO front contact and a highly reflective back contact. The doped layers are usually quite thin (10 - 30 nm), and generate an electric field extending over the i-layer, which drives the carriers generated inside the intrinsic layer to the electrodes. In our case, the back electrode consists of a double stack of Sn doped In_2O_3 (ITO) and silver, in order to reduce absorption losses. The first deposited film is the front electrode, consisting of a Transparent Conductive Material (TCM) layer, usually an oxide called in this way TCO for Transparent Conductive Oxide, which collects the carriers from the p-layer.

Transparent Conductive Oxides

In the pin configuration the light enters through the glass and the TCO layer and is trapped into the active layers by reflection on back contacts and by the light scattering properties of the front electrode.

The TCO layer is a key material for the improvement of μc-Si:H solar cells. In pin configuration, the TCO front contacts have to meet a number of requirements:

* High transparency in the active range of the absorber layer, between 400 - 1100 nm in case of μc-Si:H, to minimize optical losses by absorption and/or reflection,
* High conductivity to minimize the series resistance of the solar cells and avoid ohmic losses,
* Excellent light scattering properties through a rough surface,
* Favourable physico-chemical properties for the growth of silicon, such as a high stability to hydrogen-rich plasmas used for silicon deposition.

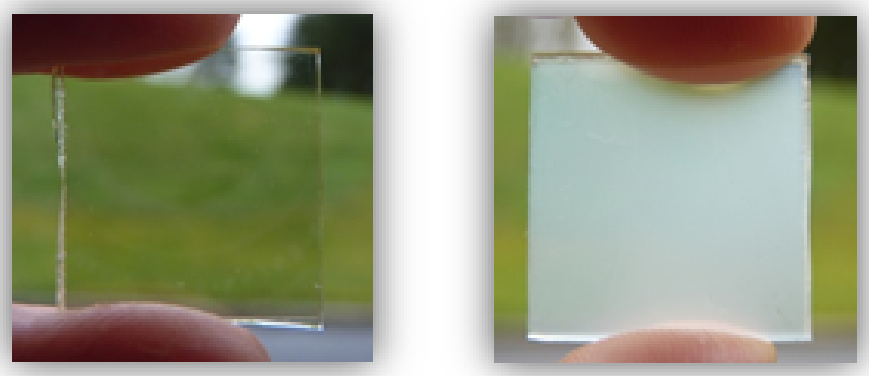

(a) As-deposited (b) After 60 s of etching

Figure 7: ZnO:Al thin film deposited on glass substrate: As-deposited (a) and after a wet chemical etching step of 60 s (b).

In our case, the TCO layer is sputtered Aluminium-doped Zinc oxide (ZnO:Al, also called AZO) thin film. While the optical and electrical properties are optimized during the

magnetron sputtering deposition, an additional step is necessary to create rough surface, and increase the diffusivity of the thin films, as shown in Figure 7.

These requirements are difficult to satisfy all together, and a compromise is often necessary to have the optimal characteristics of the solar cells.

Aim and outline of this thesis

In this thesis, the front TCO for hydrogenated silicon thin film solar cells has been studied. The optimization of this layer is crucial for the improvement of the solar cells. This development is realized in several steps, which have been optimized in this work.

The TCO studied for integration with μc-Si:H is Aluminium doped Zinc Oxide, as discussed in **Chapter 1**. In this part, the fundamentals on TCOs and ZnO:Al thin films are dealt and an overview of the literature related to TCO is presented. The structural properties of ZnO:Al material are presented, as well as the physical laws that govern the electrical and optical properties of the TCO thin films, and which have been widely used in the following sections.

Chapter 2 presents a description of the particular experimental techniques used in this work. The deposition techniques are presented, as well as the post-deposition treatment processes, and the characterization methods.

The first step for the production of pin μc-Si:H solar cells is the TCO deposition by RF magnetron sputtering, detailed in **Chapter 3**. The influence of the different deposition parameters, such as the argon pressure, the substrate temperature, the RF sputtering power, the oxygen partial pressure and the thickness of the film is reviewed. This step requires a detailed understanding of the growth mechanism, which is allowed by a deep study of the correlation between X-ray diffraction measurements and Raman spectroscopy. The relationships between the microstructural properties and the opto-electronic characteristics are studied in depth. More fundamental studies are also realized, based on the optical modelling of free electrons by combination of various optical techniques, and on the temperature-dependent conductivities.

To further improve the opto-electronic properties of the deposited TCO, additional post-deposition treatments can be performed. **Chapter 4** focuses on two different processes: a thermal annealing treatment, and a laser annealing treatment. The thermal annealing process is achieved under different atmospheres, and at various temperatures, while the influence of the fluence of the laser is studied for the laser annealing process. In both cases, the resulting opto-electronic modifications are related to the microstructural changes.

Once the interrelations between conductivity and transparency were distinguished, the deposited TCO layer is optimized in terms of surface roughness and light scattering for its integration in solar cells. **Chapter 5** first looks at the optimization of the light trapping by a wet chemical etching step. The deposition and post-deposition steps influence the surface morphology obtained after the texturation and are studied in this part. Secondly, the optimized TCO layers are used as front electrodes in hydrogenated microcrystalline silicon solar cells. The influence of the optical, electrical and morphological properties of the TCO layer on the solar cell characteristic are identified.

Finally, this work is summarized in a conclusion section, with the main contributions to the research field and further perspectives.

CHAPTER 3:
Optimization of ZnO:Al thin film deposition

CHAPTER 4:
Post-deposition treatments

CHAPTER 5:
Integration of ZnO:Al thin films in µc-Si:H solar cells

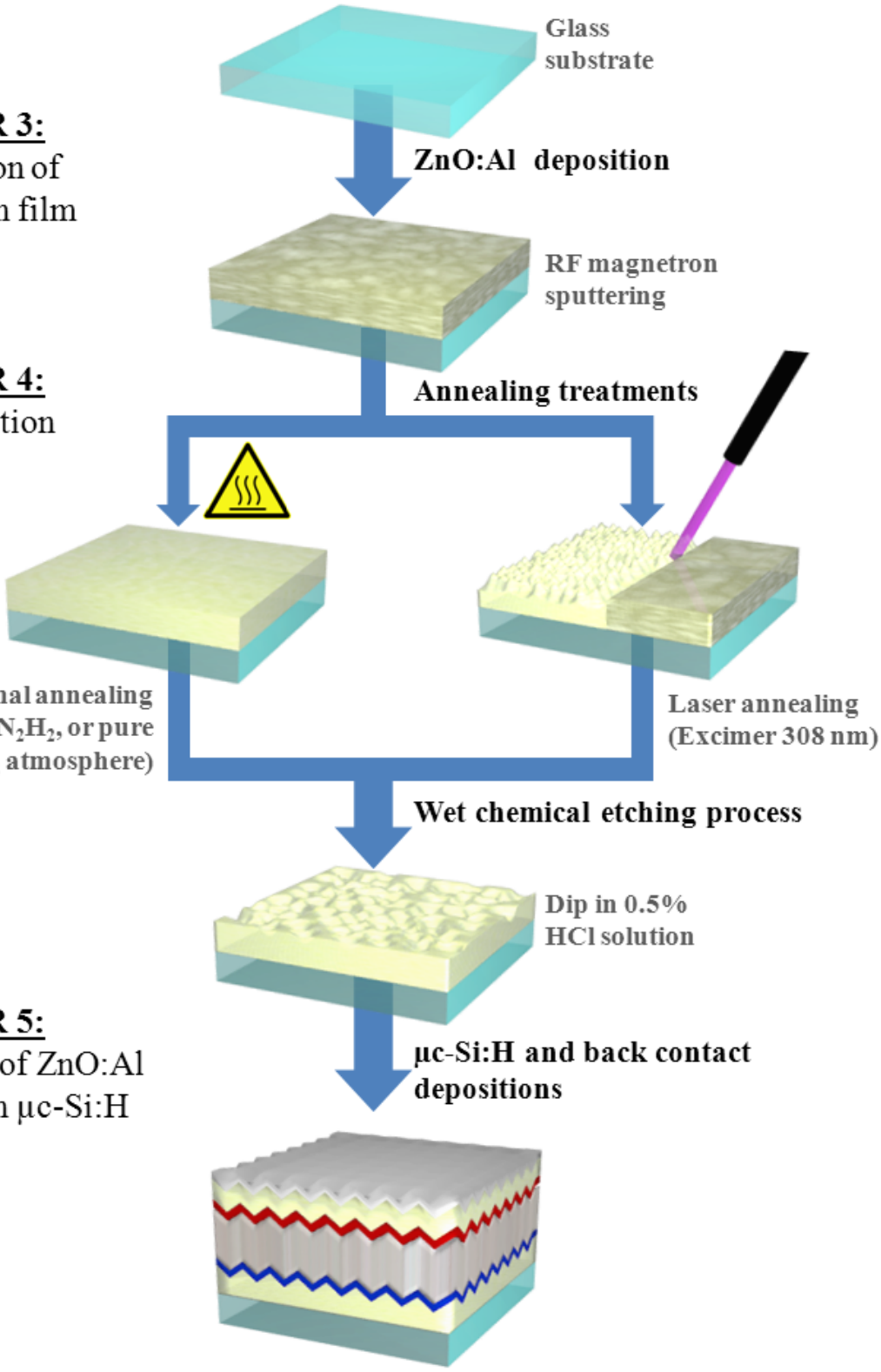

Bibliography

[1] Enerdata. Global Energy Statistical Yearbook, 2012. (cited page 1)

[2] EurObserv'ER. Photovoltaic barometer. *le journal du photovoltaïque*, 7:24, 2012. (cited page 2)

[3] IRENA. Renewable energy technologies: Cost analysis series, Solar photovoltaics. Technical report, IRENA, 2012. (cited pages v et 3)

[4] K.-H. Kim. *Hydrogenated polymorphous silicon: establishing the link between hydrogen microstructure and irreversible solar cell kinetics during light soaking.* PhD thesis, Ecole Polytechnique, 2012. (cited page 5)

[5] J. Meier, R. Flückiger, H. Keppner, and A. Shah. Complete microcrystalline p-i-n solar cell: Crystalline or amorphous cell behavior? *Applied Physics Letters*, 65(7):860, Aug. 1994. (cited page 5)

[6] M. R. Raupach, G. Marland, P. Ciais, C. Le Quéré, J. G. Canadell, G. Klepper, and C. B. Field. Global and regional drivers of accelerating CO2 emissions. *Proceedings of the National Academy of Sciences of the United States of America*, 104(24):10288–93, June 2007. (cited page 1)

[7] REN21. Renewables 2012 Global Status Report. Technical report, Renewable Energy Policy Network for the 21th century, 2012. (cited pages v, 1, 2 et 3)

[8] S. Vepřek and V. Mareček. The preparation of thin layers of Ge and Si by chemical hydrogen plasma transport. *Solid-State Electronics*, 11(7):683–684, July 1968. (cited page 5)

Chapter 1

Fundamentals on TCOs and ZnO:Al thin films

Contents

In this chapter are summarized the fundamental chemical and physical properties of TCO materials, especially ZnO:Al thin films. The physical theories on the electrical conduction mechanisms and on optical modelling are detailed.

1.1 Introduction

The Transparent Conductive Materials (TCMs) possess the characteristic of the coexistence of electrical conductivity and optical transparency. For TCO materials, this property depends on the nature, number, and atomic arrangements of metal cations in crystalline or amorphous oxide structures, and on the presence of intrinsic or intentionally introduced defects. Other TCMs are emerging recently. The important TCMs are [13, 15, 17, 18, 25]:

* Impurity-doped oxides such as ZnO, In_2O_3, SnO_2 and CdO,
* Binary or ternary metal oxide compounds such as Zn_2SnO_4, $ZnSnO_3$, $Zn_2In_2O_5$, $Zn_3In_2O_6$, Cd_2SnO_4,
* Multi-component oxides consisting of combinations of ZnO, In_2O_3 and SnO_2,
* Others emerging TCMs such as metallic nanowires or grids, carbon nano-tubes or graphene [10].

Sn-doped In_2O_3 (ITO) and F-doped SnO_2 (FTO) thin films are well known, and widely used for most applications but they present some limitations in our case. The expanding use of TCO materials, especially for the production of transparent electrodes for optoelectronic device applications, is endangered by the scarcity and high price of In. Moreover, other considerations must be taken into account for PV industry, such as the ability to deposit on large areas, the toxicology of the material, as well as the ability to introduce light scattering within the active layers of the solar cells. Moreover, F doped SnO_2 thin films exhibit a poor chemical stability against hydrogen-rich plasmas. This situation drives the search to find an alternative to these TCOs.

The best candidates to combine electrical and optical properties are doped ZnO thin films with substitutional doping such as Al, B, or Ga. ZnO:B is usually deposited by CVD, which requires a thick layer deposition at very high temperature to obtain satisfying electrical properties and light scattering feature [14]. ZnO:Ga thin films deposited by RF sputtering exhibit a high stability which makes them a good choice for ZnO doping applications. But the electrical resistivity remains higher compared to ZnO:Al thin films [4]. Most works have focused on Al-doped ZnO (AZO) which can have low resistivity (of the order of $10^{-4}\,\Omega$.cm), with non-toxic and inexpensive source materials. Because of its potential lower cost and the possibility to roughen its surface by etching, Al-doped ZnO may replace these materials in photovoltaic applications.

1.2 Structural properties

1.2.1 Crystal structure

Undoped and doped ZnO material crystallizes under ambient temperature and pressure in the wurtzite structure, which belongs to the hexagonal system with space group $C_{6\nu}^4$

($P6_3mc$). Their lattice parameters are: a = 3.2495 Å and c = 5.2069 Å at 300 K [28]. The wurtzite lattice can be considered as two interpenetrating hexagonal close-packed sublattices offset along the c-axis, as presented in Figure 1.1a. In this structure, atoms of one kind are tetrahedrally bonded to four nearest neighbours of the other kind. For doped ZnO, some sites of Zn atoms are replaced by donor atoms.

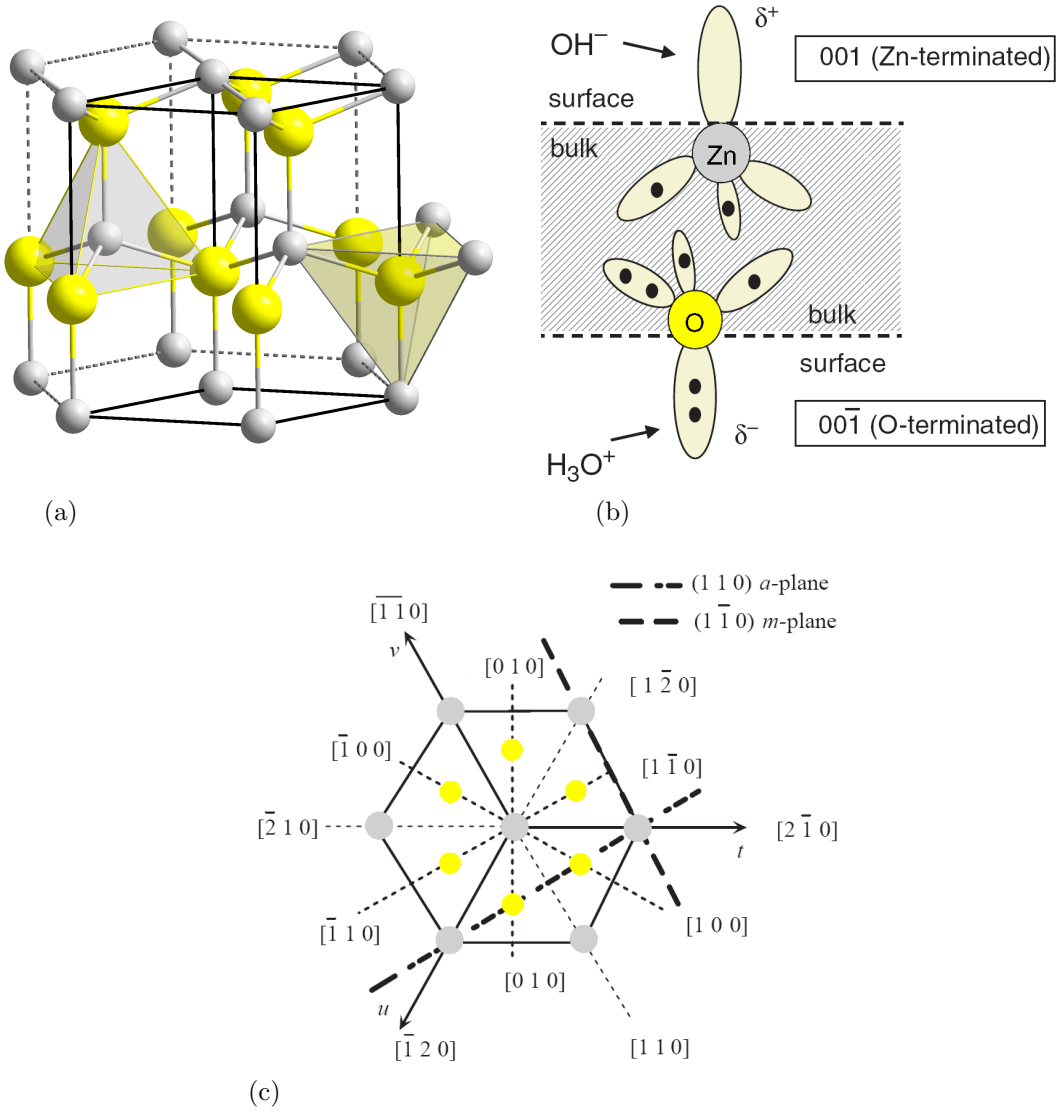

Figure 1.1: Wurtzite crystal structure with oxygen atoms (yellow) and zinc atoms (grey) (a). Model for etching mechanism by acidic and alkaline solutions on polar ZnO faces (b) [22]. Orientations and associated directions of the wurtzite structure shown as a projection on the (001) basal plane (c) [34].

Perpendicular to the c-axis, the unit cell consists of double layers composed of planes of zinc and oxygen atoms, respectively. The wurtzite structure does not present an inversion symmetry along the c-axis: the (001) and (00$\bar{1}$) terminations are respectively zinc and oxygen-terminated surfaces of the polar [001] direction.

1.2.2 Chemical etching behaviour

The Zn-O bond is mostly ionic and these polar bonds lead to planes of positively charged zinc and negatively charged oxygen atoms perpendicular to the c-axis. This characteristic induces a polar symmetry in zinc oxide, which gives rise to some unique properties of ZnO: piezoelectricity, spontaneous polarization, and a strongly anisotropic etching behaviour. While the oxygen surface is strongly etched in slightly diluted acids (HCl, H_2SO_4, HNO_3, H_3PO_4), the zinc-terminated surface is quite resistant against these acids. The dangling bonds at the surfaces exhibit partially positive (δ^+ for Zn) or partially negative (δ^- for O) charge states. This leads to different reactivity depending on the ion charge as shown in Figure 1.1b [17, 22].

In acidic solution such as HCl, the acid dissociates almost completely to hydronium H_3O^+ and chloride Cl^- ions in water. The zinc ions Zn^{2+} formed by the oxidation of the zinc atoms by the hydronium ions form complexes with up to six ligands with chloride ions and water molecules. The reaction is described as follows:

$$\begin{aligned} &ZnO_{(s)} + 2H_3O^+_{(aq)} \rightarrow Zn^{2+}_{(aq)} + 3H_2O_{(l)} \\ &Zn^{2+}_{(aq)} + xCl^-_{(aq)} + (n-x)H_2O \leftrightarrows [ZnCl_x(H_2O)_{(n-x)}]^{2-x}_{(aq)} \\ &\text{n=4 or 6}; 0 \leq x \leq n \end{aligned} \tag{1.1}$$

1.3 Thermodynamic properties

ZnO has a density of 5.606 g.cm^{-3}, which corresponds to 4.2×10^{22} ZnO molecules/cm^3 at room temperature. The thermal expansion coefficients at 300 K are 2.92×10^{-6} K^{-1} along the c-axis, and 4.75×10^{-6} K^{-1} perpendicularly to the c-axis [17]. The thermal conductivities at 300 K are 69 W/m.K along the c-axis, and 60 W/m.K perpendicularly to the c-axis. The melting point of ZnO is 2248 K.

1.4 Electrical properties

1.4.1 Energy band structure

Zinc oxide is a direct gap semiconductor with a band gap energy of 3.4 eV. The fundamental band gap E_{g0} sets the low energy limit of optical transparency (Figure 1.2), which should be superior to 3 eV to ensure transparency throughout the visible spectrum.

Stoichiometric single crystal ZnO is undoped, and pratically insulator at room temperature, with a carrier concentration of the order of $10^{13}/10^{14}$ cm^{-3}. To become conducting, the oxide must be doped to degeneracy by increasing the free carrier density enough to move the Fermi level into the conduction band, as shown in Figure 1.7b. The degenerate doping can be achieved in two different ways [17, 24, 34]:

* Creation of intrinsic donors by defects within the crystal structure,

* Introduction of extrinsic dopants.

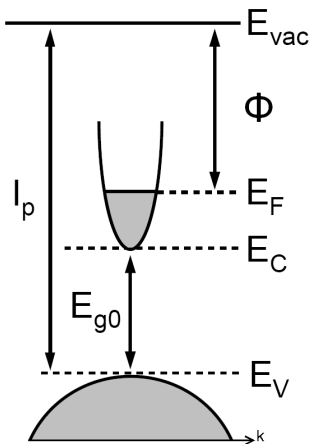

Figure 1.2: Schematic energy band structure of conventional TCO materials, with I_p, Φ, E_{g0}, E_{vac}, E_C, E_V, and E_F, the ionization potential, work function, intrinsic band gap, vacuum level, conduction band minimum, valence band maximum, and Fermi level respectively [25].

ZnO with a wurtzite structure is intrinsically a n-type semiconductor because of deviation from the stoichiometry of the ZnO crystal structure. This deviation can lead to oxygen vacancies (V_O) and zinc interstitial (Zn_i), with both having shallow energetic donor positions below the conduction band as presented in Table 1.1. Look *et al.* [31] suggested that Zn_i rather than V_O is the dominant native shallow donor in ZnO. Indeed, the activity of V_O as a shallow donor is widely discussed recently. Oxygen vacancies present a high formation energy and can not act as a shallow donor. Native defects can not explain the high n-type doping. It has been suggested that the n-type conductivity of unintentionally doped ZnO films can be due to hydrogen that acts as a shallow donor [26, 36, 48, 52]. This hypothesis is supported by the high mobility of hydrogen which can easily diffuse at low temperature inside the material.

Depending on the growth atmosphere, different defects are most likely: Under zinc-rich conditions the oxygen vacancy dominates, while the zinc vacancy and the oxygen interstitials are the most likely defects for an oxygen-rich atmosphere. Moreover, non-negligible quantity of hydrogen is present in many growth methods [17, 34]. However, the intrinsic doping is not enough to obtain reliable and conducting TCOs. First, the resistivity is only about 10^{-2} to 10^{-3} Ω.cm. Furthermore, these films are not stable at ambient conditions due to the reoxidation of the oxygen-deficient or zinc-rich films, which increases their resistivities significantly.

The extrinsic doping of ZnO is realized by introducing foreign atoms to the crystal structure. For ZnO, n-doping is easier compared to p-doping due to its high conduction band, while a p-type doping is facilitated for a low band gap material (Figure 1.2) [3, 37]. The p-type dopants have to compensate these intrinsic donor carriers. As a consequence, p-type doping issues are: the low dopant solubility, the formation of deep level, the compensation by native defects, intrinsic donor defects or extrinsic electron sources, the possible change from shallow acceptor behaviour to donor behaviour depending on the

position of the impurities inside the crystal structure, and the natural tendency of acceptor to form electrically inactive complexes with native defects or others impurities [45].

As n-type dopants, elements from column XIII such as boron, aluminium, gallium and indium are generally used. These elements have one additional valence electron compared to the zinc atoms from the column XII. During deposition, these atoms B, Al, Ga, or In, can be partially substituted to Zn, bringing one additional weakly bound electron [33,37]. The donor binding energies for the extrinsic dopants are presented in Table 1.1.

Table 1.1: Donors and acceptors, their lattice positions and energies in zinc oxide.

Element	Structure	Type	Energy	Source
Zn	Zn_i	Donor	E_C-E = 30/46 meV	[31,47,50]
H	H_i	Donor	E_C-E = 37/46 meV	[21,50]
Al	Al_{Zn}	Donor	E_C-E = 53.0 meV	[32]
Ga	Ga_{Zn}	Donor	E_C-E = 54.5 meV	[32]
In	In_{Zn}	Donor	E_C-E = 63.2 meV	[32]
O	V_O	Donor	E_C-E = 300 meV	[50]
Li	Li_{Zn}	Deep acceptor	E-E_V = 800 meV	[32,53]
Na	Na_{Zn}	Deep acceptor	E-E_V = 600 meV	[53]
N	N_O	Acceptor	E-E_V = 110 meV	[38]

On the other hand, owing to the high dispersion of the conduction band, the increase of the carrier concentration with n-doping shifts the Fermi level from the middle of the band gap toward the conduction band. When doping reaches a sufficient high level, the Fermi level crosses into the conduction band. The carrier concentration influences the band gap, as further detailed in section 1.5.2.1.

1.4.2 Carrier transport mechanisms

The degenerated characteristics of ZnO:Al materials lead them to behave like metals. The Drude model of electrical conduction is used to explain the transport properties of electrons in ZnO:Al thin films. The conductivity σ is defined as :

$$\sigma = \frac{1}{\rho} = \frac{Ne^2\tau}{m^*} = eN\mu \tag{1.2}$$

with ρ the resistivity, N the free carrier density, τ the relaxation time between two scattering events, m^* the effective mass of an electron, and μ the carrier mobility defined as $\mu = e\tau/m$.

Microscopically, the total conductivity σ of polycrystalline thin films is limited by various scattering events i, directly from the bulk σ_{bulk} or due to the presence of grain boundaries σ_{gb}, following the Matthiessen's rule:

$$\frac{1}{\sigma} = \sum_i \frac{1}{\sigma_i} = \frac{1}{\sigma_{bulk}} + \frac{1}{\sigma_{gb}} \tag{1.3}$$

The main scattering mechanisms from the bulk are :

* **Ionized impurities scattering**, due to deflection of free carriers by the potential of a charge center originating from doping impurities.

* **Phonon scattering**, by vibrations in the crystal lattice. This mode is separated into optical phonon scattering due to the interaction of electrons with the electric field induced by the lattice vibration at optical frequencies, and acoustic phonon scattering caused by the interaction of the electrons with the lattice deformation corresponding to pressure waves.

* **Piezoelectric scattering**, created from the electric fields produced by the strain associated with phonons, in a crystal without inversion symmetry.

* **Neutral impurity scattering**, due to uncharged impurity atoms.

These scattering phenomena are related to the bulk single crystal material. However, thin film TCOs are usually polycrystalline. In this case, an additional scattering mechanism occurs:

* **Grain barrier scattering**, due to the localization of acceptor centres in grain boundaries, which capture electrons from the conduction band. The grain boundaries are charged negatively and a space charge region extends into the crystallite forming a "back-to-back" Schottky potential barrier. In these cases, the current flow occurs both by thermionic emission over the barrier and by tunnelling through the barrier.

The contribution of each type of scattering can vary very strongly with temperature and/or with the impurity concentration. In the case of highly doped ZnO:Al thin films, the main scattering processes considered are ionized impurities scattering, phonons scattering and grain barrier scattering. The piezoelectric mode scattering leads to an anisotropic mobility in ZnO, but is only significant at temperatures around 100 K: the mobility is isotropic at room temperature. Concerning the neutral impurity scattering, since the shallow donors in ZnO exhibit low ionization energies as presented in Table 1.1, the concentration of neutral donors at room temperature is very low and is not taken into consideration [12].

1.4.2.1 Ionized impurities scattering

The reduction of mobility due to the ionized impurity scattering can be evaluated in the Brooks-Herring approach [6,8]. This takes into account the screening of the Coulomb field of the ionized impurity centres by the free electrons and holes.

$$\mu_{ii} = \frac{3(\varepsilon_r \varepsilon_0)^2 h^3}{Z^2 m^{*2} e^2} \frac{n}{N_i} \frac{1}{F_{ii} \zeta_d} \tag{1.4}$$

with F_{ii}, the screening function, and $\zeta_d = 1 - m_0^*/m^*$, a parameter which describes the non-parabolicity of the conduction band (m^*, m_0^*, effective masses in the conduction band and at the conduction band edge, respectively) [1,12,17].

Equation 1.4 shows an **independence of the mobility as a function of the temperature**.

1.4.2.2 Phonon scattering

Generally the scattering by optical phonons is important near and above room temperature. In the case of the ZnO thin films, up to temperatures of 300 - 400 K, the prevalent process is the scattering by acoustical phonons as reported in the literature [1, 41]. The lattice deformation scattering due to a local energetic shift of the band edges by acoustical phonons is:

$$\mu_{a-ph} = r_{a-ph} \frac{\sqrt{8\Pi} e \bar{h}^4 c_l}{3E_1^2 \sqrt{m^{*5}(kT)^3}} \tag{1.5}$$

with r_{a-ph} the Hall coefficient factor for acoustical phonon, c_l the averaged longitudinal elastic constant, E_1 the deformation potential, i.e. the energy shift of the conduction band per unit dilation, and m^* the effective electron mass.

Equation 1.5 shows a **temperature-dependence in $1/T^{3/2}$**.

1.4.2.3 Grain barrier scattering

ZnO:Al thin films are usually polycrystalline, and exhibit a large amount of grain boundaries, which constitute crystallographic disturbed regions. Acceptor centres are localized at grain boundaries, which capture electrons from the conduction band. ZnO:Al thin films are n-type semiconductors, which lead to a band bending near the grain boundary and the generation of a depletion zone on both sides of a grain barrier accompanied by an energetic barrier of height Φ_b for the electrons. The grain boundaries are charged negatively and a space charge region extends into the crystallite forming a "back-to-back" Schottky potential barrier [2, 12]. This model developed by Seto [44] is schematically described in Figure 1.3.

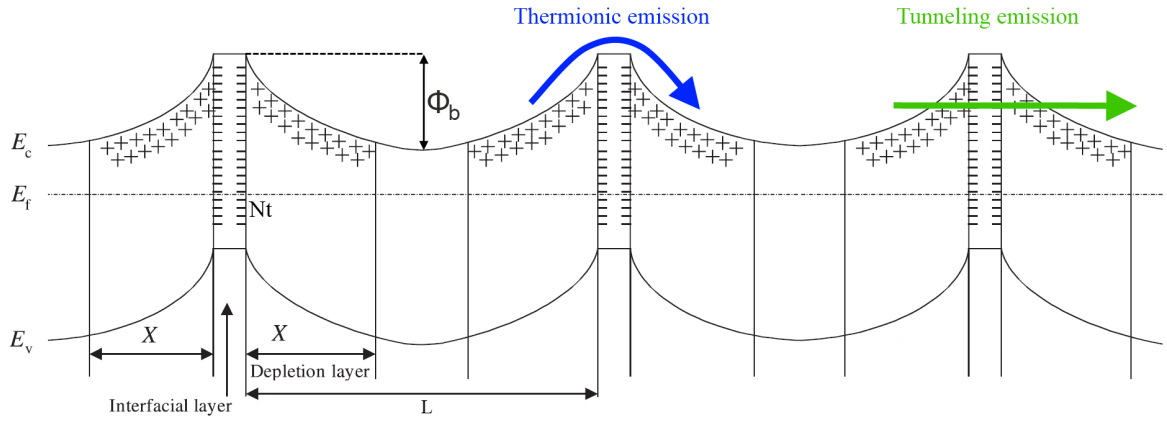

Figure 1.3: Schematic band diagram of successive grains of length L and charge carrier trap density N_t.

The potential barriers created by charged states oppose the passage of carriers from a grain to the neighbouring grains, which decrease the global mobility of the charge carriers. The carrier transport across the grain barriers is described by the classical thermionic emission and/or by quantum-mechanical tunnelling through the barriers by the electrons for very high carrier concentrations in the grains, which enable the narrowing of the

depletion width. The thermionic emission across the grain barriers with an energetic height Φ_b dominates, leading to the following effective mobility:

$$\mu_{gb} = \mu_0 exp(-\frac{\Phi_b}{kT}) \tag{1.6}$$

with T the sample temperature and k the Boltzmann constant. The factor μ_0 is the mobility inside the grain such as:

$$\mu_0 = \frac{eL}{\sqrt{2\Pi m^* kT}} \tag{1.7}$$

The grain barrier energy is a function of the carrier concentration, as presented in Figure 1.4 and is given by:

$$\Phi_b = \begin{cases} \dfrac{e^2 L^2 N}{8\varepsilon\varepsilon_0} & \text{for LN} < \text{N}_\text{t} \\ \dfrac{e^2 N_t^2}{8\varepsilon\varepsilon_0 N} & \text{for LN} > \text{N}_\text{t} \end{cases} \tag{1.8}$$

with $\varepsilon\varepsilon_0$ the static dielectric constant, N the carrier density in the grain, N_t the charge carrier trap density at the boundaries, and L the grain length.

For LN $<$ N_t, the number of carriers inside the grains is lower than the number of traps at the grain boundaries: the traps are partially filled and the carriers in the grains are completely depleted: the potential energy barrier will increase linearly with the increase of the carrier concentration (Figure 1.4a).

For LN $>$ N_t, the number of carriers inside the grains is higher than the number of traps at the grain boundaries: the traps are completely filled and only part of the grain is depleted: the potential energy barrier decreases as the inverse of the increasing carrier concentration (Figure 1.4c).

In our case, ZnO:Al thin films are highly doped, which give a high carrier concentration: the second Equation 1.8 is used, for LN $>$ N_t.

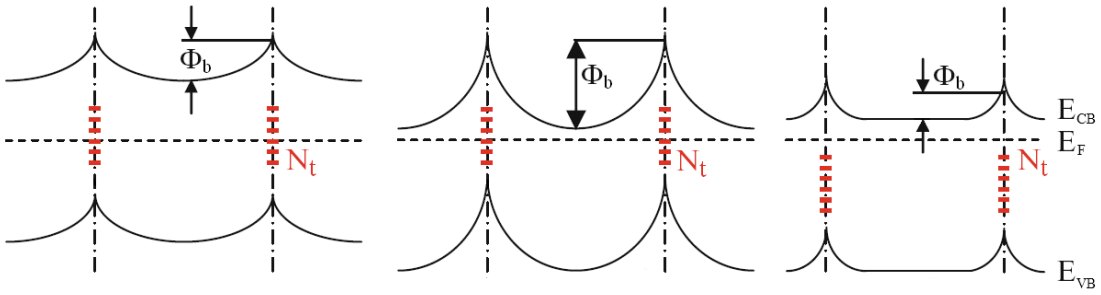

(a) LN $<$ N_t (b) LN $=$ N_t (c) LN $>$ N_t

Figure 1.4: Schematic band diagrams depending on the carrier concentration.

This model developed by Seto [44] describes non-degenerate semiconductors. Other models have been studied to elucidate grain-boundary-limited conduction in polycrystalline semiconductors for both degenerate and non-degenerate doping [40], but the Setos

formula remains the more used. In our case, the Setos model is not used for ZnO:Al thin films with a high dopant concentration, which do not exhibit an energy activation ($E_a = 0$ for a degenerately doped grain interior and $E_a > 0$ for non-degenerate doping). This implies that, at the grain boundaries, the Fermi level is situated well above the conduction band minimum. The Setos model is used for film presenting lower carrier concentrations, i.e. for degenerate semiconductors with the Fermi level below the intergrain electrostatic barrier, or for non-degenerate semiconductor.

Equation 1.6 shows a **temperature-dependence in exp(-1/T)**.

1.4.2.4 Temperature-dependent conductivities

As previously discussed, the scattering processes present different temperature-dependent mobilities, such as an independence for the ionized impurities scattering, a temperature-dependence in $1/T^{3/2}$ for phonons scattering, and a temperature-dependence in exp(-1/T) for grain barrier scattering. In this way, it is possible to determine the dominant scattering process for each sample by measuring the evolution of the mobility (or the conductivity) as a function of the temperature during the Hall effect measurements.

For our ZnO:Al thin films, the carrier concentrations are temperature-independent, which means that these films are degenerate semiconductors. Temperature-dependent mobility data of nominally undoped ZnO single crystals, reported by Hagemark *et al.*, are displayed in Figure 1.5 [20, 27].

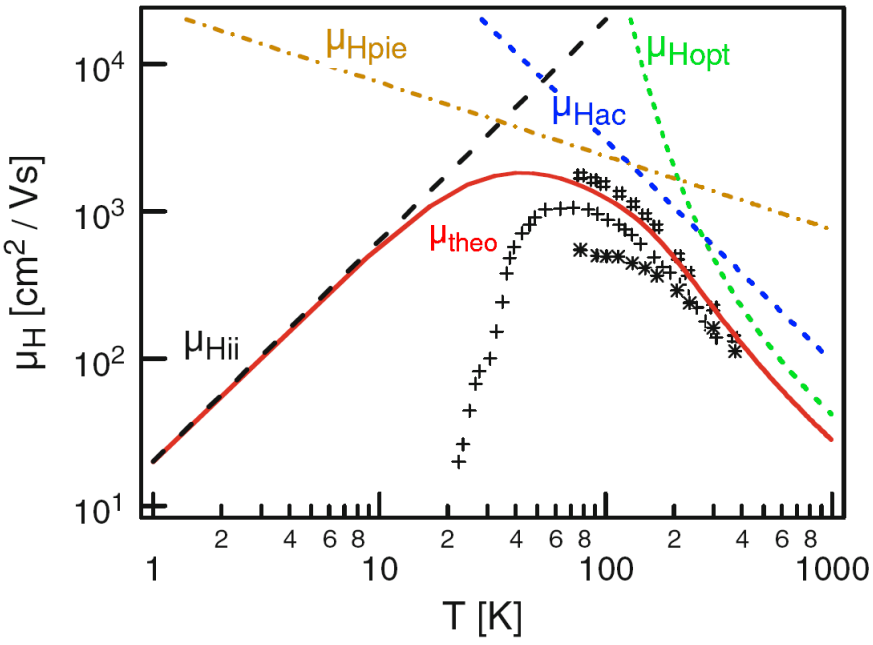

Figure 1.5: Experimental Hall mobility data of Hagemark et al. [20, 27] in comparison to the theoretical lattice mobility μ_{theo}. The crystals were vapor-phase grown, not intentionally doped, with a carrier density between 1 and 3×10^{16} cm^{-3} at RT. The contributions to the total mobility by the individual scattering processes: acoustic μ_{Hac} and polar-optical μ_{Hop} phonon, piezoelectric μ_{Hpie} and ionized impurity scattering μ_{Hii} are also shown as dashed or dotted lines.

1.5 Optical properties

1.5.1 Dielectric function

The optical constants defined as the refractive index n and the extinction coefficient k are related to the real and imaginary parts of the dielectric function at the frequency ω through Equation 1.9:

$$\varepsilon(\omega) = (n + ik)^2 \tag{1.9}$$

The main issue is to model the free carrier absorption and reflection in the infrared regime and the band gap absorption in the UV region [39, 46]. The dielectric function used in this work is split up into three different constituents which take account of the different absorption mechanisms :

$$\varepsilon(\omega) = \varepsilon_\infty + \varepsilon_{IR} + \varepsilon_{BG} \tag{1.10}$$

The first factor ε_∞ is the high frequency dielectric constant. This parameter is sometimes already included in the Drude formula [5]. This factor is commonly used in the Drude modeling of TCOs, and describes the contribution of bonded electrons at higher frequencies when the electric polarization cannot follow the oscillation of the light field [11, 49].

The second factor $\varepsilon_{\mathrm{IR}}$ is a simple Drude model defined by Equation 1.11. This model is well suited for highly degenerated semiconductor materials such as ZnO:Al, for energy $h\nu \ll E_g$ in the near infrared region [42].

$$\varepsilon(\omega) = -\frac{\omega_p^2}{\omega^2 + i\Gamma_d\omega} \tag{1.11}$$

with ω_p and Γ_d the plasma frequency and the damping term defined respectively by Equation 1.12 and Equation 1.13.

$$\omega_p^2 = \frac{e^2 N_e^{opt}}{\varepsilon_0 m^*} \tag{1.12}$$

$$\Gamma_d = \frac{e}{\mu_{opt} m^*} \tag{1.13}$$

with N_{opt} the optically active free electron density, m^* the effective mass of electrons at the bottom of the conduction band, e the elementary charge, ε_0 the vacuum permittivity and μ_{opt} the optical mobility [11].

The third factor $\varepsilon_{\mathrm{BG}}$ is the fundamental absorption of the semiconductor. An additional oscillator is necessary to fit experimental data for the whole electromagnetic spectrum. Many models have been tested: Lorentz [46], Cauchy [49], Sellmeier [9], Forouhi-Bloomer [29, 30]. For spectroscopic ellispometry, in this work, a Tauc-Lorentz is finally chosen. This empirical parameterization is based on the Tauc expression for the imaginary part of the dielectric function near the band edge, and the Lorentz oscillator model. This model considers also the inter band transitions from the valence band to higher states in the conduction band [11]. The Tauc-Lorentz model were employed initially to model the dielectric function of amorphous materials, and recently has also been applied to dielectric

function modelling of transparent conductive oxides [16, 43], and ZnO:Al thin films [23].

1.5.2 Transmittance and reflectance spectra

Figure 1.6 shows the transmittance and reflectance spectra of a typical ZnO:Al thin film.

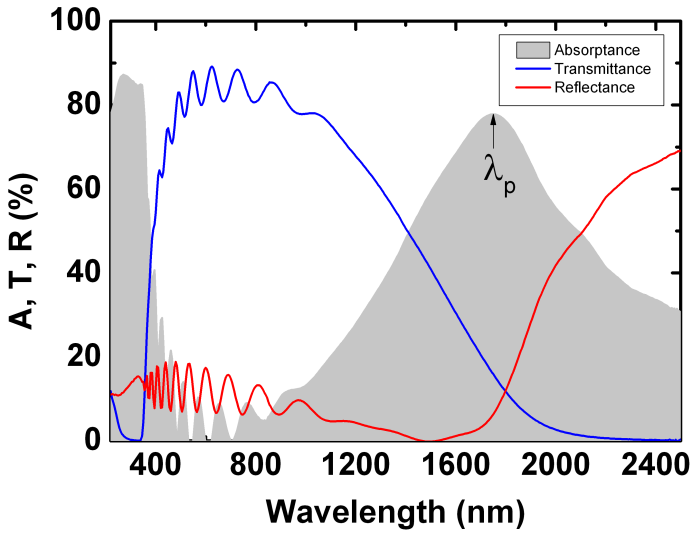

Figure 1.6: Optical spectra of typical ZnO:Al thin film.

Three different regions can be observed as a function of the wavelength: the ultraviolet region (UV) below 400 nm, the visible (VIS) and near infrared region (NIR), between 400 and 1200 nm, and the infrared region (IR) above 1200 nm.

1.5.2.1 UV region

Below 400 nm, in the UV region, the band gap absorption takes place. In this work, the optical band gap energy E_g has been obtained for the ZnO:Al thin films with various thicknesses d, from the transmittance spectra T, versus the radiation energy E, by extrapolation of the linear region of the plot $((\ln T)E/d)^2$ versus E, according to direct allowed transitions [19].

The optical band gap is related to the carrier concentration through two different phenomena as presented in Figure 1.7: the first one is the Burstein-Moss band-filling effect, which shifts the measured band-edge with increasing carrier concentration toward high energies by a term ΔE^{BM} [7, 35]. The conduction band states are filled by excess carriers from the impurities due to small density of states of ZnO near the conduction-band minimum. In this case, the bandgap broadening ΔE^{BM} is :

$$\Delta E^{BM} = \frac{\bar{h}^2}{2}(3\Pi^2 N)^{2/3}\left(\frac{1}{m_e^*} + \frac{1}{m_h^*}\right) \tag{1.14}$$

with N the free electron concentration, m_e^* and m_h^* the effective mass of electron and holes respectively.

The second phenomenon leads to a narrowing of the band gap when donor density exceeds a certain value by a term ΔE^{EX} [51]. This phenomenon is due to many body effects such as exchange energy due to electron-electron and electron-impurity interactions [45]. In this case the band gap narrowing ΔE^{EX} is:

$$\Delta E^{EX} = -\frac{e}{2\Pi\varepsilon_s}(3N\pi)^{1/3} \tag{1.15}$$

with ε_s the dielectric constant of the semiconductor.

In this way, the total optical band gap measured is :

$$E_g = E_{g0} + \Delta E^{BM} - \Delta E^{EX} \tag{1.16}$$

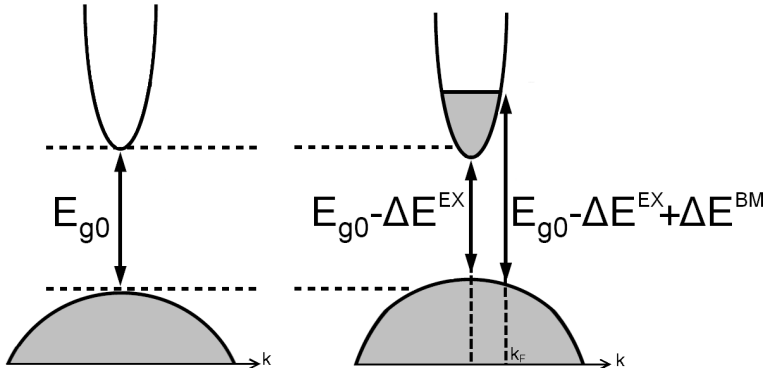

(a) Undoped ZnO (b) Heavily doped ZnO

Figure 1.7: Schematic band structure for undoped (a) and heavily doped (b) ZnO. k_F is the Fermi wave vector.

1.5.2.2 VIS and NIR regions

In this region, the ZnO:Al thin films are transparent. However, several factors limit the transparency, such as reflection losses at the interface, and residual absorption from defects or from free carriers. The oscillations observed come from the destructive and constructive interferences from the smooth film, dependent on the thickness and refractive index of the layer. The roughness of an etched film decreases the amplitude of the interferences.

1.5.2.3 IR region

From NIR region, the transmittance gradually decreases, while the reflection slowly increases. This observation is explained by the absorption of the free carriers, described by the Drude model. This is due to collective oscillations of conduction band electrons known as plasma oscillations. The maximum absorption occurs at the characteristic plasma wavelength λ_p.

1.6 Conclusion

In this chapter, the physical and chemical laws that govern the properties of the ZnO:Al thin films have been presented in detail. They are the basis to understand and interpret

the observation realized in the following chapters.

The structural properties of the material are strongly influenced by the deposition and post-deposition parameters, and modify the electrical and optical properties of the ZnO:Al thin films. The chemical properties influence the wet chemical etching and the thermodynamic properties drive the annealing processes.

Some fundamentals studies established on the carrier transport mechanisms through the measurements of the temperature-dependent conductivities, as well as on the optical modelling of free electrons have been realized and are presented in chapter 3.

Bibliography

[1] M. Addonizio, A. Antonaia, and G. Cantele. Transport mechanisms of RF sputtered Al-doped ZnO films by H2 process gas dilution. *Thin Solid Films*, 349:93–99, 1999. (cited pages 19, 20, 100 et 112)

[2] M. A. Alim, S. Li, F. Liu, and P. Cheng. Electrical barriers in the ZnO varistor grain boundaries. *Physica Status Solidi (a)*, 203(2):410–427, Feb. 2006. (cited page 20)

[3] A. Allenic. *Structural, Electrical and Optical Properties of P-type Zinc Oxide Epitaxial Films*. University of Michigan, 2008. (cited page 17)

[4] V. Assunção, E. Fortunato, A. Marques, H. Águas, I. Ferreira, M. Costa, and R. Martins. Influence of the deposition pressure on the properties of transparent and conductive ZnO:Ga thin-film produced by r.f. sputtering at room temperature. *Thin Solid Films*, 427(1-2):401–405, Mar. 2003. (cited pages 14, 70, 82 et 83)

[5] S. Brehme, F. Fenske, W. Fuhs, and E. Nebauer. Free-carrier plasma resonance effects and electron transport in reactively sputtered degenerate ZnO: Al films. *Thin Solid Films*, 342:167–173, 1999. (cited pages 23 et 97)

[6] H. Brooks. Scattering by Ionized Impurities in Semiconductors. *Physical Review*, vol. 83:879, 1951. (cited page 19)

[7] E. Burstein. Anomalous Optical Absorption Limit in InSb. *Physical Review*, 93(3):632–633, Feb. 1954. (cited page 24)

[8] D. Chattopadhyay and H. Queisser. Electron scattering by ionized impurities in semiconductors. *Reviews of Modern Physics*, 53(4):745–768, Oct. 1981. (cited page 19)

[9] Z.-H. Dai, R.-J. Zhang, J. Shao, Y.-M. Chen, Y.-X. Zheng, J.-D. Wu, and L.-Y. Chen. Optical Properties of Zinc-oxide Films Determined Using Spectroscopic Ellipsometry with Various Dispersion Models. *Journal of the Korean Physical Society*, 55(3):3–8, 2009. (cited page 23)

[10] S. De and J. N. Coleman. The effects of percolation in nanostructured transparent conductors. *MRS Bulletin*, 36(10):774–781, Oct. 2011. (cited page 14)

[11] N. Ehrmann and R. Reineke-Koch. Ellipsometric studies on ZnO:Al thin films: Refinement of dispersion theories. *Thin Solid Films*, 519(4):1475–1485, Dec. 2010. (cited page 23)

[12] K. Ellmer, A. Klein, and B. Rech, editors. *Transparent Conductive Zinc Oxide*, volume 104 of *Springer Series in Materials Science*. Springer Berlin Heidelberg, Berlin, Heidelberg, 2008. (cited pages 19 et 20)

[13] G. J. Exarhos and S. K. Sharma. Influence of processing variables on the structure and properties of ZnO films. *Thin Solid Films*, 270(1-2):27–32, Dec. 1995. (cited page 14)

[14] S. Faÿ. *L'oxyde de zinc par dépôt chimique en phase vapeur comme contact électrique transparent et diffuseur de lumière pour les cellules solaires*. PhD thesis, Ecole Polytechnique Federale de Lausanne, 2003. (cited pages 14 et 32)

[15] E. Fortunato, D. Ginley, H. Hosono, and D. C. Paine. Transparent Conducting Oxides for Photovoltaics. *MRS Bulletin*, 32(03):242–247, Mar. 2007. (cited page 14)

[16] H. Fujiwara and M. Kondo. Effects of carrier concentration on the dielectric function of ZnO:Ga and In2O3:Sn studied by spectroscopic ellipsometry: Analysis of free-carrier and band-edge absorption. *Physical Review B*, 71(7):1–10, Feb. 2005. (cited pages 24 et 97)

[17] D. Ginley, H. Hosono, and D. Paine. *Handbook of Transparent Conductors*. Springer, 2010. (cited pages 14, 16, 17 et 19)

[18] R. G. Gordon. Criteria for Choosing Transparent Conductors. *MRS Bulletin*, 25(08):52–57, Aug. 2000. (cited page 14)

[19] C. Guillén and J. Herrero. Optical, electrical and structural characteristics of Al:ZnO thin films with various thicknesses deposited by DC sputtering at room temperature and annealed in air or vacuum. *Vacuum*, 84(7):924–929, Mar. 2010. (cited pages 24, 92, 111 et 114)

[20] K. Hagemark and L. Chacka. Electrical transport properties of Zn doped ZnO. *Journal of Solid State Chemistry*, 15(3):261–270, Nov. 1975. (cited pages v et 22)

[21] D. Hofmann, A. Hofstaetter, F. Leiter, H. Zhou, F. Henecker, B. Meyer, S. Orlinskii, J. Schmidt, and P. Baranov. Hydrogen: A Relevant Shallow Donor in Zinc Oxide. *Physical Review Letters*, 88(4), Jan. 2002. (cited page 18)

[22] J. Hüpkes, J. I. Owen, S. E. Pust, and E. Bunte. Chemical etching of zinc oxide for thin-film silicon solar cells. *Chemphyschem : a European journal of chemical physics and physical chemistry*, 13(1):66–73, Jan. 2012. (cited pages v, 15, 16, 148 et 168)

[23] Y. Hwang, H. Kim, Y. Um, and H. Park. Optical properties of post-annealed ZnO:Al thin films studied by spectroscopic ellipsometry. *Materials Research Bulletin*, null(null), Apr. 2012. (cited page 24)

[24] A. Janotti and C. G. Van de Walle. Fundamentals of zinc oxide as a semiconductor. *Reports on Progress in Physics*, 72(12):126501, Dec. 2009. (cited page 16)

[25] A. Klein, C. Körber, A. Wachau, F. Säuberlich, Y. Gassenbauer, S. P. Harvey, D. E. Proffit, and T. O. Mason. Transparent Conducting Oxides for Photovoltaics: Manipulation of Fermi Level, Work Function and Energy Band Alignment. *Materials*, 3(11):4892–4914, Nov. 2010. (cited pages v, 14 et 17)

[26] S. H. Lee, T. S. Lee, K. S. Lee, B. Cheong, Y. D. Kim, and W. M. Kim. Characteristics of hydrogen co-doped ZnO:Al thin films. *Journal of Physics D: Applied Physics*, 41(9):095303, May 2008. (cited pages 17 et 112)

[27] P. Li and K. Hagemark. Low temperature electrical properties of Zn-doped ZnO. *Journal of Solid State Chemistry*, 12(3-4):371–375, Jan. 1975. (cited pages v et 22)

[28] D. Lide. *Handbook of Chemistry and Physics*. CRC Press, 74 edition, 1993. (cited page 15)

[29] Y. Liu, J. Hsieh, and S. Tung. Extraction of optical constants of zinc oxide thin films by ellipsometry with various models. *Thin Solid Films*, 510(1-2):32–38, July 2006. (cited page 23)

[30] S. Logothetidis, A. Laskarakis, S. Kassavetis, S. Lousinian, C. Gravalidis, and G. Kiriakidis. Optical and structural properties of ZnO for transparent electronics. *Thin Solid Films*, 516(7):1345–1349, Feb. 2008. (cited page 23)

[31] D. Look, J. Hemsky, and J. Sizelove. Residual Native Shallow Donor in ZnO. *Physical Review Letters*, 82(12):2552–2555, Mar. 1999. (cited pages 17 et 18)

[32] B. K. Meyer, J. Sann, D. M. Hofmann, C. Neumann, and A. Zeuner. Shallow donors and acceptors in ZnO. *Semiconductor Science and Technology*, 20(4):S62–S66, Apr. 2005. (cited page 18)

[33] T. Minami, H. Sato, H. Nanto, and S. Takata. Group III Impurity Doped Zinc Oxide Thin Films Prepared by RF Magnetron Sputtering. *Japanese Journal of Applied Physics*, 24(10):L781–L784, Oct. 1985. (cited pages 18 et 69)

[34] H. Morkoç and U. Özgür. *Zinc Oxide: Fundamentals, Materials and Device Technology*. John Wiley & Sons, 2008. (cited pages v, 15, 16 et 17)

[35] T. S. Moss. The Interpretation of the Properties of Indium Antimonide. *Proceedings of the Physical Society. Section B*, 67(10):775–782, Oct. 1954. (cited page 24)

[36] M.-S. Oh, D.-K. Hwang, J.-H. Lim, Y.-S. Choi, and S.-J. Park. Current-driven hydrogen incorporation in zinc oxide. *Applied Physics Letters*, 91(21):212102, 2007. (cited pages 17 et 112)

[37] J. Owen. *Growth, Etching, and Stability of Sputtered ZnO:Al for Thin-Film Silicon Solar Cells*. Forschungszentrum Jülich, 2011. (cited pages 17 et 18)

[38] D. Pfisterer, J. Sann, D. M. Hofmann, M. Plana, A. Neumann, M. Lerch, and B. K. Meyer. Incorporation of nitrogen acceptors in ZnO powder. *physica status solidi (b)*, 243(1):R1–R3, Jan. 2006. (cited page 18)

[39] A. Pflug, V. Sittinger, F. Ruske, B. Szyszka, and G. Dittmar. Optical characterization of aluminum-doped zinc oxide films by advanced dispersion theories. *Thin Solid Films*, 455-456:201–206, May 2004. (cited page 23)

[40] M. W. J. Prins, K.-O. Grosse-Holz, J. F. M. Cillessen, and L. F. Feiner. Grain-boundary-limited transport in semiconducting SnO2 thin films: Model and experiments. *Journal of Applied Physics*, 83(2):888, Jan. 1998. (cited pages 21 et 101)

[41] E. H. Putley. The Hall Effect and Related Phenomena. *American Journal of Physics*, 30(2):145, Mar. 1962. (cited page 20)

[42] Z. Qiao, C. Agashe, and D. Mergel. Dielectric modeling of transmittance spectra of thin ZnO:Al films. *Thin Solid Films*, 496(2):520–525, Feb. 2006. (cited page 23)

[43] P. I. Rovira and R. W. Collins. Analysis of specular and textured SnO2:F films by high speed four-parameter Stokes vector spectroscopy. *Journal of Applied Physics*, 85(4):2015, Feb. 1999. (cited page 24)

[44] J. Y. W. Seto. The electrical properties of polycrystalline silicon films. *Journal of Applied Physics*, 46(12):5247, Dec. 1975. (cited pages 20 et 21)

[45] D. Song. *Zinc Oxide TCOs (Transparent Conductive Oxides) and Polycrystalline Silicon Thin-Films for Photovoltaic Applications*. PhD thesis, New South Wales, 2005. (cited pages 18, 25 et 58)

[46] J. Steinhauser. *Low Pressure Chemical Vapor Deposited Zinc Oxide For Silicon Thin Film Solar Cells Optical And Electrical Properties*. PhD thesis, Université de Neuchâtel, 2008. (cited pages 23 et 32)

[47] F. Tuomisto, V. Ranki, K. Saarinen, and D. Look. Evidence of the Zn Vacancy Acting as the Dominant Acceptor in n-Type ZnO. *Physical Review Letters*, 91(20), Nov. 2003. (cited page 18)

[48] C. G. Van de Walle. Hydrogen as a cause of doping in zinc oxide. *Physical review letters*, 85(5):1012–5, July 2000. (cited pages 17 et 111)

[49] I. Volintiru. *Remote Plasma Deposition of Metal Oxides: Routes for Controlling the Film Growth*. PhD thesis, Eindhoven, 2008. (cited page 23)

[50] H. von Wenckstern, S. Weinhold, G. Biehne, R. Pickenhain, H. Schmidt, H. Hochmuth, and M. Grundmann. Donor levels in ZnO. *Advances in Solid State Physics*, 45:263–274, 2005. (cited page 18)

[51] P. Wolff. Theory of the Band Structure of Very Degenerate Semiconductors. *Physical Review*, 126(2):405–412, Apr. 1962. (cited page 25)

[52] B. Zhu, J. Wang, S. Zhu, J. Wu, R. Wu, D. Zeng, and C. Xie. Influence of hydrogen introduction on structure and properties of ZnO thin films during sputtering and post-annealing. *Thin Solid Films*, 519(11):3809–3815, Mar. 2011. (cited pages 17 et 111)

[53] D. Zwingel. Trapping and recombination processes in the thermoluminescence of Li-doped ZnO single crystals. *Journal of Luminescence*, 5(6):385–405, Dec. 1972. (cited page 18)

Chapter 2

Growth and Characterization techniques of ZnO:Al thin films

Contents

In this chapter, the growth techniques of ZnO:Al thin films and their post-deposition treatments are presented. The complete solar cell deposition is also exposed in this chapter. In a second part, the characterization techniques used in this thesis are presented.

2.1 Deposition and post-deposition treatments

2.1.1 RF magnetron sputtering of ZnO:Al thin films

A wide variety of thin film deposition methods has been investigated for the growth of undoped and doped ZnO: sol-gel processes [31,39,55], spray pyrolysis [3,32], pulsed-laser deposition [27,49], electrochemical deposition [56,57], molecular beam epitaxy [37,38] and atomic layer deposition [4,33]. Chemical vapor deposition is widely used for ZnO:B thin films at atmospheric pressure (AP-CVD) [26], low pressure (LP-CVD) [13,18,53] or with plasma assistance (PE-CVD) [24].

Compared to other thin-film deposition methods, magnetron sputtering is characterized by the following advantages for the deposition of undoped and doped ZnO [15]:

* Very good thickness uniformity and high density of the thin films,
* Low substrate temperatures (down to room temperature),
* Good adhesion of the films,
* High deposition rates,
* Good controllability and long-term stability of the process,
* Relatively cheap deposition method,
* Scalability to large areas [54].

The magnetron sputtering process is based on the creation of a plasma between a cathode (target) and an anode (vacuum chamber) by applying a voltage to the target as presented in Figure 2.1. The ionized gas is usually an inert gas such as Ar for a non-reactive sputtering deposition, or a gas mixture Ar + O_2 for a reactive sputtering deposition. The feature of the magnetron discharge is the magnetic confinement of the plasma in front of the target by using magnets. The deposition rate is increased due to the cycloidal orbits in the crossed electric and magnetic fields, leading to an increase of the ionization probability. The magnetic field strength is adjusted in such a way (about 50 to 200 mT) that the electrons are significantly influenced by the magnetic field while the ions are not. Therefore, magnetron discharges can be sustained at much lower pressures ($< 10^{-2}$ Pa) and/or higher current densities than the glow discharges without magnetic assistance [15].

The Ar^+ ions are accelerated towards the cathode by the electric field and bombard the target. Neutral species are ejected from the target and interact with the substrate after a straight line trajectory. Energetic negative ions O^- can also interfere during the film growth on the substrate, at very low pressure, when they possess a high mean free path, and undergo no or only few collisions. As for the secondary electrons from the target bombardment, they are kept away from the substrate due to the potential distribution in the discharge [15].

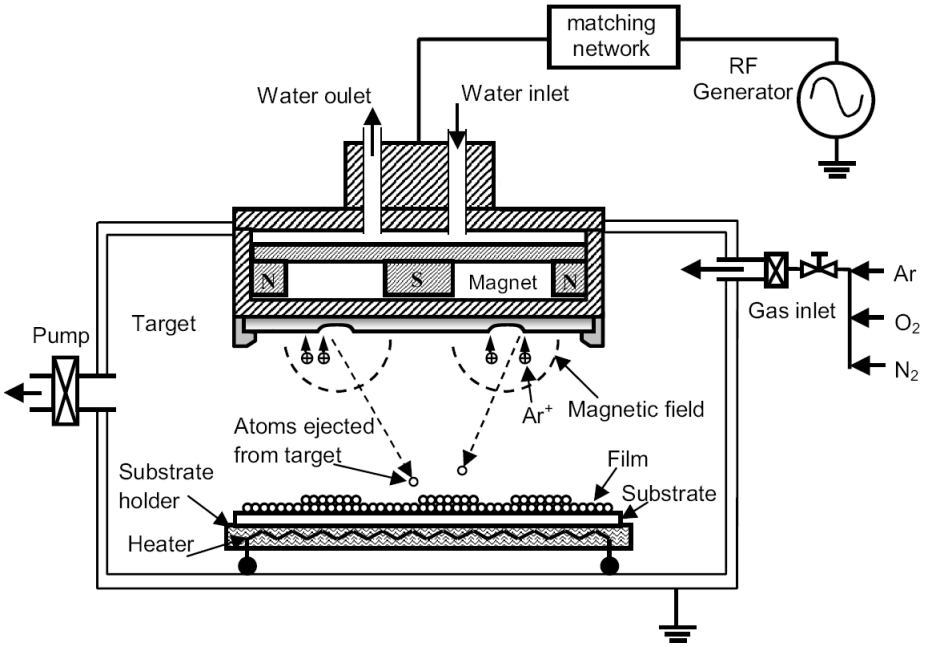

Figure 2.1: Schematic representation of a RF magnetron sputtering system.

Different excitation modes are possible: Direct Current (DC) excitation or Radio Frequency (RF) excitation, which strongly influence the potential distribution and hence the particle energies [16, 17, 29].

For non-reactive sputtering, a ceramic target is necessary for the deposition of zinc oxide, and the plasma excitation has to be performed by a RF power supply, since with DC excitation, no plasma can be ignited for insulating target. Reactive sputtering of metallic zinc or zinc alloy targets in argon/oxygen mixtures is possible, which avoids the use of expensive and mechanically fragile ceramic targets, and expensive RF power generator and matching units. Reactive sputtering is also possible for ceramic target in RF excitation mode, which gives the possibility to adjust the film stoichiometry through the reactive gas flow.

The RF power is supplied by a RF generator operating at a frequency of 13.56 MHz, connected to the cathode with an impedance matching network with variable capacitors. The confinement of the electrons in front of the cathode leads to a non-uniform erosion of the target in the areas of the highest magnetic field. This trend can lead to non-uniform deposition on the substrate, as studied in section 3.7. In this work, The ZnO:Al deposition are realized in two RF magnetron sputtering systems.

The main one is an Alliance concept DP 650 sputtering system, with equipments and deposition parameters summarized in Table 2.1. The system consists of one load lock with a transfer arm, and a vacuum chamber equipped with four planar targets of different materials as shown in Figure 2.2. Two targets are ceramic ones, and are bonded onto a copper backing plate to achieve a homogeneous cooling for ITO and ZnO:Al depositions, and two targets are metallic ones. Each target is protected by a shutter.

The second system is called "Cameleon", and has been developed in LPICM for *in-situ* measurements developed in chapter 3, with equipments and deposition parameters summarized in Table 2.2. *In-situ* resistance measurements can be performed on this system,

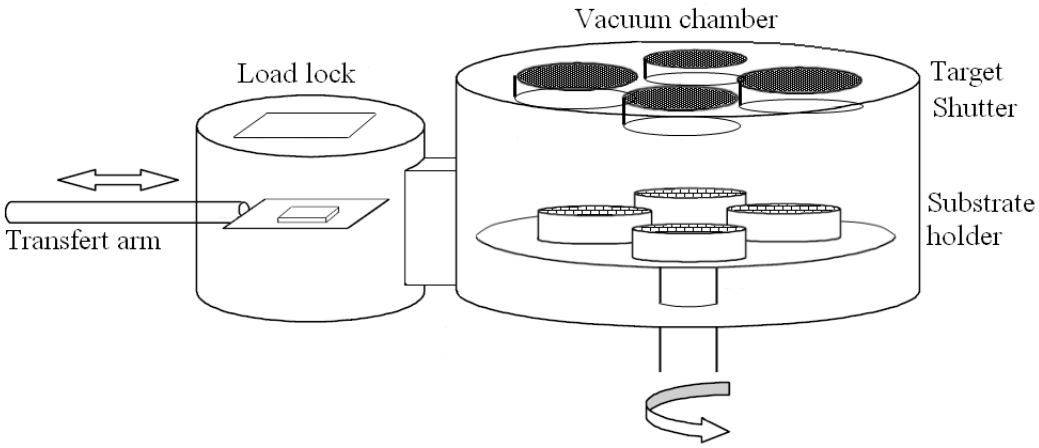

Figure 2.2: Schematic representation of the Alliance concept DP 650 system.

Table 2.1: Equipments and deposition parameters of ZnO:Al for the Alliance Concept system.

	PARAMETERS	DESCRIPTION
Equipment	Target	ZnO/Al_2O_3 (1 wt %)
		Williams Advanced Materials
		Diameter: 152 mm
		Density: 6.6 $g.cm^{-3}$
	Gauge 1	Pirani/Bayard Alpert
		Inficon BPG400
		From 10^5 to 10^{-8} Pa
	Gauge 2	Alcatel capacitance gauge
	Turbomolecular pump	Alcatel ATP400
	Rotary primary pump	Alcatel 2021
Deposition	Base pressure p_0	4×10^{-5} Pa
	Working gas	Ar and $Ar/3\%O_2$
	Working pressure p	From 0.01 to 2.2 Pa
	RF power P_W	From 50 W to 400 W
	Substrate temperature T_{sub}	From RT to 325 °C

in order to understand the first growth steps. This measurement system is presented in detail in the electrical part of the chapter, in section 2.2.4.3. The Cameleon reactor is quite simple, without load lock, as shown in Figure 2.3.

The used glass substrates are Alkaline Earth Boro-Aluminosilicate Corning Eagle XG.

2.1.2 Post-deposition treatments

In order to further improve the electrical and optical properties, a post-deposition treatment can be realized on ZnO:Al thin films. In this work, two different annealing processes have been investigated: thermal annealing process and laser annealing process.

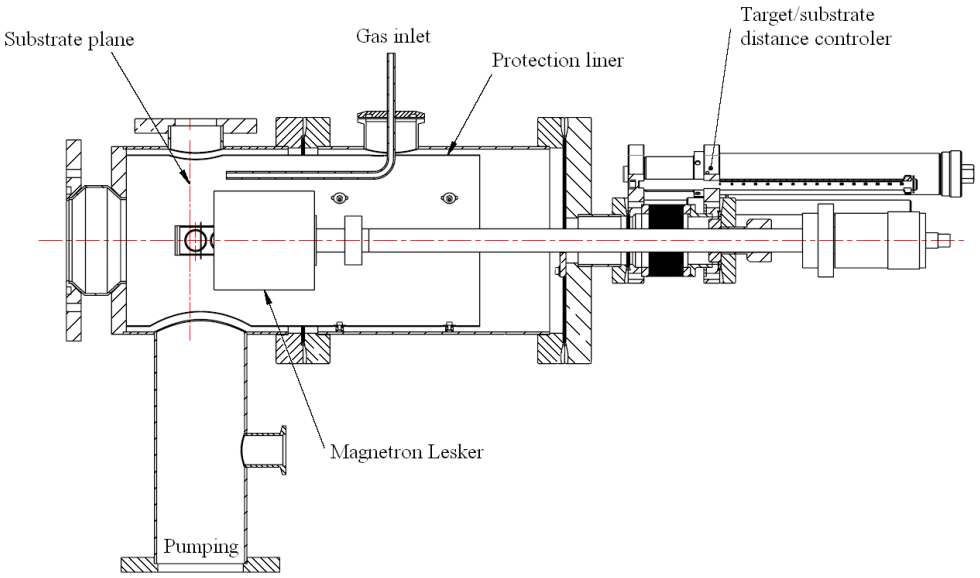

Figure 2.3: Schematic representation of the Cameleon system.

Table 2.2: Equipments and deposition parameters of ZnO:Al for the Cameleon system.

	PARAMETERS	DESCRIPTION
Equipement	Target	ZnO/Al_2O_3 (1 wt %)
		Umicore
		Diameter: 50.8 mm
		Density: 5.34 - 5.54 $g.cm^{-3}$
	Gauge 1	Baratron
	Gauge 2	Penning
	Turbomolecular pump	HiPace 300
	Primary pumps	Roots + Rotary vane pumps
Deposition	Base pressure p_0	10^{-4} Pa
	Working gas	Ar
	Working pressure p	From 0.1 to 10 Pa
	RF power P_W	From 40 W to 120 W
	Substrate temperature T_{sub}	From RT to 250 °C

2.1.2.1 Thermal annealing process

The as-deposited ZnO:Al thin films were heat-treated for 90 minutes, at a set temperature of 400, 450 or 500 °C. Three different atmospheres were investigated for the thermal annealing process: under vacuum, in N_2/H_2 at 5% of H_2 or in N_2.

Under vacuum, the heat treatment was carried out at a working pressure of 4×10^{-2} Pa from a base pressure of 5×10^{-3} Pa. The heating ramp was 15 °C/min and the samples were held at the set temperature for up to 90 minutes before cooling down at 3 °C/min. In N_2/H_2 and N_2 atmospheres, the set temperature was obtained in 5 minutes, and upheld during 90 minutes before a decrease of the temperature in 15 minutes.

2.1.2.2 Laser annealing process

The ZnO:Al thin films were laser annealed using an excimer laser (ELA) EXCICO as presented in Figure 2.4 with an emission wavelength of 308 nm. The samples are directly irradiated at the EXCICO company. Different pulses times and energies were tested, at 130 and 180 ns, and from 0 up to 1 J/cm^2 respectively. Each energy dose was delivered in a single pulse over an area of 1 cm^2.

Figure 2.4: Picture of the Excico laser annealing system.

Using this study, we were able to investigate the influence of the fluence on a single sample, by realizing a mapping at various fluences on a 5 × 5 cm ZnO:Al sample as shown in Figure 2.5.

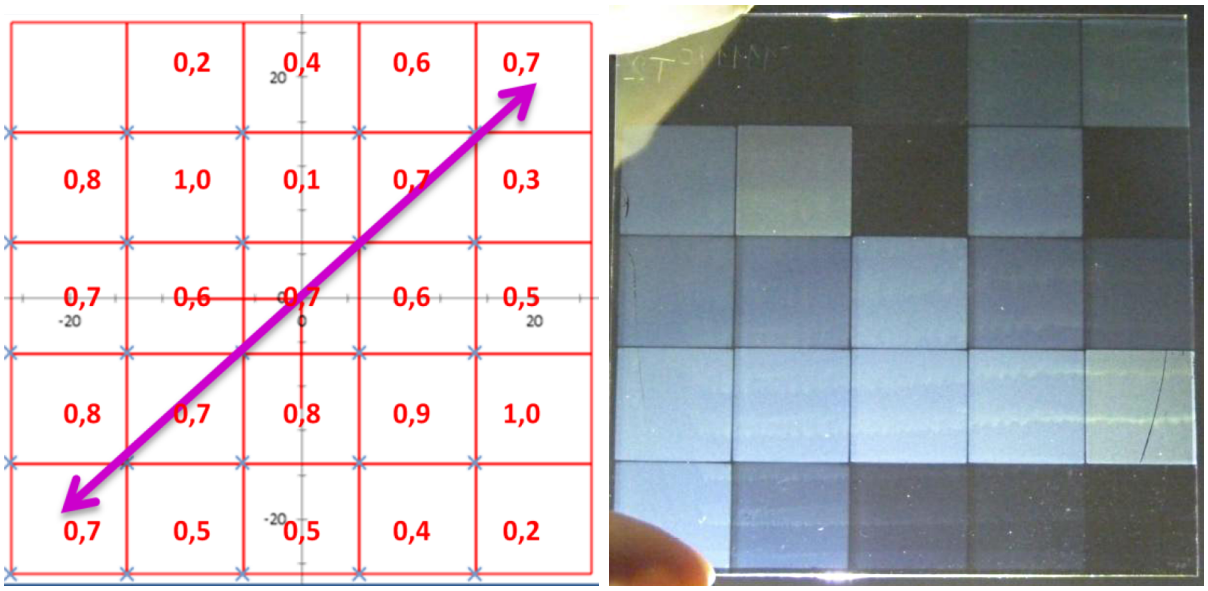

(a) (b)

Figure 2.5: (a) Schema of laser irradiation of a 5 × 5 cm ZnO:Al sample at different fluences in J/cm^2 and (b) picture of the irradiated sample.

2.1.3 Etching process

The as-deposited ZnO:Al thin films are relatively smooth. In order to increase light-trapping in the solar cell, the films were textured by a wet chemical etching step to increase the roughness of the surface of the films. In this work, the chemical texturing step is similar to the one reported by the Jülich group [28, 36] to produce textured substrates. The etching recipe consists of a dip in a dilute hydrochloric acid (HCl) solution at 0.5 w/w%. The etching time in the standard solution was generally 40 seconds. After the wet etch, the samples were rinsed with deionized water, and then in isopropanyl alcohol solution.

The influence of the etching time for different sputter ZnO:Al thin films has investigated in this work.

2.1.4 PECVD silicon deposition

The hydrogenated microcrystalline silicon depositions were made using an in-house radio frequency - Plasma Enhanced Chemical Vapour Deposition (RF-PECVD) system. A plasma excitation frequency of 13.56 MHz was used to enhance gas decomposition. Hydrogen (H_2) and silane (SiH_4) are the precursor gases for silicon deposition. The structural composition depends on the deposition process, and on the silane/hydrogen ratio in the gas mixture. The higher the silane concentration is, the lower the crystallinity of the silicon layers is [48]. Trimethylboron ($B(CH_3)_3$) and phosphine (PH_3) gases were introduced for p and n type silicon growth, respectively.

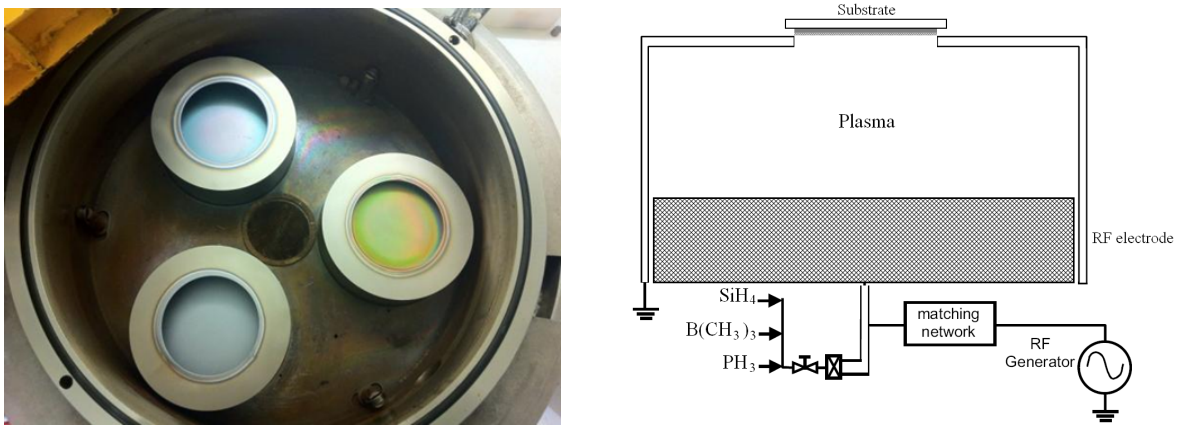

(a) (b)

Figure 2.6: Picture of the ARCAM reactor (a) and schematic representation of one of the plasma chambers of the ARCAM reactor (b).

The RF-PECVD technique is based on the deposition of films from reactive species created in the plasma at temperatures at which these gases would not be thermally dissociated. This is due to the ionization of the neutral gas molecules by the electrons accelerated in the oscillating electric field caused by the sinusoidal voltage applied to the RF electrode [30].

In this work, the reactor ARCAM[1] was used, designed and build in the early 80's, as shown in Figure 2.6, consisting in a mono-chamber, multi-plasma system [44]. The reactor can be described as an oven-like structure since it is made up of a single vessel in which all the elements are kept at the same temperature [30]. This reactor has been designed in such a way that the gas injected into the reactor, through a gas inlet that arrives below the electrode, is in contact with the entire vessel. However, the plasma itself and thus the reactive species are confined inside a plasma box as shown in Figure 2.6b. This reactor is designed to avoid cross contamination between p, i and n layers as in multi-chamber systems while keeping simplicity of single chamber reactors. Samples are located on a rotating plate which allows to start the plasma on a blank sample before rotating the substrate holder and put it in front of the plasma. The pumping of the process gases is ensured by a roots pump backed by a rotary vane pump.

Microcrystalline silicon cells were deposited in pin configuration. The temperature deposition was fixed at 165 °C, while the pressure, power, silane flow and hydrogen flow were optimized before each silicon deposition. The thickness of p and n layers were about 15 nm, and the thickness of the intrinsic layer was about 2 μm. The typical recipe for pin deposition is summarized by Table 2.3. These depositions have been realized by researchers or Ph.D. students from the laboratory whose the work is dedicated to the ARCAM reactor.

Table 2.3: Deposition parameters of pin silicon layers in the ARCAM reactor.

Layer	Gas flows	Pressure	RF power	Deposition time
p-type	H_2: 200 sccm SiH_4: 6 - 8 sccm $B(CH_3)_3$: 1.5 sccm	333 Pa	14 W	9 min
i-type	H_2: 200 sccm SiH_4: 6.5 - 13 sccm	333 Pa	10 - 14 W	202 min
n-type	H_2: 40 sccm SiH_4: 50 sccm PH_3: 2 sccm	15 Pa	1 W	6 min

2.1.5 Back contact deposition

The back contacts consist of a double stack of Indium Tin Oxide (ITO) and silver layers.

The ITO thin film was deposited by RF magnetron sputtering in the Alliance Concept reactor presented in section 2.1.1. The temperature was fixed at 180 °C, for a pressure of 0.45 Pa regulated with 41 sccm of Ar and 3 sccm of Ar/3%O_2 flows. The deposition time was 2 minutes at 200 W of power, for approximatively 80 nm of thickness.

The silver layer was deposited by thermal evaporation, in the Edwards evaporator. This technique allows to deposit materials at a relatively high deposition rate (up to 1 μm/min). The working pressure was 1×10^{-3} Pa.

[1] Action de Recherche Coordonnée sur les Matériaux Amorphes

2.2 Characterization techniques

2.2.1 Structural characterizations

The investigation of the structural properties is a key point for the understanding of the influence of the deposition parameters on the optical and electrical properties of the ZnO:Al thin films. These structural properties are studied by X-Ray Diffraction (XRD) and Raman spectroscopy.

2.2.1.1 X-Ray Diffraction measurement

X-ray diffraction is a versatile and non-destructive analytical technique to investigate the crystallography of the ZnO:Al thin films such as the preferred orientation, the crystallite size and the strain. The principle is based on constructive interference of monochromatic X-rays generated by a cathode ray tube, filtered to produce monochromatic radiation, collimated to concentrate, and directed towards the thin film. The interaction of the incident rays with the sample produces constructive interferences and a diffracted ray when conditions satisfy Bragg's Law:

$$n\lambda = 2d_{hkl}sin\theta_{hkl} \tag{2.1}$$

This law relates the wavelength of electromagnetic radiation λ to the diffraction angle θ_{hkl} and the interplanar distance of the (hkl) atomic plane in a crystalline sample $\mathrm{d_{hkl}}$. n is the integer known as the order of reflection. By scanning the sample through a range of 2θ angles, all diffraction directions of the lattice perpendicular to the substrate are obtained. Conversion of the diffraction peaks to d-spacings allows identification of preferred orientation.

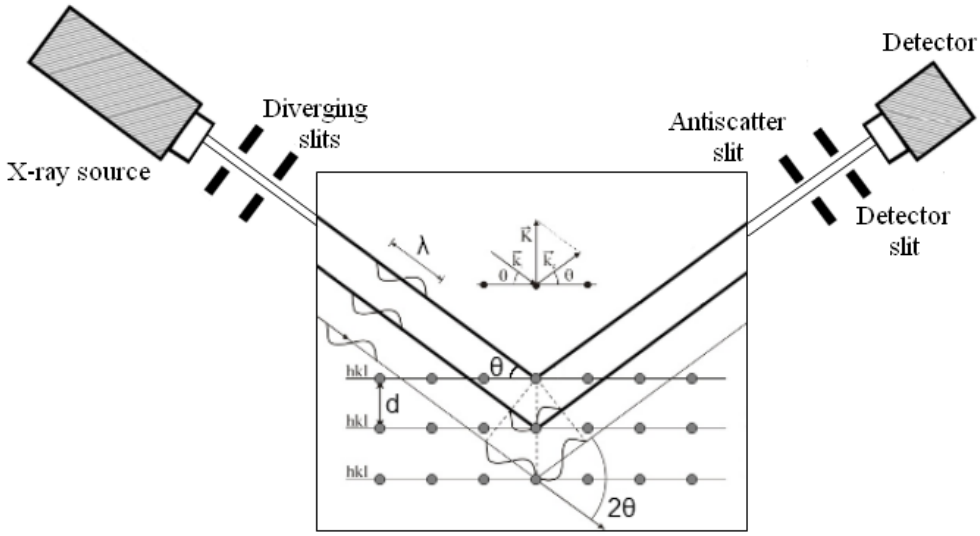

Figure 2.7: Schematic representation of θ-2θ configuration for XRD measurements.

In this work, the X-ray diffraction θ-2θ profiles were recorded with a PANalytical X'Pert powder diffractometer equipped with a Cu X-ray radiation source ($\lambda_{K\alpha 1} = 1.54059$ Å,

$\lambda_{K\alpha 2} =$ 1.54439 Å), operated at a voltage of 40 kV and current 40 mA, as schematically represented in Figure 2.7.

Williamson-Hall plots

All the films exhibit a strong c-axis preferred orientation revealed by the high intensity of the (002) reflection of ZnO:Al wurtzite structure, as shown in Figure 2.8a.

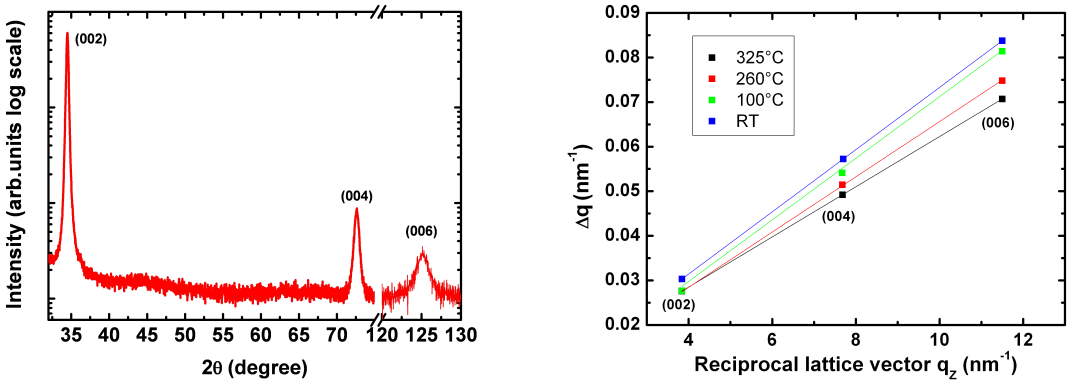

(a) (b)

Figure 2.8: Results from XRD measurements: XRD profile of ZnO:Al film deposited on glass substrate (a) and Williamson-Hall plots of films deposited at various temperatures (b).

There are different methods to extract the crystallite size and the strain information from the XRD peaks in a θ-2θ scan. The Scherrer formula provides an average size of the crystallites but neglects the strain. It is necessary to use an integral breadth method to provide average values of the size and strain [41].

The peak broadening comes from several sources:

* From the finite size of the coherent diffracting domain,
* From the strain inside the network due to crystalline defects, i.e. atoms deformed from ideal positions in a non-uniform way,
* From the instrumental effects.

The first contribution due to the finite size is independent of the diffraction plane considered, which means that the broadening in the reciprocal space Δd^* is constant:

$$\Delta d^* = \frac{1}{D} = \frac{2cos\theta\Delta\theta}{\lambda} = \frac{\beta cos\theta}{\lambda} \tag{2.2}$$

with D the thickness of the coherent diffracting domain, d the inter-reticular distance from the diffracting atomic planes, and d^* its equivalent in reciprocal space ($d^* = 1/d$). β is the Full Width at Half Maximum[2] of the diffraction peak such as $\beta = \Delta(2\theta) \approx 2\Delta\theta$.

[2]the FWHM denomination is used in the study.

The broadening in reciprocal space due to finite size effects is independent of the scattering vector q_z.

The second contribution arises from systematic shifts of atoms from their ideal positions, through point defects or poor crystallinity. These local variations are characterized by ε, corresponding to the weighted average strain:

$$\varepsilon = \frac{\Delta d}{d} = \frac{\Delta d^*}{d^*} \tag{2.3}$$

The broadening associated with strain is proportional to the scattering order.

A graphical separation of these two effects owing to their different dependence on q_z is possible by recording high-order reflections and using Williamson-Hall plots, as presented in Figure 2.8b [9,50]. The (002), (004) and (006) peaks were fitted to a linear combination of Gauss and Cauchy functions (Pseudo-Voigt function) to determine β_{exp}. Values have to be corrected from instrumental broadening, i.e. the third contribution to the peak broadening, following Equation 2.4 for a Gauss profile, or Equation 2.5 for a Cauchy profile:

$$\beta^2 = \beta_{exp}^2 - \beta_{instru}^2 \tag{2.4}$$

$$\beta = \beta_{exp} - \beta_{instru} \tag{2.5}$$

The broadening of the peaks in the reciprocal space arises from these contributions, through Equation 2.6 for a Gauss profile or Equation 2.7 for a Cauchy profile:

$$\left(\frac{\beta cos\theta}{\lambda}\right)^2 = \left(\frac{1}{D}\right)^2 + \left(\varepsilon \frac{2sin\theta}{\lambda}\right)^2 \tag{2.6}$$

$$\frac{\beta cos\theta}{\lambda} = \frac{1}{D} + \varepsilon \frac{2sin\theta}{\lambda} \tag{2.7}$$

For Williamson-Hall plots, $(\beta\cos\theta/\lambda)^2$ is plotted against $(2\sin\theta/\lambda)^2$ for each reflection for Gauss profiles or alternatively, $\beta\cos\theta/\lambda$ is plotted against $2\sin\theta/\lambda$ for Cauchy profiles. λ and θ are the wavelength and the incident angle of the X-rays, respectively. The crystallite size D and strain ε can be respectively estimated from the intercept and slope of the linear Williamson-Hall plots following Equation 2.6 for a Gauss profile or Equation 2.7 for a Cauchy one. The indication of the presence of compressive strain by a negative slope in the plot have been reported by several authors [23, 42]. In our case the appearance of positive slope tends to prove the presence of tensile strain along the [002] orientation [46].

In our case, the (002), (004) and (006) peaks do not present a pure Cauchy profile or a pure Gauss profile but show a contribution of both and are fitted by a Pseudo-Voigt function to obtain β_{exp} for each of them, so none of these equations are strictly valid for Williamson-Hall. Nonetheless, we observed that the strain extracted either from Equation 2.6 or from Equation 2.7 are similar $\pm$ 3%. The values presented in the following correspond to the average. In contrast, a Cauchy approximation systematically underestimates the width of the reflections after correction of the instrumental resolution and that of the transverse coherence length. In the following, values obtained from Gauss analyses were used to qualitatively estimate the crystallite size.

***In-situ* configuration during the thermal annealing process**

In order to better understand the structural mechanisms involved in the thermal annealing step, θ-2θ profiles were directly recorded during an *in-situ* annealing [12]. Moreover, the *in-situ* measurements avoid the uncertainty from the reproducibility of the deposition, due to the fact that for an *ex-situ* acquisition, the XRD profiles are measured on different samples annealed at various temperatures.

Different types of temperature cycles were performed. A first one consisted of an increase of the temperature from room temperature to 500 °C directly followed by a decrease. The heating and cooling down ramps were approximatively 5 °C/min.

The second run of temperature cycles consisted of isothermal measurements at fixed temperature. The set point temperature was obtained in approximatively 10 minutes for a temperature ranging from 300 to 500 °C.

In this work, XRD analyses were done by Fabien Paumier, in the Institute P PRIME, Laboratoire de Physique des Matériaux (PHYMAT), at the University of Poitiers, and were performed using a Bruker D8 diffractometer equipped with a Cu X-ray radiation source ($\lambda_{K\alpha1}$ = 1.54505 Å, $\lambda_{K\alpha2}$ = 1.5443 Å) operating at 40 kV and 40 mA, in the Bragg–Brentano geometry. This diffractometer is equipped with an Anton Paar heating chamber allowing *in-situ* annealing at a maximal temperature of 1100 °C under a controlled atmosphere or vacuum (10 Pa) [12]. θ-2θ spectra have been acquired at temperature intervals of 5 °C. Only a very small θ-2θ range was measured due to these rapid heating and cooling down phases, and thus, no Williamson-Hall treatment was possible. Only the (002) peak was recorded and no other reflection.

2.2.1.2 Raman spectroscopy

Raman spectroscopy is a fast and non-destructive technique based on inelastic scattering of monochromatic light from a laser source. Photons of the laser light are absorbed by the sample and then reemitted. The frequency of the reemitted photons is shifted up or down in comparison with their original monochromatic frequency, which is called the Raman effect. This shift provides information about vibrational, rotational and other low frequency transitions in a system.

In this work, the Raman experimental setup consists of a high-resolution Labram HR800 from Horiba Jobin Yvon Raman spectrometer in a confocal backscattering configuration. The resolution of instrument was 0.1 cm^{-1}. The accommodate objective used in this study was a 100×(NA = 0.9) objective from Olympus. A tunable Ar laser (514 nm wavelength) was employed in this confocal configuration. The energy of the excitation photon is lower than the E_g value of ZnO, and accords with the non-resonant conditions, i.e. the increase in energy from the radiation excites the electrons to an unstable virtual state, and not to a higher state of the conduction band. For all the Raman Stokes analysis, the collection time was 10 s with 6 consecutive spectrum accumulations.

Raman spectra of ZnO:Al thin films

Raman spectroscopy gives information on vibrational properties of ZnO [10,35,58]. Figure 2.9 shows the first Brillouin zone of the wurtzite ZnO and the phonon dispersion relations at room temperature. The direction ΓA of the reciprocal space corresponds to c-axis of the real space [8].

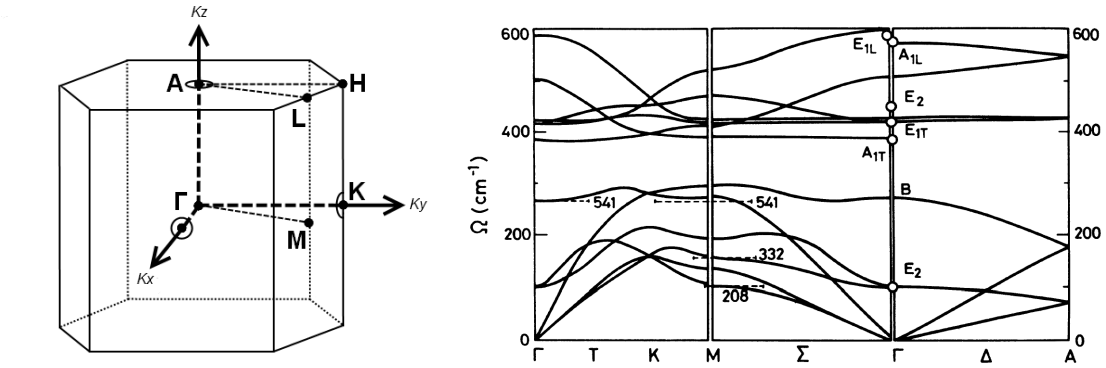

(a) (b)

Figure 2.9: (a) First Brillouin zone of the wurtzite lattice, and (b) phonon dispersion relations for ZnO at room temperature along the main symmetry directions. The white points indicate the phonons frequencies determined by Raman spectroscopy [7].

In hexagonal structures with C_{6v}^4 space group like ZnO, six sets of phonon normal modes at the Γ point are optically active modes. The phonons for wurtzite ZnO belong to the following irreducible representation:

$$\Gamma = A_1 + E_1 + 2B_1 + 2E_2 \tag{2.8}$$

The ionicity of ZnO has consequences on the vibration modes. Figure 2.10 reveals a important difference between two optical modes:

* The A_1 and E_1 modes show a total vibration of positive and negative charges. This asymmetrical stretch involves a change in dipole moment. A_1 and E_1 modes are polar ; they are IR and Raman active, as summarized in Table 2.4.

* For B_1 and E_2 modes, the vibrations of the charges are symmetrical. B_1 and E_2 modes are non-polar ; they are IR inactive, as summarized in Table 2.4. The optical mode E_2 is Raman active, contrary to the B_1 mode.

A_1 and E_1 modes split into transverse optical modes (A_1-TO and E_1-TO), resulting from beating in the basal plane, and longitudinal optical modes (A_1-LO and E_1-LO), resulting from beating along the c-axis, with different frequencies due to the macroscopic electric fields associated with LO phonons. For lattice vibrations with A_1 and E_1 symmetry, the atoms move parallel and perpendicular to the c-axis, respectively, as shown in Figure 2.10.

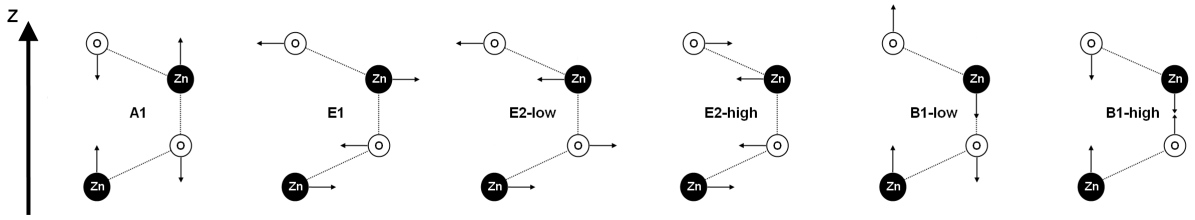

Figure 2.10: Atomic vibrations associated to optical modes in wurtzite ZnO for zone center phonons.

Table 2.4: Optical modes, their frequencies, and the configuration needed to observe them in wurtzite ZnO for zone center phonons.

Modes	Activity	Configuration	Frequency (cm^{-1})	Reference
A_1-TO	Ram.+IR	X(Y,Y)$\bar{X}$, X(Z,Z)$\bar{X}$	380	[5, 25]
E_1-TO	Ram.+IR	X(Z,Y)$\bar{X}$, X(Y,Z)Y	410 ; 413	[5, 40]
A_1-LO	Ram.+IR	Z(Y,Y)$\bar{Z}$	574 ; 579	[5, 25]
E_1-LO	Ram.+IR	X(Y,Z)Y	591	[5, 25]
E_2(low)	Raman	X(Y,Y)$\bar{X}$, X(Y,Y)Z, Z(Y,X)$\bar{Z}$, Z(Y,Y)$\bar{Z}$	101	[5, 25]
E_2(high)	Raman	X(Y,Y)$\bar{X}$, X(Y,Y)Z, Z(Y,X)$\bar{Z}$, Z(Y,Y)$\bar{Z}$	437 ; 444	[5, 25]
B_1(low)	Inactive		261	[34]
B_1(high)	Inactive		552	[34]

In addition to the selection rules mentioned above for Raman-active phonon modes, the modes detected by Raman scattering spectroscopy also depend on the scattering geometry, as presented in Table 2.4. The convention used here is the Porto notation of representing experimental scattering geometries [11]. The notation A(B,C)D means that the excitation light is incident on the sample along A axis, polarized along the B direction, and that the scattered light is detected along the D axis, polarized along the C direction. In the Z(XY,XY)$\bar{Z}$ configuration, the selection rules and the backscattering geometry of our Raman system imply that the two E_2 modes and the A_1-LO modes are expected while all other modes are forbidden (Figure 2.11a). The E_2 modes at low and high frequency and the A_1-LO mode are respectively at 101 cm^{-1}, 437 cm^{-1} and 574 cm^{-1}. The E_2(low) mode is associated with the vibration of the heavy Zn sublattice, while the E_2(high) mode involves only oxygen atoms.

In our case, some additional modes are observed for ZnO:Al thin films [6]. Raman spectra reveal vibrational modes at 275, 380, 510, 643 cm^{-1}, indicated by an asterisk in Figure 2.11b. It was suggested that these additional modes are related to defect-induced ZnO modes, which are Raman-inactive within a perfect crystal. Upon doping-induced defect formation, the translation crystal symmetry can be broken, and Raman-inactive modes may become Raman-active [34, 47]. The mode B_1(low) at the Γ point is estimated at 261 cm^{-1} by *ab initio* calculations and is not accessible with either Raman or infrared spectroscopy due to symmetry related selection rules as referred in Table 2.4. This mode may become active by disorder effects in alloys, by doping with other atoms, or by inducing defects. Taking into account that all LO modes were underestimated in the *ab initio*

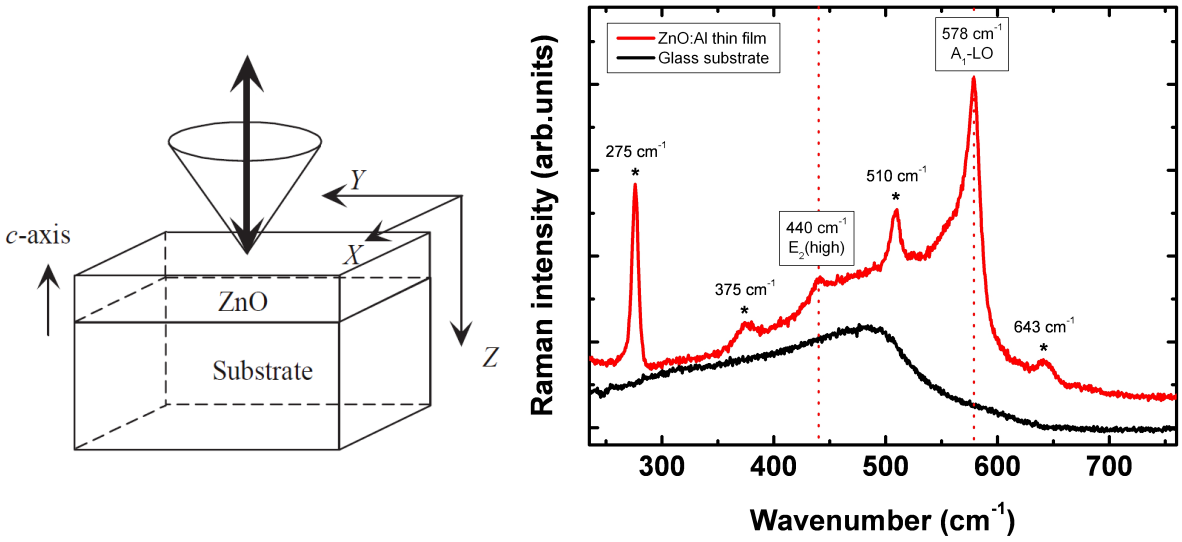

(a) (b)

Figure 2.11: Raman study: (a) Schematic representation of the Raman configuration used, in the $Z(XY,XY)\bar{Z}$ geometry, and (b) resulting Raman spectra of ZnO:Al film deposited on glass substrate. Allowed Raman modes are marked by dot vertical lines. The asterisks indicate additional modes.

calculations as observed by Manjon *et al.*, it is reasonable to assume that the B_1 silent mode is also underestimated [34, 40, 47]. In this respect, Raman modes around 275 cm^{-1} can correspond to B_1(low) mode of ZnO. It is possible to assign other observed anomalous modes to second-order modes if the previous assignment is correct. The 510 cm^{-1} mode can be attributed to the $2B_1$(low) second-order mode. The mode at 643 cm^{-1} can be assigned to the Transverse Acoustic TA + B_1(high) second-order mode. The vibration at 375 cm^{-1} mode can be attributed to the A_1-TO mode.

In-situ configuration during the thermal annealing process

In the same way than for X-ray diffraction measurements in section 2.2.1.1, Raman spectra were recorded during an *in-situ* annealing process.

In this work, the Raman system used was a Labram Aramis from Horiba Scientific, with a laser at 532 nm. The heating cell was from Linkam. A temperature cycle consisted of a heating ramp of 15 °C/min and the samples were held at 500 °C for up to 90 minutes before a slow cooling down to room temperature.

2.2.2 Morphological characterizations

The investigation of the surface morphology through Atomic Force Microscopy (AFM) and Scanning Electron Microscopy (SEM) is necessary to evaluate the influence of the sputter deposition parameters on the structure of ZnO:Al thin films. Preparation of ZnO:Al thin films usually leads to relative smooth layers. The post-deposition treatments and the wet etching step can have as a consequence to modify the surface roughness, which can be evaluated with these topography techniques. The etching behaviours are relevant for the

properties of the hydrogenated microcrystalline silicon solar cells. AFM is particularly well suited to examining semiconductors such as ZnO:Al, which are not easily evaluated at high resolution using SEM, especially on the cross-section, due to the non-conductive glass substrate, or which may suffer damage from the electron beam. However, the SEM is necessary for highly rough surface, after a laser annealing treatment for example. In fact, a coarse morphology can damage the tip and/or create artefacts during the AFM acquisition.

Furthermore, the ZnO:Al layers can be investigated in depth by imaging their cross section with Scanning Electron Microscopy or Transmission Electron Microscopy (TEM). As the ZnO:Al layer film is deposited on glass, the deposition of a very thin conductive layer of gold is required on the cross sections after preparation for SEM analysis. The cross section analysis enables to have information on growth mechanisms.

2.2.2.1 Atomic Force Microscopy AFM

The Atomic Force Microscopy (AFM) probes the surface of a sample with a sharp tip and provides high-resolution and three-dimensional information by measuring attractive and repulsive forces between the tip and the sample. In the optical detection system of the AFM, the tip is attached to the underside of a reflective cantilever, on which a diode laser is focused, as shown in Figure 2.12a. Forces between the tip and the sample surface cause the cantilever to bend or deflect. The laser spot is reflected from the cantilever onto a position-sensitive photo detector which measures the cantilever deflections as the tip is scanned over the sample. As the cantilever bends, the position of the laser spot changes.

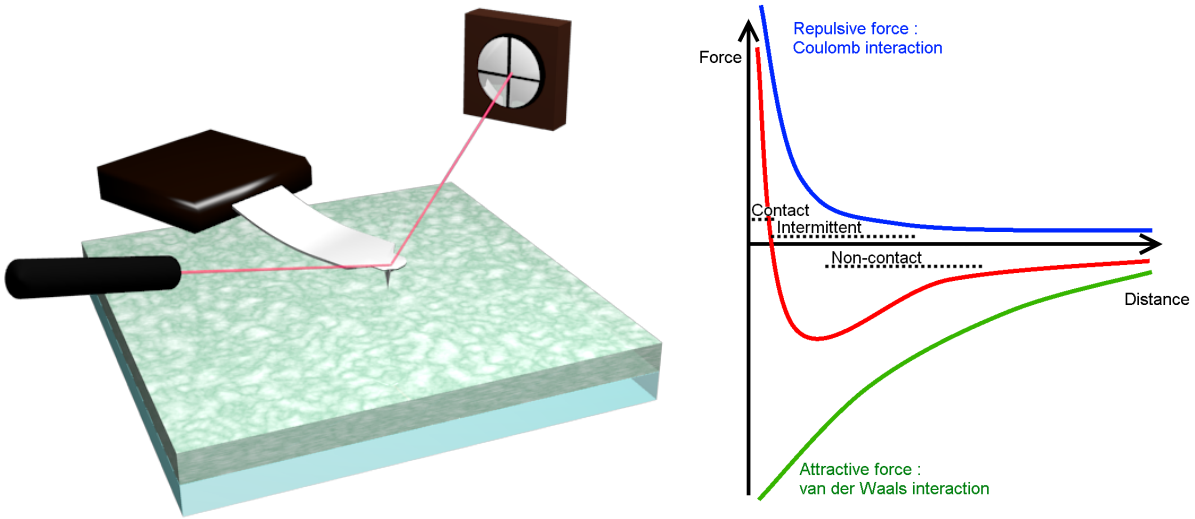

(a) (b)

Figure 2.12: Atomic Force Microscope: (a) Schematic representation and (b) forces between the tip and the sample. The red curve corresponds to the average force.

The AFM can be operated in different modes: contact, non-contact and intermittent (or tapping) modes. The mode depends on the distance between the tip and the sample, as shown in Figure 2.12b. As they approach, tip and sample atoms first weakly attract

each other. This zone of interaction is known as the non-contact regime due to the attractive van der Waals force. Closer, the repulsive force increases, it is the intermittent contact regime, where the intermittent mode can be used. When the distance between tip and sample is just a few angstroms, the total force becomes positive, the atoms are in the contact regime.

In the tapping mode, the cantilever is driven to oscillate in sinusoidal motion near its resonance frequency. When the cantilever and sample are close during each oscillation cycle, the tip moves through an interaction potential that includes long-range attractive and short term repulsive components. The complex tip-sample forces cause changes in the amplitude, phase and resonance frequency of the oscillating cantilever. Thus, topography, amplitude and phase can be collected simultaneously. A feedback system is employed to maintain the oscillation amplitude at a set point value. The difference between the amplitude and set point, called the error signal, is used as the input to the feedback system.

From the AFM data points, the Root Mean Square roughness δ_{RMS} is determined as given by:

$$\delta_{RMS} = \sqrt{\frac{1}{n}\sum_{i=1}^{n} z_i^2} \tag{2.9}$$

with n the total number of data points, and z_i the height at a given point i. The δ_{RMS} is a statistical measure of variations in the height magnitude.

In this work, the AFM images were acquired in tapping mode using a PicoPlus 5500 AFM from Agilent Technologies. The tips used are made of n-type Si, with an Al-coating on detection side, from App nano or Nanosensors. The tip height and radius are 10 - 15 μm and below 10 nm respectively, for a resonance frequency between 200 - 400 Hz.

2.2.2.2 Scanning Electron Microscopy SEM

The scanning electron microscopy (SEM) is based on a focused beam of high-energy electrons which generates a variety of signals at the surface of the samples. The signals that derive from electron-sample interactions are collected over a selected area of the surface of the sample, and a 2-dimensional image is generated [14]. The signals generated by the interaction of the accelerated electrons with the samples include secondary electrons, backscattered electrons, diffracted backscattered electrons, photons, visible light and heat. Secondary electrons and backscattered electrons are commonly used for imaging samples: secondary electrons are most valuable for showing morphology and topography on samples and backscattered electrons are most valuable for illustrating contrasts in composition in multiphase samples.

In this work, the SEM analyses were done by a field emission scanning electron microscopy (FESEM) HITACHI S4800. The magnification range spreads from 30× at low magnification mode, to 800 000× at high magnification. The electron gun is a cold cathode electron field emission type, with an accelerating voltage from 0.5 kV to 30 kV. The resolution is 1 nm for an accelerating voltage of 15 kV and a working distance of 4 mm, 2 nm for an accelerating voltage of 1 kV and a working distance of 1.5 mm.

2.2.2.3 Transmission Electron Microscopy TEM

The Transmission Electron Microscopy (TEM) images the electrons transmitted through thin samples with which they interact.

The most common mode of operation is the *bright field* imaging mode, since holes in the material appear bright. The contrast of these images is directly related to the ratio of transmitted electrons through the material: thin and amorphous regions scatter a smaller quantity of the incoming electrons and thus appear brighter [14]. For ZnO:Al sample, the polycrystalline nature of ZnO:Al thin films induces a variation of the intensity of individual grains. This operation mode is based on the particle-like nature of electrons.

A second operation mode is possible, the *dark field* imaging mode, based on the wave-like nature of the electrons. The contrast of these images is related to the Bragg configuration which scatters electron waves at discrete angles depending on the (hkl) values of atomic planes in a material. Typical diffraction patterns for polycrystalline samples consist of a series of concentric rings representing different (hkl) reflections [2, 51].

In this work, the TEM measurements were done by Rosa Ruggeri, with a JEOL 2010F transmission electron microscope with a Schottky field emission gun operating at an acceleration voltage of 200 kV. The samples have been prepared by Focused Ion Beam (FIB). This technique consists in the formation of trenches on two sides of a specific region of interest by the use of a focused Ga-ion beam. The residual specimen lamella between the two trenches can be thinned further, until it is transparent for the electron beam. This lamella is then extracted by use of a micro-manipulator needle, and put on a TEM grid to an appropriate TEM holder. This preparation is also combined with polishing of the specimen in order to reduce the FIB milling duration [2].

2.2.3 Optical characterizations

The optical properties of ZnO:Al thin films have a strong impact on the solar cell efficiency. The ZnO:Al thin film has to possess the highest transmittance in the active range of the absorber layer, and the highest reflectance after the wet etching step rear the solar cell to increase the light trapping properties. The angle of the scattered light inside the solar cell also has an influence on the increase of the short-circuit current J_{SC} of the solar cells.

2.2.3.1 UV/VIS/NIR spectrophotometry

Transmittance and reflectance measurements

In this work, transmittance and reflectance measurements were carried out using a Perkin Elmer Lambda 950 UV/VIS/NIR spectrophotometer. Two radiation sources, a deuterium lamp and a halogen lamp, cover the 200 - 2500 nm wavelength range of the spectrophotometer.

Different accessories are used to measure different signals.

The accessory used to measure overall transmittance and reflectance is the 150 mm integrating sphere, schematically represented in Figure 2.13. The two detectors used are

a photomultiplier tube PMT detector between 200 - 860.8 nm and an indium gallium arsenide InGaAs detector for the 860.8 - 2500 nm range. The sample is placed against the sphere and the beam transmitted or reflected by the sample is reflected onto the internal reflective surface of the sphere before reaching the detectors inside the sphere. The sample is placed in front of the sphere if transmittance is being measured and behind it if reflectance is being measured. The sphere's internal surface is made of a polymer which offers levels of diffuse reflectance approaching 100%.

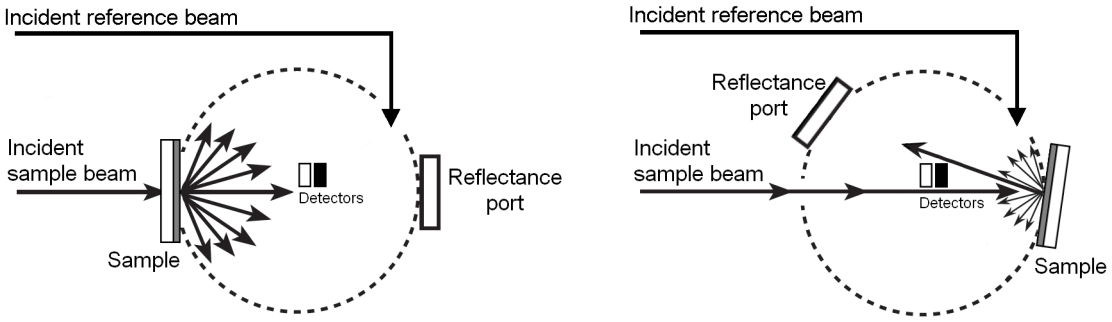

(a) (b)

Figure 2.13: Schematic representation of the (a) configuration for total transmittance, and the (b) configuration for total reflectance, with integrating sphere.

Haze factor

The accessory used to measure direct transmittance is the standard detection module. Two detectors are used, a lead sulfide PbS photomultiplier detector between 200 - 860.8 nm; and an indium gallium arsenide InGaAs detector for the 860.8 - 2500 nm range.

By combining these measurements, it is possible to calculate the haze factor H(λ), defined as the ratio between the diffuse transmittance T_{diff} and the total transmittance T_{total}:

$$H(\lambda) = \frac{T_{total}(\lambda) - T_{dir}(\lambda)}{T_{total}(\lambda)} \times 100 = \frac{T_{diff}(\lambda)}{T_{total}(\lambda)} \times 100 \tag{2.10}$$

In this work, the haze factor value was calculated at 700 nm to evaluate the scattering properties of diffusing ZnO:Al thin films after a wet etching step.

Angular Resolved Scattering measurements

An interesting measurement to estimate the scattering capability of the textured ZnO:Al thin films is the angular resolved scattering measurements. The accessory used is the absolute reflectance/transmittance analyser (ARTA) from Perkin Elmer. The ARTA is a stepper motor driven spectral goniometer tool that uses an integrating sphere as detector.

The sample is positioned on a motorized rotation stage in the centre and the integrating sphere detector is positioned behind the sample (at 180°) for transmittance measurements or at twice the incidence angle for reflectance measurements as shown in Figure 2.14. The

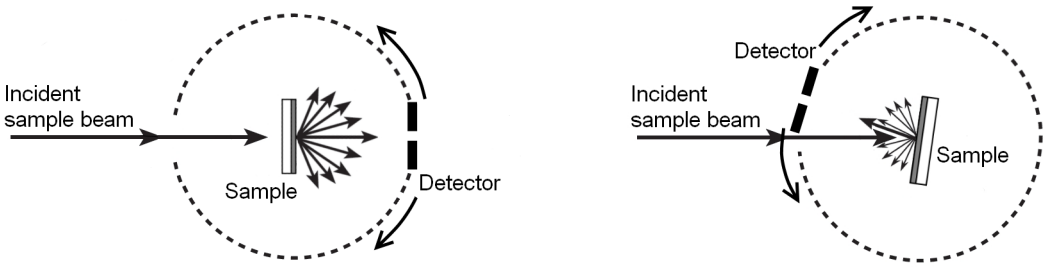

(a) (b)

Figure 2.14: Schematic representation of the (a) configuration for transmittance at 0°, and the (b) configuration for reflectance at 8°, with the ARTA accessory.

two detectors used are a photomultiplier tube PMT detector between 200 - 860.8 nm and an indium gallium arsenide InGaAs detector for the 860.8 - 2500 nm range.

2.2.3.2 Spectroscopic ellipsometry and polarimetry

Phase-modulated standard ellipsometer

Spectroscopic ellipsometry (SE) is an optical technique for the investigation of the dielectric properties of thin films. This fast and non-destructive technique can provide information on the thickness and other parameters of the films depending on the model used to fit the spectra, parameters that will be discussed later. The principle of the measurement is based on the change in the polarization state of the light upon reflection on the surface of the thin film deposited on a substrate. Ellipsometry measures the change on the polarization state of a beam after reflection on a sample.

The standard ellipsometer is made of two optical arms and a sample-holder (Figure 2.15a). The first arm, the entry, is coupled to a source of light, and includes a linear polarizer set at an azimuth P with respect to the p direction in the plane perpendicular to the input beam. The second arm, or exit arm, is used to determine the polarization of the outcoming beam. It comprises a Polarization State Analyser (PSA) and a detector which may be a single channel device (photodiode, photomultiplier...) or a multichannel one (typically a CCD coupled with a spectrometer). The PSA typically includes a polarizer and possibly other components.

Basically, in phase-modulated ellipsometry, the light intensity is modulated temporally by the action of at least one of the optical components integrating the ellipsometer, then after an harmonic analysis of the signal, the ellipsometric values are deduced. In phase-modulation ellipsometers, a photoelastic modulator can be placed between the linear polarizer and the sample, either at the entry or exit optical arm, in PMSA or the PSMA configurations respectively. Here P, M, S and A stand for fixed polarizer, modulator, sample, and fixed analyzer respectively.

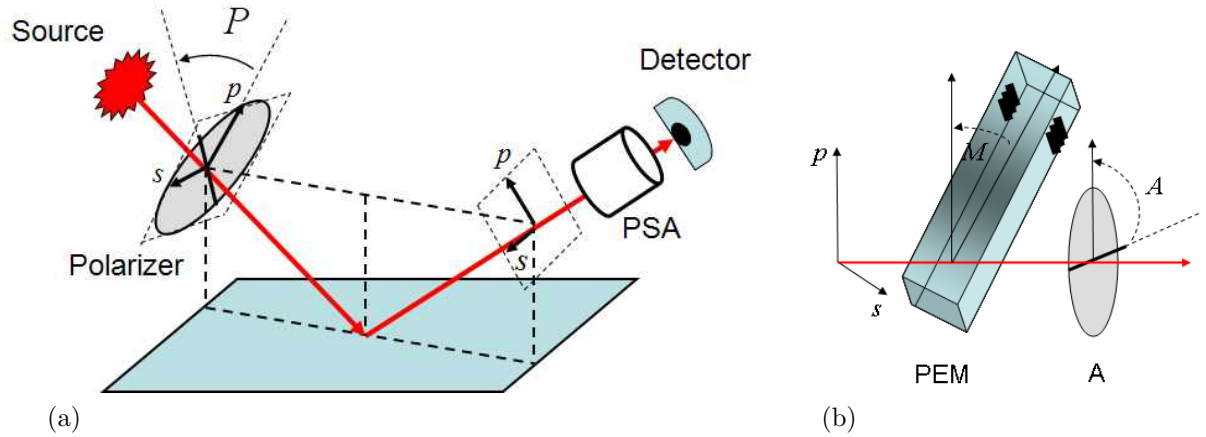

Figure 2.15: Standard ellipsometer: (a) Schematic representation and (b) Representation of a PSA comprising a photoelastic modulator (PEM) and a linear analyzer (A), set respectively at azimuths M and A.

A photoelastic modulator consists of a bar of optically isotropic material, which is made birefringent by means of an applied mechanical stress. To enhance this naturally weak effect, the applied stress is periodic and at a proper frequency to generate a stationary sound wave in the bar. The needed time dependent mechanical stress is usually applied using piezoelectric transducers attached to the end of the bar. As acoustic losses in the bar are very weak, very sharp resonances occur for ultrasonic waves, resulting in a dramatic increase of the induced birefringence with respect to a static stress. As a result, the device behaves as a retarder with a time dependent retardation δ(t), which varies sinusoidally at frequencies of several tens of kHz.

Here, the PSMA configuration is considered, in which at the entry arm the polarizer is fixed and set at an azimuth P with respect to the plane of incidence, while in the exit arm, as represented in Figure 2.15, the photoelastic modulator is set to an azimuth M and the linear analyzer is set at an azimuth angle A with respect to the plane of incidence. The detected signal then takes the form:

$$S(t) = S_0[1 + I_s sin\delta(t) + I_c cos\delta(t)] \tag{2.11}$$

with

$$I_s = sin[2(A - M)]sin2Psin2\Psi sin\Delta \tag{2.12}$$

$$I_c = sin[2(A - M)][sin2M(cos2\Psi - cos2P) + sin2Pcos2Msin2\Psi cos\Delta] \tag{2.13}$$

In practice, as δ(t) = sin(ωt), Equation 2.11 must be developed in Fourier series to express I_s and I_c as functions of the directly measured quantities, actually the amplitudes of the sin(ωt) and sin(2ωt) components of the signal. The expressions 2.13 and 2.12 show that the signal S(I_s, I_c) are maximized when A-M = 45°. Moreover it is also clear that it is not possible to unambiguously determine Ψ and Δ from a single measurement configuration. In practice, two configurations are typically used:

* M=0°, A=45°, P= 45°C, known as configuration II,
  with I_s = sin2Ψ sinΔ and I_c = sin2Ψ cosΔ,

* M=45°, A=90°, P= 45°, known as configuration III,
  with I_s = sin2Ψ sinΔ and I_c = cos2Ψ.

It is possible to shift from one configuration to the other by rotating the PSA, in order to combine the results of the two measurements for a complete and unambiguous determination of both Ψ and Δ.

In this work, the set-up is a phase modulated spectroscopic ellipsometer Uvisel from Horiba Jobin Yvon with a scanning range going from 0.75 to 4.70 eV, and the Delta psi2 software to process the data. The system measures the spectra of Δ and Ψ as functions of wavelength λ.

The dielectric function of the ZnO:Al thin films was fitted from a multi-model for the determination of the optical constants of the thin film and the extraction of its thickness, and is detailed in section 1.5.1.

Infrared polarimetry

Throughout this section, Mueller ellipsometers are described within the framework of the Stokes-Mueller formalism, which unifies the presentation of both techniques, and simplifies the algebra with respect to original descriptions of generalized ellipsometry based on Jones matrices [20–22].

Mueller Ellipsometry, or Polarimetry, is aimed at characterizing the polarimetric properties of the sample under study, by measuring the polarization changes induced by this sample on selected input polarization states, defined by a Polarization State Generator (PSG). The output polarizations are analyzed by means of a Polarization State Analyzer (PSA) followed by a detector, according to the general scheme outlined in Figure 2.16.

Figure 2.16: Schematic representation of the optical setup of a general Mueller ellipsometer. The Stokes formalisms has been used to represent the polarization properties of light. In the framework of Stokes formalisms the optical properties of the PSG, sample and PSA can be represented by matrices.

The PSG produces a set of input Stokes vectors S_i, which are transformed by the sample into MS_i (M being the Mueller matrix of the sample). These output Stokes vectors are then analysed by the PSA, which delivers the raw signals B_{ij} by projecting each vector MS_i onto its basis states. This scheme can be summarized by the matrix B = AMW, where the modulation matrix W, which characterizes the PSG, is formed by the S_i vectors in columns, while the S'_j are the line vectors of the analysis matrix A characterizing the PSA. In the most general case, B is rectangular, with m lines and n columns, where m and n respectively represent the number of states generated by the PSG and analyzed by the PSA. From this expression, it can be clearly seen that the Mueller matrix M can be retrieved from the measured data B with a simple inversion of the matrices A and W, known after calibration of the instrument.

A Mueller matrix is, in principle, a 4 × 4 matrix which contains information about the optical properties of the sample. The Mueller matrix of non-depolarizing and non-anisotropic samples, such as ZnO:Al thin films, has a particularly simple form, block diagonal, and can be expressed in terms of the ellipsometric angles Δ and Ψ as:

$$\begin{pmatrix} 1 & -cos(2\Psi) & 0 & 0 \\ -cos(2\Psi) & 1 & 0 & 0 \\ 0 & 0 & sin(2\Psi)cos\Delta & sin(2\Psi)sin\Delta \\ 0 & 0 & -sin(2\Psi)sin\Delta & sin(2\Psi)cos\Delta \end{pmatrix}$$

Thanks to this property, the results obtained with the infrared Mueller ellipsometer are compatible to those obtained with the photoelastic ellipsometer. In that way, the combination of the results obtained with both instruments allows to access to the optical properties of the sample in a very broad spectral range going from the UV to the mid IR.

The following example consists of the measurement of two crystal silicon (c-Si) wafers coated each one of a thin film of silica SiO_2 thermally grown, which is a non-depolarizing sample. Fitting the experimental Ψ and Δ evaluated to the theoretical ones obtained by a model representing the sample as a semi-infinite substrate of c-Si covered by a homogeneous layer of SiO_2 allows to estimate the thickness of the oxide film. Figure 2.17 shows the experimental Mueller matrix elements for both samples.

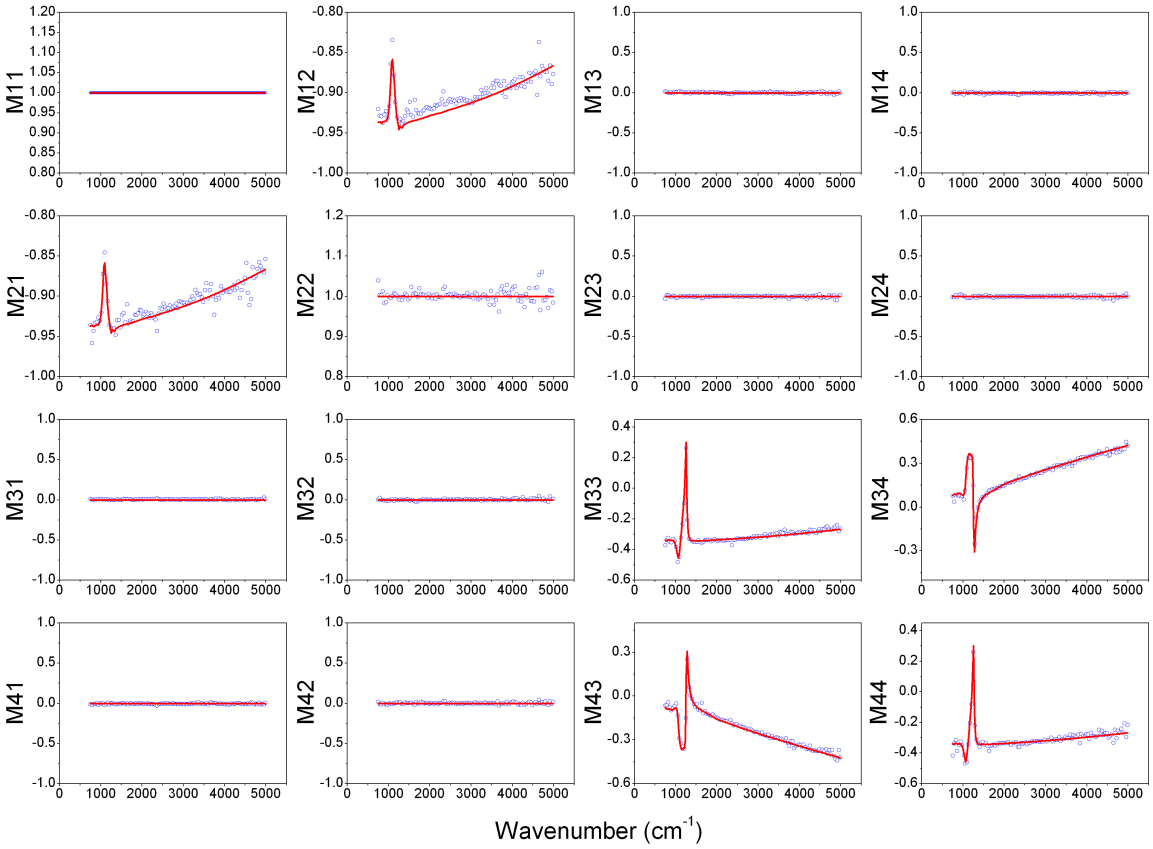

Figure 2.17: Experimental (blue dots) and best-fitted (red line) spectroscopic Mueller matrices of a silicon wafer coated with a thermal SiO_2 film of thickness 92 nm.

For this energy range, the Drude model can be used to spectrally resolve normalized Mueller matrices. In this way, Drude parameters obtained from the spectroscopic ellipsometry and infrared polarimetry are compared.

2.2.4 Electrical characterizations

The electrical properties of the ZnO:Al thin films are a key point for the improvement of hydrogenated microcrystalline silicon solar cells. The sheet resistance R_{sh} should be as small as possible to minimize ohmic losses for the transport of the photo-current. The highest conductivity σ are required, as well as a low charge carrier concentration N in order to maintain the free carrier absorption losses as low as possible.

The electrical properties, as well as the carrier transport properties of ZnO:Al thin films, can be determined by using the Hall effect. Furthermore, the measurement of eddy current on 5 cm × 5 cm ZnO:Al samples enables to have a mapping of the sheet resistance, and thus an estimation of the homogeneity of the sputter deposition.

2.2.4.1 Hall effect measurement

The Hall effect refers to the voltage difference V_H resulting from the deflection of the charged carriers by the Lorentz force as shown in Figure 2.18. The Lorentz force $F_{Lorentz}$ develops in the direction defined by the charge on the carrier e and the vector cross product of the drift velocity ν of the carriers and the magnetic field H such as presented in Equation 2.14:

$$F_{Lorentz} = e\nu \times H \tag{2.14}$$

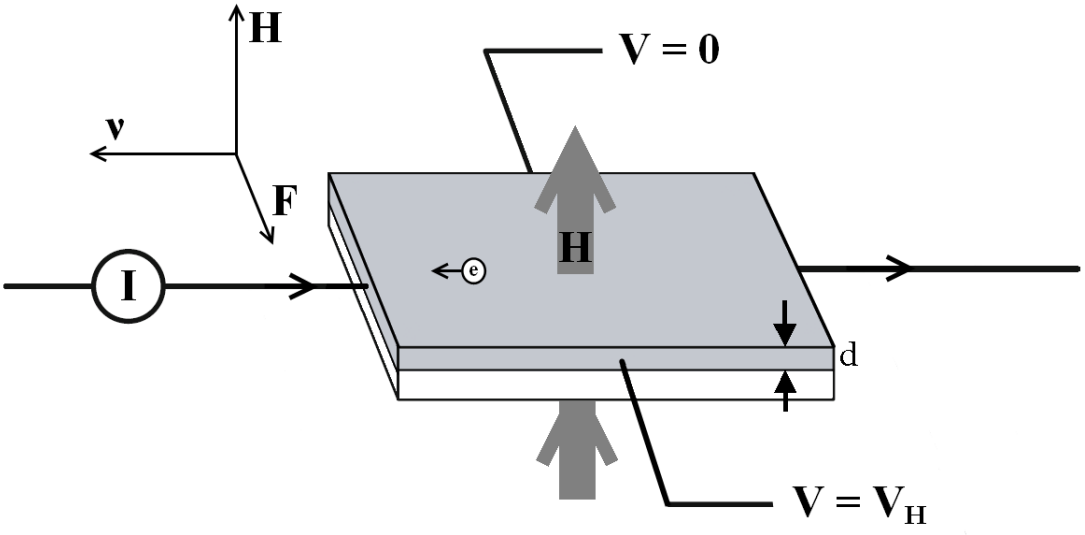

Figure 2.18: Schematic representation of the Hall effect.

Equation 2.15 provides the charge carrier density N from the measurement of the Hall voltage by the input of the current I:

$$V_H = \frac{IH}{eNd} \tag{2.15}$$

The van der Pauw sheet resistance R_{sh} can be used to find the resistivity ρ from the same sample. In this method, four small contacts are considered at the periphery of an arbitrarily shaped two dimensional sample as shown in Figure 2.19. To measure R_{sh}, a DC current is passed from one contact to the adjacent contact, while the corresponding voltage difference is measured across the two contacts on the opposing side. This measurement is repeated twice for each set of contact pairs by switching polarity and repeated for all four pairs of contacts.

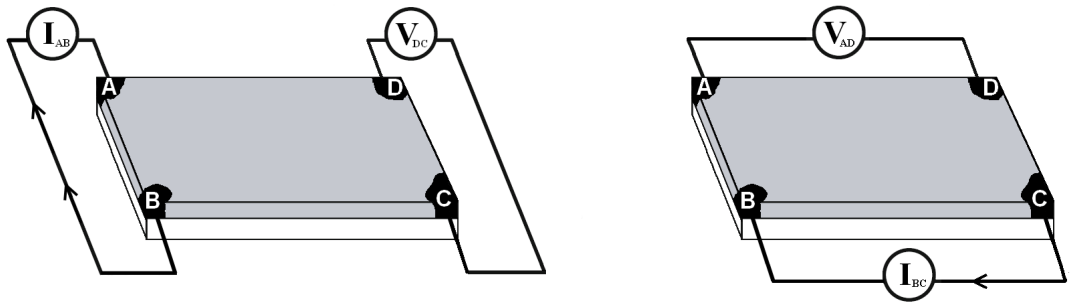

(a) (b)

Figure 2.19: Schematic representation of the van der Pauw configuration for the resistance (a) $R_{AB,DC} = V_{DC}/I_{AB}$, or (b) $R_{BC,AD} = V_{AD}/I_{BC}$.

The sheet resistance is then deduced by resolving the van der Pauw equation:

$$e^{(\frac{-\pi R_1}{R_{sh}})} + e^{(\frac{-\pi R_2}{R_{sh}})} = 1 \tag{2.16}$$

with

$$R_1 = \frac{R_{BA,CD} + R_{AB,DC} + R_{DC,AB} + R_{CD,BA}}{4} \tag{2.17}$$

$$R_2 = \frac{R_{CB,DA} + R_{BC,AD} + R_{AD,BC} + R_{DA,CB}}{4} \tag{2.18}$$

From the Hall measurements associated to the van der Pauw sheet resistance determination, the resistivity ρ and the Hall mobility μ_H are deduced with Equation 2.19 and Equation 2.20 respectively.

$$\rho = R_{sh} \times d \tag{2.19}$$

$$\mu_H = \frac{1}{eN\rho} \tag{2.20}$$

In this work, A HMS5000 from Microworld was used to obtain the Hall mobility, carrier concentration and resistivity ρ of the films by Hall effect. All the measurements were carried out utilizing a current of 1 mA, and a magnetic field of 0.550 T.

Temperature-dependent conductivity

The acquisition of the temperature-dependent charge carrier concentration and conductivity gives us information about the carrier transport inside the semiconductor.

In this work, the samples were cooled down using a liquid nitrogen cryostat for Hall effect measurements in the temperature range of 80 - 350 K.

***In-situ* configuration during the thermal annealing process**

In order to follow the electrical modifications during the annealing process, the annealing steps have been subsequently investigated through *in-situ* Hall effect measurements realized in controlled atmospheres: in air, under argon flux and low pressure conditions (10 Pa).

In this work, a HMS5300 system from Ecopia was used to evaluate the Hall mobility, carrier concentration and resistivity of the films by Hall effect. The temperature cycle consisted of an increase of the temperature from room temperature to 300 °C followed by a decrease. The heating ramps were fixed at 5 °C/min while the cooling down to room temperature was not controlled.

2.2.4.2 Sheet resistance mapping by eddy current measurement

In the eddy current measurement, a circular coil carrying current is placed above ZnO:Al thin films. The alternating current in the coil generates changing magnetic field which interacts with sample and induces eddy current in a conducting material. Variations in the phase and magnitude of these eddy currents can be monitored by measuring changes on the current firstly generated in the coil. The eddy current generated in the sample depends on the resistance of the material. Eddy current systems measure the electrical loss in the material.

In this work, the ZnO:Al samples were measured by WT2000 Semilab tools. The resistance measurements were carried out by non-contact probe head that was calibrated before measurements, for a lateral resolution of 6 mm.

2.2.4.3 *In-situ* resistance measurements

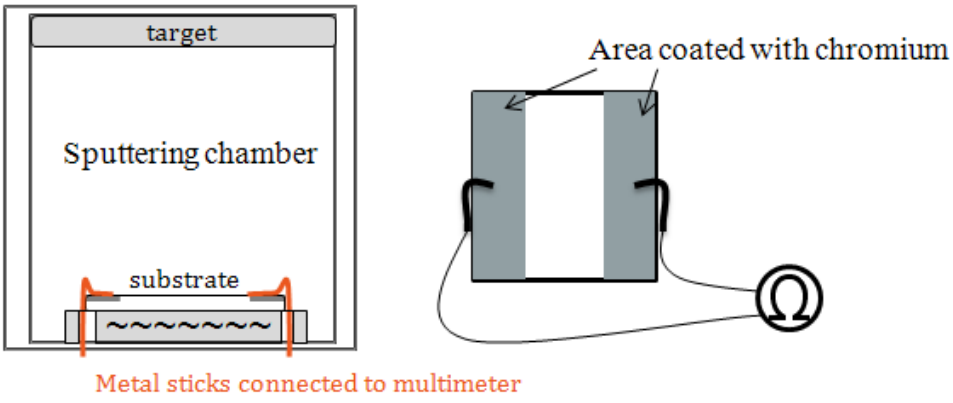

Figure 2.20: Schematic representation of the in-situ resistance system.

In order to understand the continuous change of electrical properties during the thin film growth, and to have a better understanding of the growth mechanism, a knowledge

of the first step of growth is needed. An *in-situ* resistance measurement, presented in Figure 2.20, has been implemented in the Cameleon reactor. An 1 μm-thick chromium layer was coated at the edges of the substrate in order to have a precise resistance measurements, with a conductive contact even at the first deposited nanometers. The chromium layer has a contact with 2 metal sticks which connect to a multimeter outside the chamber.

The plasma was stopped for the resistance measurements. Indeed, the *in-situ* resistance measurement versus deposition time presents some oscillations resulting from the plasma effect. These oscillations disappear when the resistance is measured just after the plasma stop. Some additional tests have been done to check the effect of the restart of layer growth on the resistance variation trend: The stop of the plasma for the acquisition seems not to influence the resistance measurements.

2.2.5 Solar cell characterizations

To compare the influence of the ZnO:Al front contact on the efficiency of the solar cells, the complete cells are characterized. The measurement of the current as a function of voltage under illumination by light provided by a solar cell simulator with a fixed standard power is necessary, as well as the estimation of the electrical sensitivity to the wavelength of the incoming light.

2.2.5.1 Illuminated current density-voltage measurement J(V)

Illuminated current density-voltage J(V) measurement is a fundamental electrical characterization technique to evaluate the performance of solar cells. The Figure 2.21 presents the shift of the diode like J(V) curve towards negative current by the value of the photo current density J_{Ph} [43, 45].

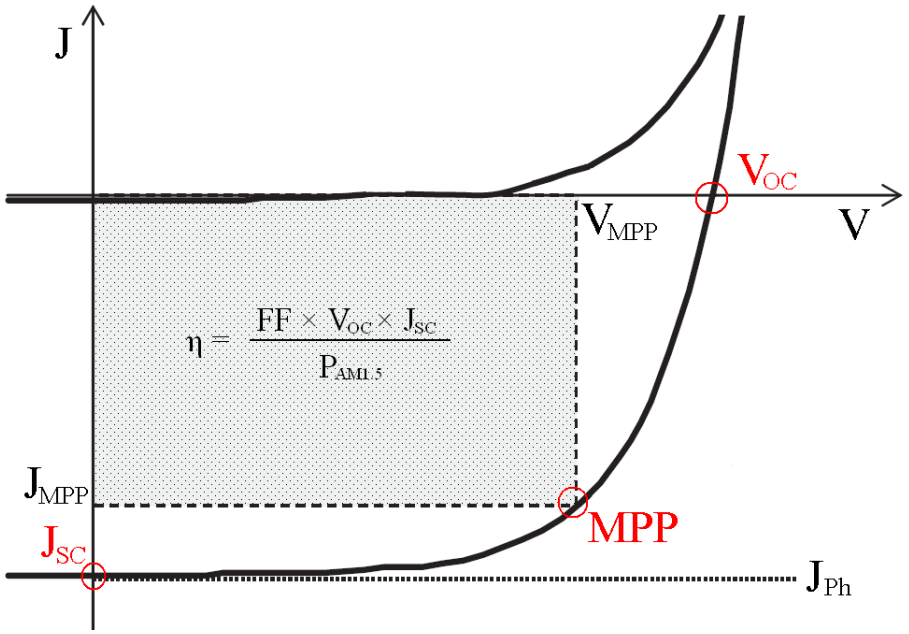

Figure 2.21: J(V) curve of μc-Si:H thin film solar cell. Efficiency η, fill factor FF, open circuit voltage V_{OC} and short-circuit current density J_{SC} are indicated, as well as the maximum power point MPP.

The open circuit voltage V_{OC} corresponds to the maximum voltage possible, when no current flows through the solar cell, and the short-circuit current density J_{SC} is defined as the current density at zero voltage, and nearly equals the photo current density J_{PH}. The maximum power density is equal to the product of current density J_{MPP} and voltage V_{MPP} at the maximum power point MPP of the solar cell. From this, the fill factor FF is calculated by the equation:

$$FF = \frac{J_{MPP} \times V_{MPP}}{J_{SC} \times V_{OC}} \tag{2.21}$$

The more "rectangular" the J(V) curve appears, the higher the FF is and better charge carriers are collected within the device [43]. To compare the solar cells, the conversion efficiency η is determined as the ratio of the maximum power over the incident light power P_{light}:

$$\eta = \frac{FF \times V_{OC} \times J_{SC}}{P_{light}} \tag{2.22}$$

Additionally, from the slope of the J(V) curve near V_{OC} and J_{SC}, approximate values of the series resistance R_s and the shunt resistance R_{sh} of the solar cell can be obtained respectively [1].

In this work, the J(V) curves were measured using a blue-enhanced halogen light source with an intensity close to 100 $mW.cm^{-2}$. Generally, J(V) curves are measured on several individual 0.125 cm^2 solar cells. Values given in this work for the electrical device parameters are the best value generally measured on 6 individual solar cells.

2.2.5.2 Spectral response

The spectral response is defined as the dependence of the collected charge carriers on the radiated photons of different wavelengths [52]. The spectral response given by Equation 2.23 is defined as the ratio of the generated photo current density J_{Ph} to the illuminated power density, which corresponds to the product of the photon energy E_{Ph} and flux Φ_{Ph}.

$$SR(\lambda) = \frac{J_{Ph}(\lambda)}{E_{Ph}(\lambda) \times \Phi_{Ph}(\lambda)} \tag{2.23}$$

The spectral distribution of photo-current is measured at a voltage equal to zero, under short-circuit conditions. However, by applying an external bias voltage, the electric field in the cell can be changed and thus can provide additional information. A negative bias voltage increases the electric field, which decreases the trapping and recombination of the charge carriers [19].

Furthermore, the SR is used to determine the external quantum efficiency EQE of a solar cell. The EQE corresponds to the number of collected photo-generated electrons-hole pairs (N_e) produced in the device par incident photon (N_{Ph}) in short-circuit conditions:

$$EQE(\lambda) = \frac{N_e(\lambda)}{N_{Ph}(\lambda)} = \frac{J_{Ph}(\lambda)}{e \times \Phi_{Ph}(\lambda)} = SR(\lambda)\frac{hc}{e\lambda} \tag{2.24}$$

with h the Planck constant, c the velocity of the light in vacuum, and e the electron charge. The short-circuit current J_{SC} is calculated from the EQE by integrating the

product of the electron charge, the quantum efficiency EQE, and the photon flux Φ_{Ph} of the spectrum over the wavelengths in the spectrum:

$$J_{sc} = e \int EQE(\lambda)\Phi_{Ph}(\lambda)d\lambda \tag{2.25}$$

As the surface of the solar cell is not well defined, and to take into account the non-accuracy of the solar simulator spectrum, the short-circuit current density J_{SC} is more accurately calculated using the external quantum efficiency measurement EQE (Equation 2.25) than the J(V) measurement.

In this work, the measurements were done at a voltage equal to 0 and for a reverse bias of -0.5 V. The spectral range between 400 and 1000 nm was examined.

2.3 Conclusion

In this chapter, the growth and characterization techniques have been discussed in detail.

The ZnO:Al thin film deposition by PVD has been presented, as well as the depositions of the different solar cell layers by PE-CVD, and the back contacts. The post-deposition treatments have been exposed. The possible treatments after the TCO sputtering are a thermal annealing process, or a laser annealing process.

These different steps have a strong influence of the properties of the thin films. Many characterization techniques have been used in this work to have a large and detailed view of the material properties. Structural attributes have been studied by a correlation between X-ray diffration measurements and Raman spectroscopy, *ex-situ* or *in-situ* during the post-deposition processes. The AFM, TEM and SEM techniques allow to investigate the morphological characteristics of the films. The opto-electronic properties are studied by UV/VIS/NIR spectroscopy, ARS measurements, Hall effect and eddy current measurements. Finally, the polarimetry technique enables us to optically model the free electrons behaviour, and the temperature-dependent conductivities to identify the limiting scattering events for the charge carrier transport.

Bibliography

[1] A. G. Aberle. Fabrication and characterisation of crystalline silicon thin-film materials for solar cells. *Thin Solid Films*, 511-512:26–34, July 2006. (cited page 58)

[2] D. Abou-Ras, T. Kirchartz, and U. Rau. *Advanced Characterization techniques for Thin film Solar Cells*. John Wiley & Sons, 2011. (cited page 48)

[3] A. Aktaruzzaman, G. Sharma, and L. Malhotra. Electrical, optical and annealing characteristics of ZnO:Al films prepared by spray pyrolysis. *Thin Solid Films*, 198(1-2):67–74, Mar. 1991. (cited page 32)

[4] K.-S. An, W. Cho, B. K. Lee, S. S. Lee, and C. G. Kim. Atomic Layer Deposition of Undoped and Al-Doped ZnO Thin Films Usingthe Zn Alkoxide Precursor Methylzinc Isopropoxide. *Journal of Nanoscience and Nanotechnology*, 8(9):4856–4859, Sept. 2008. (cited page 32)

[5] C. Arguello, D. Rousseau, and S. Porto. First-Order Raman Effect in Wurtzite-Type Crystals. *Physical Review*, 181(3):1351–1363, May 1969. (cited page 44)

[6] C. Bundesmann, N. Ashkenov, M. Schubert, D. Spemann, T. Butz, E. M. Kaidashev, M. Lorenz, and M. Grundmann. Raman scattering in ZnO thin films doped with Fe, Sb, Al, Ga, and Li. *Applied Physics Letters*, 83(10):1974, 2003. (cited page 44)

[7] J. M. Calleja and M. Cardona. Resonant Raman scattering in ZnO. *Physical Review B*, 16(8):3753–3761, 1977. (cited pages vi et 43)

[8] P.-M. Chassaing. Quelques illustrations du rôle de la surface dans des nanoparticules de ZnO, July 2009. (cited page 43)

[9] R. Chierchia, T. Böttcher, H. Heinke, S. Einfeldt, S. Figge, and D. Hommel. Microstructure of heteroepitaxial GaN revealed by x-ray diffraction. *Journal of Applied Physics*, 93(11):8918, 2003. (cited page 41)

[10] R. Cuscó, E. Alarcón-Lladó, J. Ibáñez, L. Artús, J. Jiménez, B. Wang, and M. Callahan. Temperature dependence of Raman scattering in ZnO. *Physical Review B*, 75(16), Apr. 2007. (cited pages 43 et 130)

[11] T. Damen, S. Porto, and B. Tell. Raman Effect in Zinc Oxide. *Physical Review*, 142(2):570–574, Feb. 1966. (cited page 44)

[12] C. David, T. Girardeau, F. Paumier, D. Eyidi, B. Lacroix, N. Papathanasiou, B. P. Tinkham, P. Guérin, and M. Marteau. Microstructural and conductivity changes induced by annealing of ZnO:B thin films deposited by chemical vapour deposition. *Journal of physics. Condensed matter*, 23(33):334209, Aug. 2011. (cited pages 42, 121 et 123)

[13] D. Dominé. *The role of front electrodes and intermediate reflectors in the optoelectronic*. PhD thesis, Université de Neuchâtel, 2009. (cited page 32)

[14] R. Egerton. *Physical Principles of Electron Microscopy* . Springer, 2005. (cited pages 47 et 48)

[15] K. Ellmer. Magnetron sputtering of transparent conductive zinc oxide: relation between the sputtering parameters and the electronic properties. *Journal of Physics D: Applied Physics*, 33(4):R17–R32, Feb. 2000. (cited page 32)

[16] K. Ellmer, R. Cebulla, and R. Wendt. Transparent and conducting ZnO(:Al) films deposited by simultaneous RF- and DC-excitation of a magnetron. *Thin Solid Films*, 317:413–416, 1998. (cited page 33)

[17] K. Ellmer and R. Wendt. D.c. and r.f. (reactive) magnetron sputtering of ZnO:Al films from metallic and ceramic targets: a comparative study. *Surface and Coatings Technology*, 93(1):21–26, Aug. 1997. (cited page 33)

[18] S. Faÿ. *L'oxyde de zinc par dépôt chimique en phase vapeur comme contact électrique transparent et diffuseur de lumière pour les cellules solaires*. PhD thesis, Ecole Polytechnique Federale de Lausanne, 2003. (cited pages 14 et 32)

[19] R. H.-J. Franken. *Transparent conducting oxide contacts and textured metal back reflectors for thin film silicon solar cells*. PhD thesis, Utrecht, 2006. (cited page 58)

[20] E. Garcia-Caurel, A. de Martino, and B. Drevillon. Spectroscopic Mueller polarimeter based on liquid crystal devices. *Thin Solid Films*, 455-456, 2004. (cited page 52)

[21] E. Garcia-Caurel, A. de Martino, and B. Drevillon. A broadband ellipsometer/polarimeter system, June 2007. (cited page 52)

[22] E. Garcia-Caurel, A. De Martino, J.-P. Gaston, and L. Yan. Application of Spectroscopic Ellipsometry and Mueller Ellipsometry to Optical Characterization. *ArXiv e-prints*, Oct. 2012. (cited page 52)

[23] F. Gu, S. F. Wang, M. K. Lü, G. J. Zhou, D. Xu, and D. R. Yuan. Photoluminescence Properties of SnO2 Nanoparticles Synthesized by Sol-Gel Method. *The Journal of Physical Chemistry B*, 108(24):8119–8123, June 2004. (cited page 41)

[24] K. Haga, M. Kamidaira, Y. Kashiwaba, T. Sekiguchi, and H. Watanabe. ZnO thin films prepared by remote plasma-enhanced CVD method. *Journal of Crystal Growth*, 214-215:77–80, June 2000. (cited page 32)

[25] C. Jagadish and S. J. Pearton. *Zinc Oxide Bulk, Thin Films and Nanostructures: Processing, Properties And Applications*. Elsevier, 2006. (cited page 44)

[26] Y. Kashiwaba, F. Katahira, K. Haga, T. Sekiguchi, and H. Watanabe. Heteroepitaxial growth of ZnO thin films by atmospheric pressure CVD method. *Journal of Crystal Growth*, 221(1-4):431–434, Dec. 2000. (cited page 32)

[27] H. Kim, A. Piqué, J. Horwitz, H. Murata, Z. Kafafi, C. Gilmore, and D. Chrisey. Effect of aluminum doping on zinc oxide thin films grown by pulsed laser deposition for organic light-emitting devices. *Thin Solid Films*, 377-378:798–802, Dec. 2000. (cited page 32)

[28] O. Kluth, B. Rech, L. Houben, S. Wieder, G. Schöpe, C. Beneking, H. Wagner, A. Löffl, and H. Schock. Texture etched ZnO:Al coated glass substrates for silicon based thin film solar cells. *Thin Solid Films*, 351(1-2):247–253, Aug. 1999. (cited pages 37, 148 et 158)

[29] O. Kluth, G. Schöpe, B. Rech, R. Menner, M. Oertel, K. Orgassa, and H. Werner Schock. Comparative material study on RF and DC magnetron sputtered ZnO:Al films. *Thin Solid Films*, 502(1-2):311–316, Apr. 2006. (cited page 33)

[30] M. Labrune. *Silicon surface passivation and epitaxial growth on c-Si by low temperature plasma processes for high efficiency solar cells*. PhD thesis, Ecole Polytechnique, 2011. (cited pages 37 et 38)

[31] J.-H. Lee and B.-O. Park. Transparent conducting ZnO:Al, In and Sn thin films deposited by the sol–gel method. *Thin Solid Films*, 426(1-2):94–99, Feb. 2003. (cited page 32)

[32] J.-H. Lee and B.-O. Park. Characteristics of Al-doped ZnO thin films obtained by ultrasonic spray pyrolysis: effects of Al doping and an annealing treatment. *Materials Science and Engineering: B*, 106(3):242–245, Feb. 2004. (cited page 32)

[33] V. Lujala, J. Skarp, M. Tammenmaa, and T. Suntola. Atomic layer epitaxy growth of doped zinc oxide thin films from organometals. *Applied Surface Science*, 82-83:34–40, Dec. 1994. (cited page 32)

[34] F. J. Manjón, B. Mari, J. Serrano, and A. H. Romero. Silent Raman modes in zinc oxide and related nitrides. *Journal of Applied Physics*, 97(5):053516, 2005. (cited pages 44 et 45)

[35] M. Millot, R. Tena-Zaera, V. Munoz-Sanjose, J.-M. Broto, and J. Gonzalez. Anharmonic effects in ZnO optical phonons probed by Raman spectroscopy. *Applied Physics Letters*, 96(15):152103, 2010. (cited page 43)

[36] J. Müller, B. Rech, J. Springer, and M. Vanecek. TCO and light trapping in silicon thin film solar cells. *Solar Energy*, 77(6):917–930, Dec. 2004. (cited pages 37 et 159)

[37] T. Ohgaki, Y. Kawamura, N. Ohashi, H. Kakemoto, S. Wada, Y. Adachi, H. Haneda, and T. Tsurumi. Electrical and Optical Properties of Zinc Oxide Thin Films and Heavily Aluminum-doped Zinc Oxide Thin Films Prepared by Molecular Beam Epitaxy. *MRS Proceedings*, 744, Jan. 2002. (cited page 32)

[38] T. Ohgaki, T. Kuroda, N. Ohashi, Y. Adachi, T. Tsurumi, F. Minami, and H. Haneda. Optical Properties of Heavily Aluminum-Doped Zinc Oxide Thin Films Prepared by Molecular Beam Epitaxy. *Key Engineering Materials*, 248:91–94, Aug. 2003. (cited page 32)

[39] M. Ohyama, H. Kozuka, and T. Yoko. Sol-gel preparation of transparent and conductive aluminum-doped zinc oxide films with highly preferential crystal orientation. *Journal of The American Ceramic Society*, 81(6):1622–1632, 1998. (cited page 32)

[40] U. Özgür, Y. I. Alivov, C. Liu, A. Teke, M. A. Reshchikov, S. Dogan, V. Avrutin, S.-J. Cho, and H. Morkoç. A comprehensive review of ZnO materials and devices. *Journal of Applied Physics*, 98(4):041301, Aug. 2005. (cited pages 44 et 45)

[41] J. Pannetier. *Techniques d'analyse des diagrammes de diffraction des rayons X et des neutrons par les poudres*. Formation permanente du CNRS, Nantes, 1995. (cited pages 40 et 72)

[42] R. R. Prabhu and M. Abdul Khadar. Study of optical phonon modes of CdS nanoparticles using Raman spectroscopy. *Bulletin of Materials Science*, 31(3):511–515, Sept. 2008. (cited page 41)

[43] B. Rech. *Transparent Conductive Zinc Oxide*, volume 104 of *Springer Series in Materials Science*. Springer Berlin Heidelberg, Berlin, Heidelberg, 2008. (cited pages 57 et 58)

[44] P. Roca i Cabarrocas, J. B. Chevrier, J. Huc, A. Lloret, J. Y. Parey, and J. P. M. Schmitt. A fully automated hot-wall multiplasma-monochamber reactor for thin film deposition. *Journal of Vacuum Science & Technology A: Vacuum, Surfaces, and Films*, 9(4):2331, July 1991. (cited page 38)

[45] F. Sculati-Meillaud. *Microcrystalline Silicon Solar Cells: Theory, Diagnosis and Stability*. PhD thesis, Université de Neuchâtel, 2006. (cited page 57)

[46] V. Senthilkumar, P. Vickraman, M. Jayachandran, and C. Sanjeeviraja. Structural and electrical studies of nano structured Sn1-x SbxO2 (x = 0.0, 1, 2.5, 4.5 and 7 at%) prepared by co-precipitation method. *Journal of materials science*, 21(4):343–348, 2010. (cited page 41)

[47] J. Serrano, F. J. Manjón, A. H. Romero, A. Ivanov, M. Cardona, R. Lauck, A. Bosak, and M. Krisch. Phonon dispersion relations of zinc oxide: Inelastic neutron scattering and ab initio calculations. *Physical Review B*, 81(17), May 2010. (cited pages 44 et 45)

[48] A. Shah. *Thin-film silicon solar cells*. EFPL Press, 2010. (cited page 37)

[49] A. V. Singh, R. M. Mehra, N. Buthrath, A. Wakahara, and A. Yoshida. Highly conductive and transparent aluminum-doped zinc oxide thin films prepared by pulsed laser deposition in oxygen ambient. *Journal of Applied Physics*, 90(11):5661, 2001. (cited page 32)

[50] S. Singh, T. Ganguli, R. Kumar, R. Srinivasa, and S. Major. Substrate temperature dependence of growth mode, microstructure and optical properties of highly oriented zinc oxide films deposited by reactive sputtering. *Thin Solid Films*, 517(2):661–669, Nov. 2008. (cited pages 41 et 77)

[51] S. Singh, R. Srinivasa, and S. Major. Effect of substrate temperature on the structure and optical properties of ZnO thin films deposited by reactive rf magnetron sputtering. *Thin Solid Films*, 515(24):8718–8722, Oct. 2007. (cited page 48)

[52] D. Song. *Zinc Oxide TCOs (Transparent Conductive Oxides) and Polycrystalline Silicon Thin-Films for Photovoltaic Applications*. PhD thesis, New South Wales, 2005. (cited pages 18, 25 et 58)

[53] J. Steinhauser. *Low Pressure Chemical Vapor Deposited Zinc Oxide For Silicon Thin Film Solar Cells Optical And Electrical Properties*. PhD thesis, Université de Neuchâtel, 2008. (cited pages 23 et 32)

[54] J. Szczyrbowski, A. Dietrich, and K. Hartig. Bendable silver-based low emissivity coating on glass. *Solar Energy Materials*, 19(1-2):43–53, Sept. 1989. (cited page 32)

[55] W. Tang and D. Cameron. Aluminum-doped zinc oxide transparent conductors deposited by the sol-gel process. *Thin Solid Films*, 238(1):83–87, Jan. 1994. (cited page 32)

[56] T. Yoshida, K. Terada, D. Schlettwein, T. Oekermann, T. Sugiura, and H. Minoura. Electrochemical Self-Assembly of Nanoporous ZnO/Eosin Y Thin Films and Their Sensitized Photoelectrochemical Performance. *Advanced Materials*, 12(16):1214–1217, 2000. (cited page 32)

[57] H. Zeng, J. Cui, B. Cao, U. Gibson, Y. Bando, and D. Golberg. Electrochemical Deposition of ZnO Nanowire Arrays: Organization, Doping, and Properties. *Science of Advanced Materials*, 2(3):336–358, Sept. 2010. (cited page 32)

[58] X. Zhu, H.-Z. Wu, D.-J. Qiu, Z. Yuan, G. Jin, J. Kong, and W. Shen. Photoluminescence and resonant Raman scattering in N-doped ZnO thin films. *Optics Communications*, 283(13):2695–2699, July 2010. (cited page 43)

Chapter 3

Optimization of ZnO:Al thin film deposition

Contents

This chapter deals with the main results on ZnO:Al thin film deposition by RF magnetron sputtering. The effects of the deposition parameters such as the working pressure, the substrate temperature, the thickness of the deposited layer, the power applied to the target or the gas composition have been investigated.

3.1 Introduction

Transparent and conductive sputtered ZnO thin films were first reported by Brett *et al.* in the early 1980's [9]. Many studies have since been published, dealing with the deposition parameters.

Without any post-deposition treatments, Agashe *et al.* have improved the mobility up to 44.2 $cm^2/V.s$ using a low target Al concentration of 0.5 wt% for an electrical resistivity as low as 3.7×10^{-4} Ω.cm [3]. Yoo *et al.* have obtained highly transparent (T > 85%) ZnO:Al films with electrical resistivity of 1.9×10^{-4} Ω.cm for ZnO:Al thin films deposited on glass substrate at a temperature of 300 °C and at an argon pressure of 0.27 Pa [59]. Yang *et al.* have obtained a resistivity of 4.2×10^{-4} Ω.cm at the same deposition temperature, for a sputtering power of 140 W [58].

Table 3.1: Compilation of electrical and optical properties of ZnO:Al thin films deposited by RF magnetron sputtering.

Reference	T_{sub}(°C)	P (Pa)	Target Al wt%	ρ (Ω.cm)	μ ($cm^2/V.s$)
Minani *et al.* [32]	30	0.5	2 wt%	1.9×10^{-4}	22
Igasaki *et al.* [21]	150	1.33	2 wt%,	1.4×10^{-4}	34
Löffl *et al.* [31]	270	0.38	-	2.8×10^{-4}	39
Agashe *et al.* [3]	330	0.27	0.5 wt%	3.7×10^{-4}	44
Yoo *et al.* [59]	300	0.27	2.5 wt%	1.9×10^{-4}	-
Yang *et al.* [58]	300	1	3 wt%	4.2×10^{-4}	-
Igasaki *et al.* [20]	100	0.13	2 wt%	2.5×10^{-4}	-

Ellmer *et al.* have achieved a good physical understanding concerning the relations between the plasma parameters, the energy of sputtered species and the TCO properties in the case of ZnO films produced by reactive magnetron sputtering [12]. The working pressure is an important parameter for the optimization of the ZnO:Al thin films. Igasaki *et al.* have claimed that the electrical properties were closely related to the grain size and the surface roughness and that as argon pressure during deposition was increased, the grain size was decreased and the surface roughness was increased and thus the electrical resistivity too [20]. For Song *et al.*, microstructure and morphology depending on the gas pressure are in agreement with the trend given by Thornton's structure zone model [47]. In the structure zone model, the surface structure was separated into four zones as a function of T/T_m and argon pressure, where both T and T_m are substrate temperature and coating material melting point, respectively [51, 52].

Others studies deal with some parameters, such as the target doping concentration [4, 44], or the type of substrates [27, 30, 61].

3.2 Influence of the argon pressure

In the following section, the ZnO:Al thin films studied at various gas pressures have been deposited at room temperature, with a power applied to the target of 250 W, in pure Ar atmosphere, for a deposition time of 30 minutes. Some articles deal with the influence of the gas pressure of the properties of ZnO:Al [4,25,26,41,57]. It has been observed that the sputter pressure plays a key role in determining the electrical properties. In many cases, the resistivity is the lowest at low sputter pressure [4,25,41], or at medium pressure [57].

3.2.1 Effect on deposition rate

These films have been deposited at RT. The relationship between the deposition rate and the thickness is linear. As presented in Figure 3.1, the deposition rate of the films decreases from 38.7 to 30.7 nm/min for increasing sputtering pressure from 0.01 Pa to 2.2 Pa respectively. Gas pressure can alter the growth rate through its influence on the Ar ions energy, i.e. an increase of the pressure will reduce the ion energy which leads to a decrease in the sputtering yield and thus the growth rate.

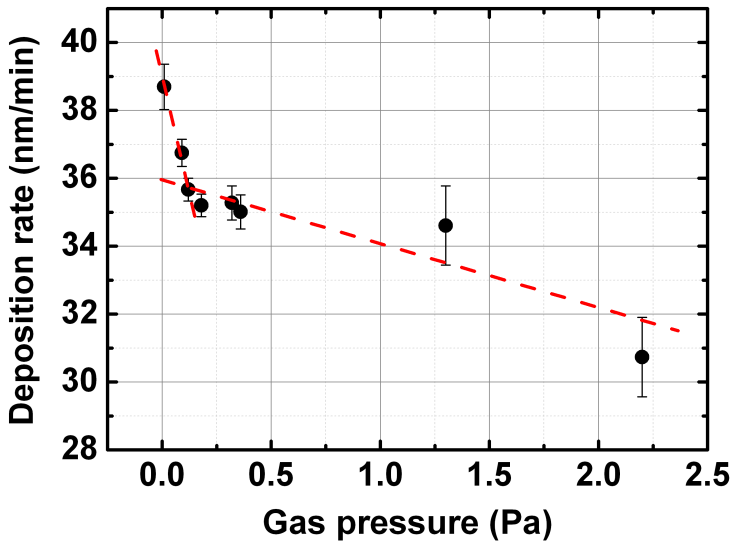

Figure 3.1: Evolution of deposition rate of ZnO:Al thin films versus gas pressure.

Two regimes are observed. At low pressure, the mean free path of argon atoms λ_{Ar} is comparable to the target-to-substrate distance (λ_{Ar} = 5 cm at 0.15 Pa) [5]. The sputtered particles arrive at the surface of the substrate with a high surface mobility, and thus a more organized growth process. The increase of the sputtering rate is higher at low pressure. For higher argon pressure, the sputtered species possess a lower mean free path (λ_{Ar} = 4 mm at 2 Pa) [5] and undergo many collisions leading to a thermalization of the film-forming particles. Thus, the increase of the working pressure decreases the surface mobility of these adsorbed species and hence the growth rate.

The decrease of the deposition rate with the increase of the working pressure, which was substantial at low pressures, is less intense from 0.12 - 0.18 Pa. This threshold value is important for ZnO:Al thin film deposition. Some strong modifications, especially morphological ones, occur at this value as shown in section 3.2.3. This pressure corresponds

probably to the transition between the regime at low pressure here there is no collision between the species of the plasma, and higher pressure where the first collisions occur.

3.2.2 Effect on microstructural properties

3.2.2.1 X-ray diffraction

The working pressure has a strong influence on the film microstructure as observed in Figure 3.2 for the XRD profiles and in Figure 3.3 for the Raman spectra of the ZnO:Al thin films deposited at various pressures.

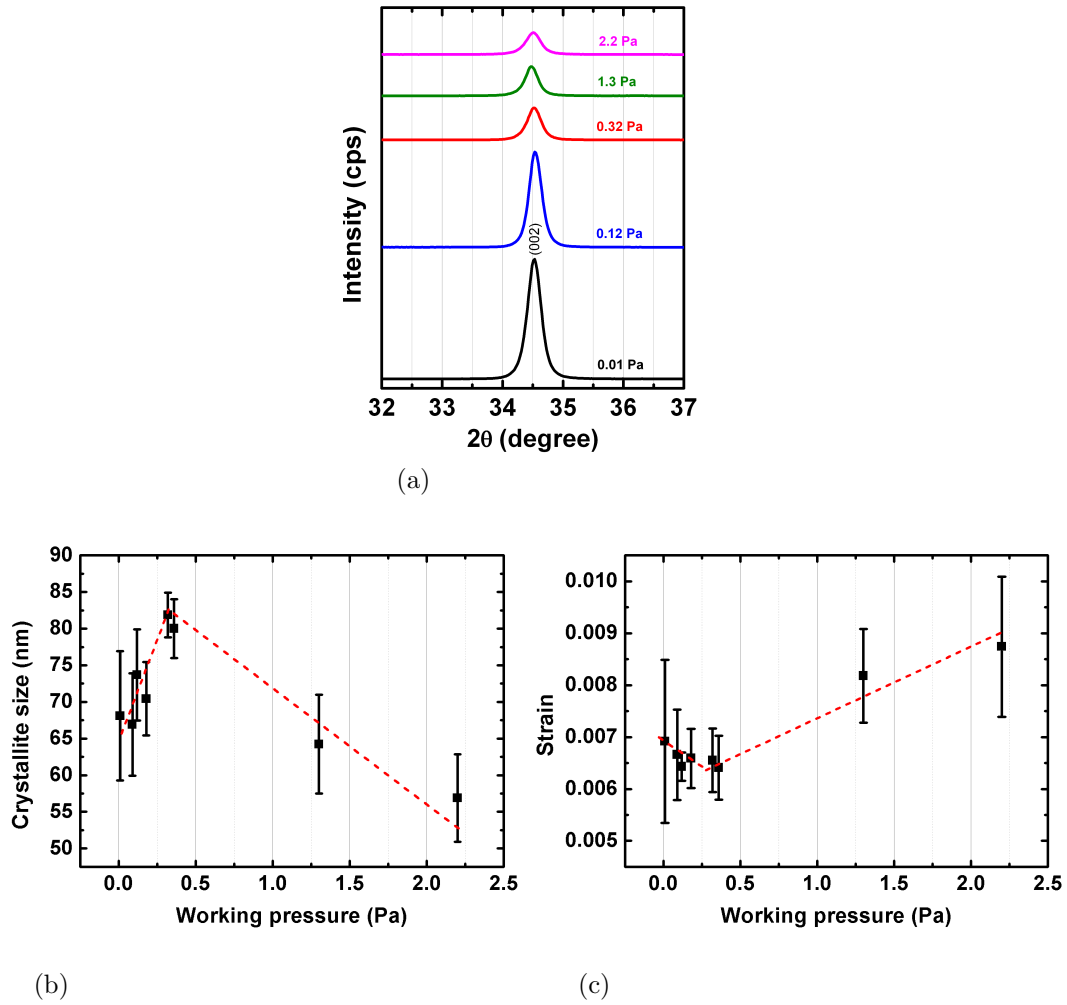

Figure 3.2: XRD profiles of ZnO:Al films deposited at various working pressures (a) and crystallite size (b) and strain (c) estimated from Williamson-Hall plots for ZnO:Al films.

All the films exhibit a strong c-axis preferred orientation revealed by the high intensity of the (002) reflection of ZnO:Al wurtzite structure. With the increase of the working pressure, a decrease of the (002) peak intensity is observed. Thin films deposited at high pressure are highly defective, while low pressure enables the growth of crystallized and (002) oriented ZnO:Al material. The vertical crystallite size and strain are estimated from the Williamson-Hall technique from the (002), (004) and (006) peaks (Figure 3.2b and

c). Different batches of depositions have been measured in order to better estimate the mean values of the crystallite size and strain. In fact, these measurements are affected by the reproducibility of the deposition process and the possible inhomogeneity of the films. Some general trends appear with the increase of the gas pressure. The strain is increasing with the gas pressure, while the crystallite size increases until an optimum value of 80 nm at around 0.3 Pa and decreases at high pressure. The strain measured from the Williamson-Hall analysis consists of non-uniform strain, i.e. systematic shift of atoms from their ideal positions, which arises from point defects (vacancies, site disorder) or poor crystallinity [39].

3.2.2.2 Raman spectroscopy

In the Raman spectra presented in Figure 3.3, the position of the A_1-LO band gradually varies from 577 cm^{-1} at 0.01 Pa to 552 cm^{-1} at 2.2 Pa. A detailed study of the correlation between the XRD and the Raman spectroscopy have been realized during this thesis. Some strong correlations between the high crystalline texturation along the [002] orientation and the position of the A_1-LO mode have arisen depending on the deposition conditions (as well as depending on the annealing processes). This band, which is highly asymmetric, arises from two contributions, a low wavenumber contribution and a high wavenumber one. The Raman spectra provide qualitative information about the crystallinity of the films. The two peaks used for the deconvolution, as presented in Figure 3.4, are attributed to different phases present in the sample: the narrow peak centred around 578 cm^{-1} is attributed to ZnO:Al crystallites while the broad peak around 550 cm^{-1} is characteristic of a disordered phase. A_1-LO peaks were fitted to pure Gauss profiles, with a linear baseline from 525 to 625 cm^{-1} which reproduces quite well the glass substrate contribution at the wavenumbers. The fits have to be considered as semi-quantitative, and further investigations have to be realized to obtain quantitative values.

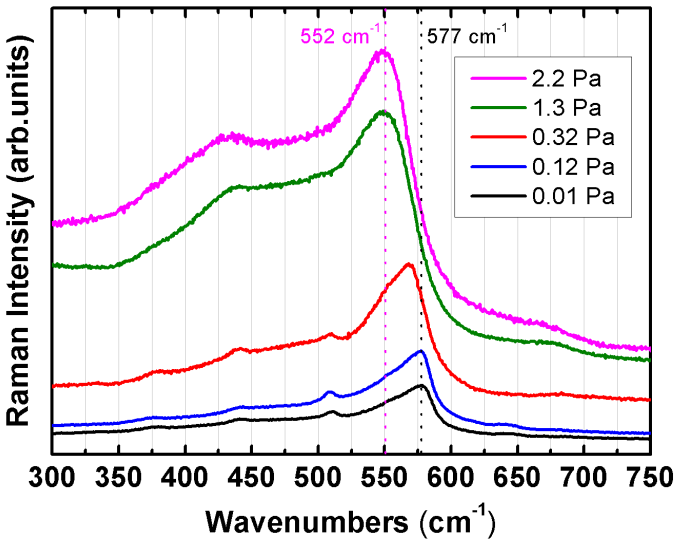

Figure 3.3: Raman spectra of ZnO:Al films deposited at various working pressures.

The apparent shift of LO modes towards lower wavenumbers is due to the increase of the low wavenumber contribution compared to the high wavenumber contribution with increasing working pressure. This effect is attributed to an increase in defects. This increase

correlates well with the significant increase in strain and the decrease in crystallinity estimated from the decrease of the intensity of (002) reflection at high deposition gas pressure with the decrease of the gas pressure (Figure 3.2). Above 0.12 Pa, the degradation of the crystallinity results from the low surface mobility of atoms at the surface of the films.

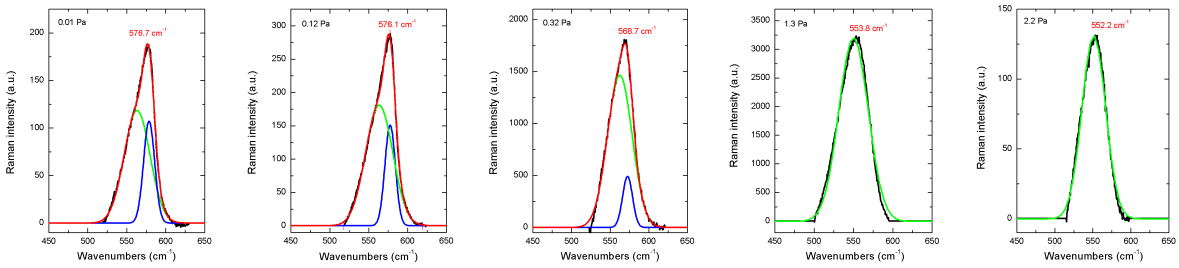

(a) 0.01 Pa (b) 0.12 Pa (c) 0.32 Pa (d) 1.3 Pa (e) 2.2 Pa

Figure 3.4: Fits of the A_1-LO band from Raman spectra of ZnO:Al films deposited at various argon pressures: (a) 0.01 Pa, (b) 0.12 Pa, (c) 0.32 Pa, (d) 1.3 Pa, and (e) 2.2 Pa.

3.2.2.3 Transmission Electron Microscopy

The microstructure of ZnO:Al thin films deposited at various gas pressures has been studied in detail by Transmission Electron Microscopy (TEM) as shown in Figure 3.5. The typical columnar structure is clearly observable for both ZnO:Al thin films.

For the ZnO:Al thin film deposited at low pressure (0.01 Pa) single grains are grown as conically shaped columns through the film thickness and the lateral grain diameter is in the range of 30 – 50 nm. The columnar grains are not single crystals but they consist of slightly tilted crystallites. It is quite difficult to relate this tilt to a consequence from the low pressure deposition or only to the position of the substrate more or less in the vertical projection of the target. Two different regions can be distinguished as a function of the thickness:

* Towards the substrate interface the layer is characterized by a system of well oriented, ordered and small crystal grains. Their growth direction, i.e. crystallographic direction orthogonal to the substrate, is the [002]. The diffraction pattern is always the same along the interface. In cross section the diffraction pattern is in the zone axis [010]. We can compare the theoretical zone axis with the experimental one as shown in Figure 3.6. A spread in the [002] direction up to 10° is also observed, producing distortions at the grain boundaries.

* After about 80 nm, the formation of large columnar shaped grains starts. When growing, they usually change direction with respect to the substrate, losing the [002] direction as observed in Figure 3.7. On top, the grains reach the lateral dimension of about 150 nm. The two regimes of growth are clearly observed in the dark field on 002 spot (Figure 3.5c): all the grains at the interface with the substrate have the same [002] orientation when selecting the 002 spot of the diffraction (Figure 3.5e). Only some columnar grains keep the [002] perpendicular to the substrate. The others, due to rotation and bending, change growth direction.

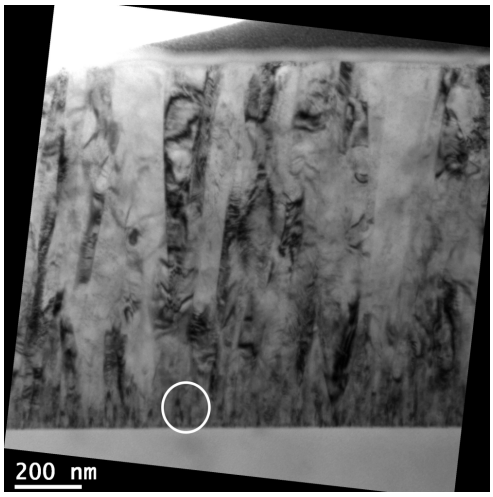

(a) 0.01 Pa: Bright field

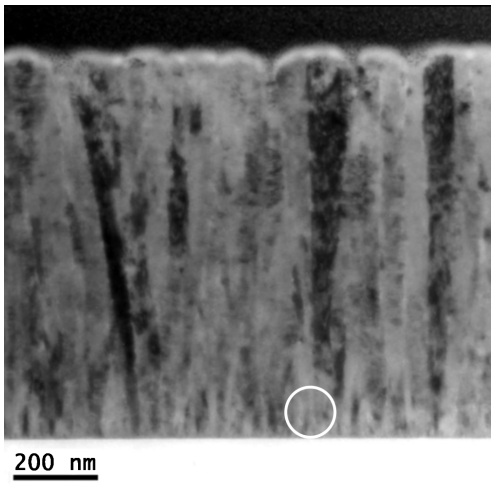

(b) 2.2 Pa: Bright field

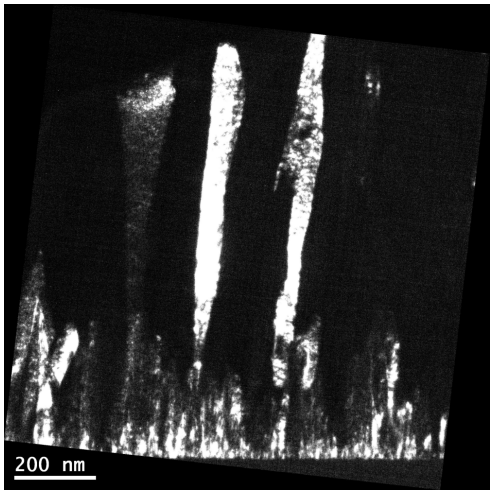

(c) 0.01 Pa: Dark field on 002 spot

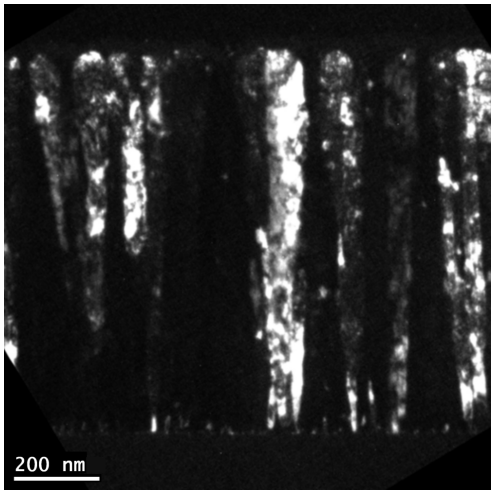

(d) 2.2 Pa: Dark field on 002 spot

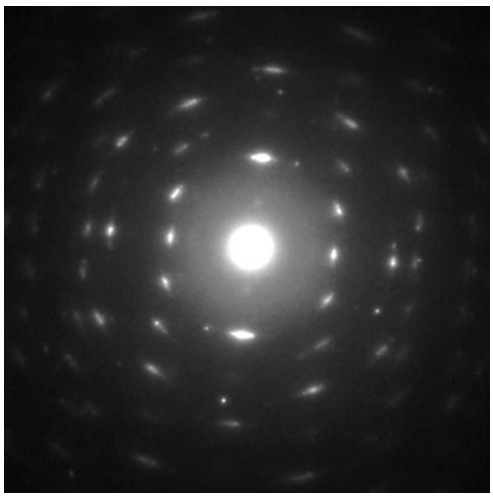

(e) 0.01 Pa: Diffraction pattern

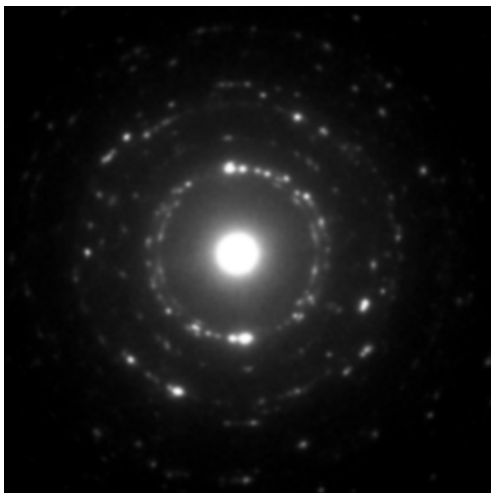

(f) 2.2 Pa: Diffraction pattern

Figure 3.5: TEM study on ZnO:Al films deposited at various pressures: Cross section bright field for film deposited at 0.01 Pa (a) and 2.2 Pa (b), Dark field on 002 spot for film deposited at 0.01 Pa (c) and 2.2 Pa (d), and diffraction pattern of the area (white circles) for film deposited at 0.01 Pa (e) and 2.2 Pa (f).

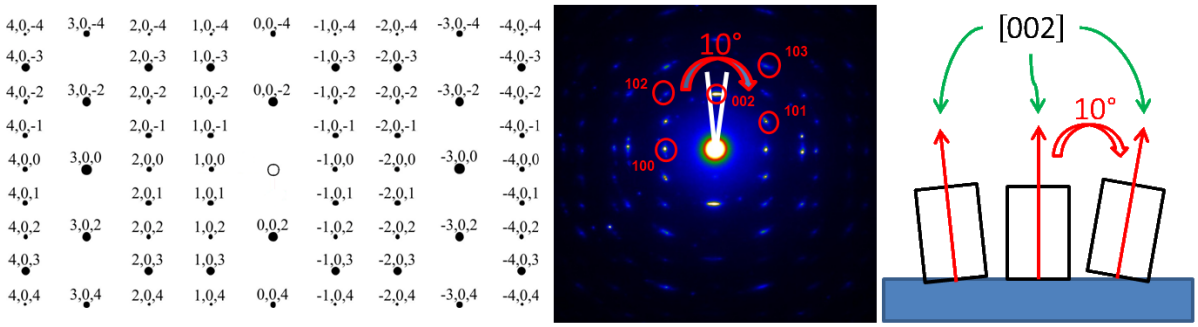

Figure 3.6: Theoretical diffraction pattern from the zone axis [010] and experimental diffraction pattern from ZnO:Al thin film deposited at 0.01 Pa near the substrate with an angular spreading in the growth direction [002].

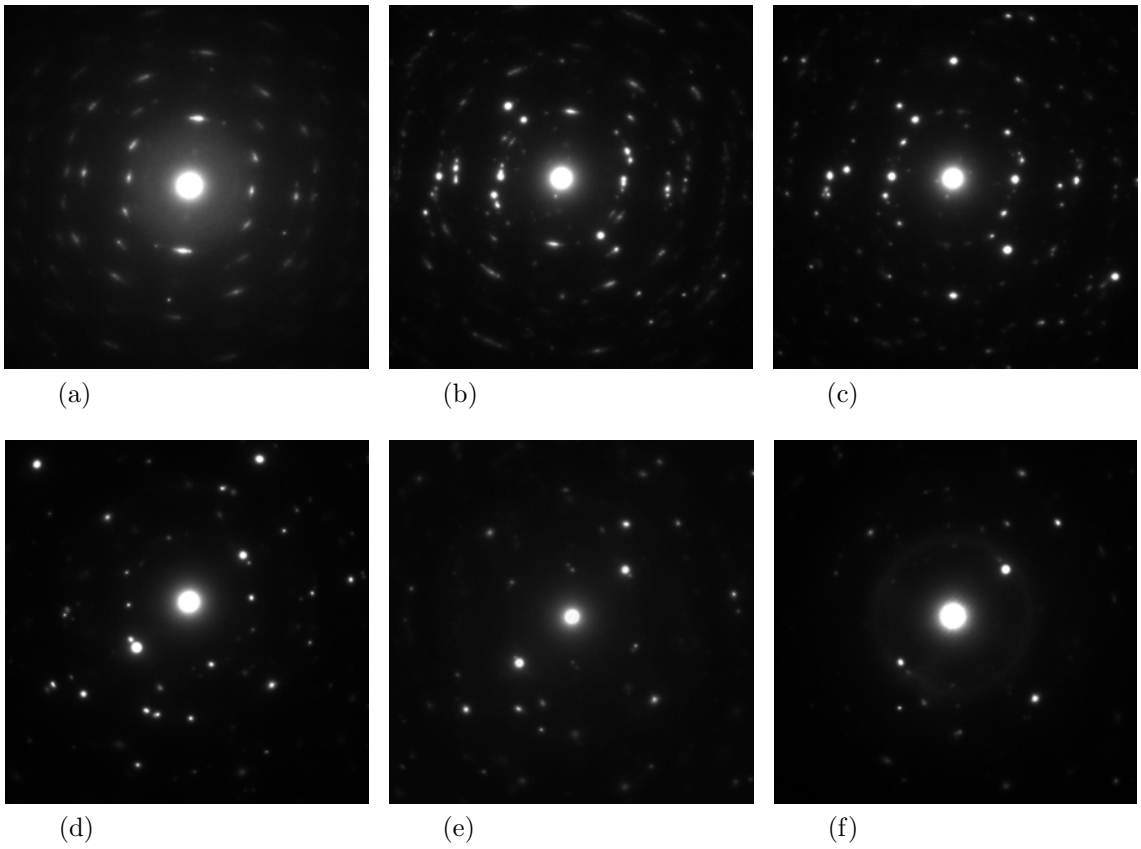

Figure 3.7: Sequence of diffraction from substrate interface (a) to surface (f) for ZnO:Al thin film deposited at 0.01 Pa.

For the ZnO:Al thin film deposited at high pressure (2.2 Pa), the distinction between the substrate interface and the bulk is less visible. The substrate interface, as well as the bulk, is highly defective, with a low [002] texture as shown in Figure 3.5d and 3.5f. The few [002] oriented grains kept their orientation during the growth of the layer. The diffraction pattern exhibits a high degree of disorder. Very similar electron diffraction patterns were obtained depending on the distance to the substrate interface.

3.2.3 Effect on morphology

The influence of the argon pressure on the morphology is studied by AFM as presented in Figure 3.8. Two different regimes are observed: At low pressure, below 0.12 Pa, the surface morphology is not clearly distinguishable while at high pressure, above 0.12 Pa, crystallites are well defined, surrounded by voids. The roughness reaches a minimum value at the transition pressure of 0.12 Pa. At low pressure, grains are not visible, a rough surface appears, as at higher pressure, but with a complete different morphology. At higher pressure, the roughness comes from the grain morphology, more pronounced. The discussion and interpretation of these observations is further detailed in section 3.4.

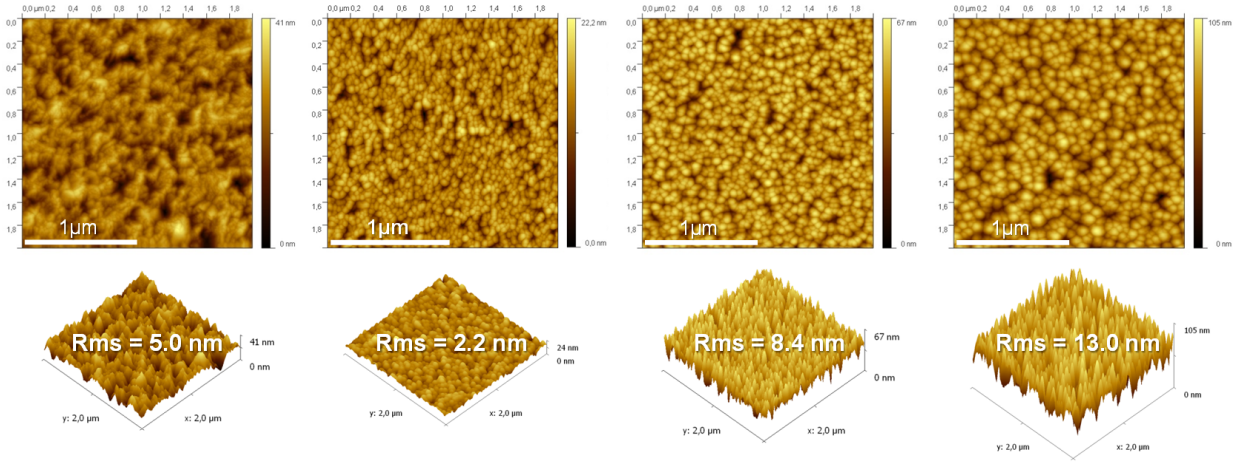

(a) 0.01 Pa (b) 0.12 Pa (c) 0.32 Pa (d) 1.3 Pa

Figure 3.8: AFM images of the ZnO:Al films deposited at various of gas pressures: (a) 0.01 Pa, (b) 0.12 Pa, (c) 0.32 Pa and (d) 1.3 Pa.

3.2.4 Effect on opto-electronic properties

Above 0.12 Pa, with the increase of the working pressure, a degradation of the electrical properties is observed, revealed by an increase in resistivity and a decrease in Hall mobility (Figure 3.9a). At high pressure, the increase in surface roughness increases the effective surface area of the film and then enhances the number of adsorption sites for oxygen. The highly porous film structure intensifies the physisorption of oxygen at the grain boundaries after deposition which are scattering centres for carriers. Oxygen adsorbed on the surface of crystallites traps electrons, decreases the carrier concentration and also decreases the Hall mobility by increasing the potential barrier at the surface of crystallites.

The defective nature of high pressure deposited ZnO:Al thin films is clearly visible on their transmittance spectra presented in Figure 3.9b. With the increase of the argon pressure, a decrease of the transmittance is observed, from 80.1% at 0.01 Pa to 9.6% at 2.2 Pa in the range between 400 and 1000 nm. The oscillations are due to the Fabry-Perot effect in the ZnO:Al thin films, and their amplitudes in the spectra are caused by optical interferences due to the change in refractive index at the interfaces.

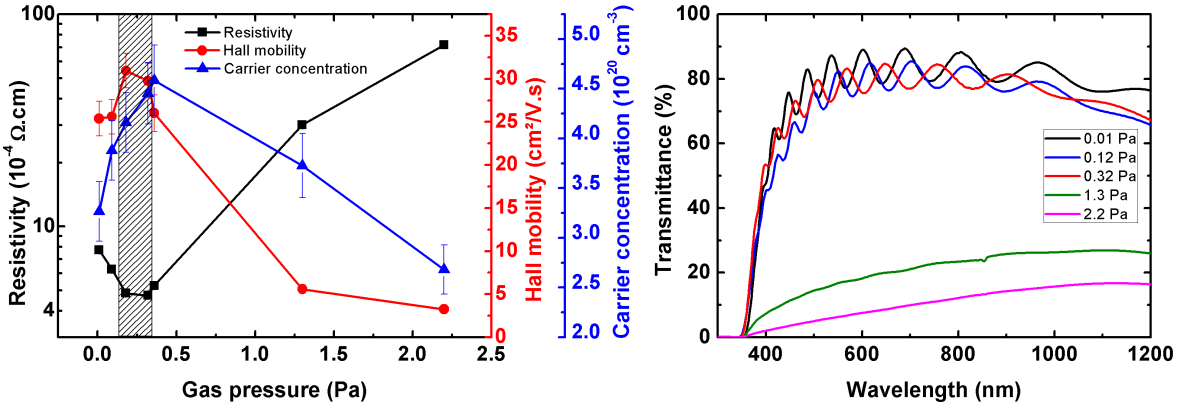

(a) (b)

Figure 3.9: Opto-electronic properties of ZnO:Al thin films deposited at various pressures: (a) Resistivity (black curve), Hall mobility (red curve) and carrier concentration (blue curve). The gray area corresponds to the electrical optimum. (b) Transmittance spectra.

3.3 Influence of the substrate temperature

In the following section, the ZnO:Al thin films studied at various substrate temperatures have been deposited at 0.12 Pa, with a power applied to the target of 250 W, in pure Ar atmosphere, for a deposition time of 30 minutes. Many articles deal with the effect of the substrate temperature on the properties of ZnO:Al thin film [12, 56, 57] and on the microstructural properties [45]. All of them report an increase of the Hall mobility with the substrate temperature. Singh *et al.* have realized a detailed microstructural analysis showing that with an increase in substrate temperature from 300 °C to 600 °C, a significant reduction in micro-strain takes place, along with a marginal increase in crystallite size [45].

3.3.1 Effect on microstructural properties

3.3.1.1 X-ray diffraction

An improvement of crystallinity is observed in X-ray diffraction profiles with increasing temperature up to 260 °C as well as an increase of the crystallite size up to 325 °C deduced from Williamson-Hall plots (Figure 3.10). These improvements are attributed to an increase in surface diffusion of the adsorbed species. The crystallite size varies from 70 nm for a sample deposited at room temperature to 100 nm at a substrate temperature of 325 °C. In parallel, the strain decreases with increasing substrate temperature. The improvement of the crystallinity is obtained thanks to a reduction in defects inside the films which involves a network relaxation.

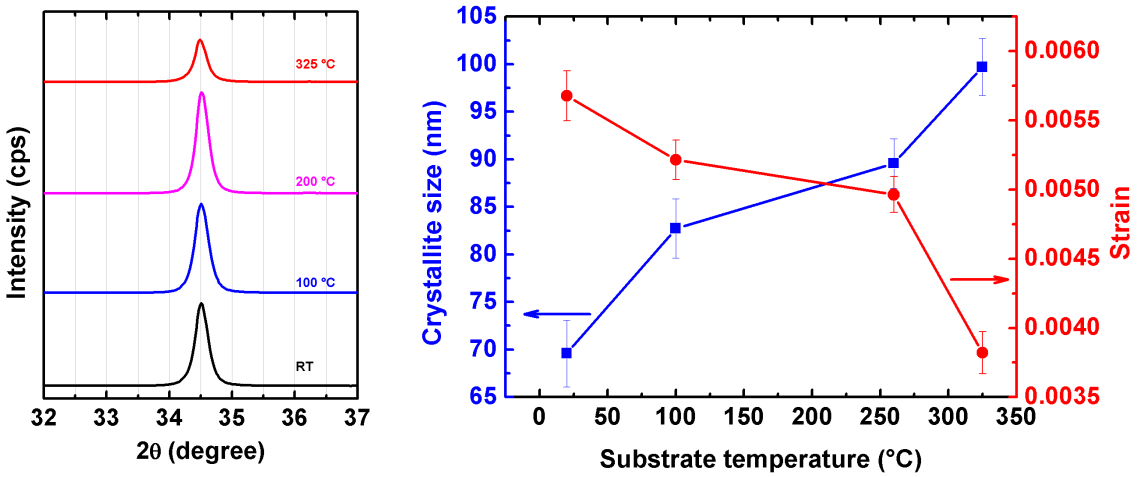

(a) (b)

Figure 3.10: XRD profiles of ZnO:Al films deposited at various substrate temperatures (a) and crystallite size and strain (b) estimated from Williamson-Hall plots for ZnO:Al films.

3.3.1.2 Raman spectroscopy

The improvement of the crystallinity is also observed by Raman spectroscopy as shown in Figure 3.11. The A_1-LO band is positioned at 577 cm^{-1}. This band is asymmetric, feature coming from two contributions: the high wavenumber contribution increases with increasing temperature compared to low wavenumber contribution as observed on the fit profiles in Figure 3.12. This trend reveals an improvement of the quality of the layer, improvement of the crystallinity and reduction in defects of the ZnO:Al films.

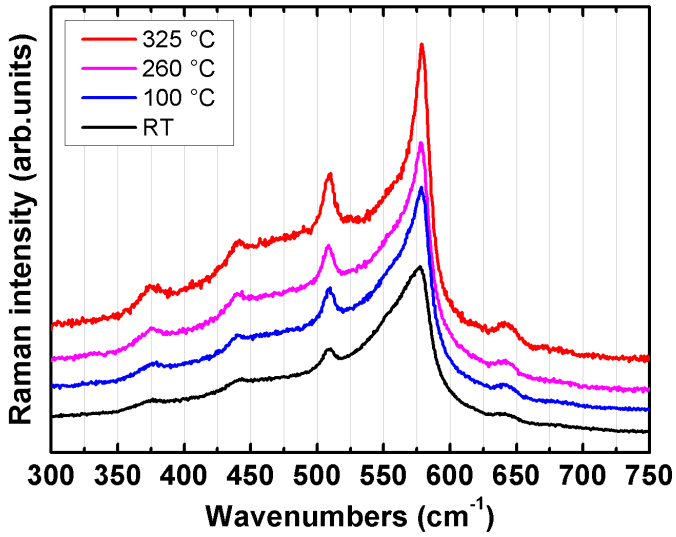

Figure 3.11: Raman spectra of ZnO:Al films deposited at various substrate temperatures.

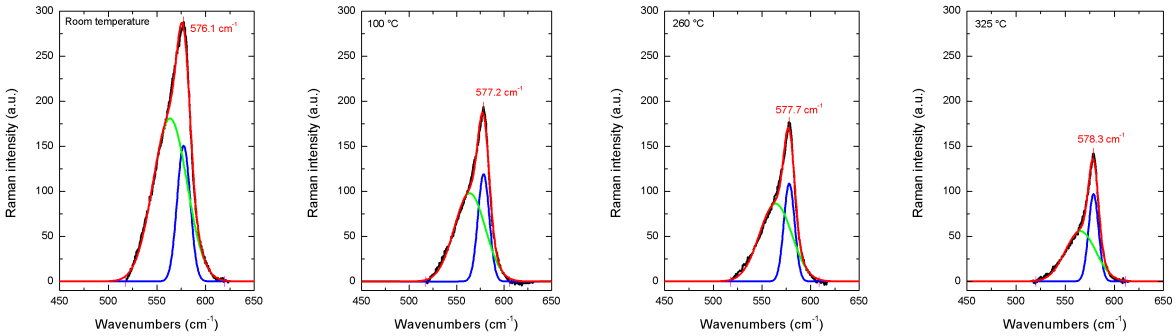

(a) RT (b) 100 °C (c) 260 °C (d) 325 °C

Figure 3.12: Fit of the A_1-LO band from Raman spectra of ZnO:Al films deposited at various substrate temperatures: (a) room temperature, (b) 100 °C, (c) 260 °C, and (d) 325 °C.

3.3.2 Effect on morphology

An increase of the lateral dimension of the columns is observed on the top of the film in AFM images, as well as an increase of the roughness (Figure 3.13). With the increase of the substrate temperature, the atoms at the surface of the growing films are more energetic and mobile and the crystallization is enhanced. This observation is further discussed in section 3.4.

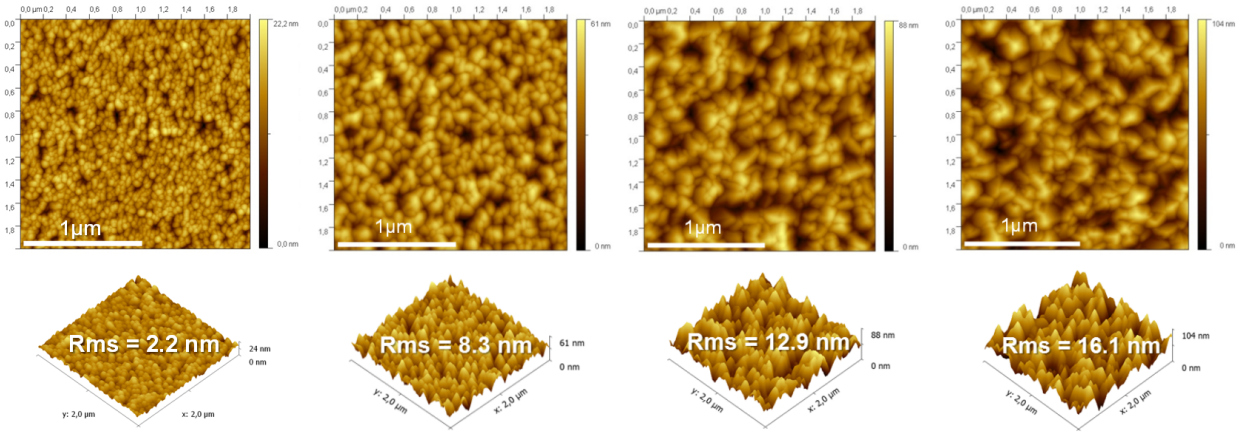

(a) RT (b) 100 °C (c) 260 °C (d) 325 °C

Figure 3.13: AFM images of the ZnO:Al films deposited at various substrate temperatures: (a) RT, (b) 100 °C, (c) 260 °C and (d) 325 °C.

3.3.3 Effect at low thickness

In order to understand the effect of the substrate temperature on the growth mechanism, ZnO:Al films are deposited at different substrate temperatures during a very short deposition time in order to compare their nucleation stages. Two 50 nm thick ZnO:Al thin films are deposited at 0.12 Pa, in pure Ar atmosphere, at RT and 325 °C respectively. The

microstructural and morphological properties are studied. It is not possible to extract the crystallite size and the strain from the Williamson-Hall plots due to the weak intensity of the (004) and (006) peaks. The crystalline quality of the films is estimated from the FWHM and the position of the (002) peak.

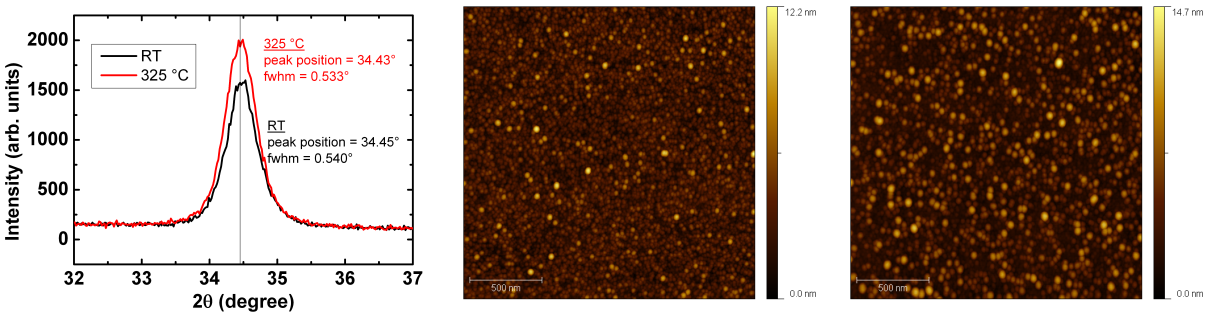

(a) (b) RT (c) 325 °C

Figure 3.14: XRD profiles of 50 nm thick ZnO:Al films deposited at RT and 325 °C (a), and AFM images of the ZnO:Al films deposited at RT (b), and 325 °C (c).

The XRD profiles, presented in Figure 3.14a, exhibit a high intensity of the (002) peak for ZnO:Al films deposited at 325 °C, as well as a lower FWHM value, and a peak position shifted to lower degrees. These observations confirm a better crystalline quality for ZnO:Al films deposited at high substrate temperature, from the first steps of nucleation. The shift in the peak position at low substrate temperature indicates a smaller distance between lattice planes, which in turn indicates stronger tensile stress. No other crystalline orientations appear.

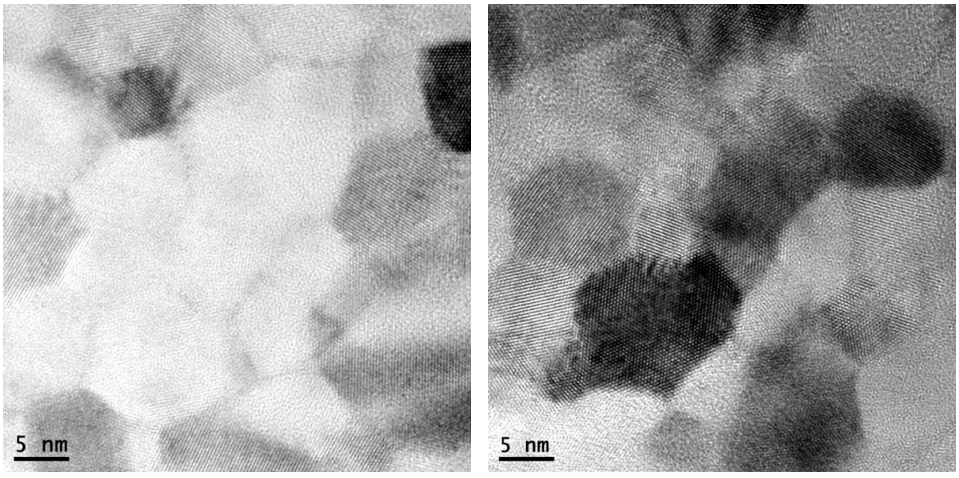

(a) (b)

Figure 3.15: High resolution plan view TEM images of early stage film growth of 50 nm thick ZnO:Al film deposited at RT and 0.12 Pa.

The TEM in cross-sectional view is a very powerful technique but is limited when investigating the early stages of ZnO:Al film growth. Here, the deposition has been

directly realized on oxide substrates with TEM employing windows etched TEM wafers, from Neyco. The central part of each TEM grid was previously etched away to create a 15 – 20 nm thick silicon nitride window through which the electron beam can pass, enabling imaging of the supported particles on a subnanometer length scale. In Figure 3.15, crystalline grains are observed, some of them with a hexagonal shape which is an indication confirming the [002] growth orientation. The grains are well-defined and crystallized.

3.3.4 Effect on opto-electronic properties

The opto-electronic properties are presented in Figure 3.16. With the increase of the substrate temperature, an increase of the carrier concentration and the Hall mobility, resulting in a decrease of the resistivity, is observed (Figure 3.16a). This improvement of the electrical properties is related to an increase of the layer density and an increase in crystallite size along the growth direction for films deposited at high substrate temperature, which results in a decrease in grain boundaries that act as scattering centres for charge carriers.

The transmittance spectra presented in Figure 3.16b show an increase of the transparency in the visible range with the increase of the substrate temperature.

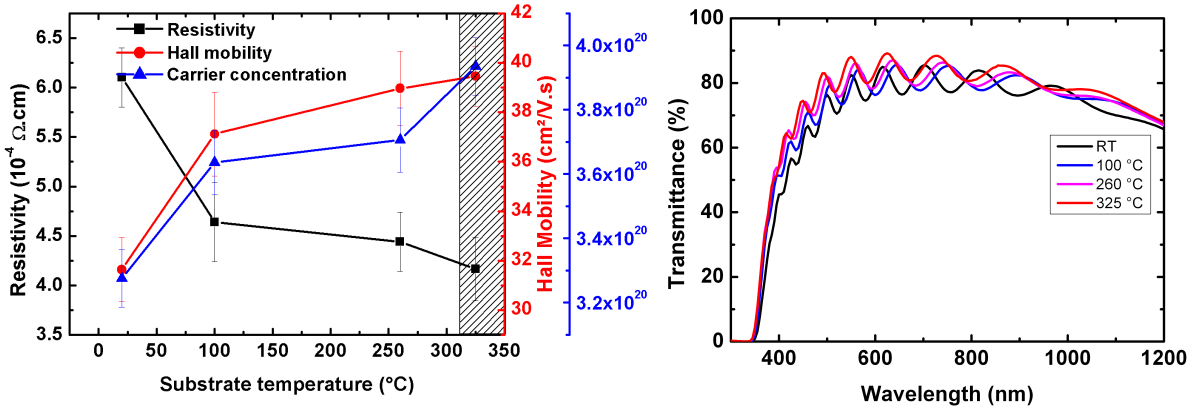

(a) (b)

Figure 3.16: Opto-electronic properties of the ZnO:Al thin films deposited at various substrate temperatures: (a) Resistivity (black curve), Hall mobility (red curve) and carrier concentration (blue curve). The dashed area corresponds to the electrical optimum. (b) Transmittance spectra.

3.4 Discussion and correlation with the growth mechanisms

3.4.1 Structure evolution with increasing argon pressure and substrate temperature

The effects of the argon pressure and the substrate temperature on microstructural and morphological properties are consistent with the Thornton's structure zone model (Figure 3.17 and Figure 3.18) [51, 52]. The structure evolution during the nucleation and growth of polycrystalline thin films [1, 7, 50] and especially ZnO thin films [24, 33, 34, 54] have been studied by other groups. The morphological evolution and texture development have been investigated, as functions of the substrate temperature [34] and gas pressure [54].

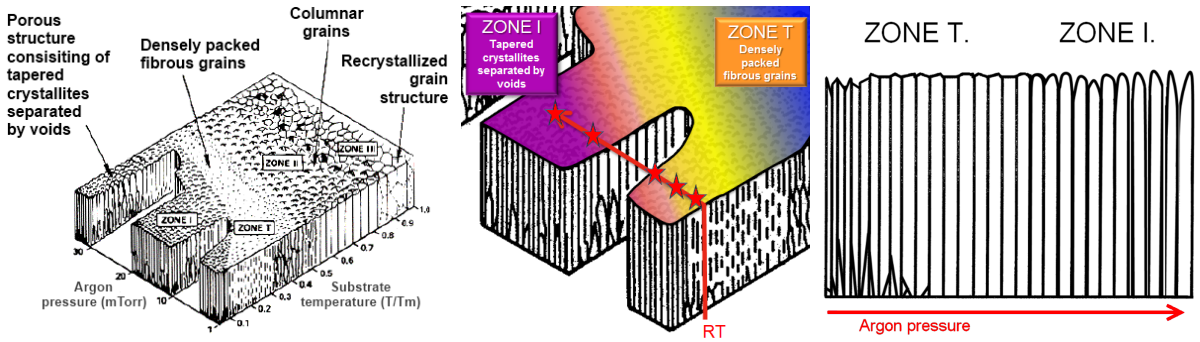

(a) (b) (c)

Figure 3.17: Thornton structure zone model correlating the argon pressure and the substrate temperature to the microstructural properties of the sputtered films [51, 52] (a). When increasing the argon pressure from 0.01 Pa to 2.2 Pa, the structure transits from zone T. to zone I. (b) and (c).

Concerning the effect of the argon pressure, an optimum is reached in terms of microstructure between 0.12 and 0.32 Pa, where the roughness of the ZnO:Al thin film is the lowest, with the highest crystallite size and relative low strain inside the network. The film is highly crystallized and [002] oriented. At lower or higher gas pressure, two different sputtering regimes appear.

At low pressure, below 0.12 Pa, the ZnO:Al films are still highly oriented, but with a smaller crystallite size (Figure 3.2) and with a slight increase of the roughness (Figure 3.8). The surface structure corresponds to the zone consisting of densely packed fibrous grains (zone T.) in the Thornton's structure zone model (Figure 3.17). At low pressure, the growing films are bombarded by positive ions and high energy neutral atoms. Negative ions may also bombard the growing surface [12]. The mean free paths of the particles are longer than the target-substrate distance ($\lambda = 5$ cm at 0.15 Pa), and due to few collisions occurring within the plasma, incident angles are close to normal and bombarding energy tends to be high [5]. This bombardment, known as the atomic peening effect, perturbed the grain growth process as clearly observed in the AFM images (Figure 3.8), and causes the atom displacement, which can lead to a decrease of the crystallite size and/or the increase of the strain inside the network [51, 52]. Adatoms are enough energetic to or-

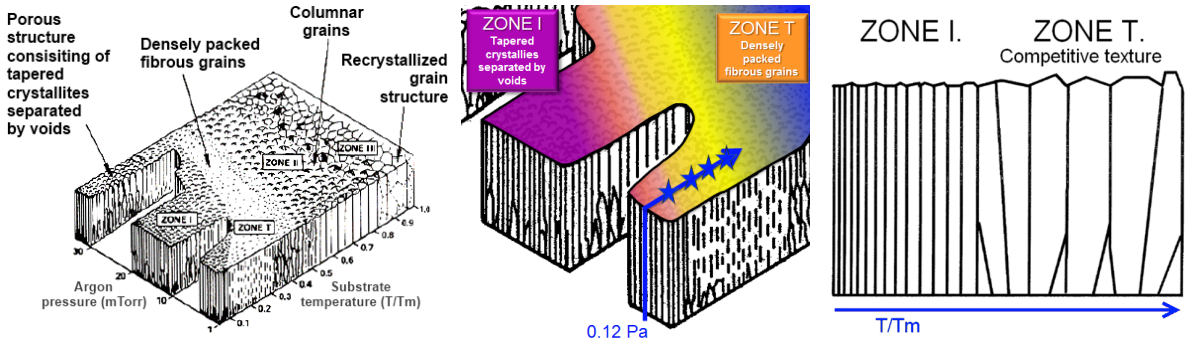

(a) (b) (c)

Figure 3.18: Thornton structure zone model correlating the argon pressure and the substrate temperature to the microstructural properties of the sputtered films [51, 52] (a). When increasing the substrate temperature from room temperature to 325 °C, the structure transits from zone I. to zone T. (b) and (c).

ganize themselves and grow in the [002] orientation but are disturbed by the destructive bombardment which decreases the grain size and increases the roughness of the films.

At high pressure, above 0.12 Pa, the films become highly defective, with a decrease of the crystallite size, and an increase of the strain inside the network due to crystalline defects (Figure 3.2). With the increase of the working pressure, the mean free path of the sputtered species decreases (λ = 4 mm at 2 Pa) [5]. The thermalization of sputtered particles through collisions limits the mobility of surface atoms and self-shadowing effect becomes pronounced at high argon pressure, leading to an increase of the surface roughness. The sputtered species undergo many collisions and as a result of their low energy, these impinging particles have low surface mobility and crystallize through a high defective way, increasing the non-uniform strain inside the network (Figure 3.2b). The structure of the films undergoes a transition from densely packed fibrous grains (zone T.) to a porous zone consisting of tapered crystallites separated by voids (zone I.). The adatoms are not enough energetic to grow in the [002] orientation.

Concerning the effect of the substrate temperature, its increase results in a transition from tapered crystallites separated by voids zone (zone I.) to a densely packed fibrous grains zone (zone T.) as observed in the Thornton's structure zone model (Figure 3.18). The increase of the crystallite size along the growth direction with substrate temperature (Figure 3.10) is accompanied with an increase of the lateral dimension of the columns observed on the top of the film in AFM images (Figure 3.13).

At low substrate temperature, in zone I., the film consists of tapered crystallites separated by voids, the surface of the glass substrate is covered by a high density of small nuclei. Crystalline grains grow out of these primary nuclei until the top of the film and the [002] oriented grains rapidly dominate over the other orientations. The nucleation density determines the lateral size of the fibres which are growing uninterruptedly side by side.

At high substrate temperature, in zone T., the film consists of densely packed fibrous grains, atoms on the surface of the glass substrate are highly energetic. The surface is covered of a low density of large islands, leading to a competitive growth of differently

oriented neighbouring islands and thus V-shaped columns. The lateral growth of the grains is faster than the vertical growth.

3.4.2 Structure evolution with increasing thickness

In the following section, the ZnO:Al thin films are studied at various thicknesses, for a deposition realized at room temperature, in pure Ar atmosphere, for a sputtering power of 250 W. Some articles deal with the effect of the thickness on the properties of ZnO:Al thin films [4, 15, 29, 43]. Lin *et al.* have observed an increase of the crystal size with the thickness [29], such as Selmi *et al.* [43]. A more detailed study was realized by Fortunato *et al.*, who have observed a continuous increase of the Hall mobility with the thickness of the ZnO:Ga thin film, while the resistivity and the carrier concentration have stabilized at a maximum value from 300 nm [15]. These results are further discussed in this section.

3.4.2.1 Morphological properties

The AFM images presented in Figure 3.19 correspond to the surface morphology on ZnO:Al thin films deposited at 325 °C or room temperature, and at two working pressures (0.12 Pa or 2.2 Pa) for different thicknesses.

The AFM images in the nucleation stage at different substrate temperatures (Figure 3.19a and b) are correlated with the Thornton's structure zone model: At low substrate temperature (Figure 3.19b), in zone I., the surface of glass is covered by a high density of small nuclei. Crystalline grains grow out of these primary nuclei in a columnar structure, and the nucleation density determines the lateral size of the columns which are growing uninterruptedly side by side. The AFM image (b) of the Figure 3.19 exhibits a smooth surface ($\delta_{\mathrm{RMS}} = 1.2$ nm) covered with small grains. At high substrate temperature (Figure 3.19a), in zone T., atoms on the surface are highly energetic. The surface is covered of a lower density of larger islands, leading to competitive growth of different oriented neighbouring islands and thus V-shaped columns. The AFM image presents a rougher surface ($\delta_{\mathrm{RMS}} = 1.9$ nm) covered with larger grains. The lateral grain size clearly increases with the thickness of the growing films, especially at high temperature (Figure 3.19a, d, g and j), when the low density of large island observed for a thickness of 50 nm leads to a competitive growth, and V-shaped columns.

Depending on the working pressure, by comparing the surface morphology of the two films, a higher roughness is visible at high working pressure from the first growing step (Figure 3.19c, f, i and l).

3.4.2.2 *Ex-situ* electrical measurements

In Figure 3.20 are presented the electrical properties of the ZnO:Al thin films deposited at RT as a function of the deposition time/thickness (from the next section 3.4.2.3). The relationship between the thickness and the deposition is linear at RT.

The carrier concentration exhibits a rapid increase from $3.5\times10^{19}\mathrm{cm}^{-3}$ to $3.2\times10^{20}\mathrm{cm}^{-3}$ until a thickness around 200 nm and then remains quite stable independently of the thickness of the film. This thickness corresponds more or less to the nucleation and growth region observed in Figure 3.5c for the first hundreds of nanometers of ZnO:Al thin film

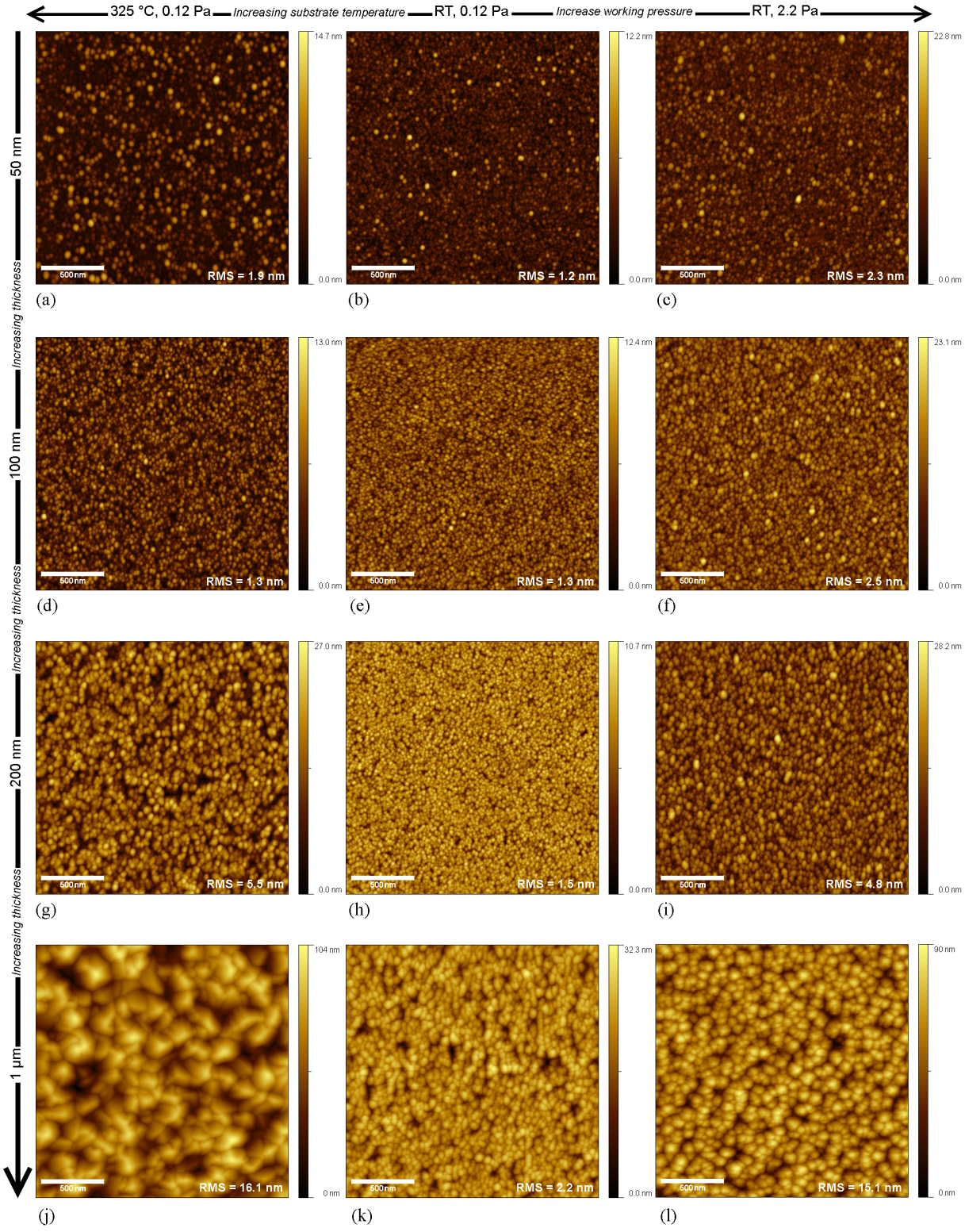

Figure 3.19: AFM images of ZnO:Al thin films deposited at various thicknesses, from 50 nm to 1 µm, and deposited under different conditions: at 325 °C and 0.12 Pa, at RT and 0.12 Pa, and at RT and 2.2 Pa.

deposited at low pressure, in comparison to the constant columnar growth region above them. The resistivity exhibits the same trend as the carrier concentration. The Hall mobility does not present the same tendency, but exhibits an increase with the thickness.

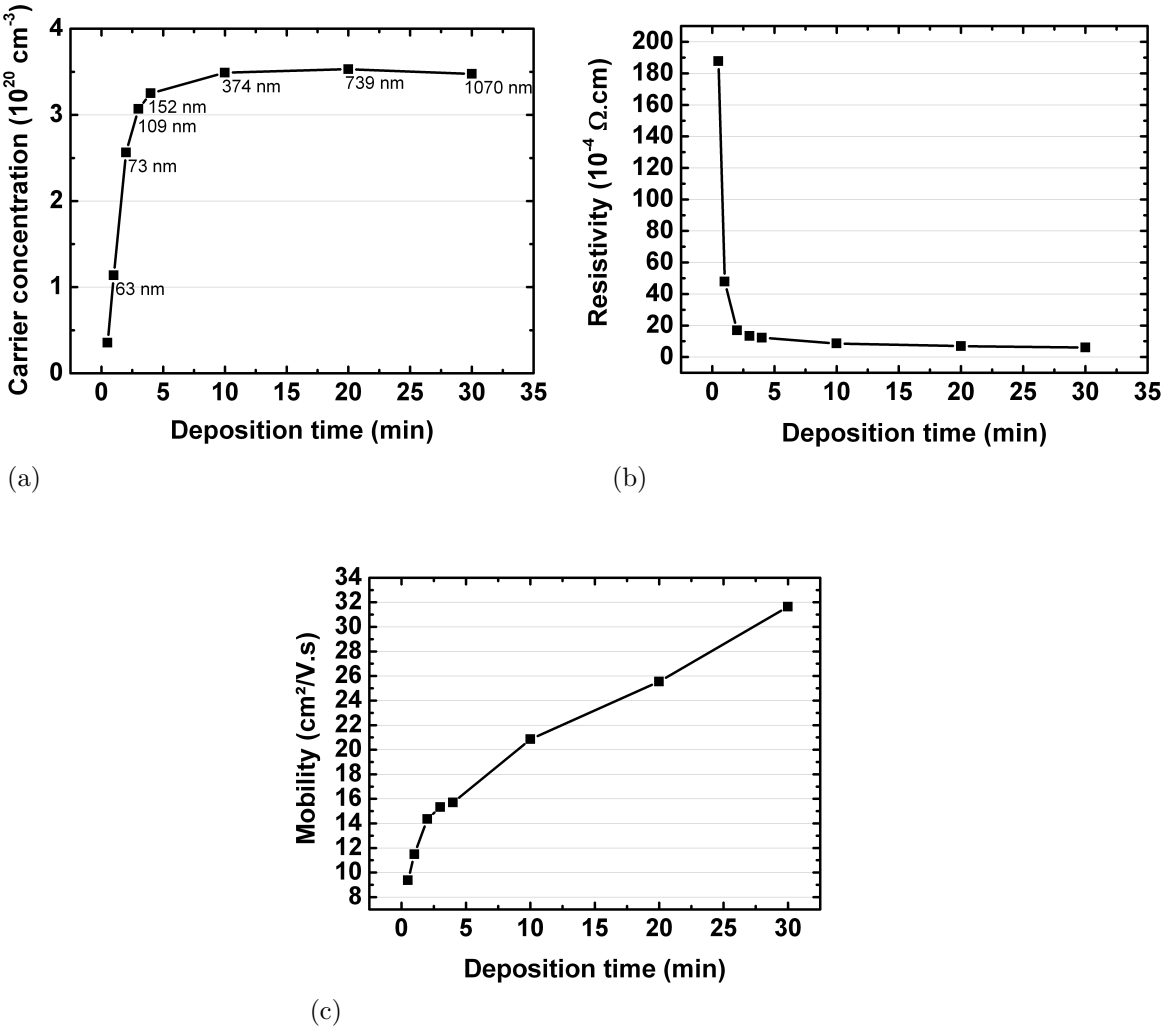

Figure 3.20: Electrical properties of the ZnO:Al thin films deposited as a function of the deposition time: (a) carrier concentration, (b) resistivity and (c) Hall mobility.

The carrier concentration depends on the bulk properties of the material. The initial strong increase of the carrier concentration is due to the high improvement of the material during the nucleation and growth phases which can be seen during the first 200 nm of growth, after which the columnar growth takes place, with a constant crystalline quality. The constant enhancement of the mobility is related to the improved crystallinity too but mainly to the increase of the crystallite size that weakens inter-crystallite boundary scattering and increases carrier lifetime. The constant increase of the lateral grain size with the thickness which can be observed in Figure 3.19 supports this conclusion.

3.4.2.3 *In-situ* resistance measurements

The relationship between the electrical properties and the thickness have been investigated at room temperature in the previous section. A more detailed study of the thickness dependence of the film's conductivity is further obtained by *in-situ* resistance measurements. The electrical properties of thin films highly depend on the deposition parameters, because they affect the growth mechanism. In order to have a better understanding of the growth mechanism, a knowledge of the first step of growth is needed. *In-situ* resistance measurements during the deposition in Cameleon reactor are realized at various substrate temperatures and argon pressures. As a function of the argon pressure, no clear differences were observed through the *in-situ* resistance measurements. We will focus on the *in-situ* measurements at various substrate temperatures. The *in-situ* resistance measurement as a function of the substrate temperature reveals some interesting trends for the understanding of the nucleation and growth stage of ZnO:Al thin films (Figure 3.21).

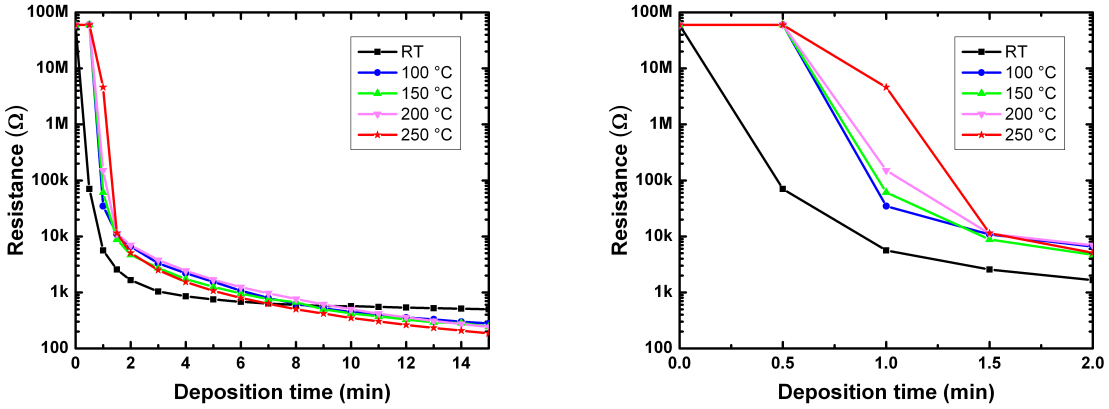

(a) (b)

Figure 3.21: In-situ resistance measurement at various substrate temperatures (a) and zoom at the first deposition steps (b).

Indeed, two distinct evolutions are observed depending on the deposition time. For a thick layer, after 10 minutes of deposition, the *in-situ* resistance exhibits the same tendency that the *ex-situ* measurements at various values of substrate temperature, i.e. the resistance is the lowest for a deposition realized at high temperature. On the other hand, surprisingly, the opposite is observed at short deposition times. The decrease of the resistance is the strongest for a deposition at room temperature. The effect of the substrate temperature on the nucleation stage is clearly observed.

At low substrate temperature, the nucleation density determines the lateral size of the fibres which are growing from the adatoms at their impinging sites [7]. The surface diffusion is weak, as well as the probability of coalescence of the initial nuclei: The surface is covered by a large density of small nuclei and the resistivity is low.

At higher substrate temperature, the surface diffusion increases, and the probability of the coalescence of the initial nuclei to larger islands too [7, 50]. The contact surfaces

between these large islands are weaker, which could explain the poorer conductivity between these islands.

This hypothesis is confirmed by the relationship between the thickness of the film as a function of the deposition time at RT and 325 °C, as shown in Figure 3.22[1]. During the first two minutes of deposition, the film structure evolution is quite different. At low temperature, the relationship is linear even after 30 seconds of deposition. The surface is covered by a large density of small nuclei, and the resistance is low thanks to a good contact between the small nuclei. At high substrate temperature, the high surface diffusion leads to the growth of the initial nuclei to larger islands. Before this coalescence, there is no or only few contacts between the islands, and as a consequence, the resistance is very high. The coalescence step leads to a slight decrease of the thickness as observed in Figure 3.22 between 30 seconds and 2 minutes of deposition, and the resistance is improved, up to exceed the value for RT deposited films.

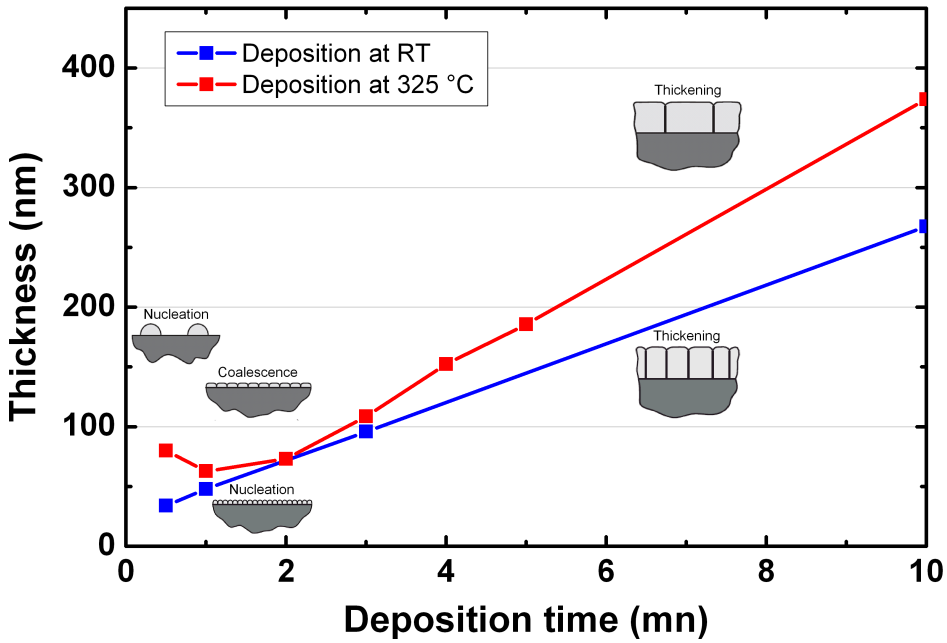

Figure 3.22: Thickness as a function of the deposition time at RT and 325 °C and corresponding structure evolution models.

3.4.3 Optimum of the opto-electronic properties

As a conclusion on the effect of the argon pressure and the substrate temperature, a mapping on the electrical and optical properties on ZnO:Al thin films can be realized as presented in Figure 3.23. This figure exhibits the resistivity and the transmittance in the wavelength range from 400 to 1000 nm as functions of the working pressure and the substrate temperature.

[1]These depositions have been realized in Alliance Concept reactor and their deposition rate values can not be quantitatively compared to the deposition rate values of the previous films deposited in Cameleon reactor.

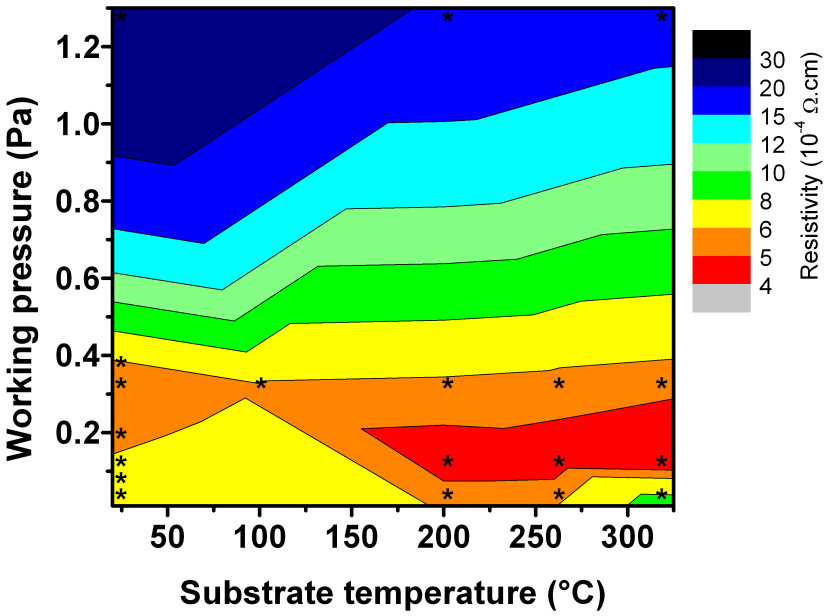

(a)

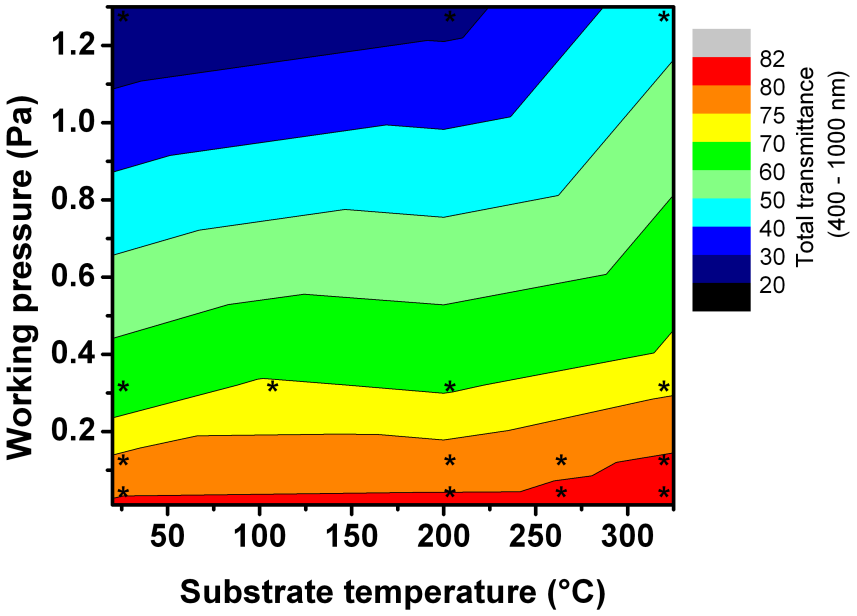

(b)

Figure 3.23: Mapping of the resistivity (a) and the transmittance in the range 400 - 1000 nm (b) as functions of the working pressure and the substrate temperature. The black stars correspond to the measured values.

The optimum properties are obtained at the highest substrate temperature, 325 °C, for an intermediate working pressure between 0.12 Pa and 0.32 Pa. This optimum corresponds to the best crystallinity, highest crystallite size and minimum strain as determined from X-ray diffraction measurements and Raman spectroscopy.

3.5 Influence of the RF sputtering power

In the following section, the ZnO:Al thin films studied at various values of the RF sputtering power have been deposited at 0.12 Pa, and at room temperature in pure Ar atmosphere. The deposition time has been fixed for each sputtering power in order to obtain a thickness of 620 ± 40 nm. Some articles deal with the effect of the power applied to the target on the properties of ZnO:Al thin films [10,18,41,46,48]. Chun *et al.* have observed an increase of the Al doping concentration with increasing sputtering power, as well as a decrease of the resistivity [10, 41], while some others studies exhibit an optimization sputtering power [18].

3.5.1 Effect on deposition rate

In order to obtain the deposition rate for each sputtering power, a study at various deposition times and RF power levels has been realized. The deposition rate is found to be constant as a function of time for a fixed sputtering power (Figure 3.24a), and to increase linearly with the sputtering power (Figure 3.24b). An increase in RF power enhances the ion flux and energy which leads to the increase in the sputtering yield and then the growth rate.

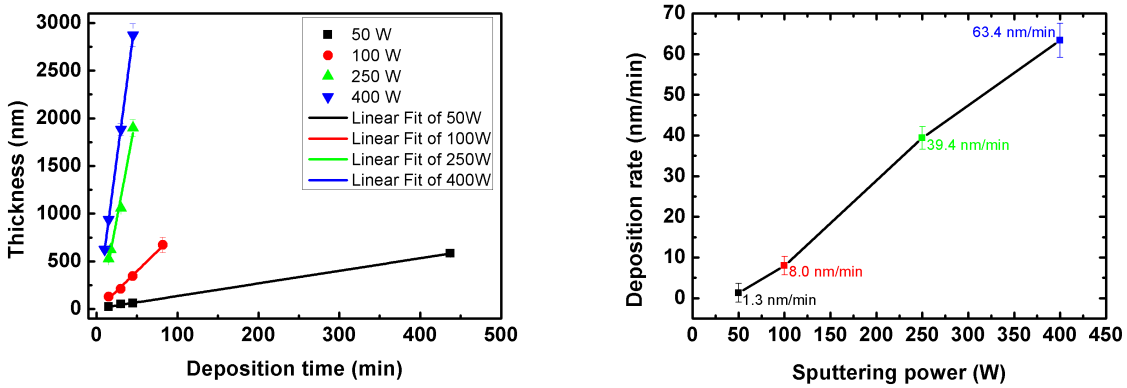

(a) (b)

Figure 3.24: Deposition rate study: Thickness of the deposited film as a function of the deposition time at various sputtering powers (a) and deposition rate as a function of the RF power (b).

3.5.2 Effect on microstructural properties

The microstructural properties of the films deposited at various sputtering powers, from 50 W to 400 W, for a thickness of 620 ± 40 nm, are studied by X-ray diffraction as presented in Figure 3.25a, and by the Williamson-Hall plot technique in Figure 3.25b. The X-ray dffraction profiles show an optimum at 100 W, sputtering power at which the intensity of the (002) peak is the highest. The Williamson-Hall plots technique reveals an increase of a tensile strain with the increasing sputtering power, as well as the highest crystallite size for a deposition realized at 100 W.

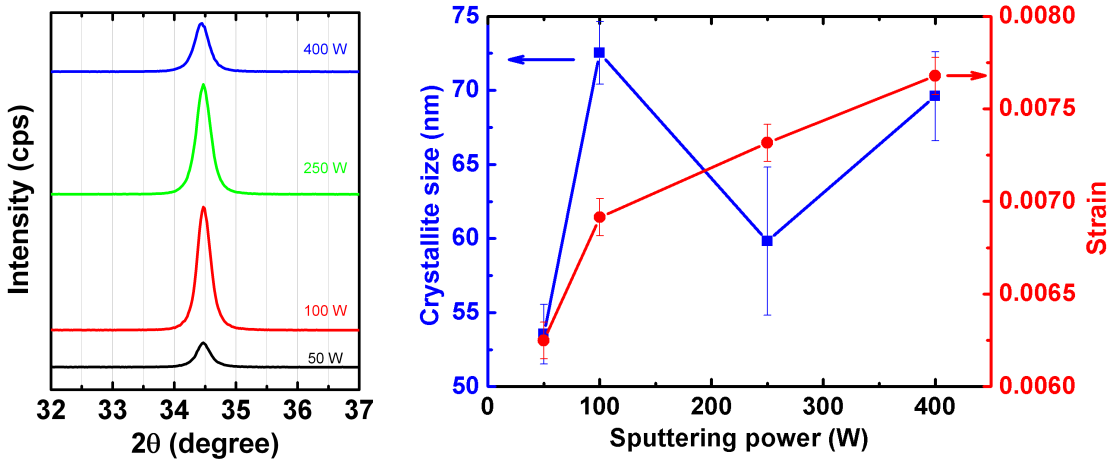

(a) (b)

Figure 3.25: XRD profiles of ZnO:Al films deposited at RT and various sputtering powers (a) and crystallite size and strain (b) estimated from Williamson-Hall plots for ZnO:Al films.

3.5.3 Effect on morphology

Figure 3.26 presents the AFM images of the ZnO:Al films deposited at various sputtering powers. The film deposited at 50 W exhibits a different morphology compared to the others with the highest roughness (25.7 nm compared to 6.5 nm for 100 W, 2.6 nm at 250 W and 2.9 nm at 400 W), probably due to the crystalline fraction of the film deposited at this power, as revealed by the (002) peak intensity.

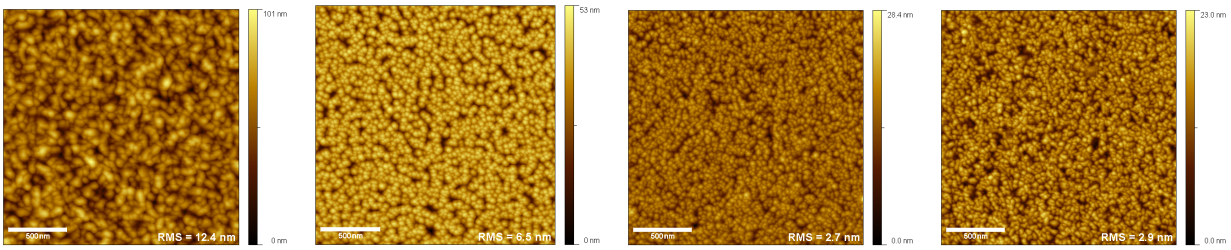

(a) 50 W (b) 100 W (c) 250 W (d) 400 W

Figure 3.26: AFM images of the ZnO:Al films deposited at various sputtering powers: (a) 50 W, (b) 100 W, (c) 250 W and (d) 400 W.

For the films deposited at 100 W and above, the lateral size of the columns seems to be the highest for the deposition realized at the sputtering power of 100 W (Figure 3.26b) Below 100 W, the surface morphology is not well defined, the material is less organized and crystallized.

3.5.4 Effects on opto-electronic properties

The Hall effect measurements exhibit an electrical optimum for a ZnO:Al deposition realized at 100 W as observed in Figure 3.27a. This optimum corresponds to the best

crystallinity presented in Figure 3.25, and the highest crystallite size. Furthermore, a strong correlation between the crystallite size and the Hall mobility can be noticed.

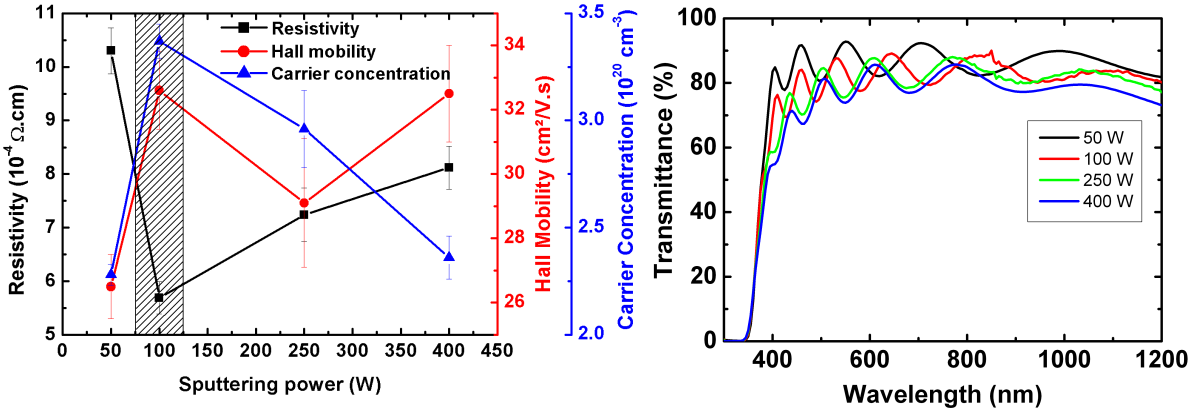

(a) (b)

Figure 3.27: Opto-electronic properties of the ZnO:Al thin films deposited at various sputtering powers: (a) Resistivity (black curve), Hall mobility (red curve) and carrier concentration (blue curve). The dashed area corresponds to the electrical optimum. (b) Transmittance spectra.

The optical spectra exhibit an increase of the total transmittance in the visible range with the decrease of the sputtering power, especially in the blue region between 400 and 500 nm. With the increase of the sputtering power, the total transmittance in the range between 400 and 1000 nm decreases from 86.5% at 50 W to 78.0% at 400 W.

The optical band gap E_g of the films can be estimated from these transmittance spectra by extrapolation of the linear region of the plot of $(h\nu(\ln T)/d)^2$ versus $h\nu$, according to the direct allowed transitions [17]. In this way, the optical band gap is estimated to increase from 3.48 ± 2 eV for a deposition realized at 50 W, to 3.56 ± 2 eV for 100 W. Then, the optical band gap slowly decreases to 3.54 ± 2 eV at 250 W and 3.51 ± 2 eV at 400 W. The behaviour in well correlated with the trend observed on the charge carrier concentration. This observation is the result of the competition between the Burstein–Moss band filling effect which shifts positively the measured band edge energy with increasing carrier concentration, and the many body effects due to electron–electron and electron–impurity interactions which lead to a narrowing of the band gap. The global effect from these two phenomena is an exponential increase of the band gap shift with the carrier concentration.

3.6 Influence of the oxygen partial pressure

In this section, the ZnO:Al thin films are studied at various oxygen partial pressures through different series at various substrate temperatures and working pressures, for a sputtering power of 250 W. The oxygen partial pressure ratio is defined as the volumetric gas flow of oxygen compared to the total gas flow (gas mixture Ar/3% O_2+Ar) in percent. Many articles report on the effect of the oxygen partial pressure on the properties

of ZnO:Al thin film [12, 28, 53], or the effect of oxygen diffusion during an annealing process [35, 60].

Due to the fact that we are working with a ceramic target of $ZnO:Al_2O_3$, no further incorporation of oxygen inside the gas mixture should be necessary. However, the influence of the oxygen partial pressure is studied. Indeed, the higher sputtering rate of oxygen with respect to Zn can create a deficiency of the oxygen inside the target which can be prevented by introducing oxygen in the gas phase.

3.6.1 Effect on opto-electronic properties

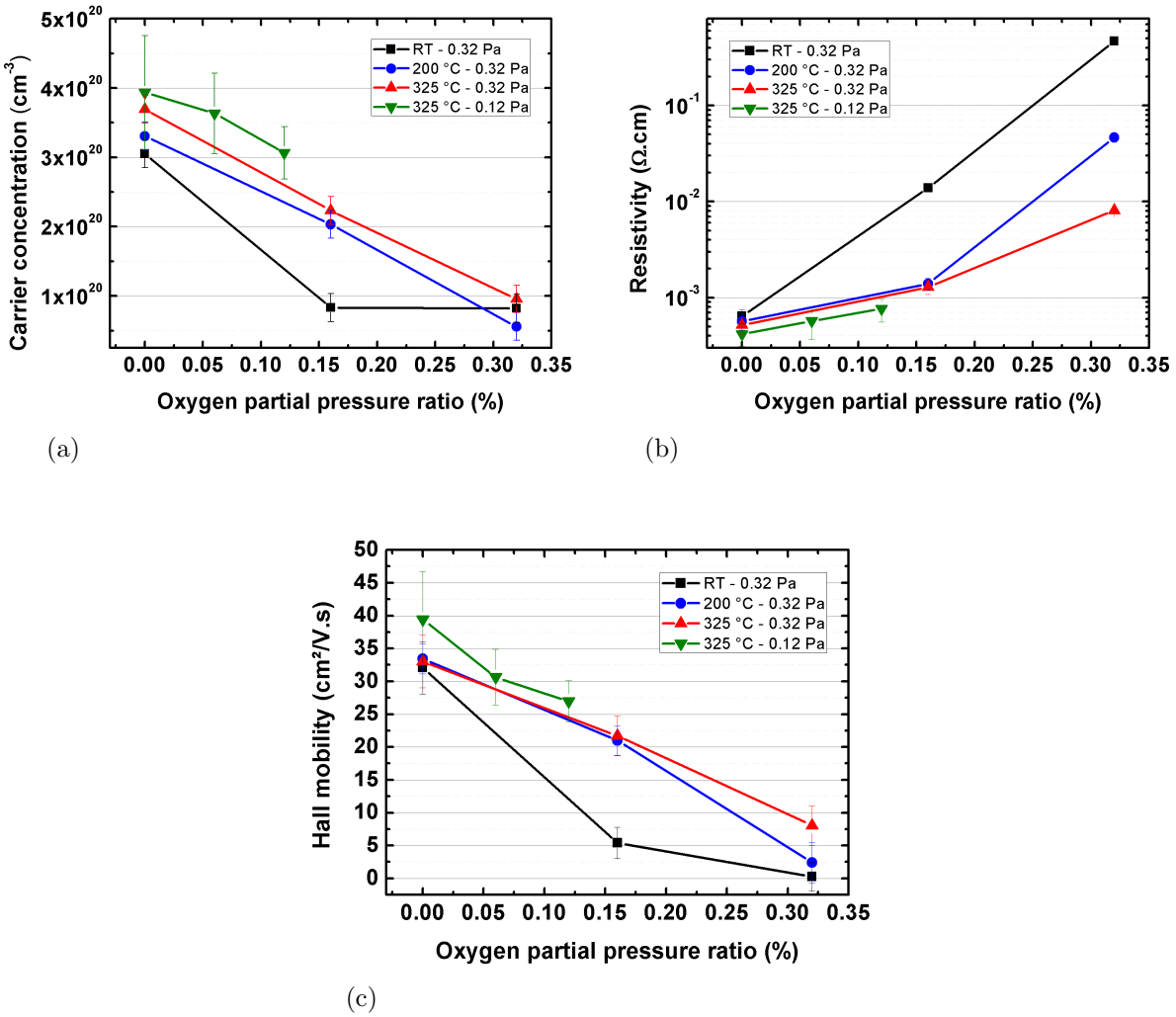

Figure 3.28: Electrical properties of the ZnO:Al thin films deposited at various oxygen partial pressure ratios: (a) Carrier concentration, (b) resistivity, (c) Hall mobility.

The addition of oxygen to the Ar gas strongly degrades the electrical properties as observed in Figure 3.28. The increase of the resistivity is due to the strong decrease of the charge carrier concentration and Hall mobility. The charge carriers principally result from intrinsic donors created by defects within the crystal structure such as oxygen vacancies

V_O, zinc interstitial Zn_i, or hydrogen interstitial H_i, and extrinsic dopants from incorporation of aluminium Al_{Zn}. The introduction of oxygen leads to the complete oxidation of zinc to ZnO, aluminium to AlO_x and filling the oxygen vacancies[2], which limit these doping mechanisms. The degradation of the resistivity is lower for films deposited at high substrate temperature, and lower working pressure, when the initial electrical properties are the best (down triangle symbols in Figure 3.28).

Moreover, the decrease of the mobility with the decrease of the charge carrier concentration suggests that the transport is limited by grain barrier scattering, as confirmed in section 3.8. The contribution of the grain boundaries is higher probably due to their preferential oxidation.

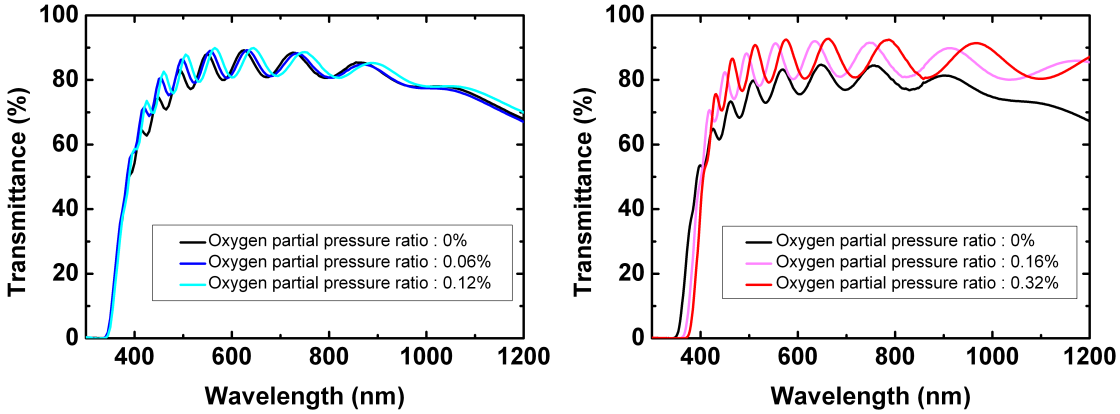

(a) (b)

Figure 3.29: Optical properties of the ZnO:Al thin films deposited at various oxygen partial pressure ratios: (a) For ZnO:Al deposited at 0.12 Pa, and 325 °C, and (b) for ZnO:Al deposited at 0.32 Pa, and room temperature.

The decrease of the charge carrier concentration is confirmed by the transmittance spectra presented in Figure 3.29. A clear shift of the absorption edge to longer wavelengths is observed, especially at high oxygen ratio in the gas phase, in Figure 3.29b. The calculated optical band gaps are presented in Table 3.2. The other observation is the improvement of the optical transmittance in the visible and NIR. For a deposition realized at 325 °C and 0.12 Pa, the transmittance increases from 80.8%, without any introduction of oxygen in the gas mixture, to 82.1% at 0.12% of oxygen partial pressure ratio, and for a deposition realized at RT and 0.32 Pa, from 77.1% without oxygen inside the gas phase to 84.1% at 0.32% of oxygen partial pressure ratio.

[2]Oxygen vacancy presents a high formation energy and its role in the n-type doping is still highly discussed.

Table 3.2: Transmittance in 400 - 1000 nm range and optical band gap for ZnO:Al thin films deposited at various values of the oxygen partial pressure ratios.

Deposition parameters	Oxygen partial pressure ratio	Transmittance (400 - 1000 nm)	Optical bang gap
325 °C - 0.12 Pa	0%	80.8%	3.54 ± 2 eV
325 °C - 0.12 Pa	0.06%	81.7%	3.56 ± 2 eV
325 °C - 0.12 Pa	0.12%	82.1%	3.55 ± 2 eV
RT - 0.32 Pa	0%	77.1%	3.50 ± 2 eV
RT - 0.32 Pa	0.16%	83.8%	3.40 ± 2 eV
RT - 0.32 Pa	0.32%	84.1%	3.34 ± 2 eV

3.7 Uniformity

In the following section, the uniformity of the films is studied in terms of their sheet resistance. Different deposition conditions are studied. These measurements are realized by eddy current measurements. The uniformity has been previously studied in some articles [22, 48]. Differences have been observed by Jeong *et al.*, who have discerned grain boundaries in the substrate periphery and not in the central substrate region, which could explain the increase of the film resistivity in the periphery of the substrate. In contrast, the variation of the optical properties across the substrate at the IR wavelengths would be due to a decrease of both the free-electron concentration and the film thickness [22].

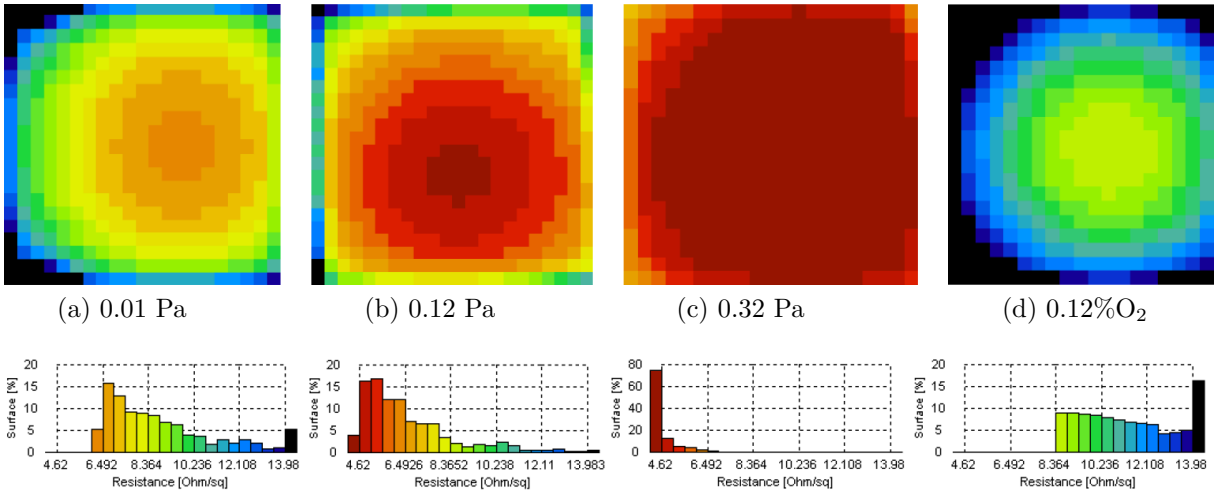

(a) 0.01 Pa (b) 0.12 Pa (c) 0.32 Pa (d) 0.12%O_2

(e) 0.01 Pa (f) 0.12 Pa (g) 0.32 Pa (h) 0.12%O_2

Figure 3.30: Mapping of the resistance and resulting statistics for ZnO:Al thin films deposited on 5 × 5 cm glass substrates at various sputtering conditions: 0.01 Pa (a,e), 0.12 Pa (b,f), 0.32 Pa (c,g) and 0.12 Pa with 0.12% of oxygen partial pressure ratio (d,h).

The whole samples have been deposited at 325 °C, for a total thickness of 1 μm, on 5 × 5 cm glass substrates. Three different working pressures are studied and are presented

in Figure 3.30, 0.01 Pa (a), 0.12 Pa (b) and 0.32 Pa (c). As predicted in the studies as functions of the working pressure and the substrate temperature (section 3.2 and section 3.3 respectively), the minimum resistance is obtained at 0.32 Pa, with 3.4 Ω/sq. Moreover, it corresponds to the more uniform ZnO:Al thin film, with a deviation of the resistance of 17%, compared to 30% for a deposition at 0.12 Pa, and 36% for a deposition at 0.01 Pa.

Another ZnO:Al thin film has been deposited, with 0.12% of oxygen partial pressure ratio, presented in Figure 3.30d. As expected, there is a strong degradation of the resistance with the addition of oxygen to the Ar gas mixture, from a minimum resistance of 4.5 Ω/sq without oxygen in the gas phase, to 8.4 Ω/sq with 0.12% of oxygen partial pressure ratio. The uniformity is better with oxygen in the gas mixture.

The non-uniformity of deposition is attributed to the magnetic confinement of the electrons in front of the target in a ring shape. This causes a race track on the target. The longer the target is used, the deeper and wider the erosion area gets. These four samples have been deposited at the same period, which enables to consider the same erosion of the target. The resistance of the material is dependent on the thickness, which means that the uniformity presented through these sheet resistance mappings can be due indistinctly from a non-uniform thickness or from a non-uniform material quality.

3.8 Fundamental studies

In order to better understand the electrical and optical behaviour of the free electrons in ZnO:Al thin films, a deeper investigation of the free-carrier absorption using the Drude model is realized, as well as an investigation of the temperature-dependent conductivity.

3.8.1 Optical modelling of free electrons

From the Drude free electron theory detailed in section 1.5.1, it is possible to link the electrical and optical properties of the ZnO:Al thin films. The electronic properties of the material are deduced from the plasma frequency ω_p, the damping term Γ_d and the high frequency dielectric constant ε_∞. The dielectric function in this region, described from the Drude model, is then written as:

$$\varepsilon(\omega) = \varepsilon_\infty - \frac{\omega_p^2}{\omega^2 + i\Gamma_d\omega} \tag{3.1}$$

Due to the free carrier absorption, the TCO film is transparent in the visible spectral range, and reflects light in the long wavelength region, with the plasma frequency roughly defining the border between the two regimes through Equation 3.2. The damping term defines the steepness of the transition with the relationship 3.3.

$$\omega_p^2 = \frac{e^2 N_e}{\varepsilon_\infty \varepsilon_0 m^*} \tag{3.2}$$

$$\Gamma_d = \frac{e}{\mu_{opt} m^*} \tag{3.3}$$

with m^* the effective mass of electrons at the bottom of the conduction band, e the elementary charge, and ε_0 the vacuum permittivity.

The region of interest of the Drude model is the IR region as shown in Figure 3.31. The plasma frequency is a function of the charge carrier concentration N_e. In this way, depending on the charge carrier concentration, the plasma frequency spreads from 1500 nm to 2500 nm or more, within the range for spectrophotometry and/or infrared polarimetry.

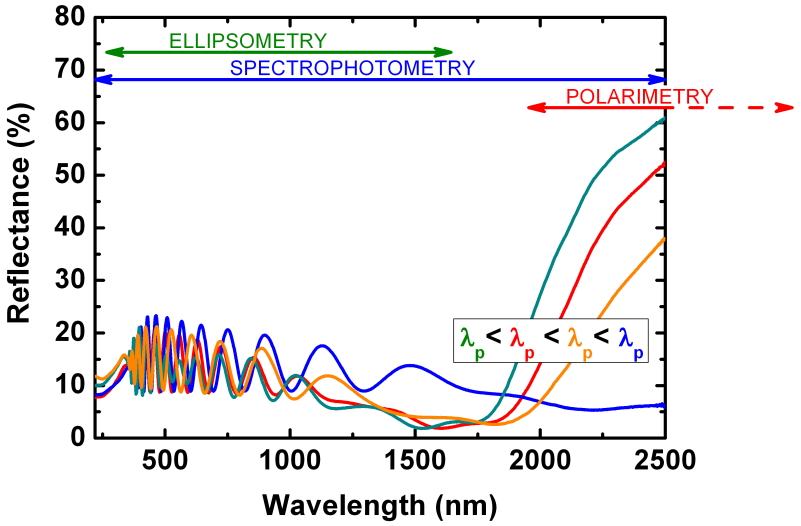

Figure 3.31: Reflectance spectra for various ZnO:Al films exhibiting different plasma wavelengths. The measurement range of the different optical techniques has been indicated.

From the spectrally resolved Mueller matrix obtained by infrared polarimetry and/or directly estimated from the reflectance spectra, the plasma frequency is obtained for a large number of samples. All samples also underwent investigation by Hall effect measurement at room temperature, from which N_e and μ_{Hall} were derived. The resulting plasma frequency is plotted as a function of the carrier concentration (Figure 3.32a). The values resulting from spectrophotometry and infrared polarimetry measurements exhibit the same tendency.

Equation 3.2 leads to the determination of effective mass as a function of carrier concentration obtained by Hall effect. An increase of $\varepsilon_\infty \omega_p^2$ versus N_e is expected. This dependency is verified in Figure 3.32b where the lines indicate the expected behaviour for different values of the effective electron mass m^* such as $m^* = m_{eff} \times m_0$ with m_0 the electron mass. The plotted $\varepsilon_\infty \omega_p^2$ values are calculated from the ε_∞ obtained with the modelling of the infrared polarimetry, or for a fixed value at 3.8 for the spectrophotometry technique. In the literature, different values of ε_∞ are used: 4 [8, 11, 49], 3.8 [23, 55]. Some works by the ellipsometry analyses using the Drude and Tauc-Lorentz models reveal reductions in ε_∞ as N_e in the films increases [16]. Other studies reported relatively large reductions from 4 to 3 [36, 37].

A linear behaviour, expected for a constant effective mass, is not observed. The effective mass increases from $0.2m_0$ for the lowest carrier concentration to $0.4m_0$ for the highest carrier concentration. These results reveal the non-parabolicity of the conduction band for high doping levels.

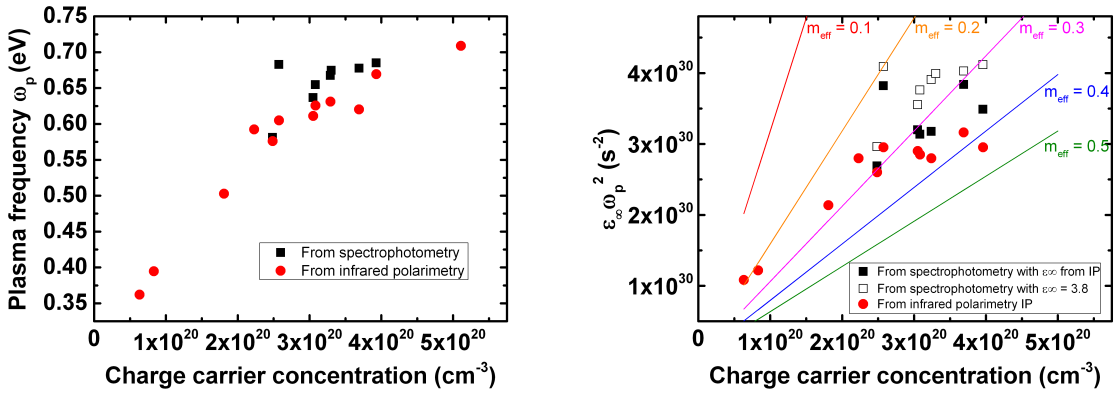

(a) (b)

Figure 3.32: Fitting values obtained by spectrophotometry and infrared polarimetry depending on the carrier concentration determined by Hall effect measurements: Plasma frequency ω_p(a) and $\varepsilon_\infty\omega_p^2$ (b). The lines correspond to effective mass values.

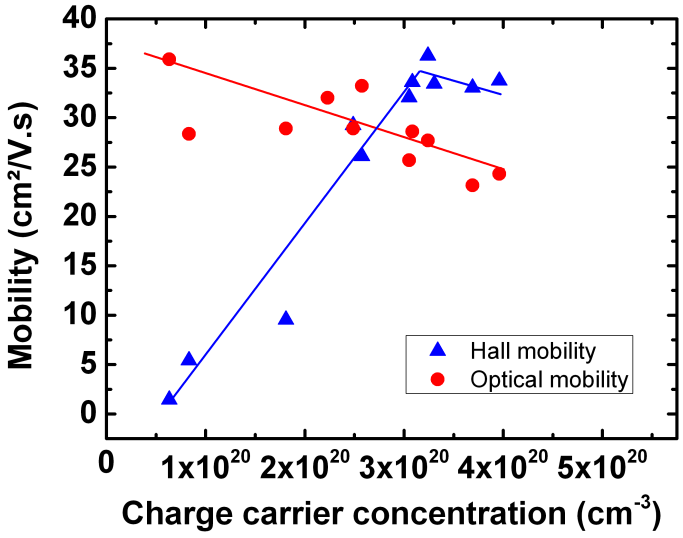

Figure 3.33: Optical mobility, determined from the infrared polarimetry, and Hall mobility as functions of the carrier concentration.

From Equation 3.3, the optical mobility is calculated and compared to the Hall mobility as presented in Figure 3.33. Two different behaviours are observed depending on the carrier concentration. For low carrier concentrations, below 2.5×10^{20} cm^{-3}, the optical mobility is clearly higher than the Hall mobility. Electrons excited by light are not affected by grain boundaries, contrary to the case of Hall effect measurements where the mobility is limited by the grain barriers. This is explained by the short path length of free electrons while moving in the high frequency electric field of the light, smaller than the typical grain size [42, 49]. The transport is limited by scattering at the grain boundaries which affects only Hall mobility.

For higher carrier concentration, the optical and Hall mobility values become similar. The free carriers which have to travel over a macroscopic length in the case of Hall excitation or at nanoscale in the case of light excitation seem to experience the same scattering mechanisms. The transport is limited by the ionized impurities scattering which affects both optical and Hall mobilities.

3.8.2 Temperature-dependent conductivities

It is possible to correlate optical modelling of free electrons with the temperature-dependent conductivities. In order to further analyse the transport processes in ZnO:Al thin films, temperature-dependent mobility and charge carrier concentration values have been measured by Hall effect. The charge carrier concentration does not show any variation versus temperature as reported in Figure 3.34a. The fact that none of the samples shows energy activation of the carrier concentration indicates these thin films are degenerated semiconductors.

The temperature-dependent mobility values, seen in Figure 3.34b, exhibit different behaviours depending on the charge carrier concentration in the films. Films with the lowest mobilities, corresponding to whose with the lowest carrier concentration, show a slight increase of mobility with increasing temperature while ZnO:Al films with the higher mobility values, also displaying higher carrier concentrations, show a decrease of their mobility when increasing temperature. The opposite behaviours for high and low charge carrier concentrations are caused by multiple contributions of scattering processes to the conduction mechanism of polycrystalline films.

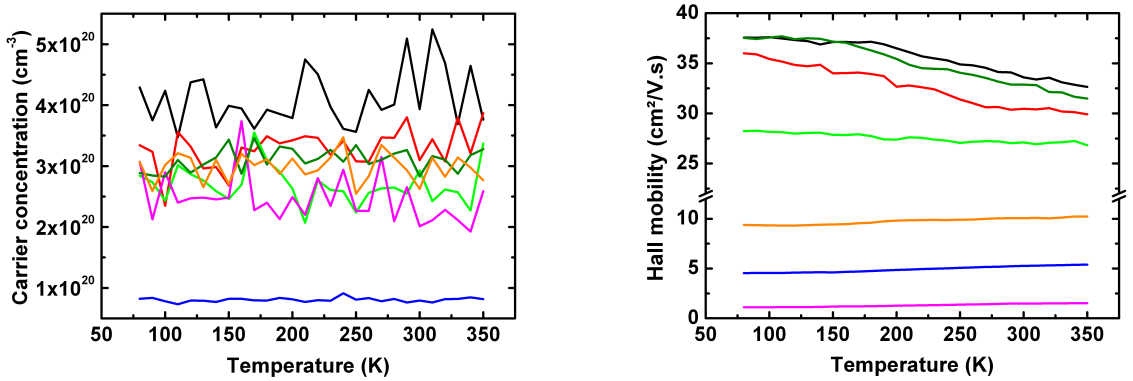

(a) (b)

Figure 3.34: Evolution of carrier concentration (a) and Hall mobility (b) versus temperature. The carrier concentration for each sample is quite constant while different behaviours on the Hall mobility are visible depending on carrier concentration.

For polycrystalline TCO thin films, the conduction mechanism is restricted by two scattering processes from the bulk: i) the phonon scattering caused by the scattering of the charge carriers by vibrations in the crystal lattice ; ii) the scattering by ionized impurities due to deflection of free carriers by the potential of a charge center originating

from doping impurities. An additional scattering event appears at the grain-barriers due to the polycrystalline nature of the ZnO:Al thin film, as presented in section 1.4.2. These scattering processes present different temperature-dependences: a dependence in exp(-1/T) for the grain barrier scattering *gb*, plus a dependence from the bulk which consists of two components: one due to ionized impurities *ii* which is independent of T, and a second one presenting a dependence in $T^{-3/2}$ for phonon scattering *ph* as presented in the following equation for the conductivity:

$$\frac{1}{\sigma} = \frac{1}{\sigma_0 exp(-\Phi_b/kT)} + \frac{1}{\sigma_{ii}} + \frac{1}{\sigma_{ph}T^{-3/2}} \tag{3.4}$$

with

$$\sigma_0 = e^2 LN/\sqrt{2\pi m^* kT} \tag{3.5}$$

and

$$\Phi_b = \begin{cases} \dfrac{e^2 L^2 N}{8\varepsilon\varepsilon_0} & \text{for LN} < \text{N}_t \\ \dfrac{e^2 N_t^2}{8\varepsilon\varepsilon_0 N} & \text{for LN} > \text{N}_t \end{cases} \tag{3.6}$$

with σ_0 the conductivity inside the grain, Φ_b the energy barrier height at the grain boundaries, L the grain size, N the carrier density in the bulk, and N_t the charge carrier trap density at the grain boundaries. From these dependences, it is possible to determine the dominant scattering process for each sample by measuring the evolution of the conductivity as a function of the temperature by the Hall effect measurements.

For the samples exhibiting an increase of the mobility/conductivity with increasing temperature, the extended Seto model for grain barrier-limited transport is applied [13,14]. The temperature-independent term corresponding to ionized impurities contribution is added such as:

$$\frac{1}{\sigma} = \frac{1}{\sigma_0 exp(-\Phi_b/kT)} + \frac{1}{\sigma_{ii}} \tag{3.7}$$

For the samples presenting a decrease of mobility/conductivity with increasing temperature, the model corresponding to metal-like behaviour is applied such as [2]:

$$\frac{1}{\sigma} = \frac{1}{\sigma_{ii}} + \frac{1}{\sigma_{ph}T^{-3/2}} \tag{3.8}$$

These two different behaviours depend on the carrier concentration. The grain barrier scattering is the limiting process below 2.5×10^{20} cm^{-3}, while above 2.5×10^{20} cm^{-3}, the conduction exhibits metal-like conductivity curves.

3.8.3 Conclusion: comparison of the deposition parameters

We have studied the effect of the deposition parameters on the electrical and optical properties of ZnO:Al thin films. Different substrate temperatures, total pressures and oxygen partial pressures are explored. It is found that the electrical transport is limited by grain barriers for ZnO:Al thin films deposited at high oxygen concentration. For these samples, the Hall mobility and optical mobility differ. The properties of the films are presented in Table 3.3.

Table 3.3: Results of the fits on the curves of the conductivity as a function of the temperature for a conduction model of grain barrier limited transport.

Deposition			GRAIN BARRIER LIMITED TRANSPORT					
T_{sub} (°C)	p (Pa)	O_2 (%)	N_e (10^{20} cm^{-3})	μ_{Hall} (cm^2/V.s)	$\mu_{optical}$ (cm^2/V.s)	Φ_b (meV)	L (nm)	N_t (10^{13} cm^{-2})
RT	0.32	0.16	0.8	5.4	28.4	5	2.7	-
325	0.32	0.16	1.8	9.6	28.9	5	7.3	3.8
200	0.32	0.32	0.6	1.5	35.9	6	0.9	-

The samples fitted with a grain barrier-limited transport show a temperature dependence of the conductivity that corresponds to a barrier height of 5 or 6 meV. The interior of the grains is degenerately doped, as is evidenced by the temperature-independence of the carrier density. The energy barrier height Φ_b at the grain boundaries corresponds to the energy between the top of the barrier and the Fermi level. The measured temperature-independence of the carrier density leads us to think that the energy difference between the Fermi level and the conduction band minimum inside the grains is larger than k_BT. These values are consistent with previous works [13, 40].

The ZnO:Al thin films deposited at the highest oxygen partial pressure and lowest substrate temperature exhibit the lowest charge carrier concentration and Hall mobility and on the other hand, the highest optical mobility as predicted in the section 3.6. An increase of the substrate temperature improves the electrical properties but does not compensate an increase of the oxygen partial pressure. The estimation of the grain size gives very low values, from 7.3 nm for a deposition realized at 325 °C, for 0.16% of oxygen partial pressure, to 0.9 nm for a deposition realized at 200 °C, for 0.32% of oxygen partial pressure. In the same way, the films deposited at the highest oxygen partial pressure and lowest substrate temperature present the highest energy barrier height at the grain boundary Φ_b. The ZnO:Al film deposited at 325 °C, for 0.16% of oxygen partial pressure, is in the case $LN>N_t$ (Equation 3.6), the carrier trap density can be estimated, and grain boundaries are isolated to make the grains partially depleted. The two other ZnO:Al films are in the case $LN<N_t$, the carrier trap density cannot be estimated, and the depletion regions for each grain boundary are overlapped, with a higher activation energy [19]. This behaviour can be discussed by comparing average grain size L with the Debye screening length expressed as $L_d = ((\varepsilon\varepsilon_0 kT)/(e^2N))^{1/2}$. For the sample deposited at 325 °C, for 0.16% of oxygen partial pressure, the average grain size is larger than $2L_d$, a potential barrier is created because of band bending, and the mobility is thermally activated. For the two other samples, L is in the range (or lower) than the Debye screening length, the conduction band becomes flat [6, 38].

The highly doped ZnO:Al films, above 2.5×10^{20} cm^{-3}, deposited at high temperature and/or without additional oxygen in the gas phase, are modelled by a bulk limited transport. Due to the considerable degeneration for these films, grain boundary scattering can be neglected, as the barriers become narrow. The Hall mobility and optical mobility are quite similar. For these samples, at low temperature, the conductivity is constant, the transport is limited by ionized impurities scattering. Above a threshold temperature value, the conductivity decreases with the increase of the temperature. Accordingly, the phonon scattering is dominant. These results indicate a transition from semiconductor

Table 3.4: Results of the fits on the curves of the conductivity as a function of the temperature for a conduction model of bulk limited transport.

Deposition			BULK LIMITED TRANSPORT			
T_{sub} (°C)	p (Pa)	O_2 (%)	N_e (10^{20} cm^{-3})	μ_{Hall} (cm^2/V.s)	$\mu_{optical}$ (cm^2/V.s)	Transition temperature (K)
RT	0.01	0	2.5	29.2	28.9	324 ± 5
325	0.01	0	2.6	26.1	33.2	315 ± 5
RT	0.32	0	3.1	32.0	25.7	300 ± 5
325	0.32	0	3.7	33.0	23.2	249 ± 5
200	0.32	0.06	3.1	33.6	28.6	257 ± 5
325	0.32	0.06	3.2	36.3	27.7	250 ± 5

to metal, occurring at a certain transition temperature depending on the ZnO:Al thin film as presented in Table 3.4. A decrease of the transition temperature is observed for dominating metallic conduction over the semiconductor conduction as it is the case for ZnO:Al thin films deposited at the highest temperature.

3.9 Conclusion

In order to optimize the opto-electronic properties of the ZnO:Al thin films, it is necessary to find an optimum of the deposition parameters such as argon pressure, substrate temperature, RF sputtering power, oxygen partial pressure and time of deposition.

An optimal pressure to obtain the highest transmittance in the visible and the lowest resistivity is found in the range between 0.12 Pa and 0.32 Pa. Two opposite behaviours explain the difference in growth: at low pressure, the ZnO:Al growing films are damaged by bombardment of negative ions and high energy neutral atoms, effect known as the atomic peening effect, while at high pressures, the films become highly defective due to the thermalization of sputtered particles, and their resulting lower surface mobility. In the case of the substrate temperature, the highest temperature (325 °C attainable in the Alliance concept reactor) leads to the best opto-electronic properties. The evolutions of these two parameters have been discussed within the Thornton's structure zone model. Concerning the RF sputtering power, the lowest resistivity is reached at 100 W, thanks to a higher cristallinity and a higher crystallite size. The transmittance is the highest in the visible at lower RF sputtering power. The addition of oxygen to argon during the sputtering results in a slight increase of the optical properties, which does not compensate the dramatic degradation of the electrical properties. Finally the influence of the deposition time is studied. The evolution of the electrical properties is related to the deposition mechanisms: nucleation or bulk growth.

The optical modelling of free electrons and the modelling of temperature-dependent conductivities enable the understanding of the conduction mechanisms. For ZnO:Al thin films of low carrier concentrations, the conduction mechanism is limited by grain boundaries, such as for ZnO:Al thin films deposited at high oxygen partial pressure. For highly doped ZnO:Al thin films, the transport is limited by the bulk. The grain barriers scattering becomes negligible. The Hall mobility and optical mobility are comparable.

Bibliography

[1] M. Adamik, P. Barna, and I. Tomov. Columnar structures in polycrystalline thin films developed by competitive growth. *Thin Solid Films*, 317(1-2):64–68, Apr. 1998. (cited page 82)

[2] M. Addonizio, A. Antonaia, and G. Cantele. Transport mechanisms of RF sputtered Al-doped ZnO films by H2 process gas dilution. *Thin Solid Films*, 349:93–99, 1999. (cited pages 19, 20, 100 et 112)

[3] C. Agashe. Efforts to improve carrier mobility in radio frequency sputtered aluminum doped zinc oxide films. *Journal of Applied Physics*, 95(4):1911, 2004. (cited page 69)

[4] C. Agashe, O. Kluth, G. Schöpe, H. Siekmann, J. Hüpkes, and B. Rech. Optimization of the electrical properties of magnetron sputtered aluminum-doped zinc oxide films for opto-electronic applications. *Thin Solid Films*, 442(1-2):167–172, Oct. 2003. (cited pages 69, 70 et 84)

[5] V. Assunção, E. Fortunato, A. Marques, H. Águas, I. Ferreira, M. Costa, and R. Martins. Influence of the deposition pressure on the properties of transparent and conductive ZnO:Ga thin-film produced by r.f. sputtering at room temperature. *Thin Solid Films*, 427(1-2):401–405, Mar. 2003. (cited pages 14, 70, 82 et 83)

[6] R. Ayouchi, D. Leinena, F. Martin, M. Gabasa, E. Dalchieleb, and J. R. Ramos-Barradoa. Preparation and characterization of transparent ZnO thin films obtained by spray pyrolysis. *Thin Solid Films*, 426(1-2):68–77, Feb. 2003. (cited page 101)

[7] P. Barna and M. Adamik. Fundamental structure forming phenomena of polycrystalline films and the structure zone models. *Thin Solid Films*, 317(1-2):27–33, Apr. 1998. (cited pages 82 et 87)

[8] S. Brehme, F. Fenske, W. Fuhs, and E. Nebauer. Free-carrier plasma resonance effects and electron transport in reactively sputtered degenerate ZnO: Al films. *Thin Solid Films*, 342:167–173, 1999. (cited pages 23 et 97)

[9] M. J. Brett, R. W. Mc Mahon, J. D. Affiniato, and R. Parsons. High rate planar magnetron deposition of transparent, conducting, and heat reflecting films on glass and plastic. *Journal of Vacuum Science & Technology A: Vacuum, Surfaces, and Films*, 1(2):352, Apr. 1983. (cited page 69)

[10] B. S. Chun, H. C. Wu, M. Abid, I. C. Chu, S. Serrano-Guisan, I. V. Shvets, and D. S. Choi. The effect of deposition power on the electrical properties of Al-doped zinc oxide thin films. *Applied Physics Letters*, 97(8):082109, 2010. (cited page 90)

[11] R. Clanget. Ionized impurity scattering in degenerate In2O3. *Applied Physics*, 2(5):247–256, Nov. 1973. (cited page 97)

[12] K. Ellmer. Magnetron sputtering of transparent conductive zinc oxide: relation between the sputtering parameters and the electronic properties. *Journal of Physics D: Applied Physics*, 33(4):R17–R32, Feb. 2000. (cited pages 69, 77, 82 et 93)

[13] K. Ellmer and R. Mientus. Carrier transport in polycrystalline ITO and ZnO:Al II: The influence of grain barriers and boundaries. *Thin Solid Films*, 516(17):5829–5835, July 2008. (cited pages 100, 101 et 161)

[14] K. Ellmer and R. Mientus. Carrier transport in polycrystalline transparent conductive oxides: A comparative study of zinc oxide and indium oxide. *Thin Solid Films*, 516(14):4620–4627, May 2008. (cited page 100)

[15] E. Fortunato, A. Goncalves, V. Assuncao, A. Marques, H. Aguas, L. Pereira, I. Ferreira, and R. Martin. Growth of ZnO: Ga thin films at room temperature on polymeric substrates: thickness dependence. *Thin Solid Films*, 442:121 – 126, 2003. (cited page 84)

[16] H. Fujiwara and M. Kondo. Effects of carrier concentration on the dielectric function of ZnO:Ga and In2O3:Sn studied by spectroscopic ellipsometry: Analysis of free-carrier and band-edge absorption. *Physical Review B*, 71(7):1–10, Feb. 2005. (cited pages 24 et 97)

[17] C. Guillén and J. Herrero. Optical, electrical and structural characteristics of Al:ZnO thin films with various thicknesses deposited by DC sputtering at room temperature and annealed in air or vacuum. *Vacuum*, 84(7):924–929, Mar. 2010. (cited pages 24, 92, 111 et 114)

[18] D. Han, Y. Wang, S. Zhang, L. Sun, R. Han, S. Matsumoto, and Y. Ino. Influence of sputtering power on properties of ZnO thin films fabricated by RF sputtering in room temperature. *Science China Information Sciences*, 55(4):951–955, July 2011. (cited page 90)

[19] F. M. Hossain, J. Nishii, S. Takagi, A. Ohtomo, T. Fukumura, H. Fujioka, H. Ohno, H. Koinuma, and M. Kawasaki. Modeling and simulation of polycrystalline ZnO thin-film transistors. *Journal of Applied Physics*, 94(12):7768, Dec. 2003. (cited page 101)

[20] Y. Igasaki and H. Kanma. Argon gas pressure dependence of the properties of transparent conducting ZnO:Al films deposited on glass substrates. *Applied Surface Science*, 170:508–511, 2001. (cited page 69)

[21] Y. Igasaki and H. Saito. The effects of deposition rate on the structural and electrical properties of ZnO:Al films deposited on (1120) oriented sapphire substrates. *Journal of applied physics*, 70(7):3613–3619, 1991. (cited page 69)

[22] S. Jeong and J. Boo. Influence of target-to-substrate distance on the properties of AZO films grown by RF magnetron sputtering. *Thin Solid Films*, 447-448:105–110, Jan. 2004. (cited page 95)

[23] Z.-C. Jin, I. Hamberg, and C. G. Granqvist. Optical properties of sputter-deposited ZnO:Al thin films. *Journal of Applied Physics*, 64(10):5117, Nov. 1988. (cited page 97)

[24] Y. Kajikawa. Texture development of non-epitaxial polycrystalline ZnO films. *Journal of Crystal Growth*, 289(1):387–394, Mar. 2006. (cited page 82)

[25] J. Kar, S. Kim, B. Shin, K. Park, K. Ahn, W. Lee, J. Cho, and J. Myoung. Influence of sputtering pressure on morphological, mechanical and electrical properties of Al-doped ZnO films. *Solid-State Electronics*, 54(11):1447–1450, Nov. 2010. (cited page 70)

[26] D.-K. Kim and H.-B. Kim. Dependence of the properties of sputter deposited Al-doped ZnO thin films on base pressure. *Journal of alloys and compounds*, 522:69–73, 2012. (cited page 70)

[27] P. Kuppusami, G. Vollweiler, D. Rafaja, and K. Ellmer. Epitaxial growth of aluminium-doped zinc oxide films by magnetron sputtering on (001), (110), and (012) oriented sapphire substrates. *Applied Physics A*, 80(1):183–186, Feb. 2004. (cited page 69)

[28] Y.-P. Liao, J.-H. Zhang, S.-X. Li, Z.-S. Guo, J. Cao, W.-Q. Zhu, and X. Li. Structural evolution of ZnO films deposited by rf magnetron sputtering on glass substrate. *Physica Status Solidi (a)*, 207(8):1850–1853, Aug. 2010. (cited page 93)

[29] S.-S. Lin and J.-L. Huang. Effect of thickness on the structural and optical properties of ZnO films by r.f. magnetron sputtering. *Surface and Coatings Technology*, 185(2-3):222–227, July 2004. (cited page 84)

[30] Y. Lin, M. Chen, C. Kuo, and W. Yen. Electrical and optical properties of ZnO:Al film prepared on polyethersulfone substrate by RF magnetron sputtering. *Colloids and Surfaces A: Physicochemical and Engineering Aspects*, 337(1-3):52–56, Apr. 2009. (cited page 69)

[31] A. Löffl, S. Wieder, B. Rech, O. Kluth, C. Beneking, and H. Wagner. Al-doped ZnO films for thin-film solar cells with very low sheet resistance and controlled texture. In *Proc. 14th Europ. PV Sol. En. Conf.*, page 2089, Barcelona, 1997. (cited page 69)

[32] T. Minami, H. Sato, H. Nanto, and S. Takata. Group III Impurity Doped Zinc Oxide Thin Films Prepared by RF Magnetron Sputtering. *Japanese Journal of Applied Physics*, 24(10):L781–L784, Oct. 1985. (cited pages 18 et 69)

[33] E. Mirica, G. Kowach, and H. Du. Modified Structure Zone Model to Describe the Morphological Evolution of ZnO Thin Films Deposited by Reactive Sputtering. *Crystal Growth & Design*, 4(1):157–159, Jan. 2004. (cited page 82)

[34] E. Mirica, G. Kowach, and P. Evans. Morphological evolution of ZnO thin films deposited by reactive sputtering. *Crystal growth & Design*, 2004. (cited page 82)

[35] A. Morita, I. Watanabe, and H. Shirai. Chemical activity of oxygen atoms in the magnetron sputter-deposited ZnO films. *Thin Solid Films*, 519(20):6903–6909, Aug. 2011. (cited page 93)

[36] T. Nagatomo, Y. Maruta, and O. Omoto. Electrical and optical properties of vacuum-evaporated indium-tin oxide films with high electron mobility. *Thin Solid Films*, 192(1):17–25, Nov. 1990. (cited page 97)

[37] Y. Ohhata, F. Shinoki, and S. Yoshida. Optical properties of r.f. reactive sputtered tin-doped In2O3 films. *Thin Solid Films*, 59(2):255–261, May 1979. (cited page 97)

[38] J. W. Orton and M. J. Powell. The Hall effect in polycrystalline and powdered semiconductors. *Reports on Progress in Physics*, 43(11):1263–1307, Nov. 1980. (cited page 101)

[39] J. Pannetier. *Techniques d'analyse des diagrammes de diffraction des rayons X et des neutrons par les poudres*. Formation permanente du CNRS, Nantes, 1995. (cited pages 40 et 72)

[40] M. W. J. Prins, K.-O. Grosse-Holz, J. F. M. Cillessen, and L. F. Feiner. Grain-boundary-limited transport in semiconducting SnO2 thin films: Model and experiments. *Journal of Applied Physics*, 83(2):888, Jan. 1998. (cited pages 21 et 101)

[41] S. Rahmane, M. Djouadi, M. Aida, N. Barreau, B. Abdallah, and N. Hadj Zoubir. Power and pressure effects upon magnetron sputtered aluminum doped ZnO films properties. *Thin Solid Films*, 519(1):5–10, Oct. 2010. (cited pages 70 et 90)

[42] F. Ruske, a. Pflug, V. Sittinger, B. Szyszka, D. Greiner, and B. Rech. Optical modeling of free electron behavior in highly doped ZnO films. *Thin Solid Films*, 518(4):1289–1293, Dec. 2009. (cited page 98)

[43] M. Selmi, F. Chaabouni, M. Abaab, and B. Rezig. Studies on the properties of sputter-deposited Al-doped ZnO films. *Superlattices and Microstructures*, 44(3):268–275, Sept. 2008. (cited page 84)

[44] a. V. Singh. Doping mechanism in aluminum doped zinc oxide films. *Journal of Applied Physics*, 95(7):3640, 2004. (cited page 69)

[45] S. Singh, T. Ganguli, R. Kumar, R. Srinivasa, and S. Major. Substrate temperature dependence of growth mode, microstructure and optical properties of highly oriented zinc oxide films deposited by reactive sputtering. *Thin Solid Films*, 517(2):661–669, Nov. 2008. (cited pages 41 et 77)

[46] D. Song. Effects of rf power on surface-morphological, structural and electrical properties of aluminium-doped zinc oxide films by magnetron sputtering. *Applied Surface Science*, 254(13):4171–4178, Apr. 2008. (cited page 90)

[47] D. Song, A. G. Aberle, and J. Xia. Optimisation of ZnO:Al films by change of sputter gas pressure for solar cell application. *Applied Surface Science*, 195(1-4):291–296, July 2002. (cited page 69)

[48] D. Song, P. Widenborg, and W. Chin. Investigation of lateral parameter variations of Al-doped zinc oxide films prepared on glass substrates by rf magnetron sputtering. *Solar energy materials and*, 73:1–20, 2002. (cited pages 90 et 95)

[49] J. Steinhauser, F. S., N. Oliveira, E. Vallat-Sauvain, and C. Ballif. Transition between grain boundary and intragrain scattering transport mechanisms in boron-doped zinc oxide thin films. *Applied Physics Letters*, 90(14):142107, 2007. (cited pages 97 et 98)

[50] C. Thompson. Structure evolution during processing of polycrystalline films. *Annual review of materials science*, 30(12):159–190, 2000. (cited pages 82 et 87)

[51] J. A. Thornton. Influence of apparatus geometry and deposition conditions on the structure and topography of thick sputtered coatings. *Journal of Vacuum Science and Technology*, 11(4):666, July 1974. (cited pages vii, 69, 82 et 83)

[52] J. A. Thornton. Influence of substrate temperature and deposition rate on structure of thick sputtered Cu coatings. *Journal of Vacuum Science and Technology*, 12(4):830, July 1975. (cited pages vii, 69, 82 et 83)

[53] T. Tsuji and M. Hirohashi. Influence of oxygen partial pressure on transparency and conductivity of RF sputtered Al-doped ZnO thin films. *Applied Surface Science*, 157(1-2):47–51, Mar. 2000. (cited page 93)

[54] F. C. M. van de Pol, F. R. Blom, and T. J. A. Popma. R.F. planar magnetron Sputtered thin film ZnO films. *Thin Solid Films*, 204:349–364, 1991. (cited page 82)

[55] I. Volintiru, M. Creatore, and M. C. M. van de Sanden. In situ spectroscopic ellipsometry growth studies on the Al-doped ZnO films deposited by remote plasma-enhanced metalorganic chemical vapor deposition. *Journal of Applied Physics*, 103(3):033704, 2008. (cited page 97)

[56] R. Wen, L. Wang, X. Wang, G.-H. Yue, Y. Chen, and D.-L. Peng. Influence of substrate temperature on mechanical, optical and electrical properties of ZnO:Al films. *Journal of Alloys and Compounds*, 508(2):370–374, Oct. 2010. (cited page 77)

[57] L. Yang, S. Jie, and D. Fan. Effects of Sputtering Gas Pressure and Substrate Temperature on Optical Properties of ZnO : Al Thin Films fabricated by RF Magnetron Sputtering. *Advances in Optoelectronics and Micro/Nano-Optics (AOM), 2010 OSA-IEEE-COS*, pages 1–4, 2010. (cited pages 70 et 77)

[58] Y. Yang, X. Zeng, Y. Zeng, L. Liu, and Q. Chen. Deposition of quasi-crystal Al-doped ZnO thin films for photovoltaic device applications. *Applied Surface Science*, 257(1):232–238, Oct. 2010. (cited page 69)

[59] J. Yoo, J. Lee, S. Kim, K. Yoon, I. J. Park, S. Dhungel, B. Karunagaran, D. Mangalaraj, and J. Yi. High transmittance and low resistive ZnO:Al films for thin film solar cells. *Thin Solid Films*, 480-481:213–217, June 2005. (cited page 69)

[60] Z. Zhan, J. Zhang, Q. Zheng, D. Pan, J. Huang, F. Huang, and Z. Lin. Strategy for Preparing Al-Doped ZnO Thin Film with High Mobility and High Stability. *Crystal Growth & Design*, 11(1):21–25, Jan. 2011. (cited page 93)

[61] D. Zhang, T. Yang, Q. Wang, and D. Zhang. Electrical and optical properties of Al-doped transparent conducting ZnO films deposited on organic substrate by RF sputtering. *Materials Chemistry and Physics*, 68(1-3):233–238, Feb. 2001. (cited page 69)

Chapter 4

Post-deposition treatments

Contents

In this chapter, post-deposition treatments are investigated. The influence of thermal annealing and excimer (XeCl = 308 nm) laser annealing (ELA) on the microstructural, electrical and optical properties are studied.

4.1 Thermal annealing treatments

The effects of post-deposition annealing atmosphere (under vacuum, in 5% H_2 in N_2 atmosphere, or in pure N_2 atmosphere) and temperature (400, 450, or 500 °C) on the microstructural, optical and electrical properties of ZnO:Al thin films have been investigated.

4.1.1 Introduction

The annealing treatments on undoped and doped ZnO have been studied over the past thirty years. Minami *et al.* have observed an increase of the resistivity of the ZnO films with temperature up to 400 °C by one to ten orders of magnitude in various ambients such as vacuum, inert gases and air. This degradation of the electrical properties has been explained by the chemisorption of oxygen at the grain boundaries which can act as an scattering centre for the charge transport [29]. The increased resistivity can be returned to the resistivity of its virgin state by heat treatment in a hydrogen ambient at temperatures near 400 °C [18].

Chang *et al.* have investigated the effect of the post-deposition thermal treatments on RF sputtered ZnO:Al thin films. A significant grain agglomeration into clusters was observed after hydrogen annealing at 500 °C. The resistivity of the annealed films increased in air due to the chemisorption of oxygen at the grain boundaries and surface measured by XPS but decreased in hydrogen atmosphere down to 8.76 $\times 10^{-4}\Omega$.cm at 500 °C for 1 h [5].

An optical study has been realized by Mehan *et al.*, who have seen an initial decrease and subsequent increase in the refractive indices of RF magnetron-sputtered ZnO films with the annealing time at a fixed-annealing temperature of 380 °C in air. The initial decrease was attributed to a lattice contraction, and the latter increase was explained in terms of the increase in packing density of the films upon annealing [17].

Oh *et al.* prepared ZnO:Al films by RF magnetron co-sputtering at room temperature and thermally treated them in hydrogen ambient at 300 °C. The weakly absorbed oxygen species on films were removed by the hydrogen-annealing treatment which increased the electrical conductivity and it was concluded that hydrogen effectively passivates the surface and grain boundaries [23, 24].

A Raman study has been realized by Windisch *et al.* on ZnO powders and thin films exposed to hydrogen at different concentrations and temperatures [33]. Two different behaviours are observed depending on the conditions. At low concentrations of hydrogen in a gaseous environment at approximately 400 °C, the hydrogen diffuses into the ZnO and occupied oxygen vacancies contributing to a reduction in intensity of Raman bands associated with the defect. At higher concentrations of hydrogen generated during electrochemical polarization in aqueous solution at 25 °C, the hydrogen diffuses into the ZnO,

both filling oxygen vacancies and populating interstitial sites. In this role, hydrogen imparts sufficient electron density to the Zn and/or structural disorder to enhance vibration modes that are forbidden or typically weak in native ZnO.

Guillén *et al.* have grown ZnO:Al films with various thicknesses by magnetron sputtering at room temperature. The samples have been subsequently annealed at temperatures ranging from 150 to 450 °C in air or vacuum. Heating in air or vacuum increases the crystalline lattice together with some increase of the visible transmittance and a decrease of the electrical resistance. It has been found that grain barrier scattering is dominant for these samples although it becomes lower for thicker and vacuum-heated layers, which achieve larger crystallite sizes and higher carrier concentrations together with higher mobilities. Besides, the increment in the carrier concentration is related to some increase in the lattice distortion or elongation in the hexagonal c-axis that can be due to the creation of donor metal interstitial defects [32]. Gap energy widening is also related to carrier concentration increase, but additional electron-electron and electron-impurity scatterings have the opposite effect that is found more important for the thickest films [10]. The same study had been previously realized on ITO thin films [9].

The influence of thermal annealing on electrical properties of ZnO:Ga films has been studied by Makino *et al.* by means of Hall effect measurements and optical characterization based on Drude model analysis for transmission and reflection spectra in air and N_2 gas atmosphere. Annealing at high temperature caused a decrease in the Hall mobility and an increase in optical mobility, difference attributed to carrier scattering at grain boundaries [16].

Lennon *et al.* have annealed ZnO:Al thin films in a N_2 flow and have shown an improvement in the electrical and optical properties. An increase in the estimated crystallite size was observed after annealing. The surfaces of all layers investigated were oxygen deficient, and the density of oxygen vacancies was found to increase following the anneal. The incorporation of metallic Al interstitials into the ZnO matrix was believed to be partially responsible for improved optical transmittance [14].

Yang *et al.* have studied the effects of thermal annealing in pure N_2 and N_2 with 4% H_2 atmosphere on AZO films grown on quartz substrates at RT by RF magnetron sputtering [35]. It was found that the crystallinity of the AZO films was improved with the annealing and that the resistivity continuously increased with increasing annealing temperature. The resistivity of the AZO thin film annealed in N_2 was higher than for that annealed in N_2 + 4% H_2. This is attributed to the desorption of adsorbed oxygen from the grain boundaries and production of additional oxygen vacancies that act as donor centres by removal of oxygen from ZnO matrix. Annealing in N_2 + 4% H_2 slightly narrows the optical band gap, and annealing in a N_2 makes the band gap narrower, which can be interpreted as a blue shift phenomenon due to the Burstein Moss shift.

Recently, Zhu *et al.* have shown that adding H_2 in the deposition atmosphere improved the crystallinity of the films, decreased lattice constant, increased band gap, decreased the resistivity, but exhibited poor conductive stability with aging [38]. They suggest that the formed main defect is oxygen vacancy V_O and hydrogen interstitial H_i when H_2 is introduced during deposition, which decreases the resistivity. During an additional

Ar + H_2 annealing, hydrogen would remove negatively charged oxygen species near grain boundaries to decrease the resistivity, and grain boundaries are passivated by formation of a number of V_O-H complex. They propose the following equation to explain the increase of the carrier concentration with the incorporation of hydrogen:

$$\begin{aligned} &ZnO + H_2 \rightarrow Zn + H_2O + V_O \text{ and then } V_O \rightarrow V_O^{\cdot\cdot} + 2e^- \\ &2O^{2-} + H_2 \rightarrow 2OH^- + 2e^- \\ &2V_O + H_2 \rightarrow 2H_O \text{ and then } 2H_O \rightarrow 2H_O^{\cdot} + 2e^- \end{aligned} \tag{4.1}$$

Some authors have studied the influence of the incorporation of hydrogen during the deposition. Addonizio *et al.* have sputtered ZnO:Al with pure Ar and Ar/H_2 gas mixtures. They have shown that a low hydrogen dilution is able to produce a noticeable improvement of the conductivity by the activation of the Al dopants. The columnar structure is maintained at low hydrogen dilution but is degraded to spherical shaped domain at higher dilution. Carrier mobility is limited by bulk mechanisms at low dilution, particularly by acoustical phonon and ionized impurity scattering. At high dilution, the grain boundaries limit the charge transport [1]. Other groups have investigated the improvement of the electrical and optical properties through the incorporation of hydrogen during the sputtering [8, 13, 27, 30] or by current-drive incorporation [25].

More recently, Berginski *et al.* have shown that the electrical properties can be enhanced upon vacuum annealing. They have also tried to anneal ZnO:Al after the wet chemical etching step, which improved the optical properties [2].

Finally, one interesting work has been realized by Ruske *et al.* who have strongly decreased the resistivity of annealed ZnO:Al films by using silicon capping layers to prevent the decrease of the carrier concentration during the process [28]. The mobility increases up to 67 cm^2/V.s at 650 °C, resulting in a resistivity of 1.4×10^{-4} Ω.cm. The mobility increase is most likely obtained by reduced grain boundary scattering.

The effects of a post-deposition thermal annealing have been widely studied these last years but the investigations do not lead to the same results and same interpretations. In order to further improve the electrical and optical properties of ZnO:Al thin films, we have studied the effects of different annealing atmospheres (under vacuum, in 5% H_2 in N_2 atmosphere, or in pure N_2 atmosphere) and temperatures (400, 450, or 500 °C) on the microstructural, optical and electrical properties of the films.

4.1.2 Experimental procedure

ZnO:Al thin films were deposited in the Alliance concept reactor at room temperature by RF magnetron sputtering using a ZnO/Al_2O_3 (1 wt %) ceramic target and a RF power of 250 W. Depositions were carried out in pure argon atmosphere for the first set of samples and in an Ar/O_2 gas mixture for the second set of samples in order to have 0.06% of O_2 in the reactive mixture. The study was realized at a working pressure of 0.12 Pa.

The as-deposited ZnO:Al thin films were subsequently heat-treated under vacuum, in N_2/H_2 atmosphere or in pure N_2, at an annealing temperatures of 400 °C, 450 °C or 500 °C. The annealing procedures are detailed in Figure 4.1.

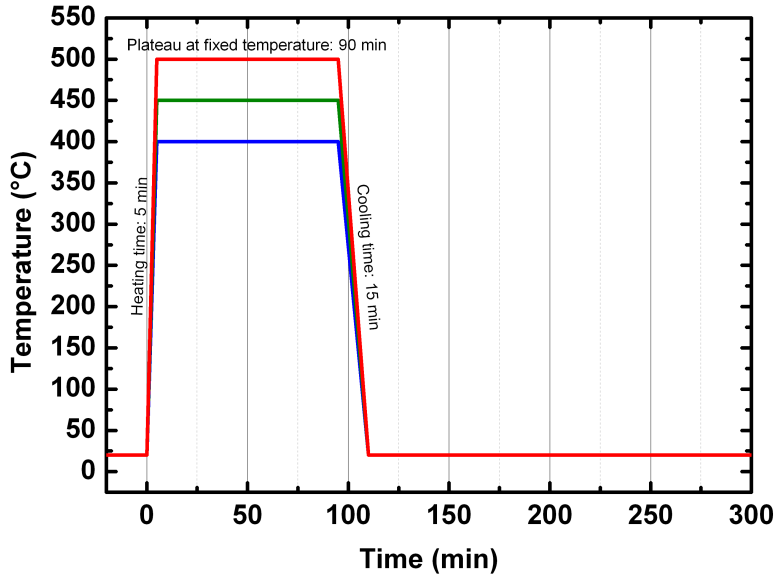

(a) Under vacuum

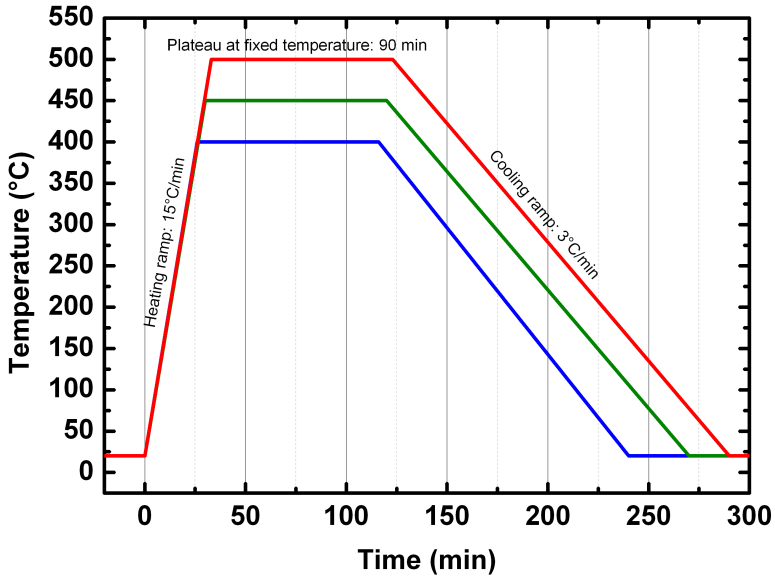

(b) In N_2/H_2 and N_2 atmospheres

Figure 4.1: Annealing temperature control as a function of time for the annealing process under vacuum (a) and in N_2/H_2 and N_2 atmospheres (b).

4.1.3 Optical properties

The optical transmittance in the 300 - 1500 nm wavelength range for the as-deposited and annealed ZnO:Al thin films deposited in pure Ar atmosphere is shown in Figure 4.2. All films exhibit an increase from 80% up to 85% of the transmittance in the visible range after the annealing step. A reduced fringe amplitude is observed after the N_2/H_2 annealing at 500 °C, due to an increase of the roughness of the film.

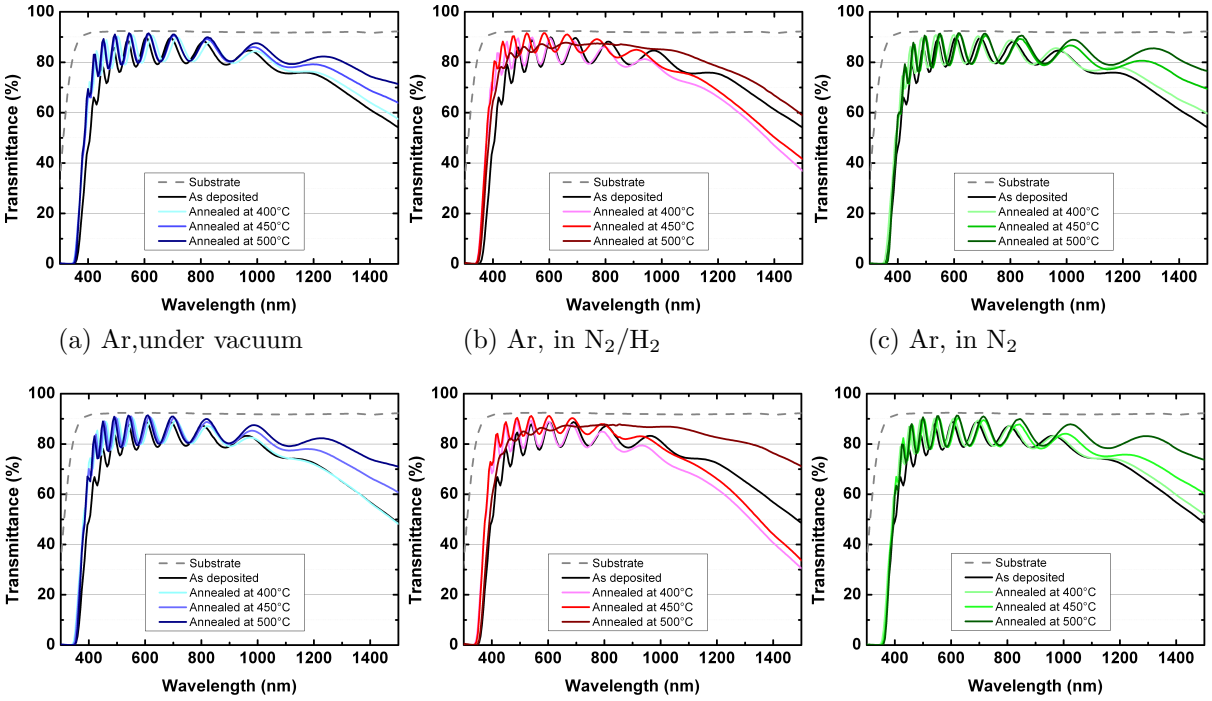

(a) Ar,under vacuum (b) Ar, in N_2/H_2 (c) Ar, in N_2

(d) Ar/O_2, under vacuum (e) Ar/O_2, in N_2/H_2 (f) Ar/O_2, in N_2

Figure 4.2: Optical transmittance spectra of ZnO:Al thin films deposited in pure Ar atmosphere, as deposited and annealed under vacuum (a), in N_2/H_2 atmosphere (b), and in pure N_2 atmosphere (c), and deposited in Ar/O_2 gas mixture and annealed under vacuum (d), in N_2/H_2 atmosphere (e), and in pure N_2 atmosphere (f). Gray dash lines correspond to glass substrate.

For the annealing under vacuum and in N_2/H_2 atmosphere, the absorption edge shifts towards shorter wavelengths, while in pure N_2 atmosphere, a shift towards higher wavelengths is observed after the annealing process. The optical band gap E_g of the films can be estimated from the transmittance spectra T of ZnO:Al sample of a thickness d versus the photon energy $h\nu$ by extrapolation of the linear region of the plot of $(h\nu(\ln T)/d)^2$ versus $h\nu$, according to the direct allowed transitions [10].

The optical band gap increases from 3.47 eV for the as-deposited ZnO:Al thin film to 3.55 eV, 3.51 eV, and 3.46 eV after the annealing step respectively at 400, 450 and 500 °C under vacuum, and to 3.57 eV, 3.54 eV and 3.47 eV after the annealing step respectively at 400, 450 and 500 °C in N_2/H_2 atmosphere as shown in Table 4.1. Several reasons can lead to a variation of the band gap, including crystallite size, internal stress and/or free carrier concentration. The effective optical band gap widening for highly n-doped thin films is proportional to the increase of the carrier concentration owing to a blocking of the lowest states of the conduction band by excess electrons, creating a shift of the Fermi level in the conduction band known as the Burstein-Moss effect.

The ZnO:Al thin films reveal different optical trends after the annealing step in pure N_2. The optical band gap remains stable, from 3.47 eV for the ZnO:Al thin film as-deposited to 3.46 eV, 3.44 eV, and 3.39 eV after the annealing step respectively at 400, 450 and 500 °C in pure N_2 atmosphere.

Table 4.1: Optical band gap for ZnO:Al thin films as deposited and annealed under vacuum, in N_2/H_2 atmosphere and in pure N_2 atmosphere, at 400, 450 and 500 °C. The values are ± 2 eV.

		OPTICAL BAND GAP		
Deposition	Annealing	Vacuum	N_2/H_2	N_2
Ar	As dep.	3.47 eV	3.47 eV	3.47 eV
Ar	400 °C	3.55 eV	3.57 eV	3.46 eV
Ar	450 °C	3.51 eV	3.54 eV	3.44 eV
Ar	500 °C	3.46 eV	3.47 eV	3.39 eV
Ar/O_2	As dep.	3.42 eV	3.42 eV	3.42 eV
Ar/O_2	400 °C	3.50 eV	3.55 eV	3.48 eV
Ar/O_2	450 °C	3.50 eV	3.54 eV	3.40 eV
Ar/O_2	500 °C	3.47 eV	3.49 eV	3.37 eV

4.1.4 Electrical properties

4.1.4.1 Hall effect measurements at room temperature

The electrical properties of the ZnO:Al thin films as functions of the annealing temperature under vacuum atmosphere, in N_2/H_2 atmosphere and in pure N_2 atmosphere are shown in Figure 4.3. A clear increase of the carrier concentration is observed with the annealing process in hydrogen-rich atmosphere, while annealing in pure N_2 leads to a decrease in carrier concentration. The carrier density remains quite stable under vacuum annealing. In all cases, a strong decrease of the carrier concentration is observed for annealing at 500 °C.

An improvement of the Hall mobility and resistivity is observed after an annealing step in vacuum and N_2/H_2 atmosphere at 400 °C. The annealing process in pure N_2 leads to a degradation of the electrical properties. The increase of the carrier concentration along with the increase in mobility after annealing in N_2/H_2 induces the decrease of resistivity. Surprisingly, the strong increase of the carrier concentration does not lead to a strong increase of the Hall mobility, but more to an increase comparable to that of the annealing under vacuum. Comparatively, the resistivity is the lowest for the N_2/H_2 annealed sample at 400 °C with $3.5\times10^{-4}\,\Omega$.cm for a Hall mobility of 39 $cm^2/V.s$. The annealing at 500 °C under 5% H_2 in N_2 atmosphere leads to a strong deterioration of the films.

These different behaviours depending on the annealing atmosphere can be explained by the analysis of the conduction mechanism based on the temperature-dependent conductivity measurements.

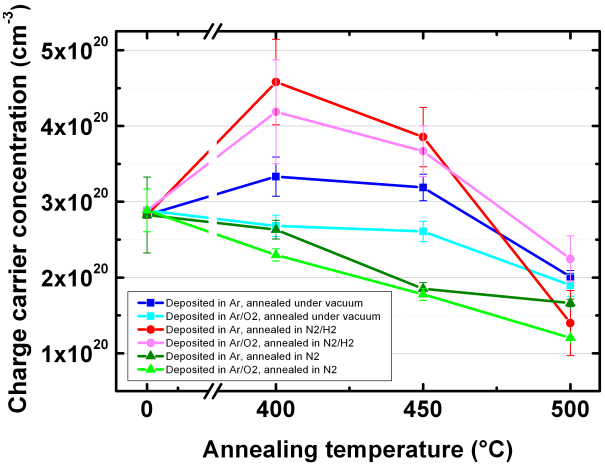

(a) Charge carrier concentration

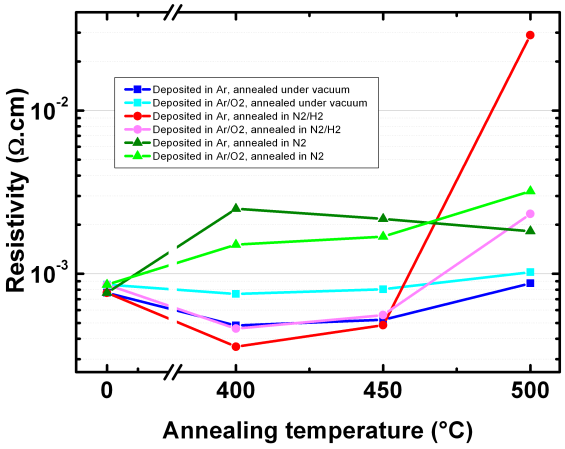

(b) Resistivity

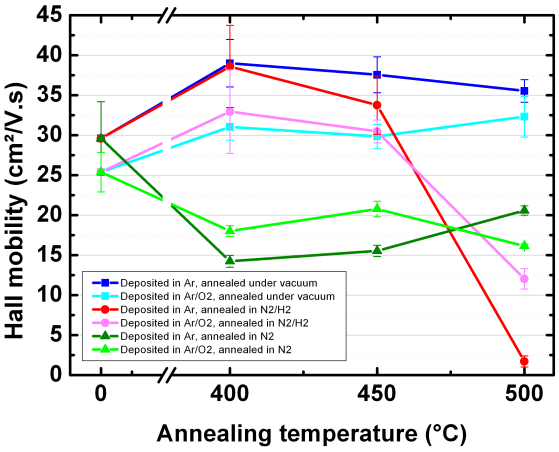

(c) Hall mobility

Figure 4.3: Electrical properties as functions of the annealing temperature under vacuum (squares), in N_2/H_2 atmosphere (dots) and in pure N_2 atmosphere (triangles) for ZnO:Al deposited in pure Ar atmosphere (dark color) or in Ar/O_2 gas mixture (light color): (a) Charge carrier concentration, (b) resistivity, and (c) Hall mobility.

4.1.4.2 Temperature-dependent conductivity

In order to analyse the conduction mechanisms of the annealed ZnO:Al thin films, carrier concentrations and conductivities were measured by Hall effect as a function of temperature. The carrier concentrations are temperature-independent, that means that these films are degenerate semiconductors.

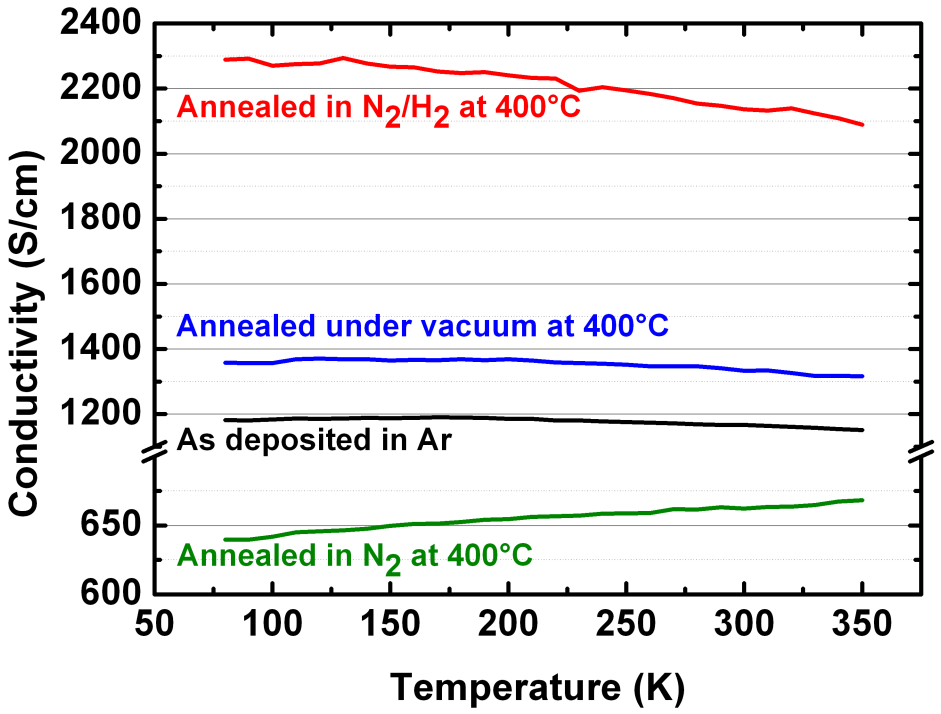

Figure 4.4: Evolution of conductivity as a function of the temperature for ZnO:Al thin films deposited in pure Ar, as-deposited and annealed at 400 °C in different atmospheres.

Depending on the annealing atmosphere, different trends are observed on the evolution of the conductivity as a function of the temperature during the Hall effect measurements (Figure 4.4). These different trends are fitted by the expression corresponding to the different scattering processes. Films annealed in pure N_2 atmosphere show an increase of the conductivity with increasing temperature. This increase reveals a grain barrier limited transport. These experimental data are fitted by taking into account the grain barrier scattering and the ionized impurities scattering through the following expression:

$$\frac{1}{\sigma} = \frac{1}{\sigma_0 exp(\Phi_b/kT)} + \frac{1}{\sigma_{ii}} \tag{4.2}$$

For ZnO:Al thin films as-deposited and annealed in N_2/H_2 atmosphere and under vacuum, the decrease of the conductivity with the temperature is correlated with scattering by ionized impurities and phonons by the following expression:

$$\frac{1}{\sigma} = \frac{1}{\sigma_{ii}} + \frac{1}{\sigma_{ph} T^{-3/2}} \tag{4.3}$$

Table 4.2: Results of the fits on the curves of the conductivity as a function of the temperature for a conduction model of grain barrier limited transport.

		GRAIN BARRIER LIMITED TRANSPORT		
Deposition	Annealing	Φ_b (meV)	L (nm)	N_t (10^{13} cm^{-2})
Ar	N_2 at 400 °C	5	14.4	4.6
Ar	N_2 at 450 °C	7	47.4	4.6
Ar	N_2 at 500 °C	9	99.6	5.0
Ar/O_2	N_2 at 400 °C	8	78.5	5.6
Ar/O_2	N_2 at 450 °C	9	120.5	5.2
Ar/O_2	N_2 at 500 °C	6	28.5	3.5
Ar	N_2/H_2 at 500 °C	6	1.8	3.6

The fits reveal different trends depending on the annealing temperature presented in Tables 4.2 and 4.3. For ZnO:Al thin films annealed in pure N_2 atmosphere, the increase of the annealing temperature leads to an increase of the barrier height and a decrease of the charge carrier trap density within the grain. The grain size increases with the annealing temperature, probably due to a reduction in point defect and/or dislocation density.

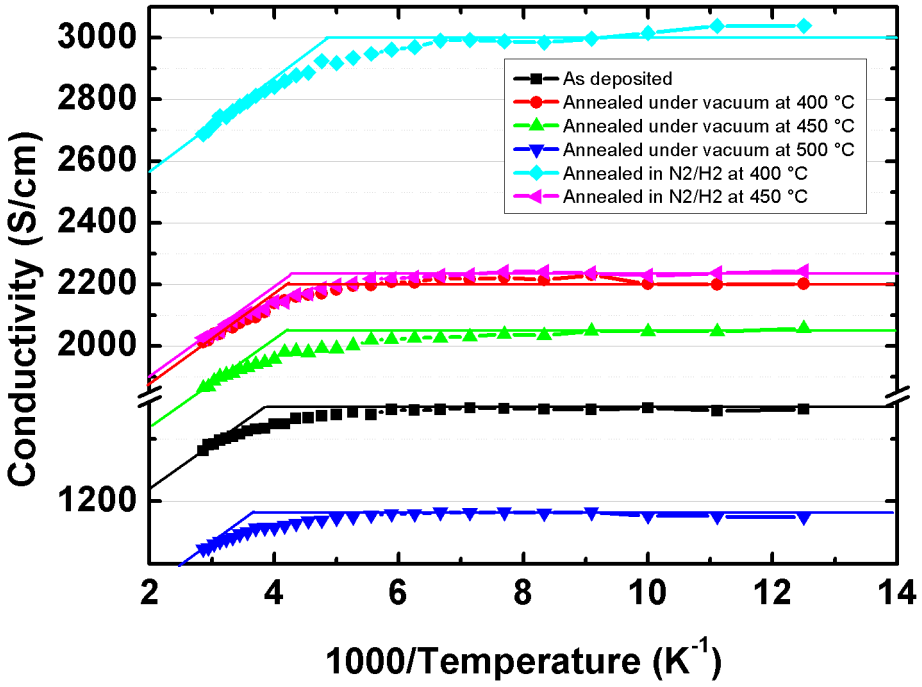

Figure 4.5: Evolution of conductivity as a function of 1000/T for ZnO:Al thin films deposited in pure Ar, as-deposited and annealed in different atmospheres.

For ZnO:Al thin films annealed under vacuum and in N_2/H_2 atmosphere, the dominant scattering processes are due to phonons and ionized impurities. Figure 4.5 shows the conductivity as a function of 1000/T. Two different behaviours are observed: at low temperature, the conductivity is constant; the transport is limited by ionized impurities

Table 4.3: Results of the fits on the conductivity as functions of the temperature for a conduction model of bulk limited transport.

		BULK LIMITED TRANSPORT Transition temperature (K)	
Deposition	Annealing	Vacuum	N_2/H_2
Ar	As dep.	260	260
Ar	400 °C	238	204
Ar	450 °C	238	234
Ar	500 °C	273	-
Ar/O_2	As dep.	270	270
Ar/O_2	400 °C	270	239
Ar/O_2	450 °C	264	259
Ar/O_2	500 °C	278	293

scattering, known to be temperature-independent for degenerate semiconductors. Above a threshold temperature value, the conductivity is reduced with the increase of the temperature. Highly conductive ZnO:Al thin films exhibit a metallic behaviour at higher temperature, this trend can be attributed to the decrease in the mean scattering time of excess electrons in the conduction band [19]. Accordingly, phonon scattering is the dominant mechanism for explaining temperature-dependent carrier transport. These results indicate a transition from semiconductor to metal, occurring at a certain transition temperature depending on the ZnO:Al thin film, as presented in Table 4.3. In this table, the transition temperatures are deduced from the conductivity curves presented in Figure 4.5, between the two different behaviours. Between as-deposited ZnO:Al thin film and samples annealed at 400 °C, a decrease of the transition temperature is observed, the metallic conduction becomes dominant over the semiconductor one. The ZnO:Al thin films annealed at 400 °C in N_2/H_2 atmosphere exhibits the most metallic behaviour.

The ZnO:Al thin film annealed at 500 °C in N_2/H_2 atmosphere cannot be fitted by the bulk limited conduction mechanism due to a strong degradation of the material.

4.1.4.3 Mobility versus carrier concentration

The mobility exhibits different behaviours depending on the carrier concentration (Figure 4.6).

For ZnO:Al thin films annealed in pure N_2 atmosphere, the mobility remains low due to the grain barrier limited transport. The N_2 atmosphere creates acceptor centres at grain boundaries, which trap electrons from the conduction band. The grain boundaries are charged negatively and a space charge region extends into the crystallite forming a double Schottky potential barrier. The barrier width and height at the grain boundaries are inversely proportional to the carrier density. For films annealed under vacuum and in N_2/H_2 atmosphere, i.e. with high carrier concentration above 2.5×10^{20} cm^{-3}, the grain barrier limitation becomes negligible, the transport is limited by the bulk. Annealing in N_2/H_2 atmosphere leads to a strong increase of the carrier concentration, which decreases the resistivity but limits the mobility by phonon scattering and ionized impurity scattering.

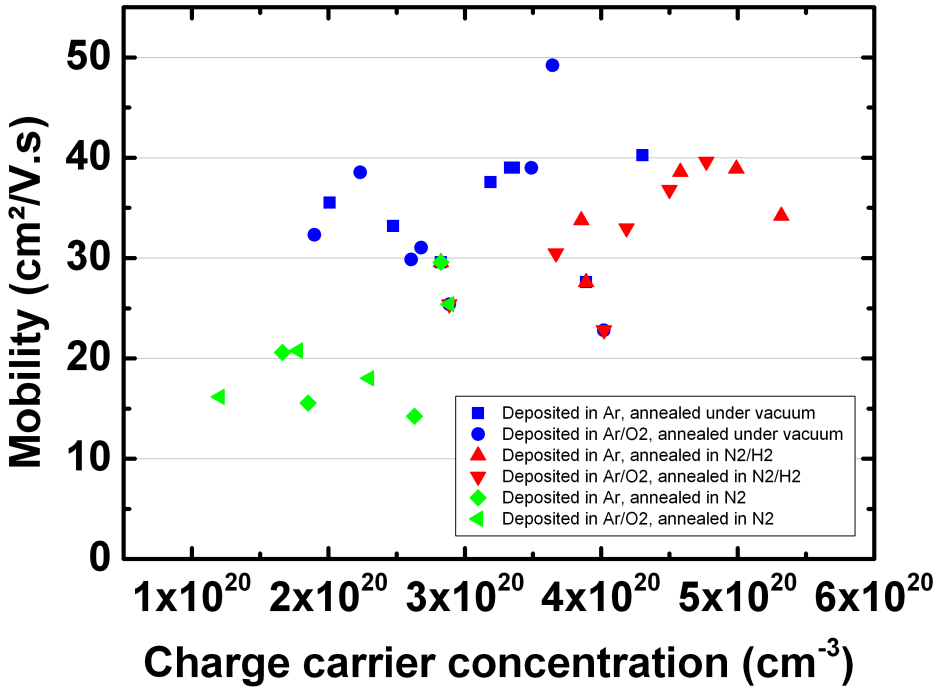

Figure 4.6: Mobility versus carrier concentration for ZnO:Al thin films annealed in different atmospheres.

4.1.5 Microstructural properties through *ex-situ* studies

4.1.5.1 X-Ray diffraction studies

X-ray diffractograms obtained for as-deposited and annealed ZnO:Al thin films exhibit a strong c-axis preferred orientation revealed by the high intensity of the (002) reflection of wurtzite structure. No Williamson-hall studies are presented here. Indeed, the *in-situ* XRD measurements during the annealing presented in section 4.1.6.1 do not allow a Williamson-Hall study, due to the necessity to measure the XRD profiles very quickly to follow the heating and cooling down phases, and thus, the θ-2θ range was focused on the (002) peak, and not on the other reflection (004) and (006). In order to compare the resulting values, only the lattice parameter d_{002} and the $FWHM_{002}$ are presented here. d_{002} corresponds to the uniform strain along the [002] orientation, and the $FWHM_{002}$ gives an information about the vertical grain size (with the contribution of the non-uniform strain).

Concerning the $FWHM_{002}$ parameter, the evolution of the values is unclear. The standard average on these values is quite high, which does not enable the observation of a clear behaviour. On the contrary, the fit of the (002) peak enable a very good estimation of the position of the (002) peak, and thus of the d_{002}. As summarized in Table 4.4, the interplanar distance increases with the annealing step up to 400 °C, no matter is the annealing atmosphere, and then remains stable or slightly decreases. The uniform strain is slightly higher for ZnO:Al thin films deposited in pure Ar atmosphere.

Table 4.4: Microstructural parameters extracted from Pseudo-voigt fit of the (002) peak from the XRD profiles for ZnO:Al thin films annealed in different atmospheres. $FWHM_{002}$ ± 0.02°, d_{002} ± 0.0001 Å.

		MICROSTRUCTURAL PARAMETERS					
		Vacuum		N_2/H_2		N_2	
Deposition	Annealing	$FWHM_{002}$ (°)	d_{002} (Å)	$FWHM_{002}$ (°)	d_{002} (Å)	$FWHM_{002}$ (°)	d_{002} (Å)
Ar	As dep.	0.24	2.598	0.24	2.598	0.24	2.598
Ar	400 °C	0.27	2.601	0.26	2.600	0.27	2.600
Ar	450 °C	0.26	2.600	0.25	2.599	0.24	2.599
Ar	500 °C	0.26	2.599	0.26	2.596	0.26	2.599
Ar/O_2	As dep.	0.24	2.593	0.24	2.593	0.24	2.593
Ar/O_2	400 °C	0.29	2.602	0.24	2.600	0.29	2.598
Ar/O_2	450 °C	0.24	2.599	0.29	2.598	0.27	2.597
Ar/O_2	500 °C	0.28	2.599	0.28	2.598	0.26	2.589

4.1.5.2 Raman spectroscopy studies

Raman spectroscopy can provide qualitative information about the orientation of the films and can be correlated with X-ray diffraction. The Raman spectra of the annealed ZnO:Al thin films presented in Figure 4.7 are dominated by the A_1-LO vibrations around 578 cm^{-1}. With increasing annealing temperature, the A_1-LO is apparently shifted towards higher wavenumbers, suggesting an increase of the [002] orientation and/or a reduction in defects of the ZnO:Al annealed. This increase of the crystallinity is correlated with the improvement of the electrical and the optical properties of the films.

The strong difference between the as-deposited ZnO:Al thin film and the annealed ones is clearly observed on the Raman spectra, but the effect of the temperature and especially the effect of the annealing atmosphere is quite difficult to distinguish (if there is an effect). One explanation could be that some errors can appear due to the fact that the measurements are realized on different samples annealed at various temperatures, and under different atmospheres. The *in-situ* XRD measurements, and *in-situ* Raman spectroscopy avoid these errors.

4.1.6 Microstructural properties through *in-situ* studies

X-ray diffraction measurements and Raman spectroscopy have been performed *in-situ* at high temperature in order to characterize the evolution of the thin films with annealing temperature. Indeed, it is not obvious to interpret the microstructural modifications observed through *ex-situ* XRD and Raman spectroscopy due to the fact that the measurements are realized at different times and not on the same sample, which can induce some errors. Thanks to the *in-situ* measurements, these sources of possible errors are absent.

4.1.6.1 X-Ray diffraction studies

These studies have been realized at the University of Poitiers from the Institute P PRIME, Laboratoire de Physique des Matériaux PHYMAT [7]. Two kinds of *in-situ* X-ray diffraction measurements have been realized, depending on the evolution of the annealing temperature, to understand the kinetics of the microstructural changes: A first one consisted

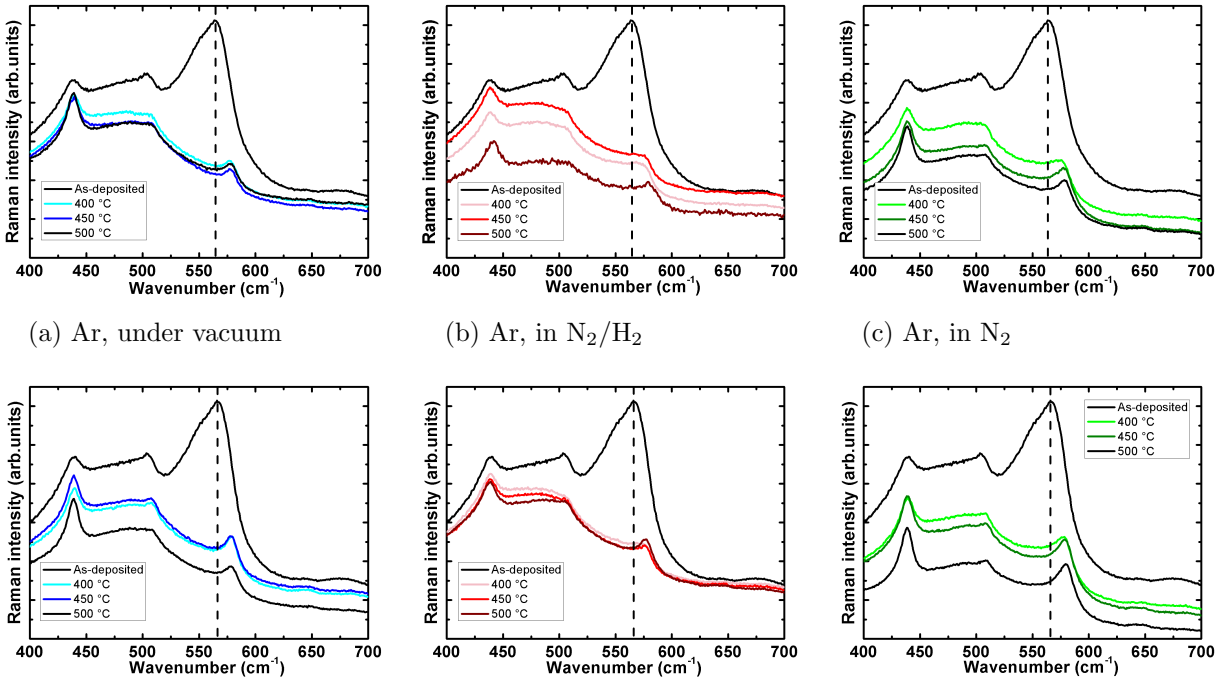

(a) Ar, under vacuum (b) Ar, in N_2/H_2 (c) Ar, in N_2

(d) Ar/O_2, under vacuum (e) Ar/O_2, in N_2/H_2 (f) Ar/O_2, in N_2

Figure 4.7: Raman spectra of ZnO:Al thin films deposited in pure Ar atmosphere, as deposited and annealed under vacuum (a), in N_2/H_2 atmosphere (b), and in pure N_2 atmosphere (c), and deposited in Ar/O_2 gas mixture and annealed under vacuum (d), in N_2/H_2 atmosphere (e), and in pure N_2 atmosphere (f).

of an increase of the temperature from room temperature to 500 °C directly followed by a decrease (Figure 4.8a). The heating and cooling down ramps were approximatively 5 °C/min. In a second run, the cycles of temperature consisted of isothermal measurements at a fixed temperature (Figure 4.8b). The set-point temperature was obtained in approximatively 10 minutes for a temperature ranging from 300 to 500 °C.

Series of samples have been deposited at room temperature, and at various values of the deposition pressure (0.01 Pa, 0.12 Pa or 2.2 Pa) or the deposition atmosphere (pure Ar or Ar/O_2 gas mixture). The *in-situ* XRD study during annealing has been performed in air, under argon flux and low pressure conditions (10 Pa)[1]. For one deposition condition, the *in-situ* XRD measurements were realized under various atmospheres on co-deposited films in order to avoid the uncertainty from the reproducibility of the deposition.

Controlled heating and cooling down

Two cycles of heating and cooling down (from RT to 500 °C) were performed in order to decorrelate the microstructural modifications and the mechanical dilatation from the heating as presented in Figure 4.9. During the first heating phase, position and intensity of the (002) peak, as well as the FWHM, indicate some intrinsic modifications whereas their evolutions demonstrate a pure linear behaviour with temperature during the cool-

[1]Unfortunately, the atmospheres studied in the previous section were not available for the *in-situ* XRD measurements.

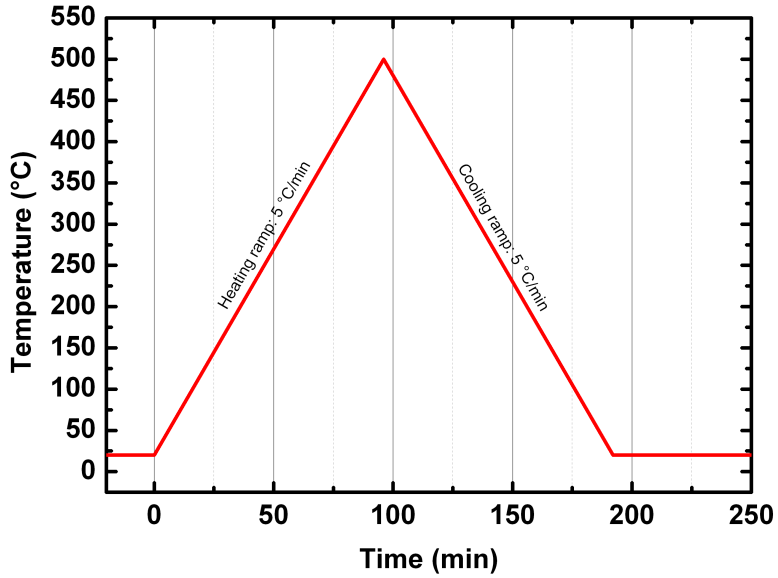

(a) Controlled heating and cooling down

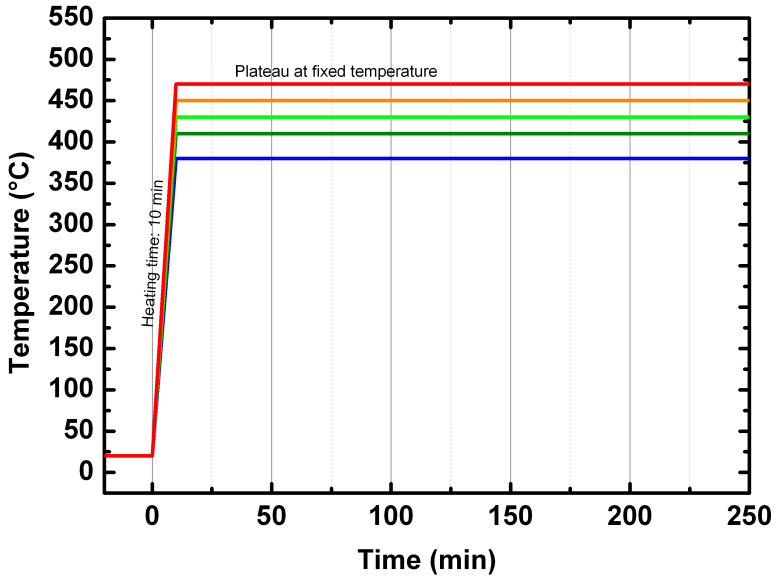

(b) Isothermal measurements

Figure 4.8: Annealing temperature control as a function of time for the in-situ XRD measurements during the annealing processes: (a) Controlled heating and cooling down, and (b) isothermal measurements.

ing phase. During the second cycle, both heating and cooling phases are perfectly linear and superimposed with the cooling step of the first cycle [7]. Assuming that this linear behaviour is characteristic of thermal stress modifications in the ZnO/glass stack and due to the mechanical dilatations of the heating chamber, the fitted parameters have been corrected by subtracting the characteristic slope of this linear behaviour. The intensities of the (002) peak obtained in this way are then translated in terms of variations

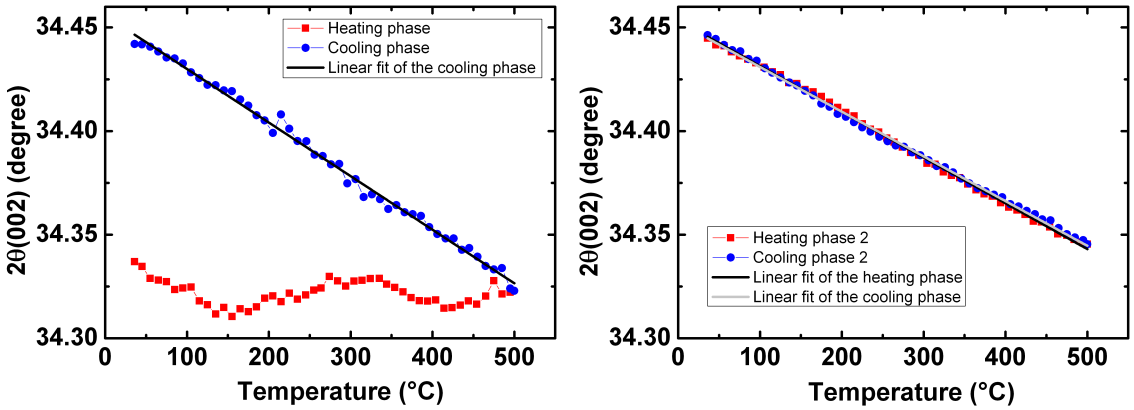

(a) (b)

Figure 4.9: Position of the (002) peak obtained by XRD as a function of the annealing temperature during the heating and cooling stages: (a) First cycle and (b) second cycle.

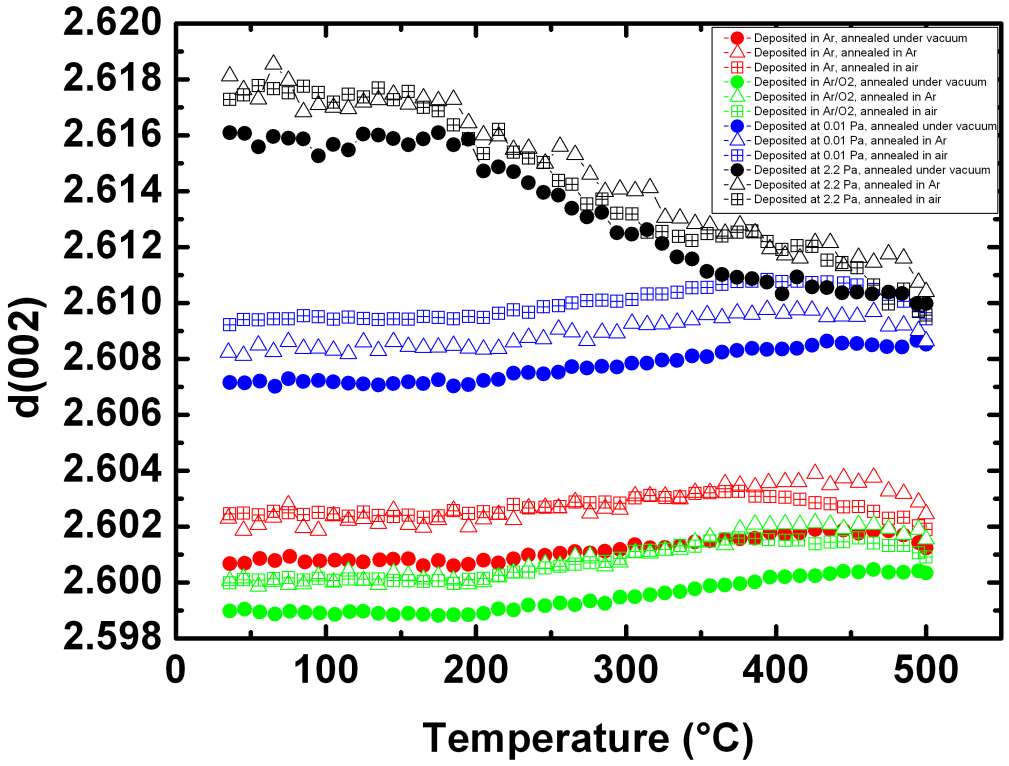

Figure 4.10: Evolution of the interplanar distance d_{002} as a function of the annealing temperature, for ZnO:Al deposited at 0.12 Pa in pure Ar (red symbols), in Ar/O_2 (green symbols) at 0.01 Pa (blue symbols) and at 2.2 Pa (black symbols), and subsequently annealed under vacuum (filled symbols), in Ar (open symbols) and in air (cross symbols).

$\Delta A_{002}(T) = A_{002}(T) - A_{002}(RT)$ plotted in Figure 4.12. The absolute values are given for the FWHM and the lattice parameter.

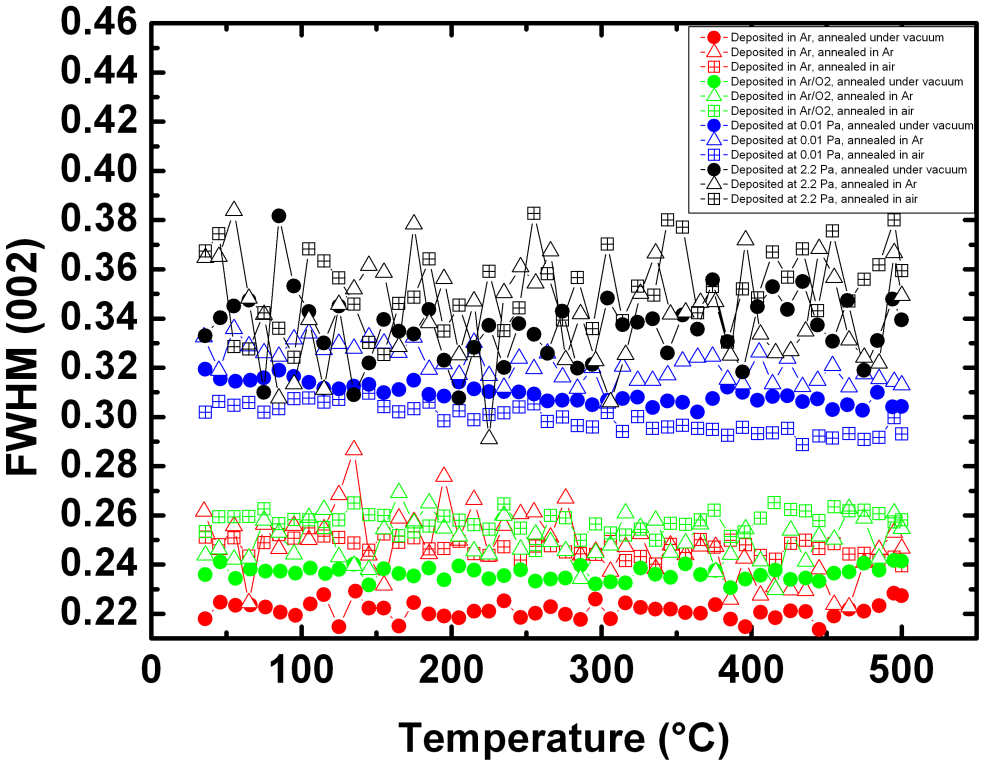

Figure 4.11: Evolution of the $FWHM_{002}$ as a function of the annealing temperature, for ZnO:Al deposited at 0.12 Pa in pure Ar (red symbols), in Ar/O_2 (green symbols) at 0.01 Pa (blue symbols) and at 2.2 Pa (black symbols), and subsequently annealed under vacuum (filled symbols), in Ar (opened symbols) and in air (cross symbols).

The interplanar distance d_{002} strongly depends on the deposition parameters, as shown in Figure 4.10. At high pressure (2.2 Pa), the interplanar distance is high, around 2.618 Å. This is due to a highly defective material, which extents the lattice distance, and thus increases the tensile strain as observed in Figure 3.2c from section 3.2. The same observation is realized at low pressure, previously explained in section 3. The ZnO:Al thin films deposited at the optimum pressure, 0.12 Pa, exhibit the lowest interplanar distance, around 2.602 Å for samples deposited in pure Ar, and 2.600 Å for samples deposited in Ar/O_2 gas mixture (Figure 4.10). The interpretation of the as-deposited films microstructure is correlated with the $FWHM_{002}$ shown in Figure 4.11. The films deposited at extreme values of pressure (2.2 and 0.01 Pa) exhibit a higher $FWHM_{002}$, which means that the crystallite size along the [002] orientation is lower than the crystallite size at the optimum pressure (0.12 Pa) by considering the Scherrer formula.

The main parameter strongly impacting the microstructure is the annealing temperature, particularly on ZnO:Al thin films deposited at high pressure (2.2 Pa). At these pressures, the films are highly defective, and the annealing process strongly improves their microstructure. This improvement leads to a decrease of the interplanar distance (Figure 4.10) due to the reorganisation of the atoms. For films deposited at 0.12 Pa or at 0.01 Pa, a first increase of the lattice distance d_{002} is observed between 350 and 450 °C depending on the deposition and/or the annealing atmosphere, followed by a decrease until the end of the heating phase. The evolution of the FWHM with the annealing temperature

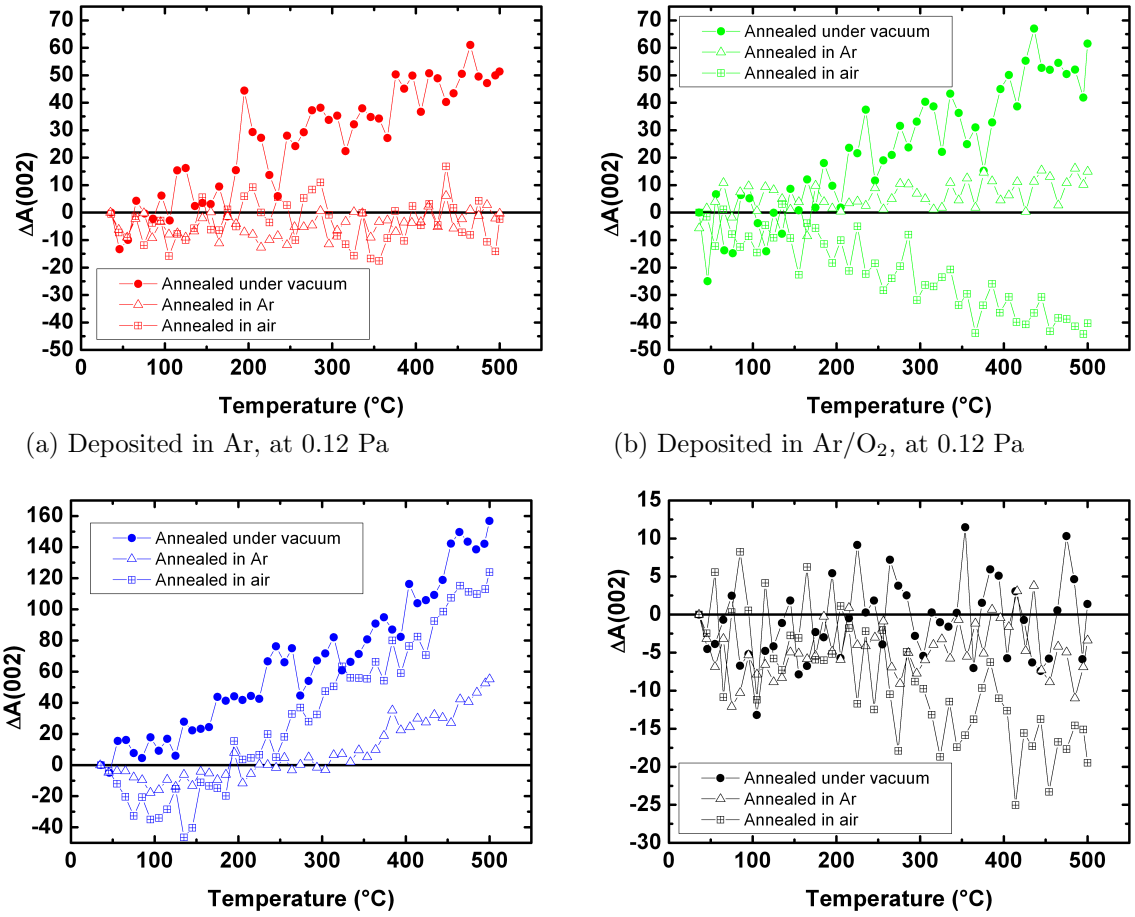

(a) Deposited in Ar, at 0.12 Pa

(b) Deposited in Ar/O_2, at 0.12 Pa

(c) Deposited in Ar, at 0.01 Pa

(d) Deposited in Ar, at 2.2 Pa

Figure 4.12: Evolution of the ΔA_{002} as a function of the annealing temperature, for ZnO:Al deposited at 0.12 Pa in pure Ar (a), in Ar/O_2 (b) at 0.01 Pa (c) and at 2.2 Pa (d), and subsequently annealed under vacuum (filled symbols), in Ar (opened symbols) and in air (cross symbols).

does not show any obvious change, the crystallite size remains constant (Figure 4.11). The influence of the annealing atmosphere on the microstructural characteristics is null or very weak: the evolution of the d_{002} or the $FWHM_{002}$ as a function of the annealing temperature is the same for all annealing atmospheres. These observations are consistent with the *ex-situ* measurements.

The variations of the intensity of the (002) peak presented in Figure 4.12 exhibit different behaviours depending on the deposition atmosphere and annealing atmosphere. The samples annealed under vacuum present an increase of the intensity of the (002) with the annealing temperature, except for the sample deposited at high pressure which is quite stable. This increase reveals an improvement of the crystallinity of these thin films under vacuum. From samples annealed in air, the crystallinity is slightly degraded or stable, while the annealing in Ar keeps the crystallinity quite stable.

Isotherms

The isothermal measurements are carried out in order to decorrelate the effect of the temperature and the time of the annealing. The isotherms are done at 450 °C, with a heating phase as fast as possible (10 minutes).

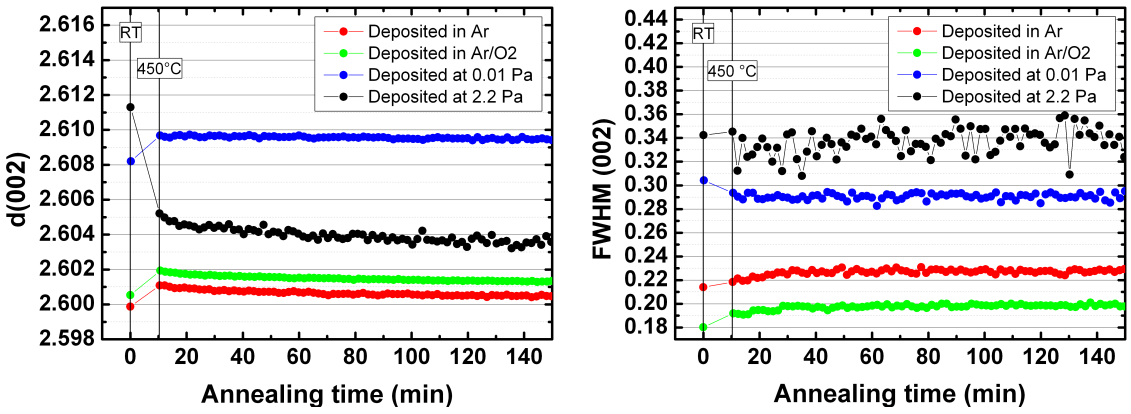

(a) (b)

Figure 4.13: Evolution of the d_{002} (a), and $FWHM_{002}$ (b) as a function of the annealing time at 450 °C, for ZnO:Al deposited at 0.12 Pa in pure Ar (red symbols), in Ar/O_2 (green symbols), at 0.01 Pa (blue symbols) and at 2.2 Pa (black symbols), and subsequently annealed under vacuum.

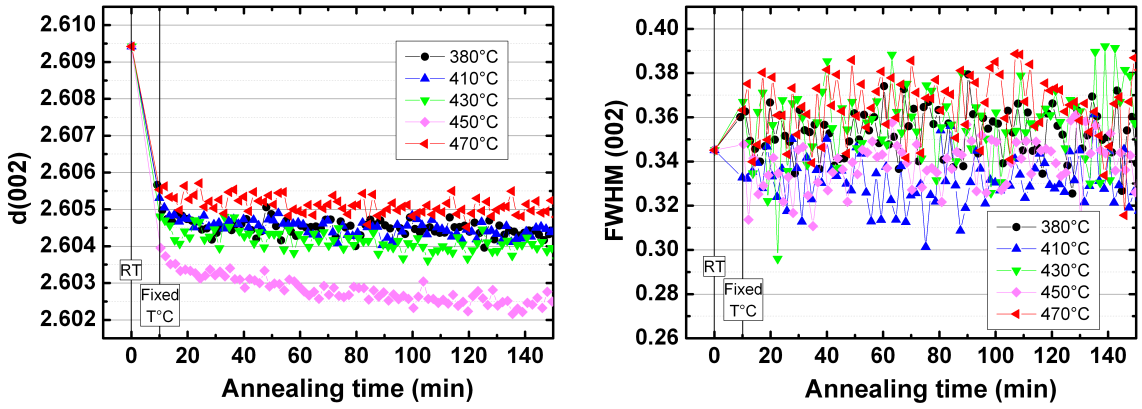

(a) (b)

Figure 4.14: Evolution of the d_{002} (a) and $FWHM_{002}$ (b) as functions of the annealing time and the annealing temperature for ZnO:Al deposited at 2.2 Pa, and subsequently annealed under vacuum.

The results presented in Figure 4.13 clearly prove that the microstructural changes occur at the very first step of the annealing, during the heating process, i.e. during the first 10 minutes. When the setting value of the temperature is obtained, the microstructure has already been modified and remains stable with the annealing time. As for controlled heating and cooling down measurements, the same trends are observed, i.e. a strong decrease of the interplanar lattice distance for ZnO:Al films deposited at 2.2 Pa, and a

slight increase for the films deposited at lower pressure, with or without oxygen in the gas phase. The FWHM of the (002) peak remains stable.

Finally, different temperatures are tested as presented in Figure 4.14. The results show the evolution of the interplanar lattice distance and the FHWM as functions of the annealing time at various annealing temperatures for ZnO:Al deposited at 2.2 Pa, i.e. presenting the strongest changes. While the FWHM does not show any modifications with the annealing step, the d_{002} exhibits a decrease, up to 2.602 Å at 450 °C, which tends to the lattice parameters c/2 of ZnO.

In-situ Hall effect measurements

As the *in-situ* XRD measurements have not been realized in the same atmospheres than the first annealing processes, *in-situ* Hall effet measurements are realized for the annealing at low pressure, in Ar flow and in air, to more clearly correlate the *in-situ* XRD measurements and the resulting electrical properties.

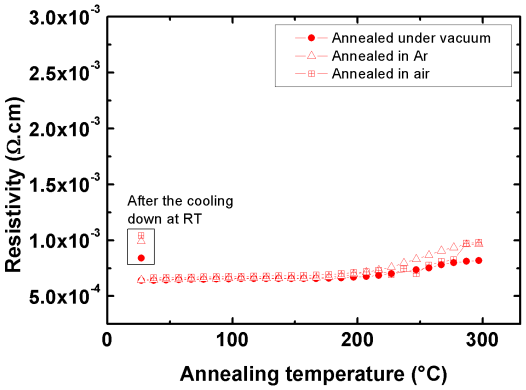

(a) Deposited in Ar, at 0.12 Pa

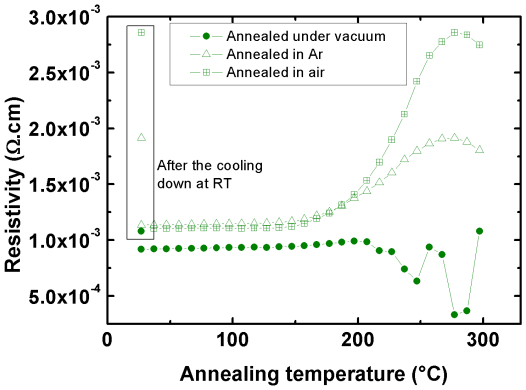

(b) Deposited in Ar/O_2, at 0.12 Pa

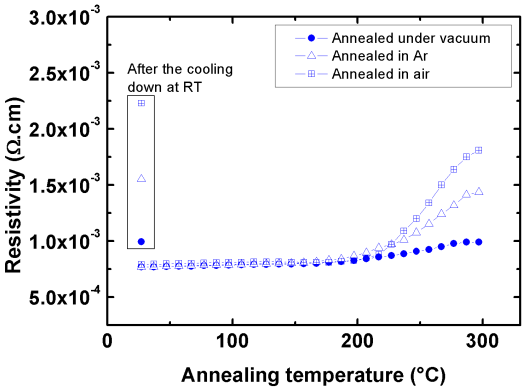

(c) Deposited in Ar, at 0.01 Pa

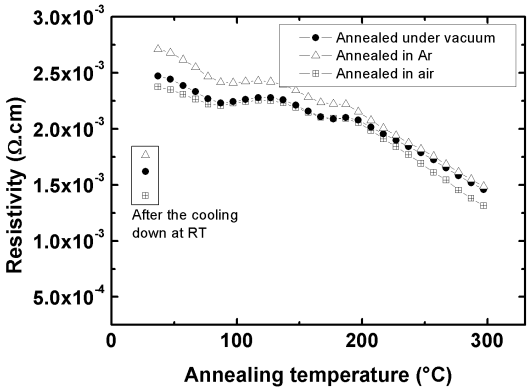

(d) Deposited in Ar, at 2.2 Pa

Figure 4.15: Evolution of the ΔA_{002} as a function of the annealing temperature, for ZnO:Al deposited at 0.12 Pa in pure Ar (a), in Ar/O_2 (b), at 0.01 Pa (c) and at 2.2 Pa (d), and subsequently annealed under vacuum (filled symbols), in Ar (opened symbols) and in air (cross symbols).

In Figure 4.15 are presented the evolution of the resistivity as a function of the annealing temperature up to 300 °C for the four annealing atmospheres. The as-deposited films exhibit different resistivities depending on their deposition pressure. The lowest resistivity is achieved for a deposition at 0.12 Pa, as expected, and correlated with the largest grain size (lowest FWHM), and the lowest interplanar distance along the [002] orientation. The resistivity is quite satisfying for a deposition realized at 0.01 Pa but is much degraded for high pressure deposited films. These observations are also consistent with the initial lattice parameter and the FWHM values we measured.

The evolution of the resistivity is studied as a function of the annealing parameters. The modifications observed during the heating phase are due to the material modifications and not to a conduction process change due to the temperature of measurement. This is confirmed by the resistivity values after the cooling down to room temperature which are more or less in the same range than at the end of the heating phase. Different behaviours are observed depending on the deposition pressure and annealing temperature. The best material, deposited at 0.12 Pa, is quite stable with the annealing step, and exhibits a slight increase of the resistivity, while the thin film deposited at low pressure presents a stronger decrease of the resistivity depending on the annealing temperature, and the resistivity of the film deposited at high pressure is strongly improved. Films annealed under vacuum seem to show a slower degradation compared to an annealing step in argon flow, and especially compared to the annealing process in air. The electrical and microstructural properties are strongly correlated. The lowest resistivity corresponds to the lowest interplanar distance along the [002] orientation and an increase of the resistivity corresponds to an increase of d_{002}. Moreover, the evolution of the resistivity follows the the evolution of the interplanar distance: a decrease of the lattice parameter leads to a decrease of the resistivity.

4.1.6.2 Raman spectroscopy studies

The effect of the annealing temperature has also been studied by *in-situ* Raman spectroscopy, to be correlated with the X-ray diffraction study. The same series of samples as for the X-ray diffraction study have been used, i.e ZnO:Al thin films deposited at room temperature, and at various deposition pressures (0.01 Pa, 0.12 Pa or 2.2 Pa) or deposition atmospheres (pure Ar or Ar/O_2 gas mixture). The *in-situ* Raman study during annealing has been performed in air. The cycle of heating and cooling down was performed from RT to 500 °C, with a plateau at 500 °C of 90 minutes, as shown in Figure 4.16.

As previously observed in section 3, the Raman spectroscopy and the X-ray diffraction measurements can be correlated in order to estimate the crystal quality of the films. The asymmetric A_1-LO band arises from two contributions, a low wavenumber contribution (disordered material) and a high wavenumber one (crystalline material). Indeed, the relative area of the disordered (low wavenumber contribution) and crystalline (high wavenumber contribution) peaks enables to compare the degree of crystallinity corresponding to different spectra, revealed by an apparent shift of the LO mode.

Mappings of the A_1-LO peak position as a function of the annealing temperature are presented in Figure 4.17. The Raman spectra for ZnO:Al thin films as-deposited present an intense A_1-LO peak. This peak is shifted towards low wavenumbers for a highly defective films such as ZnO:Al thin films deposited at high pressure (A_1-LO at 551 cm^{-1},

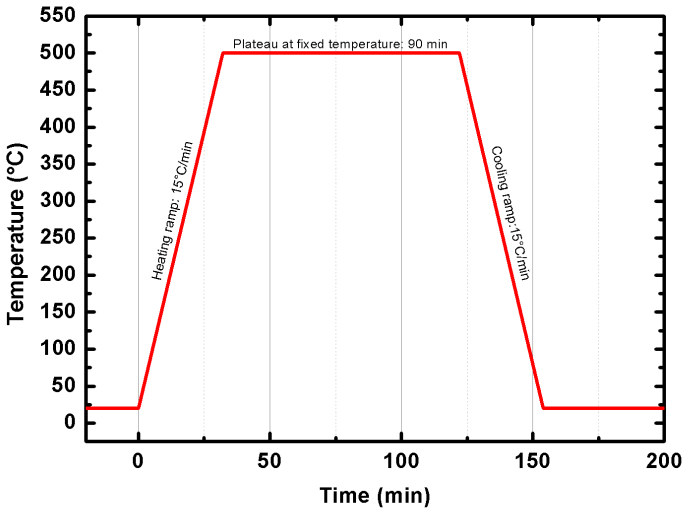

Figure 4.16: Annealing temperature control as a function of time for the in-situ Raman measurements during the annealing processes.

Figure 4.17d), while it is positioned at higher wavenumbers for ZnO:Al thin films highly crystalline films deposited at lower pressures. The same observation has been previously done in section 3.

While we expected a shift of the A_1-LO peak towards higher wavenumbers during the annealing process, the opposite result is obtained. The A_1-LO Raman peak redshifts and broadens as temperature increases. This is due to the fact that the Raman active modes are related to the vibrations of atoms, strongly dependent on the temperature of the measurements: The Raman spectra detect the microstructural properties of the materials, which are temperature-dependent. The shift of the A_1-LO peak towards 550 cm^{-1} is due to the heating of the sample rather than to structural changes. The effects of temperature have been previously observed and interpreted by Cuscó *et al* [6]. The A_1-LO mode occurs at frequencies that lie in a plateau of the two-phonon DOS with a relatively high density of states. The behaviour of the A_1-LO mode is well described by a dominant decay channel localized around a single set of frequencies such as the Ridley channel [6]. This involves the decay of the longitudinal optical (LO) mode into a mode of the transverse acoustic (TA) branches and a mode of the transverse optical (TO) branches. The anisotropy of the force constants in the wurtzite structure causes the transverse branches to split along the main symmetry lines of the Brillouin zone. Thus, modes from different split TO and TA branches can provide decay channels for A_1-LO mode.

As a consequence, the true effect of annealing of ZnO:Al thin films is only observed after the cooling down to room temperature, at the end of the annealing process. The A_1-LO peak is observed at a higher wavenumber position than before the annealing process, due to an improvement of the crystallinity of the material, whatever the deposition conditions. Moreover, the intensity of the peak is lower, providing a supplementary observation correlated with an improvement of the crystalline quality of the films, as previously observed.

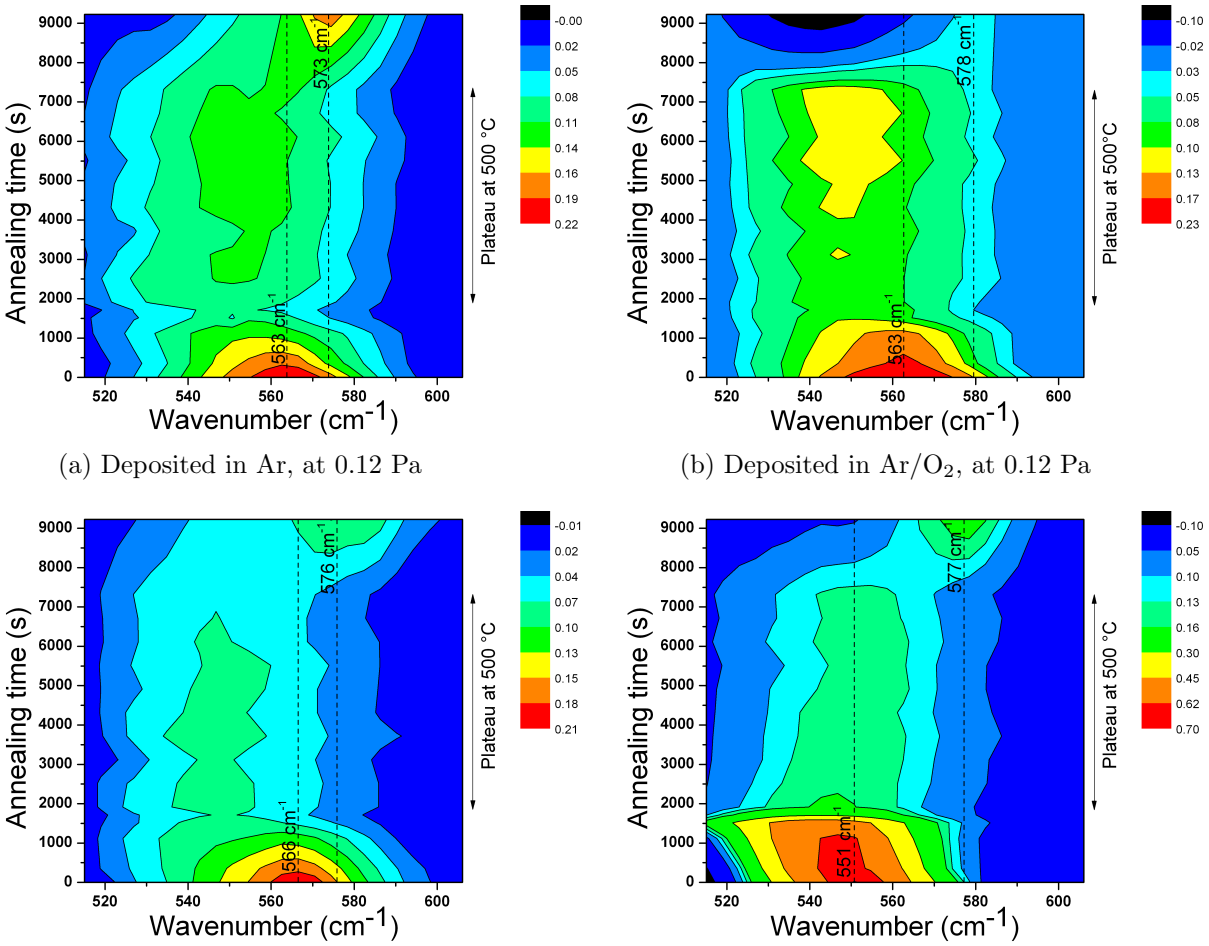

(a) Deposited in Ar, at 0.12 Pa

(b) Deposited in Ar/O_2, at 0.12 Pa

(c) Deposited in Ar, at 0.01 Pa

(d) Deposited in Ar, at 2.2 Pa

Figure 4.17: Evolution of the A_1-LO peak with the annealing cycle from ZnO:Al deposited at 0.12 Pa in pure Ar (a), in Ar/O_2 (b), at 0.01 Pa (c) and at 2.2 Pa (d), and subsequently annealed in air at 500 °C during 90 minutes.

4.1.7 Conclusion

ZnO:Al thin films present different microstructural, optical and electrical properties between the as-deposited and annealed states, strongly depending on the annealing atmosphere for the electrical properties, and depending on the annealing temperature for the microstructural modifications.

The annealing atmosphere has a strong impact on the electrical changes with the annealing step after 90 minutes at fixed temperature. In N_2/H_2, the annealing process leads to a strong increase of the charge carrier concentration, while in pure N_2, the carrier concentration is strongly decreased, and under vacuum, it remains stable. Thus, the atmospheres have different consequences on the electrical conduction, but it seems that a long annealing step is necessary to observed these modifications: The *in-situ* Hall effect measurements (under low pressure, in air, and in Ar flow) shown only weak differences depending on the annealing atmospheres, perhaps because these three atmospheres have the same effect, or more probably because the annealing time was not enough to observe a modification of the electrical conduction.

With the evolution of the carrier concentration, some differences appear on the mobility and the resistivity. In pure N_2, a decrease of the mobility is observed, while in N_2/H_2 and under vacuum, the resistivity decreases and the mobility increases. While the resistivity is the lowest for an annealing in N_2/H_2, the mobility is more or less the same compared to the annealing under vacuum. These differences are explained by an analysis of the temperature-dependent conductivities, which reveals that the mobility after an annealing in N_2/H_2 is limited by ionized impurities scattering, while the N_2 annealing leads to a grain-barrier limited transport, with acceptor centres at the grain boundaries.

The microstructural modifications depend on the annealing temperatures and on the deposition conditions but are the same no matter is the annealing atmosphere. With the annealing step on ZnO:Al thin film deposited at 0.12 Pa and at room temperature, the interplanar distance increases up to the optimum temperature and then slowly decreases. The evolution of the parameters is the smallest for the best material, i.e. sputtered at 0.12 Pa. The tendency strongly depends on the pressure during the ZnO:Al sputtering process. The layers deposited at high pressure show an improvement of the electrical properties and a decrease of the interplanar distance d_{002} while the films sputtered at lower pressure, 0.01 Pa and 0.12 Pa, exhibit an increase of the resistivity and an increase of the lattice parameter. Our study demonstrates a strong relationship between the lattice parameter and the resistivity of ZnO:Al films: the lowest resistivity is achieved for the lowest interplanar distance along the [002] orientation. These observations have been realized on samples annealed only by a heating and cooling phase, and without a plateau at high temperature.

To summarize, the microstructural modifications occurs at the very first annealing step, even during the heating phase, and remain stable at high temperature during a longer time. The electrical properties are influenced by the microstructural modification in short term, and in longer term by the annealing atmosphere, which modify the electrical conduction by the creation of acceptor centres at the grain boundaries (N_2 annealing) or the creation of ionized impurities in the material (N_2/H_2 annealing).

4.2 Laser annealing treatments

The use of excimer laser annealing (ELA) to improve the electrical, optical and morphological properties of ZnO:Al thin films deposited at room temperature is investigated in this section. These studies, funded through the FUI-LaText project, are rely on the effects of a combined excimer laser annealing and chemical etching process (**La**ser **Tex**turing, the LaText process) on room-temperature sputtered ZnO:Al thin films.

The evolution of the optoelectronic properties of room-temperature sputtered ZnO:Al thin films during the ELA process has been examined in detail: the bulk structural changes induced during laser annealing through X-ray diffraction measurements and Raman spectroscopy, correlated with the optical and electrical properties changes, as well as the change in surface morphology and optical haze induced by the laser process.

4.2.1 Introduction

A first work on laser annealing of ZnO thin films was published in 1984 by Bertolotti *et al.* [3]. Laser annealing was carried out by using a CO_2 laser source ($\lambda = 10.6\ \mu$m) on ZnO films deposited on Corning glass, and SiO_2/(111)Si substrates by RF diode sputtering. The treatment did not affect refractive index but produced a marked decrease for guided mode losses.

After this first significant study, many studies have been published on ZnO thin films deposited by various techniques. Laser annealing treatments have been realized on sol-gel derived ZnO thin films. Nagase *et al.* prepared zinc oxide films by using KrF excimer laser irradiation of sol-gel derived precursor film on glass substrates. Low energy fluences produced low crystallinity with weak [002] orientation, producing crystal growth of close-packed ZnO crystals in an upper layer, while irradiation at high energy fluences produced high crystallinity, larger grain size and smooth film surface [21]. Laser processing creates oxygen vacancies in contrast to conventional heat-treatment, resulting in a decrease in electrical resistivity of the films. Films irradiated at high fluence shift from a band structure with direct band gap to an indirect one [22]. These films have been studied by photoluminescence [21], and green cathodoluminescence [20].

Winfield *et al.* have observed the crystallization of sol-gel deposited amorphous films to hexagonal wurtzite zinc oxide, by the use of a laser annealing process with a laser pulse repetition rate of 25 Hz, a pulse energy of 5.9 mJ, giving a fluence of 225 mJ/cm^2 [34].

Tsang *et al.* have irradiated sol-gel derived ZnO:Al thin films by using an excimer laser leading to a significant improvement of the structural, electrical and optical characteristics of the films. The resistivity of laser irradiated film (EL = 250 mJ) was $4.4\times10^{-2}\ \Omega$.cm and an optical transmittance of about 90%, results correlated with a strong [002] orientation [31].

Recently, Kim *et al.* have studied the effect of KrF excimer laser annealing on sol-gel derived ZnO films by photoluminescence. They have concluded that laser annealing removed or filled intrinsic defects such as O and Zn vacancies or interstitials [12]. This result is in contradiction with the observation of Nagase *et al.* [21, 22].

A report by Ozerov *et al.* showed an improved exciton lifetime when pulsed laser ablated nanocrystalline thin films of ZnO are exposed to ArF excimer laser radiation (193 nm, 15 ns) [26], whereas another reported improved optical properties but worsened electronic characteristics of ZnO films deposited by a chemical spray pyrolysis when exposed to radiation from both a continuous-wave CO_2 laser and a pulsed XeCl excimer source [4].

Laser annealing has also been tested on laser assisted molecular beam (LAMBD) deposited ZnO thin films, notably by Li *et al.*, and Yen *et al.* Hall-effect measurements have shown that undoped ZnO films change from n-type with mobility values in the range of 200 cm^2/V.s to p-type material with mobility value of 73 cm^2/V.s, after laser annealing [15, 36].

Finally, RF magnetron sputtered ZnO thin films have been annealed using an excimer

laser in few works. Yen *et al.* have studied various annealing techniques, including rapid thermal annealing (RTA), laser annealing (LA), and furnace annealing (FA) in nitrogen atmosphere for ZnO thin films [37]. Moreover, Kim *et al.* have investigated the effects of laser annealing on ZnO thin film transistors (TFTs) [11]. No previous work has been found on ZnO:Al thin films deposited by RF magnetron sputtering, and subsequently annealed by an excimer laser treatments for photovoltaic applications.

4.2.2 Experimental procedure

ZnO:Al thin films were deposited in the Alliance concept reactor at room temperature by RF magnetron sputtering using a ZnO/Al_2O_3 (1 wt %) ceramic target and a RF power of 250 W. Depositions were carried out in pure argon atmosphere, at a working pressure of 0.12 Pa. The ZnO:Al thin films were laser annealed (ELA) using an excimer laser ($\lambda = 308$ nm, pulses of 130 or 180 ns). Up to 25 different fluences of ELA treatment were investigated per 5 × 5 cm substrate, from 0 to 1 J/cm^2.

4.2.3 Optical properties

In Figure 4.18, a decrease in transmittance in the long wavelength region can be observed, presumably due to an increase in free-carrier density. The zoom of the wavelength range of interest for thin film silicon devices shows an increase of the total transmittance in the visible range up to 0.60 J/cm^2 for ZnO:Al annealed at 130 ns per shot, and up to 0.70 J/cm^2 for ZnO:Al annealed at 180 ns per shot. These optima correspond to the highest [002] orientation observed in section 4.2.6. Above this threshold value, a strong degradation of the transmittance in the visible range is observed.

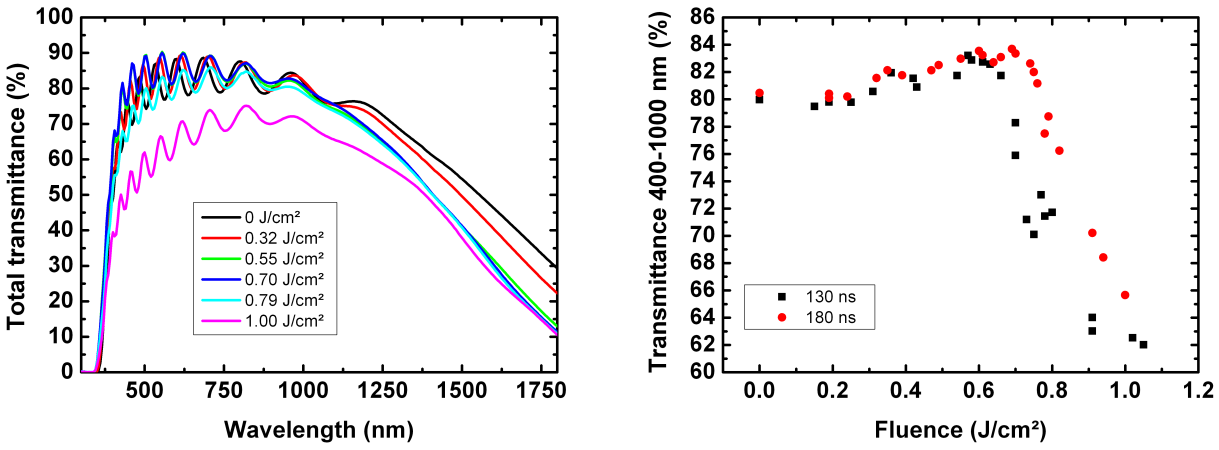

(a) (b)

Figure 4.18: Optical properties: (a) Total transmittance measurements as functions of the ELA fluences for ZnO:Al thin films annealed at 180 ns per shot, and (b) average total transmittance in the range between 400 and 1000 nm as a function of the ELA fluences for ZnO:Al thin films annealed at 130 ns per shot (black squares) or 180 ns per shot (red dots).

4.2.4 Electrical properties

For ZnO:Al thin films in their as-deposited and ELA states, at different fluences and using a pulse length of either 130 ns or 180 ns, it can be seen in Figure 4.19 that the charge carrier concentration increases with the fluence. A net improvement of the electrical properties is observed for samples annealed at 130 ns per shot; for a fluence between 0.19 and 0.31 J/cm^2, the increased carrier concentration combines with an increase in the mobility from 29.1 to 34.4 cm^2/V.s at 0.19 J/cm^2, and resulting in a decrease of the resistivity from $8.2\times10^{-4}\,\Omega$.cm to $6.0\times10^{-4}\,\Omega$.cm at 0.25 J/cm^2. At higher fluences, above 0.36 J/cm^2, a degradation of the electrical properties is observed. However, some scatter in the data is observed and some areas retain acceptable properties ($< 10^{-3}\,\Omega$.cm) for fluences up to 0.8 cm^2/V.s. For the samples treated using a pulse length of 180 ns, the scatter in the data is even larger: above 0.5 J/cm^2, some areas retain acceptable properties (1.0 - $2.0\times10^{-3}\,\Omega$.cm) up to 0.8 J/cm^2, whereas others become too much resistive ($> 5.0\times10^{-3}\,\Omega$.cm). The evolution of the electrical properties is correlated with the microstructural modifications further detailed in the next section.

4.2.5 Morphological properties

In this section, the morphological properties of ZnO:Al films are presented as functions of the fluence applied to the material, in Figure 4.20 for ZnO:Al thin films deposited at 0.01 Pa, and in Figure 4.21 for ZnO:Al thin films deposited at 0.12 Pa. A dramatic change in the surface morphology is observed for samples annealed with a fluence from 0.62 J/cm^2, for ZnO:Al deposited at 0.01 Pa, and from 0.55 J/cm^2 for ZnO:Al deposited at 0.12 Pa. A significant smoothing of the surface is observed, accompanied by the formation of flat areas, that will be referred as grains, of few dozens of nanometers forming domains of micrometer size separated by cracks. Above a certain threshold value (0.83 J/cm^2 at 0.01 Pa ZnO:Al, 0.78 J/cm^2 for 0.12 Pa ZnO:Al), the top surface of some domains begins flaking off, resulting in a missing puzzle piece appearance. At the highest fluences, some nanospheres appear on the surface of the annealed films. This behaviour is explained in the following section by the microstructural studies.

4.2.6 Microstructural properties

4.2.6.1 X-Ray diffraction studies

X-ray (θ - 2θ scans) diffractograms obtained for as-deposited and annealed ZnO:Al thin films (ELA 180 ns) exhibit a strong c-axis preferred orientation revealed by the high intensity of the (002) reflection of wurtzite structure as shown in Figure 4.22.

An increase of the intensity of the (002) peak is observed up to 0.70 J/cm^2, followed by a decrease of this intensity at higher fluences. This behaviour indicates an improvement of the crystallinity of the films along the [002] orientation up to a fluence of 0.70 J/cm^2. This observation is accompanied by a shift in 2θ position of the (002) peak. For the as-deposited ZnO:Al thin film, the (002) peak is located at 34.53°, it shifts until 34.50° at a fluence of 0.70 J/cm^2 and then increases to 34.6°. This shift can be an indication of a

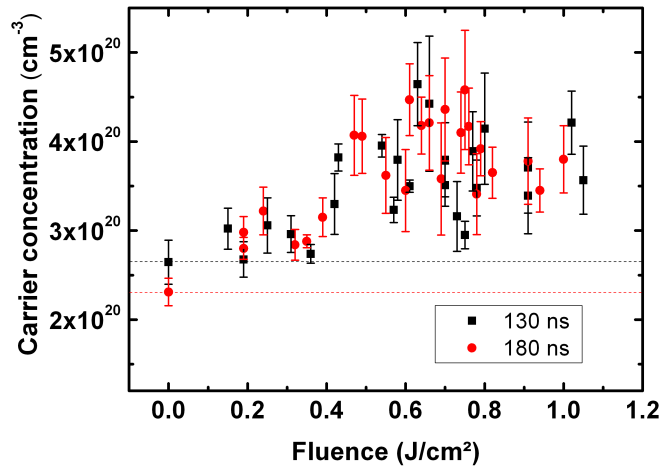

(a) Charge carrier concentration

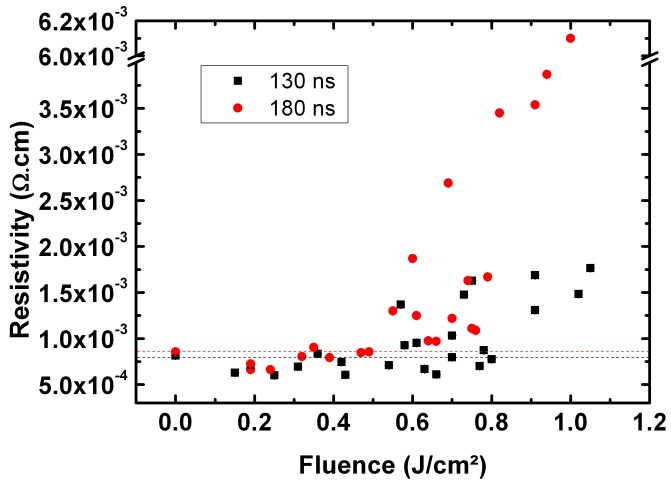

(b) Resistivity

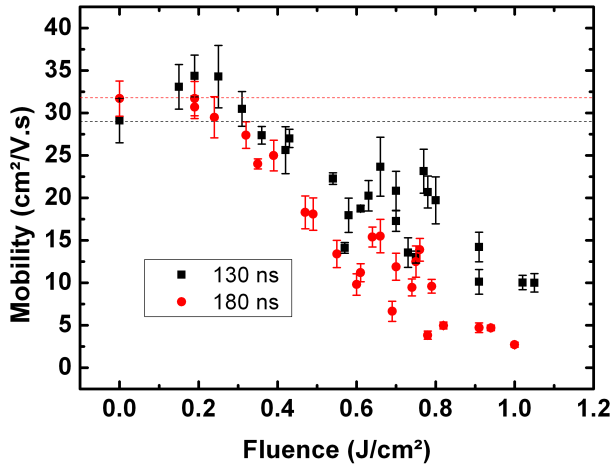

(c) Hall mobility

Figure 4.19: Electrical properties as functions of the ELA fluences for ZnO:Al thin films annealed at 130 ns per shot (black squares) or 180 ns per shot (red dots): (a) Charge carrier concentration, (b) resistivity and (c) Hall mobility.

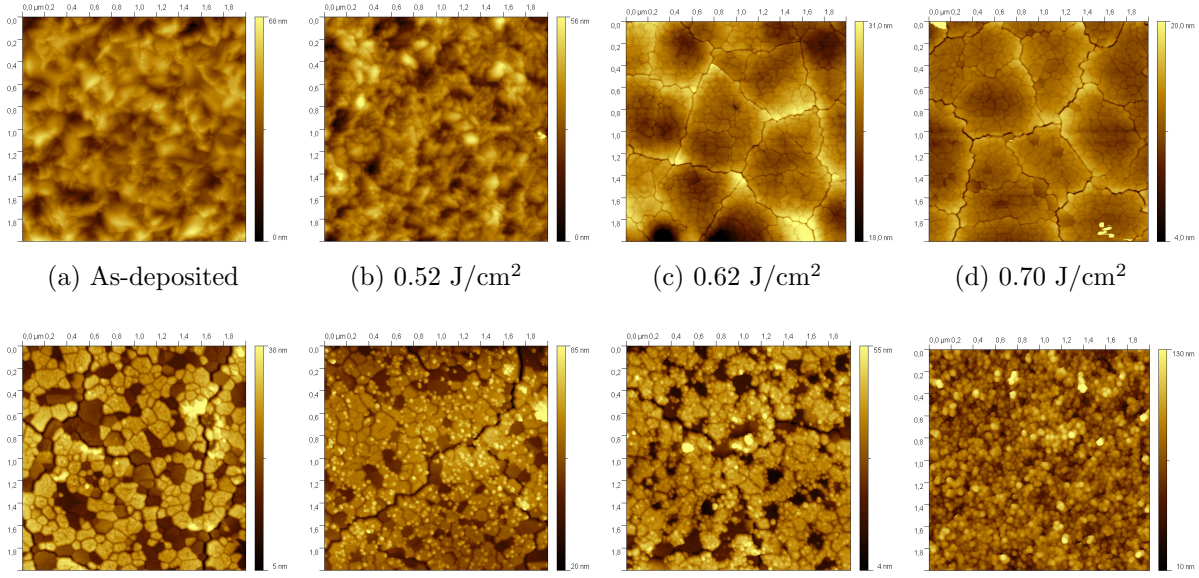

(a) As-deposited (b) 0.52 J/cm^2 (c) 0.62 J/cm^2 (d) 0.70 J/cm^2

(e) 0.83 J/cm^2 (f) 0.91 J/cm^2 (g) 1.05 J/cm^2 (h) 1.54 J/cm^2

Figure 4.20: AFM images of surface of ZnO:Al thin film deposited at 0.01 Pa, after undergoing ELA at various fluences.

change in uniform strain inside the layer[2]. A decrease in 2θ position reveals an extension of the inter-reticular distance d_{002} from the diffracting atomic planes along the [002] orientation.

Crystallite size and strain along the [002] orientation can be obtained from the distribution of the scattered intensity in reciprocal space from Williamson-Hall plots. The crystallite size and strain along the [002] orientation reveal a slight increase of the grain size followed by a decrease as presented in Figure 4.22.

4.2.6.2 Raman spectroscopy studies

In the Raman spectra presented in Figure 4.23, E_2(high) and A_1-LO modes are observed, as well as some additional modes at 380 and 510 cm^{-1}. It was suggested that these additional modes are related to defect-induced ZnO modes, which are Raman-inactive within a perfect crystal. Upon doping-induced defect formation, the translation crystal symmetry can be broken, and Raman-inactive modes may become Raman-active.

The Raman spectra of this series of ZnO:Al thin films are dominated by the A_1-LO vibrations. This mode shifts from 571 cm^{-1} for the as-deposited thin film, to 577 cm^{-1} for a fluence of 0.70 J/cm^2 and then decreases to 564 cm^{-1}. From this apparent shift, we can conclude that, with increasing the fluence of the ELA up to 0.70 J/cm^2, the high wavenumber contribution increases compared to the low wavenumber contribution. This trend suggests an improvement of the crystallinity and/or a reduction in defects of the ZnO:Al films, followed by a degradation of the material at higher fluences.

[2]This strain is different from the strain estimated from the Williamson-Hall plots, which corresponds to the non-uniform strain, i.e. atoms deformed from ideal positions in a non-uniform way

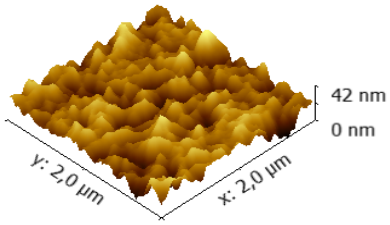

(a) As-deposited

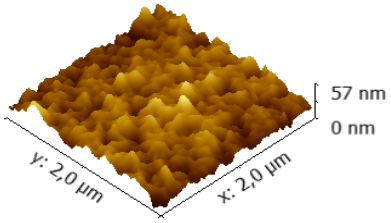

(b) 0.32 J/cm^2

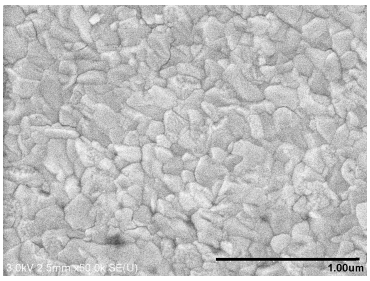

(c) 0.32 J/cm^2

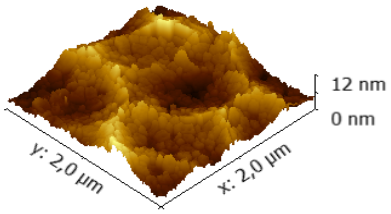

(d) 0.55 J/cm^2

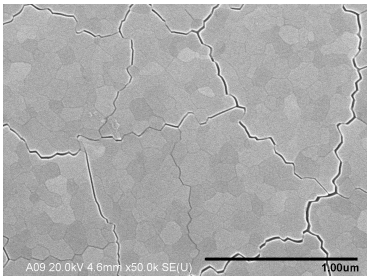

(e) 0.55 J/cm^2

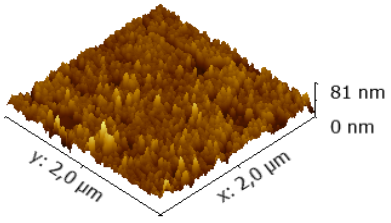

(f) 0.78 J/cm^2

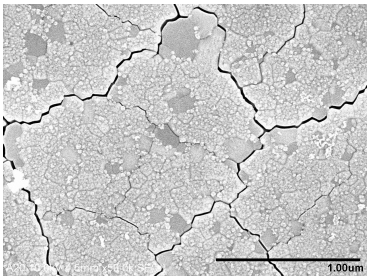

(g) 0.78 J/cm^2

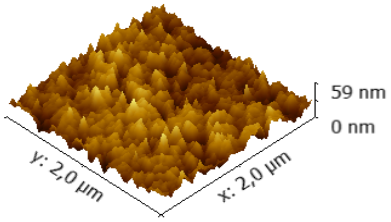

(h) 1.00 J/cm^2

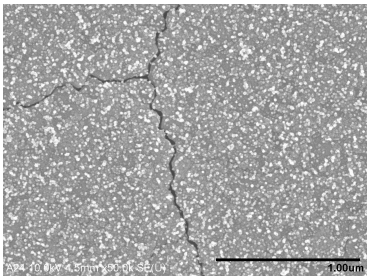

(i) 1.00 J/cm^2

Figure 4.21: AFM 3D topography and SEM images of surface of ZnO:Al thin film deposited at 0.12 Pa after undergoing ELA at various fluences.

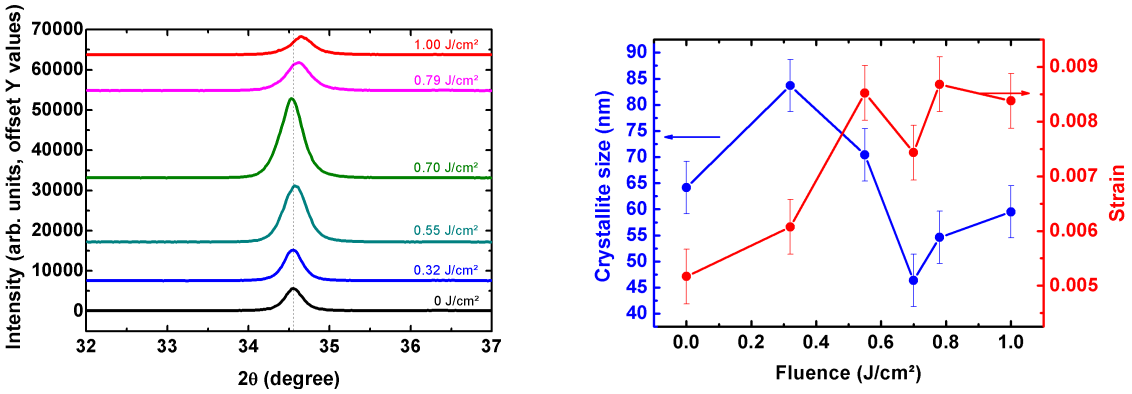

(a) (b)

Figure 4.22: XRD profiles (a), and crystallite size (blue line) and strain (red line) along the c-axis estimated from Williamson-Hall plots (b) for as-deposited and ELA ZnO:Al thin films at various fluences.

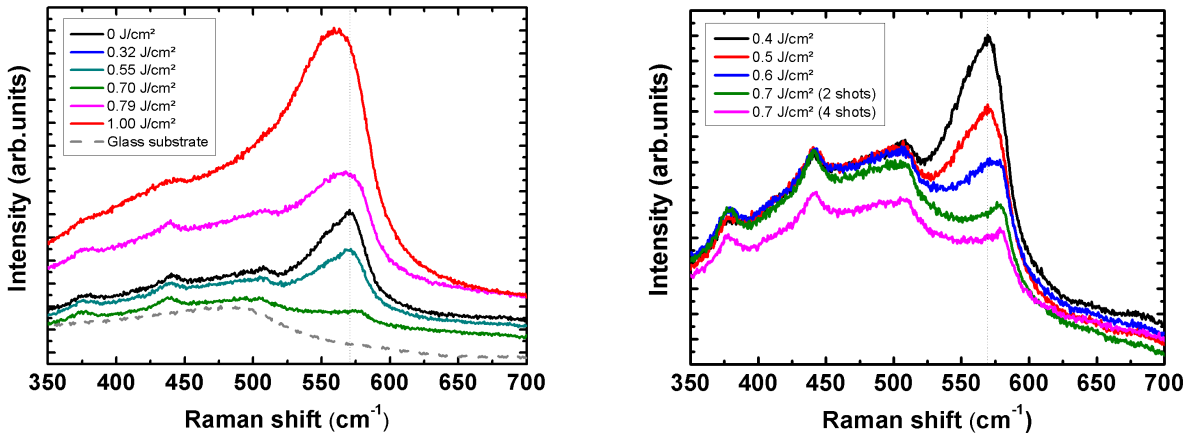

(a) (b)

Figure 4.23: Raman spectra of as-deposited and ELA ZnO:Al thin films for various fluences. (a) From 0 to 1 J/cm^2. (b) Detailed study from 0.4 to 0.7 J/cm^2.

With the increase of the fluence, the crystallinity along the [002] orientation is improved until an optimal fluence of 0.70 J/cm^2, and then is strongly degraded above this fluence. Exactly the same trend is observed in Raman spectroscopy. Moreover, this microstructural threshold value corresponds to an extreme morphological change as shown in Figure 4.21. A significant smoothing of the surface is observed, accompanied by the formation of domains separated by cracks. These domains are on the order of 1 - 2 μm in size, which is larger than the thickness of the film. These morphological and microstructural studies indicate that the sample undergoes a deep structural modification involving melting of the material and recrystallization. At the threshold fluence of 0.70 J/cm^2, the film has been fully melted, and random nucleation events, spaced sufficient far apart, lead to a lateral crystallization. The contraction during crystallization may lead to the cracks observed and to an amorphous boundary caused by quenched material at the domain edge. This lateral crystallization hypothesis is not in contradiction with the grain size and strain calculated from Williamson-Hall plots (Figure 4.22). Indeed, the Williamson-hall study

gives information along the [002] orientation, i.e. in the c-axis. The increase of the (002) intensity related to the slight increase and then decrease in the (002) crystallite size up to 0.70 J/cm^2 can be explained by the melting process. With the increase of the fluence, the thickness of melted material increases. The recrystallisation occurs in the c-axis, leading to an increase of the crystallite size along this orientation, and an improvement of the crystallinity of the material. From the threshold fluence of 0.70 J/cm^2, the material melts through its total thickness. From this fluence, a lateral recrystallization occurs, which leads to the formation of the large domains observed by AFM and SEM. The crystallite size along the [002] orientation is not affected by this lateral recrystallization. Above 0.70 J/cm^2, the top surface of some domains begins flaking off and shows the formation of nanospheres, in addition to the flaking behaviour, with a degradation of the material. The crystallite size in [002] orientation remains quite low.

4.2.7 Conclusion

Excimer laser annealing (ELA) of room-temperature sputtered ZnO:Al films leads to improved optical properties, and good electrical properties up to a laser fluence of 0.7 J/cm^2. Exposure at various laser fluences induces both a surface morphology change, as well as a crystalline rearrangement of the bulk, as shown through XRD, Raman spectroscopy and AFM/SEM imaging. Above a critical fluence, determined for these films to be around 0.7 J/cm^2 for the samples treated using a pulse length of 180 ns, and around 0.6 J/cm^2 for a pulse length of 130 ns, a dramatic change in the film morphology is observed, as the natural nanotexture of the surface is suppressed, a smoothing occurs, and large grains separated by cracks are formed. For a process of 180 ns pulses, with the increase of the fluence, the crystallinity along the [002] orientation is improved until the optimum at 0.7 J/cm^2, and then is strongly degraded above this threshold fluence.

4.3 Conclusion

In this chapter, two different post-deposition treatments have been investigated: a thermal annealing treatment, and a laser annealing treatment.

Thermal annealing treatments have been investigated under various annealing atmospheres (under vacuum, in 5% H_2 in N_2 atmosphere, or in pure N_2 atmosphere) and annealing temperatures (400, 450, or 500 °C). While annealing in pure N_2 leads to a strong degradation of the electrical properties, the vacuum and N_2/H_2 atmosphere increases in a significant way the Hall mobility. Thanks to a metallic conduction, the increase of the resistivity is higher for an annealing in N_2/H_2 compared to vacuum. The best opto-electronic properties are obtained for a N_2/H_2 annealing at 400 °C with 3.5 $\times 10^{-4}$ Ω.cm for a Hall mobility of 39 cm^2/V.s, and an optical transmittance of 81.2% between 400 and 1000 nm.

Laser annealing treatments have been realized on ZnO:Al thin films deposited at RT with an excimer laser, at various fluences. This treatment leads to extreme modifications of the surface morphology, with a slight improvement of the opto-electronic properties. The best opto-electronic properties are obtained at 0.25 J/cm^2, with 6.0×10^{-4} Ω.cm for a Hall mobility of 34 cm^2/V.s, and an optical transmittance of 79.8% between 400 and

1000 nm. These properties are highly satisfying taking into account that the main interest of this process is the surface morphology changes, which can induce a higher light trapping after wet etching, as discussed in the next chapter.

Bibliography

[1] M. Addonizio, A. Antonaia, and G. Cantele. Transport mechanisms of RF sputtered Al-doped ZnO films by H2 process gas dilution. *Thin Solid Films*, 349:93–99, 1999. (cited pages 19, 20, 100 et 112)

[2] M. Berginski, J. Hüpkes, W. Reetz, B. Rech, and M. Wuttig. Recent development on surface-textured ZnO:Al films prepared by sputtering for thin-film solar cell application. *Thin Solid Films*, 516(17):5836–5841, July 2008. (cited pages 112 et 148)

[3] M. Bertolotti, A. Ferrari, A. Jaskow, A. Palma, and E. Verona. Laser annealing of ZnO thin films. *Journal of Applied Physics*, 56(10):2943, Nov. 1984. (cited page 133)

[4] G. Bhaumik, A. Nath, and S. Basu. Laser annealing of zinc oxide thin film deposited by spray-CVD. *Materials Science and Engineering: B*, 52(1):25–31, Mar. 1998. (cited page 133)

[5] J. F. Chang, W. C. Lin, and M. H. Hon. Effects of post-annealing on the structure and properties of Al-doped zinc oxide films. *Applied Surface Science*, 183:18–25, 2001. (cited page 110)

[6] R. Cuscó, E. Alarcón-Lladó, J. Ibáñez, L. Artús, J. Jiménez, B. Wang, and M. Callahan. Temperature dependence of Raman scattering in ZnO. *Physical Review B*, 75(16), Apr. 2007. (cited pages 43 et 130)

[7] C. David, T. Girardeau, F. Paumier, D. Eyidi, B. Lacroix, N. Papathanasiou, B. P. Tinkham, P. Guérin, and M. Marteau. Microstructural and conductivity changes induced by annealing of ZnO:B thin films deposited by chemical vapour deposition. *Journal of physics. Condensed matter*, 23(33):334209, Aug. 2011. (cited pages 42, 121 et 123)

[8] J. N. Duenow, T. a. Gessert, D. M. Wood, D. L. Young, and T. J. Coutts. Effects of hydrogen content in sputtering ambient on ZnO:Al electrical properties. *Journal of Non-Crystalline Solids*, 354(19-25):2787–2790, May 2008. (cited page 112)

[9] C. Guillén and J. Herrero. Structure, optical, and electrical properties of indium tin oxide thin films prepared by sputtering at room temperature and annealed in air or nitrogen. *Journal of Applied Physics*, 101(7):073514, 2007. (cited page 111)

[10] C. Guillén and J. Herrero. Optical, electrical and structural characteristics of Al:ZnO thin films with various thicknesses deposited by DC sputtering at room temperature and annealed in air or vacuum. *Vacuum*, 84(7):924–929, Mar. 2010. (cited pages 24, 92, 111 et 114)

[11] J.-J. Kim, J.-Y. Bak, J.-H. Lee, H. S. Kim, N.-W. Jang, Y. Yun, and W.-J. Lee. Characteristics of laser-annealed ZnO thin film transistors. *Thin Solid Films*, 518(11):3022–3025, Mar. 2010. (cited page 134)

[12] K. Kim, S. Kim, and S. Y. Lee. Effect of excimer laser annealing on the properties of ZnO thin film prepared by sol-gel method. *Current Applied Physics*, 12(2):585–588, Mar. 2012. (cited page 133)

[13] S. H. Lee, T. S. Lee, K. S. Lee, B. Cheong, Y. D. Kim, and W. M. Kim. Characteristics of hydrogen co-doped ZnO:Al thin films. *Journal of Physics D: Applied Physics*, 41(9):095303, May 2008. (cited pages 17 et 112)

[14] C. Lennon, R. B. Tapia, R. Kodama, Y. Chang, S. Sivananthan, and M. Deshpande. Effects of Annealing in a Partially Reducing Atmosphere on Sputtered Al-Doped ZnO Thin Films. *Journal of Electronic Materials*, 38(8):1568–1573, Mar. 2009. (cited page 111)

[15] M. Li, W. Anderson, N. Chokshi, R. L. DeLeon, and G. Tompa. Laser annealing of laser assisted molecular beam deposited ZnO thin films with application to metal-semiconductor-metal photodetectors. *Journal of Applied Physics*, 100(5):053106, Sept. 2006. (cited page 133)

[16] H. Makino, N. Yamamoto, A. Miyake, T. Yamada, Y. Hirashima, H. Iwaoka, T. Itoh, H. Hokari, H. Aoki, and T. Yamamoto. Influence of thermal annealing on electrical and optical properties of Ga-doped ZnO thin films. *Thin Solid Films*, 518(5):1386–1389, Dec. 2009. (cited page 111)

[17] N. Mehan, V. Gupta, K. Sreenivas, and A. Mansingh. Effect of annealing on refractive indices of radio-frequency magnetron sputtered waveguiding zinc oxide films on glass. *Journal of Applied Physics*, 96(6):3134, 2004. (cited page 110)

[18] T. Minami, H. Nanto, S. Shooji, and S. Takata. The stability of zinc oxide transparent electrodes fabricated by R.F. magnetron sputtering. *Thin Solid Films*, 111(2):167–174, Jan. 1984. (cited page 110)

[19] S. Myong, J. Steinhauser, R. Schluchter, S. Faÿ, E. Vallatsauvain, A. Shah, C. Ballif, and A. Rufenacht. Temperature dependence of the conductivity in large-grained boron-doped ZnO films. *Solar Energy Materials and Solar Cells*, 91(14):1269–1274, Sept. 2007. (cited page 119)

[20] T. Nagase, T. Ooie, H. Kominami, Y. Nakanishi, and N. Mizutani. Green cathodoluminescence properties of zinc oxide films prepared by excimer laser irradiation of a sol-gel-derived precursor. *Japanese journal of applied physics*, 42(3):1179–1184, 2003. (cited page 133)

[21] T. Nagase, T. Ooie, Y. Makita, S. Kasaishi, M. Nakatsuka, and N. Mizutani. Morphology, Structure and Photoluminescence Properties of Zinc Oxide Films Prepared by Excimer Laser Irradiation of Sol–Gel-Derived Precursors. *Japanese Journal of Applied Physics*, 40(Part 1, No. 11):6296–6303, Nov. 2001. (cited page 133)

[22] T. Nagase, T. Ooie, and J. Sakakibara. A novel approach to prepare zinc oxide films: excimer laser irradiation of sol-gel derived precursor films. *Thin Solid Films*, 357(2):8, 1999. (cited page 133)

[23] B.-Y. Oh, M.-C. Jeong, D.-S. Kim, W. Lee, and J.-M. Myoung. Post-annealing of Al-doped ZnO films in hydrogen atmosphere. *Journal of Crystal Growth*, 281(2-4):475–480, Aug. 2005. (cited page 110)

[24] B.-Y. Oh, M.-C. Jeong, and J.-M. Myoung. Stabilization in electrical characteristics of hydrogen-annealed ZnO : Al films. *Applied Surface Science*, 253:7157–7161, 2007. (cited page 110)

[25] M.-S. Oh, D.-K. Hwang, J.-H. Lim, Y.-S. Choi, and S.-J. Park. Current-driven hydrogen incorporation in zinc oxide. *Applied Physics Letters*, 91(21):212102, 2007. (cited pages 17 et 112)

[26] I. Ozerov, M. Arab, V. Safarov, W. Marine, S. Giorgio, M. Sentis, and L. Nanai. Enhancement of exciton emission from ZnO nanocrystalline films by pulsed laser annealing. *Applied Surface Science*, 226(1-3):242–248, Mar. 2004. (cited page 133)

[27] Y. R. Park, J. Kim, and Y. S. Kim. Effect of hydrogen doping in ZnO thin films by pulsed DC magnetron sputtering. *Applied Surface Science*, 255(22):9010–9014, Aug. 2009. (cited page 112)

[28] F. Ruske, M. Roczen, K. Lee, M. Wimmer, S. Gall, J. Hüpkes, D. Hrunski, and B. Rech. Improved electrical transport in Al-doped zinc oxide by thermal treatment. *Journal of Applied Physics*, 107(1):013708, 2010. (cited page 112)

[29] S. Takata, T. Minami, and H. Nanto. The stability of aluminium-doped ZnO transparent electrodes fabricated by sputtering. *Thin Solid Films*, 135(2):183–187, Jan. 1986. (cited page 110)

[30] S. J. Tark, M. G. Kang, S. Park, J. H. Jang, J. C. Lee, W. M. Kim, J. S. Lee, and D. Kim. Development of surface-textured hydrogenated ZnO:Al thin-films for μc-Si solar cells. *Current Applied Physics*, 9(6):1318–1322, Nov. 2009. (cited page 112)

[31] W. Tsang, F. Wong, M. Fung, J. Chang, C. Lee, and S. Lee. Transparent conducting aluminum-doped zinc oxide thin film prepared by sol–gel process followed by laser irradiation treatment. *Thin Solid Films*, 517(2):891–895, Nov. 2008. (cited page 133)

[32] C. G. Van de Walle. Hydrogen as a cause of doping in zinc oxide. *Physical review letters*, 85(5):1012–5, July 2000. (cited pages 17 et 111)

[33] C. F. Windisch, G. J. Exarhos, C. Yao, and L.-Q. Wang. Raman study of the influence of hydrogen on defects in ZnO. *Journal of Applied Physics*, 101(12):123711, 2007. (cited page 110)

[34] R. Winfield, L. Koh, S. O'Brien, and G. M. Crean. Excimer laser processing of ZnO thin films prepared by the sol–gel process. *Applied Surface Science*, 254(4):855–858, Dec. 2007. (cited page 133)

[35] W. Yang, Z. Wu, Z. Liu, A. Pang, Y.-l. Tu, and Z. C. Feng. Room temperature deposition of Al-doped ZnO films on quartz substrates by radio-frequency magnetron sputtering and effects of thermal annealing. *Thin Solid Films*, 519:31–36, 2010. (cited page 111)

[36] T. Yen, M. Li, N. Chokshi, S. J. Kim, A. N. Cartwright, Y. Jeong, and W. A. Anderson. Analysis and Applications of ZnO Semiconductor Films Deposited by Laser and Sputtering Techniques. *MRS Proceedings*, 957(-1), Jan. 2006. (cited page 133)

[37] T. Yen, D. Strome, S. J. Kim, A. N. Cartwright, and W. A. Anderson. Annealing Studies on Zinc Oxide Thin Films Deposited by Magnetron Sputtering. *Journal of Electronic Materials*, 37(5):764–769, Dec. 2007. (cited page 134)

[38] B. Zhu, J. Wang, S. Zhu, J. Wu, R. Wu, D. Zeng, and C. Xie. Influence of hydrogen introduction on structure and properties of ZnO thin films during sputtering and post-annealing. *Thin Solid Films*, 519(11):3809–3815, Mar. 2011. (cited pages 17 et 111)

Chapter 5

Integration of ZnO:Al films in microcrystalline silicon solar cells

Contents

This chapter deals with the main results on the wet etching step realized on ZnO:Al thin films after deposition or post-deposition treatments. The influence of the deposition parameters, post-deposition parameters and etching time on the surface morphology, and opto-electronic properties after the etching step have been investigated. In our study, the chemical texturation follows the Jülich recipe, consisting of a dip in a 0.5% HCl solution [18–20]. In a second part, these films are used as a substrate in microcrystalline silicon solar cell characteristics, and their impacts on solar cells are studied.

5.1 Wet chemical etching step

5.1.1 Introduction

Because as-deposited films obtained by sputtering are quite flat, the etching step is a key point for the light confinement by the TCO layer in silicon solar cells. This technique for the development of a specific surface roughness for silicon thin film solar cells was first experimentally realized and published a decade ago by Kluth *et al.* [18–20]. They have studied the etching behaviour in 0.5% HCl solution of Al doped ZnO films prepared by RF magnetron sputtering depending on the sputtering parameters and have described the etching trends as a function of the compactness of the film by modifying the Thornton model initially used for sputtered metal growth. The influence of the deposition conditions on the etching properties of ZnO:Al thin films has been widely studied after these studies by other groups, such as Kim *et al.* for the influence of the working Ar gas pressure, substrate temperature and RF power [17], or Berginski *et al.* who have studied the influence of the amount of alumina in the target as well as the substrate temperature [3]. Specifically, the variation of the sputter pressure leads to films with significantly different etching behaviours in diluted acids [27, 37, 38].

The influence of post-deposition treatments has been similarly studied such as the effect of the vacuum annealing on the etching properties of ZnO:Al thin films [2, 32].

An important model has been developed by Hüpkes *et al.* to explain the etching behaviour of polycrystalline ZnO depending on the structural material properties and etching agent [11].

Some articles deal with the optimization of the surface roughness by other techniques, for example by two-step processes, or by dry etching. Moon *et al.* have prepared ZnO:Al films using a two-step sputtering involving the variation of oxygen pressure. The seed layers were deposited under various Ar to oxygen pressure ratios, and the bulk layers were prepared under pure Ar, to optimize the haze factor [25]. Highly surface-textured ZnO:Al films have been fabricated by Wan *et al.* at room temperature by a two-step magnetron sputtering process and using an oxygen-deficient ZnO target with small grain sizes [35]. Concerning the dry plasma etching, some groups work on Inductively Coupled Plasma (ICP) in Cl_2/Ar [12, 15], CH_4/H_2/Ar [12, 16, 33], and BCl_3/Cl_2/Ar [24, 36] or by ion RF-sputter etching [8, 9]. These results are encouraging but are not at the same maturity level than the wet etching process.

The haze factor is a key value to evaluate the wet chemical etching step and the resulting surface roughness. The haze factor has been improved by fabricating AZO films by

metal-organic chemical vapor deposition (MOCVD) by performing glass-substrate etching before film deposition [10]. Recently, Konagai *et al.* have developed ZnO films with high haze value using a glass substrate etching before film deposition [21]. An additional but fundamental information for the optimization of the light scattering properties of the films is the angle resolved and spectrally resolved scattering dependencies of transmitted light. This measurement has been the object of several works these last years [5,7].

Some groups have developed a method to both quantitatively and qualitatively describe the scattering characteristics from single-scan AFM data and to simulate the scattering dependencies of the light [22]. The group of Delft has also widely worked on the scattering properties, especially by the comparison of different surface morphologies obtained by random texture, one-dimensional periodic texture, or modulated surface texture achieved by combining 1D periodic grating or large random surface texture with additional finer random surface features [13].

5.1.2 Influence of the argon pressure and the substrate temperature

First of all, the etching rate estimated from the total thickness (bulk + roughness) by ellipsometry is studied as a function of the substrate temperature and argon pressure as presented in Figure 5.1[1]. Films deposited at low working pressure and high substrate temperature exhibit the lowest etching rate.

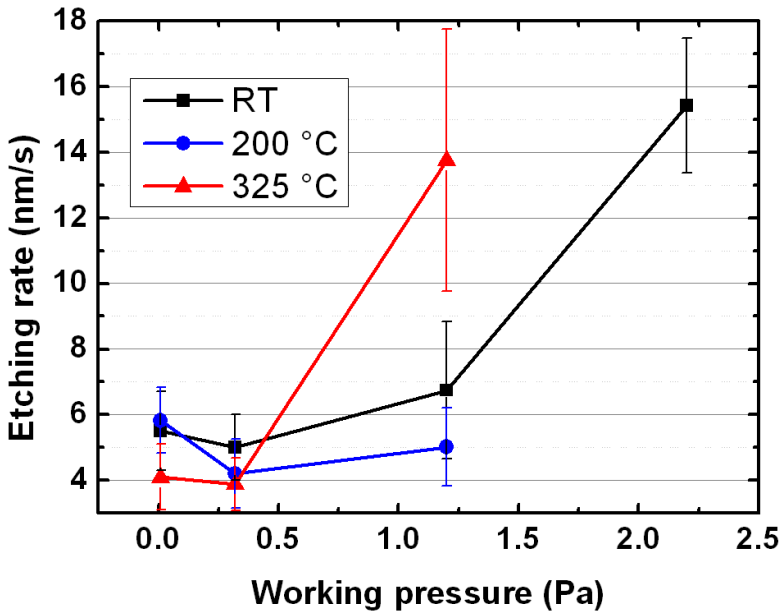

Figure 5.1: Etching rate of the wet chemical etching step as a function of the working pressure at various substrate temperatures.

In the same way, the AFM images of the ZnO:Al thin films presented in Figure 5.2 as a function of the working pressure and in Figure 5.3 as a function of the substrate

[1]Since the films develop surface roughnesses, some errors about the estimation of the total thickness by ellipsometry have to be taken into account.

temperature exhibit different surface morphologies after 40 s of chemical etching. At low pressure, the surface morphology obtained after etching consists of shallow craters of large opening angles (Figure 5.2d). The δ_{RMS} of this sample is evaluated at around 47 nm.

With the increase of the working pressure, the surface morphology changes from crater structure to hill structure, with a narrowing of the opening angles and an increase of the δ_{RMS} up to 142 nm (Figure 5.2e).

At the highest pressure, the layer is homogeneously etched, chemical etching has no impact on the surface morphology (δ_{RMS} around 17 nm) but only reduces the film thickness (Figure 5.2f).

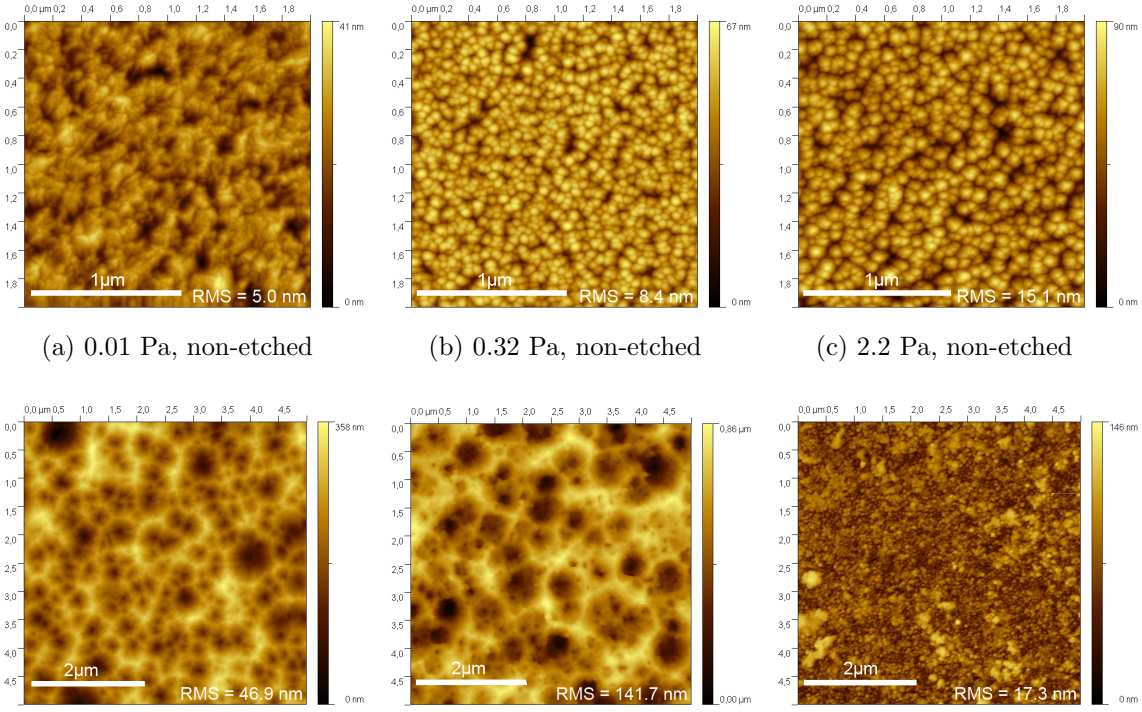

(a) 0.01 Pa, non-etched (b) 0.32 Pa, non-etched (c) 2.2 Pa, non-etched

(d) 0.01 Pa, etched 40 s (e) 0.32 Pa, etched 40 s (f) 2.2 Pa, etched 40 s

Figure 5.2: AFM images of the ZnO:Al films as function of the working pressure: 0.01 Pa before etching (a) and after (d), 0.32 Pa before etching (b) and after (e), and 2.2 Pa before etching (c) and after (f).

In the same way, for a thin film deposited at higher temperature, the structure varies from hill morphology with lower opening angle and a high δ_{RMS} (142 nm) to crater morphology with higher opening angle and a low δ_{RMS} (58 nm) (Figure 5.3).

These trends can be explained by the microstructural properties of ZnO:Al thin films. The growth of ZnO:Al sputtered films is oriented in the [002] direction, highly for low pressure deposited sample and weakly for thin film deposited at high pressure. The (002) plane is a zinc-terminated surface, which means that this plane, and thus the whole top surface of the sputtered film, exhibit poor etching properties. Only grain boundaries present a higher potential for etching. As a consequence, films presenting poorer microstructural properties, i.e. lower [002] orientation and/or lower compactness, are more easily etched. Moreover, the density of the film strongly influences its etching properties. Indeed, a high compactness leads to a lower physisorption of oxygen at the grain boundaries and to the

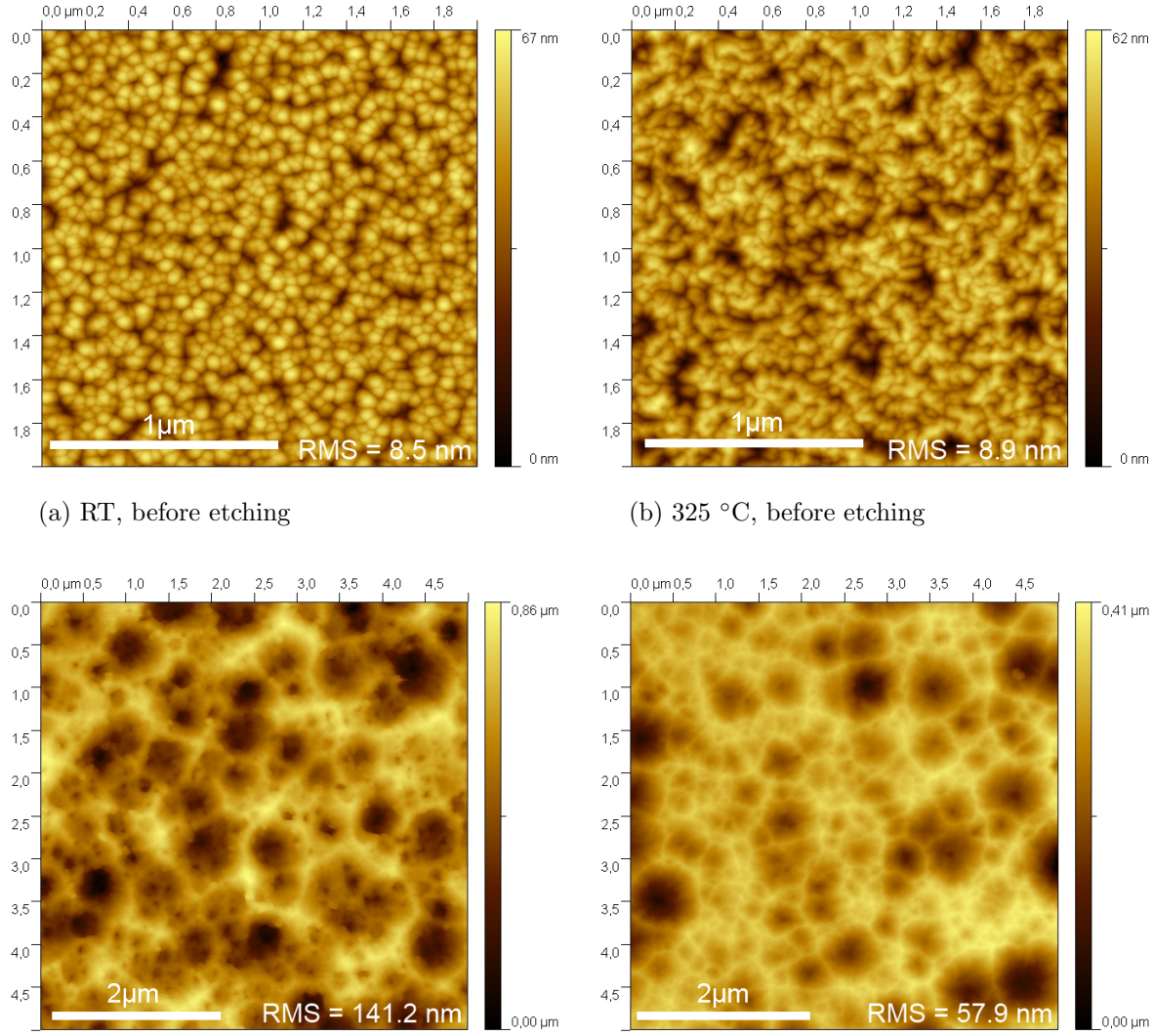

(a) RT, before etching

(b) 325 °C, before etching

(c) RT, etched 40 s

(d) 325 °C, etched 40 s

Figure 5.3: AFM images of the ZnO:Al films as function of the substrate temperature: RT before etching (a) and after (c), and 325 °C before etching (b) and after (d).

limitation of the penetration of the water-hydronium clusters inside the grain boundaries. The penetration of water-hydronium cluster can be sterically prohibited for dense films.

As a consequence, different surface morphologies after the wet chemical etching step raise from these dependencies. A strong [002] orientation and/or a very compact structure and a resulting robustness against etching limit the vertical etch. Only the horizontal etch is possible, which creates a crater morphology with large opening angles, such as for films deposited at low working pressure and high substrate temperature.

The etching properties of porous films and/or less oriented are not limited to the horizontal etch, which leads to an etching in depth. The surface after etching presents a hill structure, with smaller opening angles and higher δ_{RMS} values, such as for films deposited at low substrate temperature and intermediate working pressure.

Films with too poor microstructural properties, such as films deposited at higher pressures, present a high etch potential, with a high etching rate in both horizontal and vertical orientations. The global etching rate is higher, and the layer is homogeneously etched.

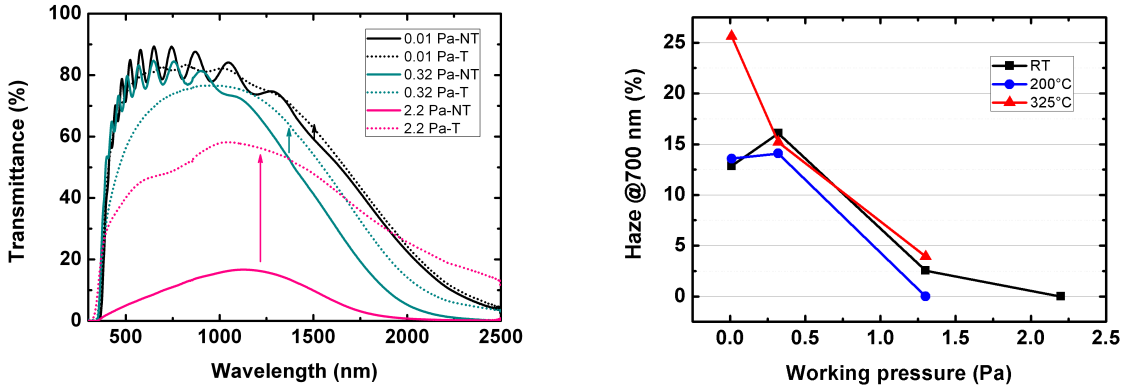

(a) (b)

Figure 5.4: Total transmittance of the ZnO:Al films deposited at various working pressures before (solid lines) and after etching (dashed lines) (a) and the resulting haze at 700 nm (b).

These observations have direct consequences on the optical properties as presented in Figure 5.4. For the same initial layer thickness (1 μm), films deposited at high working pressure, i.e. presenting lower crystallinity, exhibit a high increase of their transmittance upon wet etching, due to the high thickness loss, while crystalline layers present only a smoothing of the transmittance due to the high roughness of the surface. The same tendency is observed depending on the substrate temperature.

The haze factor estimated at 700 nm (Figure 5.4b) is linked to the surface morphology. The largest opening angles, such as for films deposited at low working pressure and high substrate temperature, lead to the highest haze.

The electrical properties are not presented here. They are directly linked to the thickness of the films as presented in section 3.

5.1.3 Influence of the RF sputtering power and initial thickness

These thin films have been deposited at room temperature, under a working pressure of 0.32 Pa. For thin films deposited at various RF powers and initial thicknesses, their microstructure and density influence in the same way their etching behaviour.

The initial thickness of ZnO:Al layer strongly influences its etching rate. As shown in Figure 5.5, the etching rate is high for very thin films and then slowly decreases and stabilizes until a quasi non-etch behaviour with the increase of the initial thickness. ZnO:Al polycrystalline films are usually formed through the nucleation of small crystals on the substrate surface. These defective films of very low thickness exhibit a very high etching rate. With the following growth steps, the films become continuous with the coalescence

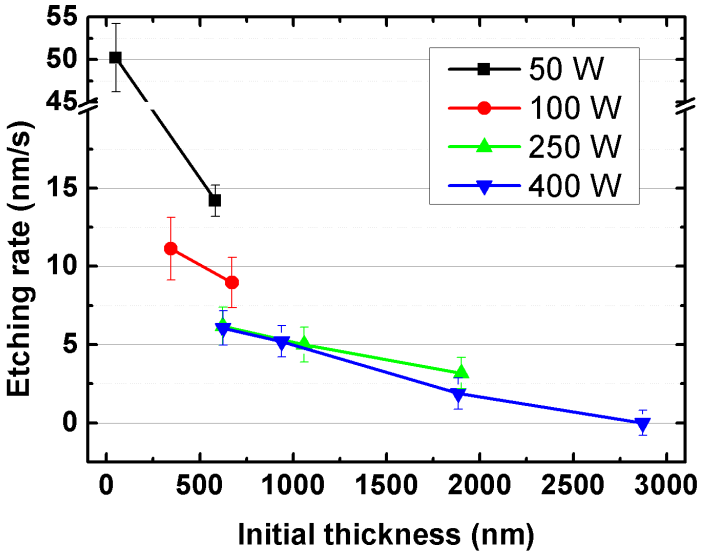

Figure 5.5: Etching rate of the wet chemical etching process as a function of the initial thickness of films deposited at various values of RF sputtering power.

of the isolated nuclei and the compactness increases with the thickening and the growth of the layer. The nucleation layer (between 150 and 300 nm depending on the sputtering conditions) presents a higher etching potential than the denser layer growing on it. The same tendency is observed through the AFM images presented in Figure 5.6. The poor crystallinity and porosity of thin layer lead to highly etched films while thick layers are weakly attacked.

The effect of the RF power has also been studied. As shown in Figure 5.5, the films deposited at low RF power seem to be etched faster. For the same initial thickness, around 600 nm, the etching rate is increasing with the decrease of the RF power. In the section 3.5, we have observed that thin films deposited at a RF power of 50 W are more defective compared to the other ones. The [002] orientation was the most pronounced at 100 W and then was slightly decreasing. The crystallinity of the deposited films cannot totally explain the observations concerning the etching behaviour, and the porosity of the films can only be estimated from the AFM images and does not show clear trends to explained the dependency of the etching rate with the RF power.

The haze factor depends strongly on the initial thickness and thus on the thickness variation during the wet chemical etching step as observed in Figure 5.7. For the same time of texturation, the haze value increases with the initial thickness, which means that a low thickness loss leads to a higher haze. This observation, which is not trivial, can be explained by the AFM images (Figure 5.6). At high initial thickness, the thickness loss is weak, and the surface morphology shows craters with large opening angles created by the texturation, leading to a δ_{RMS} value of 69 nm, the haze value is high. With the decrease of the RF power, the opening angles decrease and thus the haze factor, and the δ_{RMS} value increases to 142 nm. At low RF power, the layer is homogeneously etched and the δ_{RMS} decreases to 40 nm.

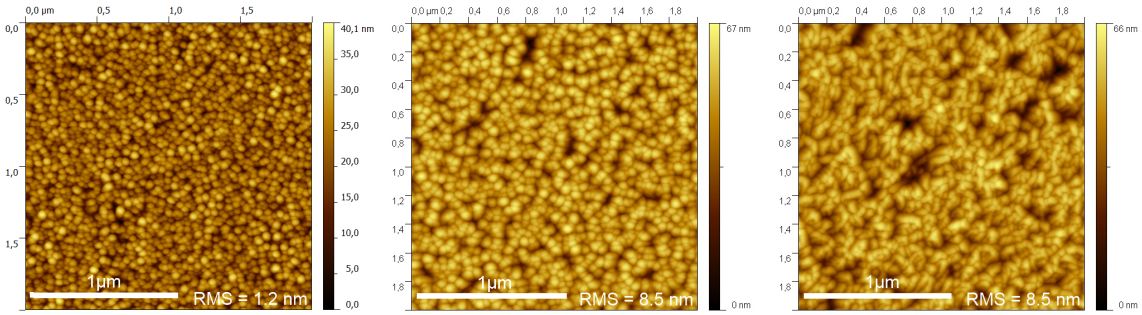

(a) 345 nm, non-etched (b) 1058 nm, non-etched (c) 1882 nm, non-etched

(d) 122 nm, etched 20 s (e) 848 nm, etched 40 s (f) 1807 nm, etched 40 s

Figure 5.6: AFM images of the ZnO:Al films deposited at various initial thicknesses: from a low thickness before etching (a) and after (d), from an intermediate thickness before etching (b) and after (e), and from a high thickness before etching (c) and after (f).

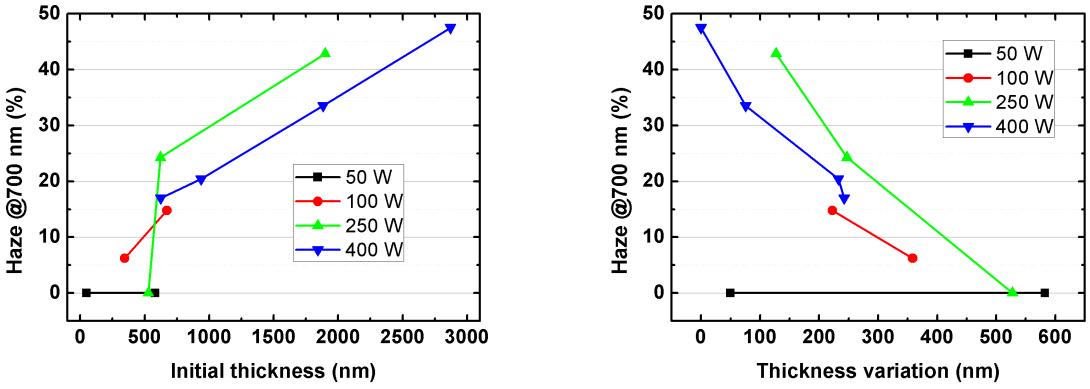

(a) (b)

Figure 5.7: Haze at 700 nm upon etching in HCl for 40 s of the ZnO:Al films deposited at various sputtering powers as a function of the initial thickness (a) and the thickness variation (b).

This increase of the haze factor with the increase of the initial thickness and thus with the decrease of the thickness loss is correlated with the angular resolved scattering measurement presented in Figure 5.8. With the increase of the initial thickness, the direct transmittance, i.e. the signal between 175 and 185°, decreases due to the higher absorption

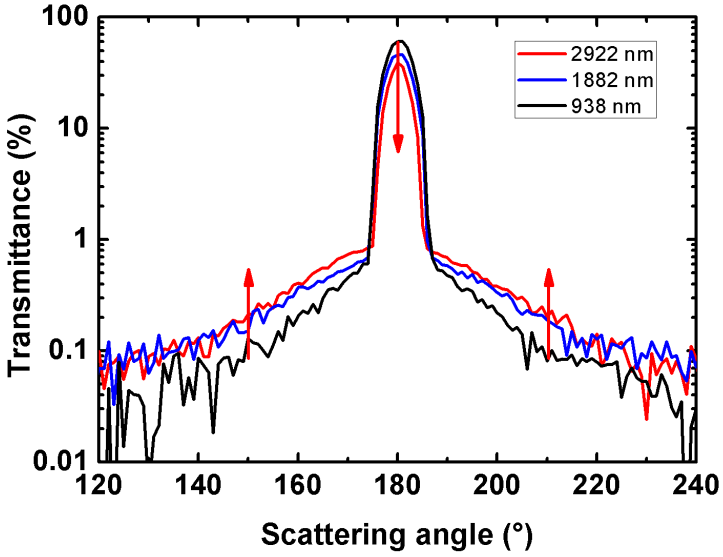

Figure 5.8: Angular resolved scattering at 700 nm of ZnO:Al thin films of various initial thicknesses.

of thicker layer, but the diffuse transmittance at lower and higher angles increases due to the increase of the opening angles of the craters.

5.1.4 Influence of the oxygen partial pressure

These layers have been deposited at room temperature, under a working pressure of 0.32 Pa and a RF power applied to the target of 250 W, for an initial thickness before etching around 1 μm.

The oxygen partial pressure has a strong influence on the etching behaviour of ZnO:Al thin films. As explained previously, the O-faces are etched very rapidly in acidic solution due to their negatively charged dangling bonds which act as attractive centres for hydronium ions H_3O^+. The increase in oxygen partial pressure leads to a faster etching rate as observed in Figure 5.9.

With the increase of oxygen in the gas phase during the sputtering, the etching shifts from a highly anisotropic behaviour with a high δ_{RMS} after etching (142 nm) and a weak thickness loss (210 nm) without oxygen in the gas phase, to a homogeneous texturation with a low δ_{RMS} (22 nm) and a high thickness loss (437 nm) at 0.32% of oxygen partial pressure (Figure 5.10.

These trends are also observed on the total transmittance in Figure 5.11. As the texturation changes from vertical etching to horizontal etching, the haze factor at 700 nm decreases with the increase of oxygen partial pressure ratio.

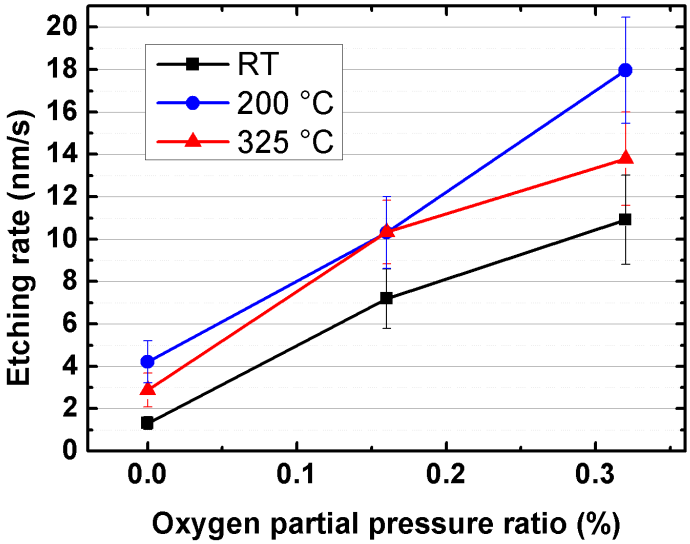

Figure 5.9: Etching rate of the wet chemical etching step as a function of the oxygen partial pressure ratio at various substrate temperatures.

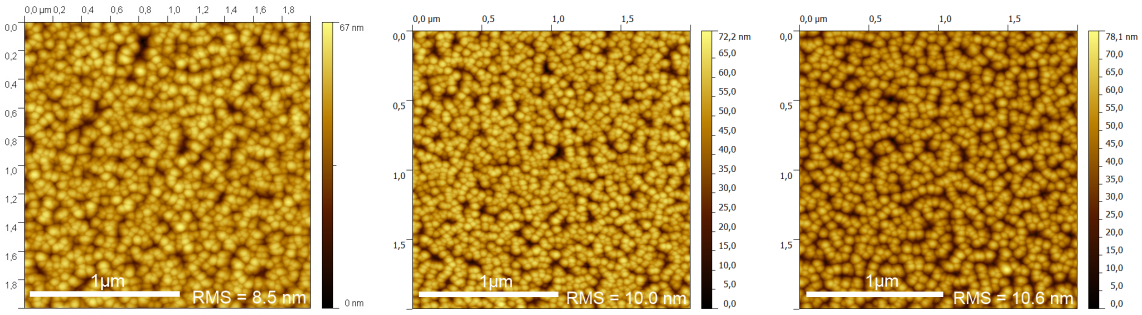

(a) $0\%O_2$, non-etch. (b) $0.16\%O_2$, non-etch. (c) $0.32\%O_2$, non-etch.

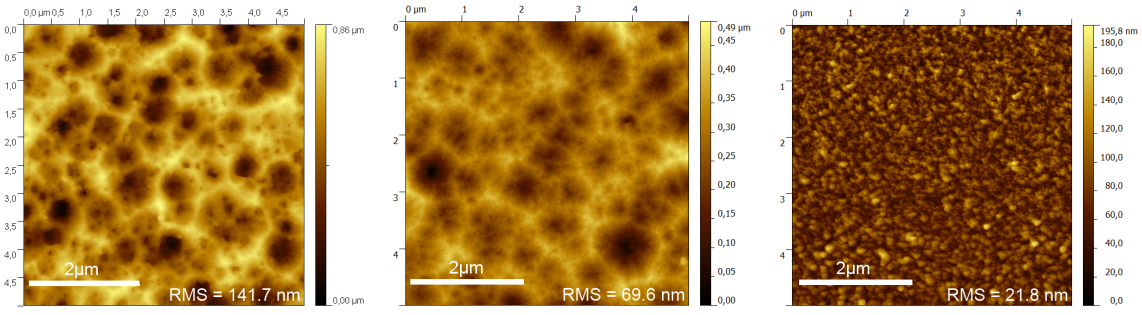

(d) $0\%O_2$, etched 40 s (e) $0.16\%O_2$, etched 40 s (f) $0.32\%O_2$, etched 40 s

Figure 5.10: AFM images of the ZnO:Al films deposited at various oxygen partial pressures: without oxygen in the gas phase before etching (a) and after (d), with 0.16% of O_2 before etching (b) and after (e), and with 0.32% of O_2 before etching (c) and after (f).

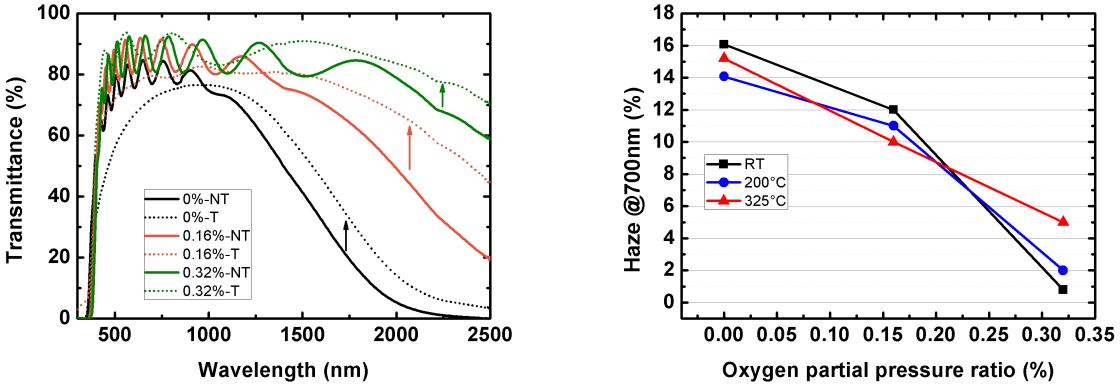

(a) (b)

Figure 5.11: Total transmittance of the ZnO:Al films deposited at various oxygen partial pressures non-textured (NT) and textured (T) (a) and the resulting haze at 700 nm.

5.1.5 Influence of the etching time

The influence of the etching time is studied in this part. The AFM images are presented in Figure 5.12, and reveal a crater-like morphology. With the increase of the etching time, the craters seem to widen and deepen. The thickness is difficult to estimate due to high roughness of the top surface but seems to decrease linearly with the etching time.

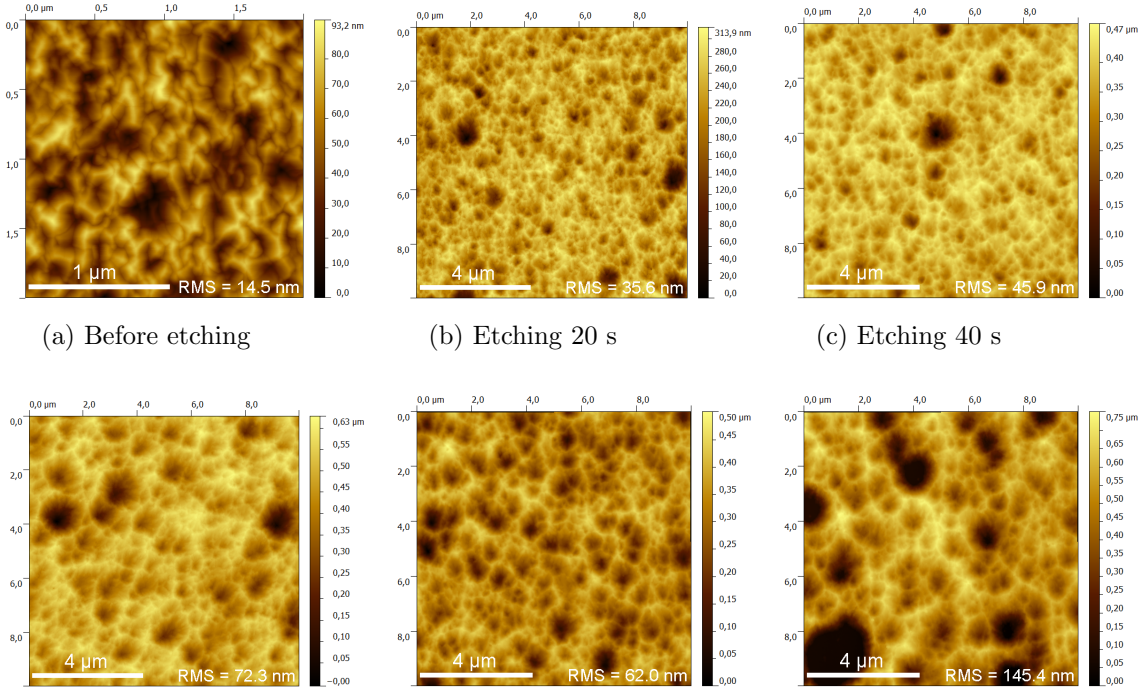

(a) Before etching (b) Etching 20 s (c) Etching 40 s

(d) Etching 60 s (e) Etching 80 s (f) Etching 120 s

Figure 5.12: AFM images of the ZnO:Al films deposited at various etching times.

5.1.6 Conclusion

The wet chemical etching step is the key process for the light trapping optimization of ZnO:Al thin films before their integration as the front electrode of a hydrogenated microcrystalline silicon solar cells. For chemical texturation, we have used the Jülich recipe, consisting of a dip in a 0.5% HCl solution [18–20].

The etching behaviour is highly influenced by the sputtering parameters, through the density, the microstructure, and/or the oxygen content of the film. These parameters modify the resulting surface morphology and the etching rate of the texturation process and, as a consequence, the optical and electrical properties of the ZnO:Al thin films. For their use in solar cells, the lowest thickness loss (for the lowest degradation of the electrical properties) and a surface morphology consisting of large craters (for the highest haze factor) is the optimum. In this way, the best ZnO:Al thin films are deposited at the highest possible temperature (325 °C) and at the optimum working pressure (between 0.12 and 0.32 Pa). The highest initial thickness is the best considering the texturation process. The RF sputtering power, the highest power provides the highest haze factor and the lowest thickness variation for the same initial thickness. Even a slight incorporation of oxygen in the gas phase induces an important increase of the etching rate and a decrease of the δ_{RMS} of the etched films. Finally the etching time increases the δ_{RMS} and the haze factor but also leads to an increase of the resistivity. This parameter needs to be optimized depending of the initial film, in terms of solar cells applications, and will be deeper studied in the following part.

The microstructure, density, and/or oxygen content of the ZnO:Al films modify their chemical etching behaviour. First, the microstructure of the films, through the orientation of the grains at the top surface, reacts differently in acidic solution. A well-defined sputtered film (strongly [002] oriented, large crystallites, no crystalline defects) exhibits only (002) planes at the surface, i.e. Zn-terminated planes, which are not attacked in HCl solution. The grain boundaries or other kinds of microstructural defects are areas of higher etch potential. First, they provide a possible access path for hydronium ions to O-terminated planes. Moreover, oxygen (from an eventual external pollution), preferentially locates at these defective areas, resulting in an additional increase of the etch potential. An increase of oxygen in the gas phase during deposition leads to the same results. Finally, the compactness of the films allows or inhibits the penetration of the hydronium ions inside the film.

The wet chemical etching process follows the same rules on annealed ZnO:Al thin films, by a thermal treatment or by a laser annealing process, and will be detailed in the following part.

5.2 Integration in μc-Si:H solar cells

The cells consist of p-μcSi:H/i-μcSi:H/n-aSi:H with back contacts ITO/Ag. The recipe of the silicon layer deposition has been optimized in parallel of the different batches of microcrystalline on in-house ZnO:Al in order to have the best solar cells and to increase the accuracy of the results. In this way, it is difficult to compare the whole absolute values

of the solar cell characteristics, but only batch by batch. A reference ZnO:Al sample has been added to each run in order to have a global view of the silicon deposition and to check the reproducibility of the deposition. However, in the following part, only the solar cells realized in the same batch (3 ZnO:Al in-house + 1 reference sample) are compared.

5.2.1 Introduction

In superstrate configuration, the requirements for the TCO layer are high transparency, high conductivity and an optimized surface roughness to create light trapping inside the absorber layers. The surface morphology for light confinement results in an enhancement of the cell absorption for long wavelengths and thus an increase in short-circuit current density.

For microcrystalline silicon solar cells, different approaches to improve the generated current have been studied [1]. The ways to realize efficient light trapping schemes by using textured TCOs as light scattering, highly conductive and transparent front contact in silicon pin solar cells have been widely studied, in particular by the Jülich group [26, 28–30, 34]. Stability and damp heat test issues have been studied for thin film silicon solar cells [4].

A strong effort has been done on modelling solar cell characteristics. The effect of surface roughness of ZnO:Al films on the light scattering in the a-Si:H solar cells has been investigated by optical modelling [23]. Mathematical model relates the surface morphology of randomly surface-textured thin films with the intensity distribution of scattered light [14, 31].

5.2.2 Effect of the sputtering parameters

5.2.2.1 Influence of the argon pressure and the substrate temperature

In a first series of solar cells, we investigate the effect of the substrate temperature (RT and 325 °C) and the working pressure (0.01 Pa and 0.32 Pa) of the ZnO:Al thin films on the characteristics of the solar cells. Hydrogenated microcrystalline silicon solar cells have been deposited on 1 μm thick ZnO:Al films sputtered at 250 W, without additional oxygen in the gas phase.

Table 5.1: Deposition parameters, properties of the ZnO:Al thin films, and resulting solar cell characteristics for ZnO:Al thin films deposited at various substrate temperatures and working pressures. The characteristics are measured after annealing of the solar cell at 150 °C, during 30 minutes. The ZnO:Al thin films were not textured for this series.

Deposition		Properties		SOLAR CELL CHARACTERISTICS			
T_{sub} (°C)	p (Pa)	ρ (mΩ.cm)	T (400-1000 nm) (%)	R_s (Ω)	J_{SC} (mA/cm^2)	FF (%)	η (%)
RT	0.01	0.83	80.7	4.71	-14.3	65.6	4.22
325	0.01	0.71	81.2	3.94	-15.9	65.4	4.54
RT	0.32	0.70	77.1	4.31	-14.7	65.5	4.20
325	0.32	0.58	74.1	4.17	-14.1	67.1	4.28

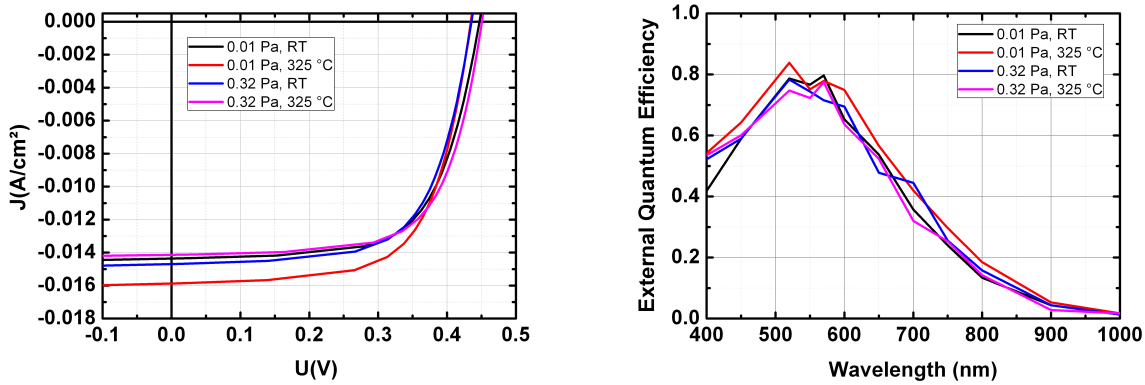

(a) J(V) (b) EQE

Figure 5.13: Illuminated current density voltage measurements and external quantum efficiency for μc-Si:H on ZnO:Al front contact deposited at various substrate temperatures and working pressures. The characteristics are measured after annealing of the solar cell at 150 °C, during 30 minutes.

For this first test, no chemical etching of the surface has been realized in order to compare only the TCO properties. The two ZnO:Al parameters which influence the solar cell properties are the resistivity ρ and the transparency T presented in Table 5.1. The J(V) characteristics are presented in Table 5.1[2]. As presented previously, an increase of the substrate temperature leads to an improvement of the ZnO:Al opto-electronic properties. The highest transparency is achieved at the lowest pressure, but the resistivity is the lowest at 0.32 Pa compared to 0.01 Pa. These trends are observed for these samples too (except for the transmittance of the ZnO:Al film deposited at 325 °C, 0.32 Pa). The improvement of the transparency leads to a higher short circuit current density, while the decrease of the resistivity results in a decrease of the series resistance.

The J(V) and EQE measurements show the improvement of the J_{SC} for the solar cells deposited on ZnO:Al films sputtered at 0.01 Pa and 325 °C as presented in Figure 5.13. The higher optical transparency leads to higher EQE.

5.2.2.2 Influence of the wet chemical etching step

This study deals with the effect of the etching time on the solar cell characteristics. The ZnO:Al films have an initial thickness of 2 μm, and have been deposited at 325 °C, with 0.06% of oxygen in the gas phase. They have been etched 60 seconds and 90 seconds.

Table 5.2 presents the results of the solar cell characteristics. The positive influence of the ZnO:Al surface structure on the J_{SC} is clearly observed on Figure 5.14. Two principal effects are observed depending on the wavelength. At short wavelengths (400 - 600 nm), the enhanced EQE for solar cells on rough ZnO:Al is due to an improved light coupling into the device thanks to an anti-reflection effect of the rough interface between front TCO and silicon. The reduced reflection is due to gradual refractive index matching at the interface. The second effect, at higher wavelengths (600 - 1000 nm), is light trapping

[2]The characteristics are measured after annealing of the solar cell at 150 °C, during 30 minutes.

Table 5.2: Etching parameters, properties of the ZnO:Al thin films and resulting solar cell characteristics for ZnO:Al thin films as-deposited and etched during various times. The characteristics are measured on as-deposited solar cells.

Etching time (s)	Properties ρ (mΩ.cm)	T (%)	δ_{RMS} (nm)	Haze 700 nm (%)	SOLAR CELL CHARACTERISTICS R_s (Ω)	J_{SC} (mA/cm^2)	V_{OC} (mV)	FF (%)	η (%)
0	0.74	79	8	0	4.23	-18.2	411	59.3	4.43
60	0.98	72	48	32	4.25	-21.9	402	55.0	4.85
90	1.40	68	92	43	4.57	-22.6	407	54.0	4.98

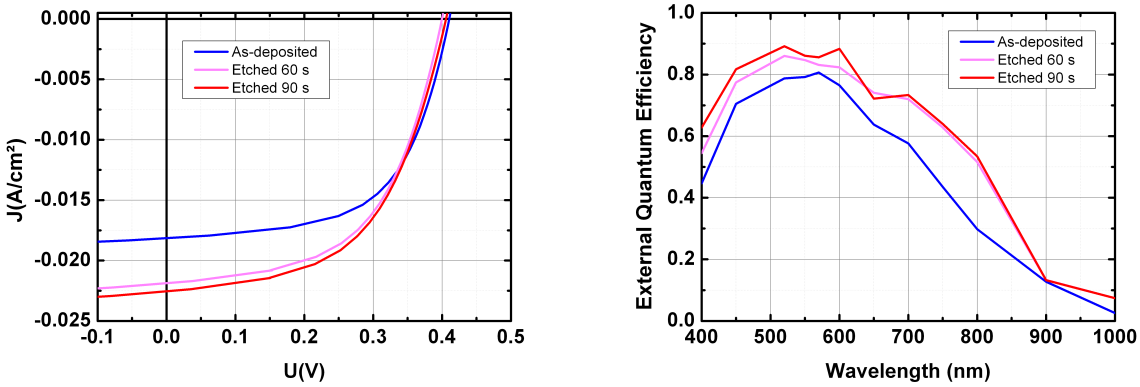

(a) J(V) (b) EQE

Figure 5.14: Illuminated current density voltage measurements and external quantum efficiency for μc-Si:H on ZnO:Al front contact as-deposited and etched during various times. The characteristics are measured on as-deposited solar cells.

into the active layers of the solar cell. The rough surface increases the light path within the silicon absorber, and hence increases the absorption and the current generation. The decrease of the total transmittance in the visible range is compensated by the high increase of the haze factor.

Another observation from the solar cell characteristics is the increase of the series resistance with the etching of the ZnO:Al thin film. A thinner ZnO:Al thin film has a higher resistivity and thus a higher series resistance, which decreases fill factor due to TCO series resistance losses.

Moreover, the wet chemical etching step has an influence on the open circuit voltage V_{OC}. The highest V_{OC} value is obtained for the ZnO:Al film with the overall smoothest surface structure, i.e. the lowest total surface area [6]. The V_{OC}, as well as the FF, is strongly influenced by the TCO/p interface. The increase of the TCO/p interface created by the roughness of the etched TCO layer leads to an increase of the recombination events at this interface.

5.2.2.3 Influence of the etching time

The wet chemical etching step increases the current generation and thus the solar cell efficiency. But the texturation time needs to be optimized. Here, ZnO:Al films have an initial thickness of 2 μm, and have been deposited at 325 °C, without oxygen inside the gas phase. They have been etched 40, 80 and 120 seconds.

Table 5.3: Etching parameters, properties of the ZnO:Al thin films and resulting solar cell characteristics for ZnO:Al thin films etched during various times. The characteristics are measured on as-deposited solar cells.

Etching time (s)	Properties ρ (mΩ.cm)	T (%)	δ_{RMS} (nm)	Haze 700 nm (%)	SOLAR CELL CHARACTERISTICS R_s (Ω)	J_{SC} (mA/cm^2)	V_{OC} (mV)	FF (%)	η (%)
40	0.70	67	182	68	3.42	-23.0	374	57.8	4.96
80	0.87	69	225	84	2.98	-23.4	399	61.4	5.73
120	1.35	72	199	90	3.09	-22.9	405	61.8	5.72

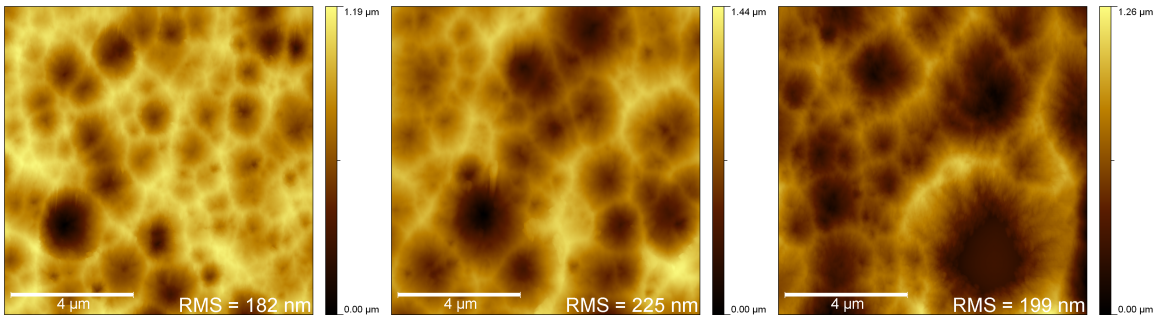

(a) Etched 40 s (b) Etched 80 s (c) Etched 120 s

Figure 5.15: AFM images of ZnO:Al thin films etched during various times.

The etching time increase leads to a widening and a deepening of the craters, clearly observed in Figure 5.15. The effect of the etching time increases the haze factor but limits the δ_{RMS} when the flat interface glass/TCO is reached as shown in Table 5.3, after an etching time of 120 s. From an etching time from 40 s to 80 s, the short circuit current is following the increase of the δ_{RMS}, but then decreases at 120 s. The V_{OC} and FF are surprisingly not affected by the decrease of the current generation. The V_{OC} and FF are influenced by the growth of silicon on the TCO surface, that is why it is difficult to make general correlations. The degradation of the efficiency is due to this decrease of the current generation.

5.2.3 Effect of the post-deposition treatments

5.2.3.1 Influence of the thermal annealing

The ZnO:Al films have been deposited in pure argon atmosphere, at 250 W, for a total thickness of 1 μm. The substrate temperature has been fixed at room temperature, the

working pressure at 0.12 Pa. The effects of post-deposition annealing atmospheres (under vacuum and in N_2/H_2) on the solar cell characteristics have been investigated. The annealing step has been realized at 450 °C, during 90 minutes.

Table 5.4: Post-deposition parameters, properties of the ZnO:Al thin films and resulting solar cells characteristics for ZnO:Al thin films as-deposited and annealed under various atmospheres. The characteristics are measured on as-deposited solar cells.

Post-deposition	Properties		SOLAR CELL CHARACTERISTICS			
Annealing atmosphere	ρ (mΩ.cm)	T (400-1000 nm) (%)	R_s (Ω)	J_{SC} (mA/cm^2)	FF (%)	η (%)
As-deposited	0.73	80.5	4.64	-16.42	59.6	3.83
Vacuum	0.60	83.7	4.48	-14.51	62.2	3.62
N_2/H_2	0.42	84.9	4.23	-16.06	61.4	3.88

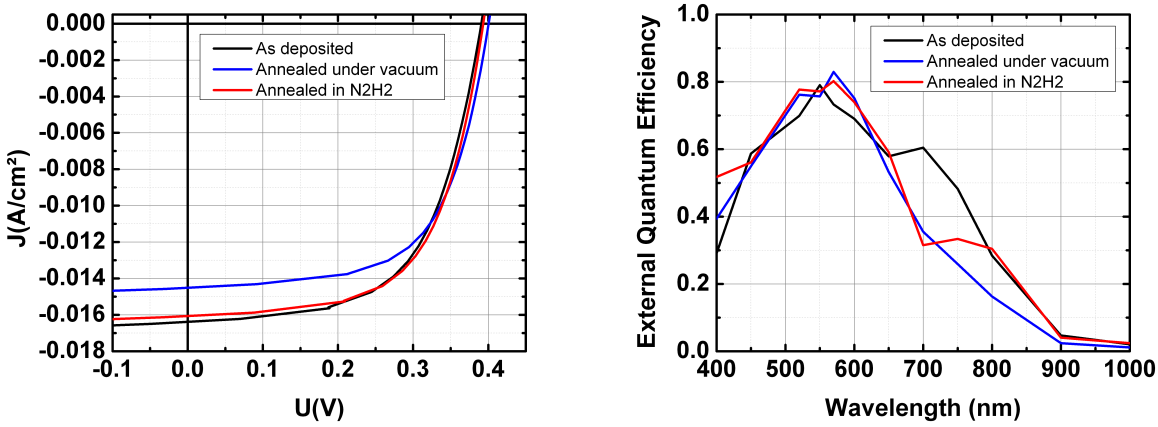

(a) J(V) (b) EQE

Figure 5.16: Illuminated current density voltage measurements and external quantum efficiency for µc-Si:H on ZnO:Al front contact as-deposited and annealed under various atmospheres. The characteristics are measured on as-deposited solar cells.

As previously studied, the annealing step under vacuum or in N_2/H_2 leads to an improvement of the electrical and optical properties of the ZnO:Al thin films. First, the improvement on the resistivity of the ZnO:Al thin films results in a decrease of the series resistance as observed in Table 5.4. The series resistance decreases from 4.64 Ω to 4.48 Ω under vacuum and 4.23 Ω in N_2/H_2. However, the second improvement on the optical transmittance does not lead to an increase of the J_{SC} as expected.

The illuminated current density voltage measurements and external quantum efficiency for μc-Si:H on ZnO:Al presented in Figure 5.16 give some indications for the decrease of the J_{SC} with the annealing step. First, this observation can be explained by the fact that the increase of the transmittance with the annealing step is mainly taking place at low

wavelengths, due an increase of the band gap energy. The J_{SC} is calculated from the EQE by convolution with the AM 1.5g solar spectrum and by integrating over the wavelength range. Much less solar radiance is incident at these shorter wavelengths, which can explain the inefficiency of the increase of the transmittance on the solar cell characteristics. Secondly, the EQE curves exhibit an irregular behaviour at higher wavelengths, which can be due to interference fringes from the flat ZnO:Al layer. These interferences explain the decrease of the J_{SC}. In this way, it is quite difficult to correlate ZnO:Al transmittance and J_{SC}.

5.2.3.2 Influence of the etching on thermal annealed ZnO:Al films

The films deposited and annealed under the same conditions as in the previous section are then etched 40 s.

Table 5.5: Post-deposition parameters, properties of the ZnO:Al thin films and resulting solar cell characteristics for ZnO:Al thin films without annealing and annealed under various atmospheres, and then etched during 40 s. The characteristics are measured on as-deposited solar cells.

Post-dep.	Properties				SOLAR CELL CHARACTERISTICS				
Ann. atm.	ρ (mΩ.cm)	T (%)	δ_{RMS} (nm)	Haze 700 nm (%)	R_s (Ω)	J_{SC} (mA/cm²)	V_{OC} (mV)	FF (%)	η (%)
No-ann.	0.92	77.9	100	28	3.69	-23.6	382	56.8	5.14
Vacuum	0.78	79.5	48	11	3.48	-23.1	375	57.7	5.01
N_2/H_2	0.69	79.6	45	6	3.34	-22.9	376	58.1	5.01

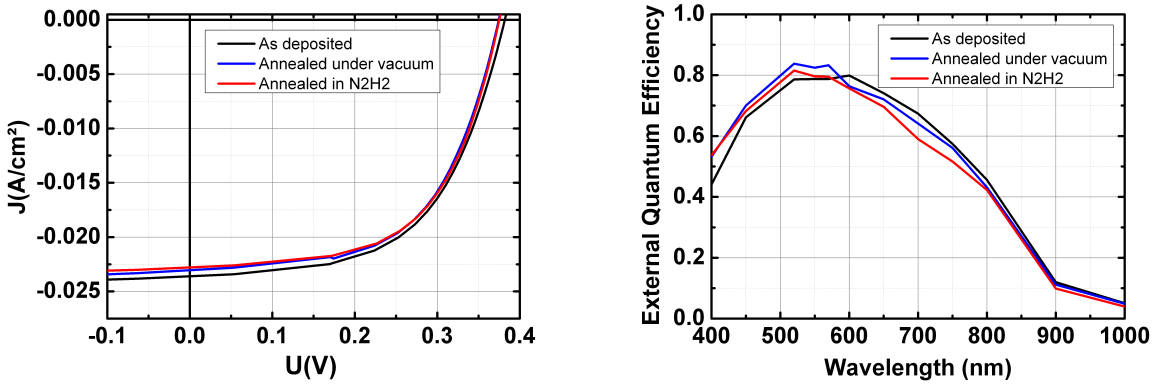

(a) (b)

Figure 5.17: Illuminated current density voltage measurements and external quantum efficiency for μc-Si:H on ZnO:Al front contact without annealing and annealed under various atmospheres, and then etched during 40 s. The characteristics are measured on as-deposited solar cells.

First, the same correlation between the resistivity and series resistance can be done as observed in Table 5.5. Concerning the J_{SC}, the solar cell on ZnO:Al non-annealed and

then etched 40 s exhibits the best short circuit current density. Figure 5.17 allows us to understand this tendency. As for the ZnO:Al front contacts before etching, at short wavelengths, the EQE is higher for films annealed due to the increase of the band gap energy. However, at higher wavelengths, the EQE is the best for non-annealed ZnO:Al films. The more efficient light trapping is the reason for the increase of the J_{SC}. The tendency can be understood thanks to the AFM images presented in Figure 5.18. The annealed front contact, no matter the atmosphere, exhibits a complete different surface morphology after etching than the non-annealed sample. The craters of annealed ZnO:Al layers are smaller, less wide and deep. The annealing step increases the compactness of the ZnO:Al film, and improves the crystallinity of the material. The consequence of this morphology is a lower δ_{RMS} and haze factor as observed in Figure 5.19, which limits the J_{SC} of the solar cells deposited on the top of these front electrodes.

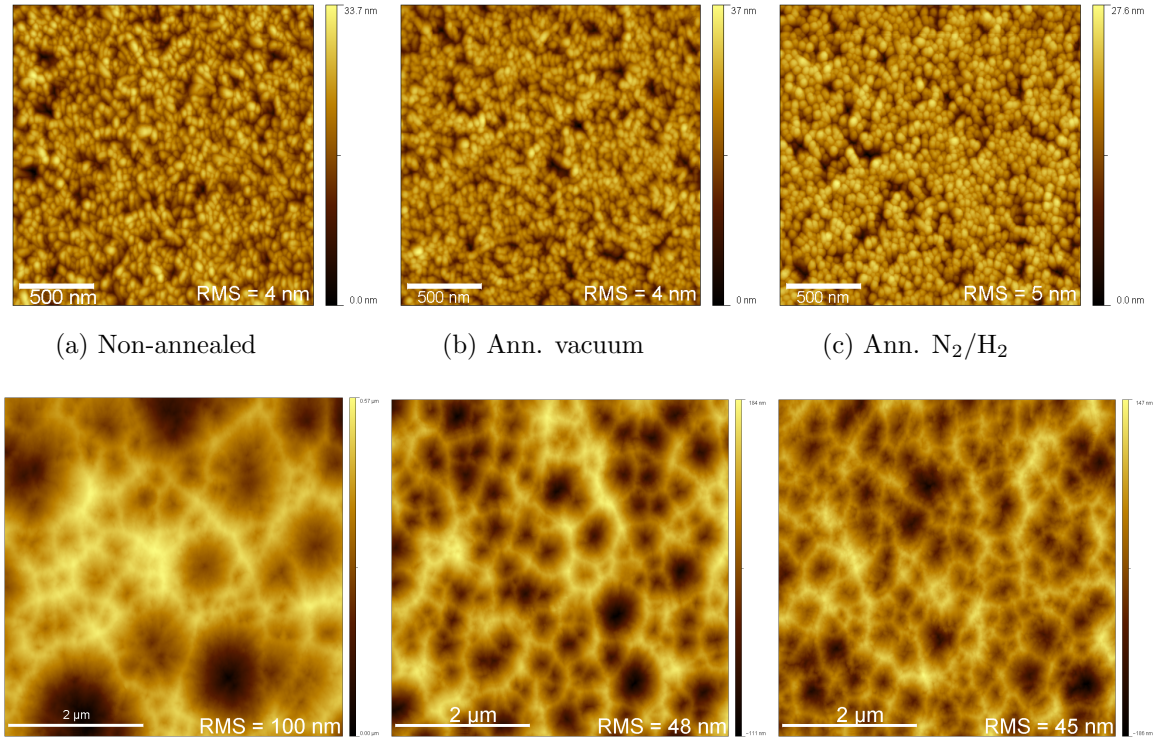

(a) Non-annealed (b) Ann. vacuum (c) Ann. N_2/H_2

(d) Non-annealed (e) Ann. vacuum (f) Ann. N_2/H_2

Figure 5.18: AFM images of ZnO:Al thin films without annealing and annealed under various atmospheres, and then etched during 40 s.

One way to improve the J_{SC} of solar cells deposited on annealed ZnO:Al thin films is to increase the texturation time in order to increase the size of the craters. The effect of the etching time is presented in Table 5.6, compared to the solar cells deposited on layers etched 40 s. A longer wet chemical etching step increases in the same way the J_{SC} for front electrodes with or without the annealing step, but the degradation of the series resistance is much more faster for ZnO:Al non-annealed than for annealed samples. These behaviours lead to an increase of the efficiency of the solar cells deposited on annealed front contact, while the solar cells deposited on non-annealed TCOs, etched 70 s, have a lower efficiency.

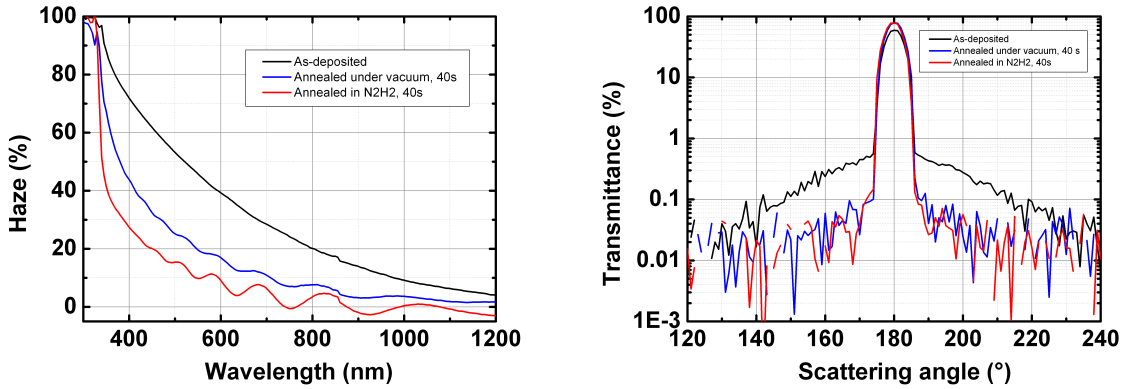

(a) (b)

Figure 5.19: Optical properties of the ZnO:Al after thermal annealing and etching 40 s: (a) Haze factor as a function of the wavelength, (b) Angular resolved scattering at 700 nm.

Table 5.6: Post-deposition parameters and evolution of the resulting solar cell characteristics for ZnO:Al thin films etched during 70 s compared to films etched during 40 s previously presented in Table 5.5.

Post-deposition Annealing atmosphere	SOLAR CELL CHARACTERISTICS R_s (%)	J_{SC} (%)	η (%)
Non-annealed	+52%	+4%	-4%
Vacuum	+10%	+3%	+18%
N_2/H_2	+12%	+5%	+17%

5.2.3.3 Influence of the laser annealing

In this study, the ZnO:Al films have been deposited in pure argon atmosphere, at 250 W, for a total thickness of 1 μm. The substrate temperature has been fixed at room temperature, and the working pressure at 0.12 Pa. The effects of the fluence of the post-deposition laser annealing (from 0.00 to 1.07 J/cm^2) on the solar cell characteristics have been investigated.

Figure 5.20 presents the EQE of the solar cells deposited on ZnO:Al front contacts after the laser annealing step, and the chemical texturation step. Two different behaviours are observed depending on the fluence applied to the ZnO:Al layers.

From 0.00 to 0.51 J/cm^2, there is first a slight decrease of the J_{SC} until 0.35 J/cm^2, and then a strong improvement of the light trapping, and thus an increase of the J_{SC} of the solar cell, as observed in Figure 5.21a.

In parallel, in this range of fluences, the series resistance remains quite stable as observed in Figure 5.21c due to the competition of the decrease of the resistivity of ZnO:Al thin films with the ELA process as previously observed, and the increase of the resistivity with the etching process. At low fluences, the structure of the films are not strongly

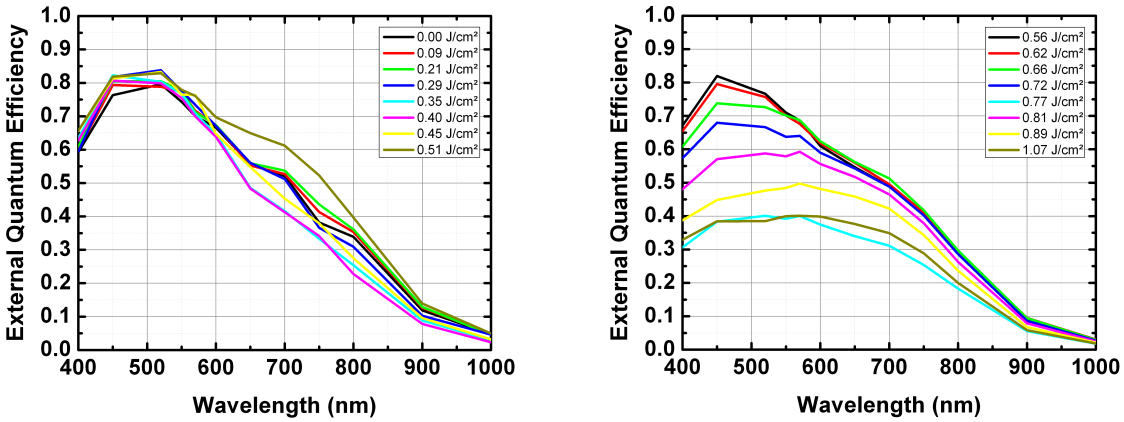

(a) From 0 to 0.51 J/cm^2

(b) From 0.56 to 1.07 J/cm^2

Figure 5.20: External quantum efficiency for µc-Si:H on ZnO:Al front contact laser annealed at various fluences: from 0 to 0.51 J/cm^2 (a) and from 0.56 to 1.07 J/cm^2 (b), and then etched 40 s. The characteristics are measured after annealing at 150 °C, during 30 minutes.

influenced by the ELA process. The compactness of the layer is more or less the same and the etching process is weak.

From 0.56 to 1.07 J/cm^2, the impressive change in morphology of the thin films with the ELA process leads to a high etch of the cracks and grain boundaries. The electrical properties of the TCO are strongly deteriorated, and thus the series resistance of the solar cells (Figure 5.21c). Especially, the changes in the morphology have dramatic consequences on the V_{OC}.

Due to the morphology, the J_{SC} remains quite high, at least up to 0.77 J/cm^2. The EQE spectra stay high at long wavelengths, but the dramatic morphologies induce a defective TCO/p interface, and thus a decrease of the EQE at lower wavelengths (Figure 5.20).

The chemical texturation process has been studied as a function of the laser fluence for a ZnO:Al film as shown in Figure 5.22. The effect of the fluence on the surface morphology has been previously studied, in section 4.2. These films undergo a chemical etching during 10 s.

For the first range of fluences, from 0.00 to 0.51 J/cm^2, the improvement of the crystallinity previously observed leads to a better definition of the craters after the texturation step. This surface morphology has as a consequence the increase of the haze factor, and thus an improvement of the J_{SC}.

For the second range of fluences, from 0.56 to 1.07 J/cm^2, the chemical etching leads to a complete different morphology. The cracks and the grain boundaries are etched preferentially. Indeed, sputtered ZnO:Al thin films are Zn-terminated polycrystalline films, with a (002) plane. Grain boundaries and cracks exhibit other planes which are accessible to the etching ions. It is clearly the case for ZnO:Al thin films after ELA process above

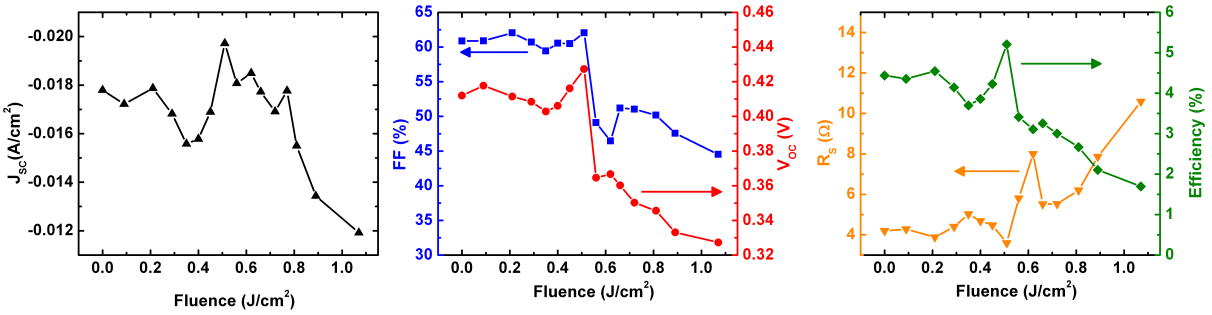

(a) J_{SC} (b) FF and V_{OC} (c) R_s and η

Figure 5.21: Solar cell characteristics from the illuminated current density voltage measurements for µc-Si:H on ZnO:Al front contact annealed at various fluences: (a) J_{SC}, (b) FF and V_{OC}, and (c) R_s and η. The characteristics are measured after annealing at 150 °C, during 30 minutes.

0.56 J/cm^2. The etching process is strongly accelerated at cracks with an important enlargement, but slightly at the grain boundaries. This difference can be explained by the accessibility of these preferentially etched planes. The dissolved HCl molecules form large water hydronium clusters which can easily penetrate cracks but not grain boundaries due to steric effet [11].

These behaviours depending on the fluence induce a global decrease of the efficiency of the solar cells with the increase of the fluence, except in the range from 0.35 to 0.56 J/cm^2. At these fluences, the slight improvement of the resistivity of the annealed ZnO:Al films matches with their excellent light trapping properties.

5.2.4 Conclusion

The integration of the TCO layer in microcrystalline silicon solar cells is the final step of the optimization of the films. The correlation between the ZnO:Al properties and the solar cell characteristics is not always obvious, but some strong dependencies are observed.

The series resistance is strongly dependent on the resistivity of the TCO layer. In this way, the sputtering parameters, as well as the post-deposition treatments, need to be optimized in order to have the lowest resistivity. A decrease of the thickness by the wet chemical etching process induces an increase of the series resistance compared to the solar cells deposited on non-textured TCOs.

In terms of short-circuit current density, the total transmittance in the active range of the absorber layers has a strong influence, as well as the roughness of the ZnO:Al thin film, which has to be optimized, with a surface consisting of large craters. As presented previously, the wet chemical etching step is strongly influenced by the sputtering parameters but also by the post-deposition treatments. The thermal annealing leads to a decrease of the series resistance of the solar cells, but also to small craters morphology after etching, compared to non-annealed samples, for the same time of texturation. A longer time of texturation is necessary to increase the haze factor and the craters size,

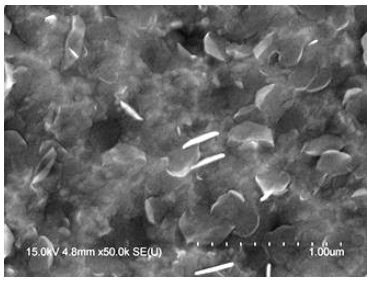

(a) 0.00 J/cm^2

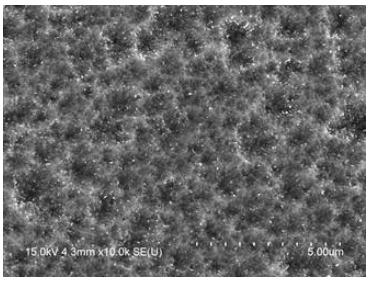

(b) 0.00 J/cm^2, etch.

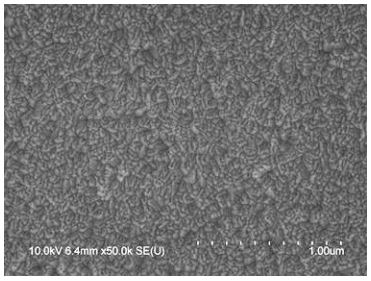

(c) 0.39 J/cm^2

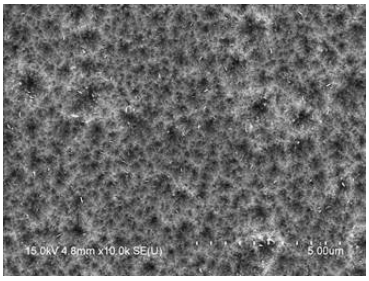

(d) 0.39 J/cm^2, etch.

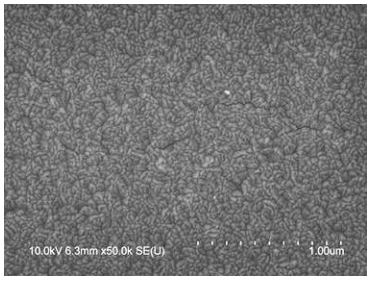

(e) 0.45 J/cm^2

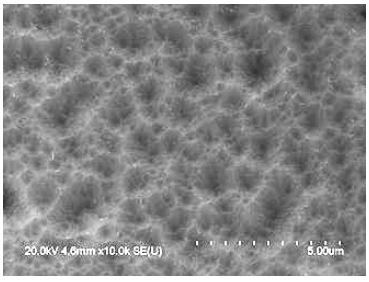

(f) 0.45 J/cm^2, etch.

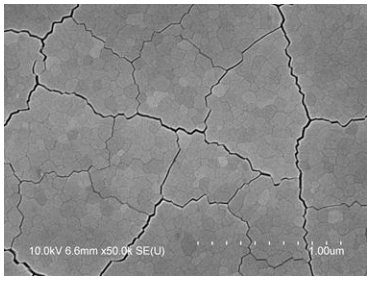

(g) 0.73 J/cm^2

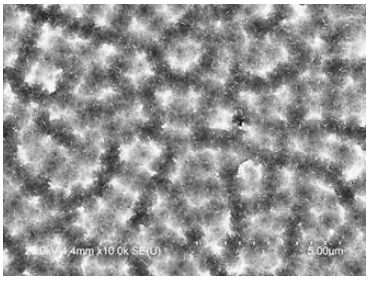

(h) 0.73 J/cm^2, etch.

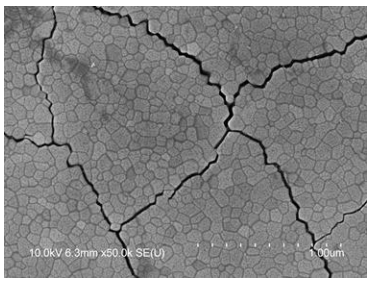

(i) 0.82 J/cm^2

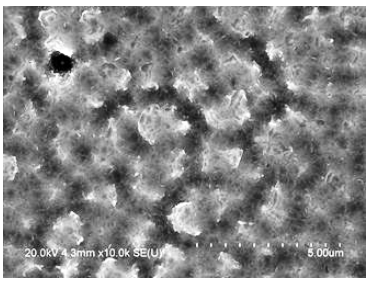

(j) 0.82 J/cm^2, etch.

Figure 5.22: SEM images of surface of ZnO:Al thin films annealed at various fluences (a, c, e, g and i) and then etched 10 s (b, d, f, h, and j).

and as a consequence, the solar cell efficiency.

The solar cells deposited on laser annealed ZnO:Al thin films exhibit different trends depending on the fluence. From 0.36 to 0.56 J/cm^2, the J_{SC} presents a strong increase, due to an improved light trapping after texturation. In parallel, the series resistance slightly decreases due the the annealing up to 0.51 J/cm^2, which induces a high improvement of the solar cell efficiency. From 0.56 J/cm^2, the dramatic change in surface morphology due to the laser annealing and worsening by the etching step induces a drop in V_{OC} due to the defective TCO/p interface.

The optimization of the deposition and post-deposition treatments is indispensable to improve the solar cell characteristics, through the decrease of the resistivity to minimize the series resistance, the increase of the total transmittance and the surface roughness and its resulting light trapping properties to increase the J_{SC}. The surface morphology influences the V_{OC}, and thus the FF, by changing the TCO/p interface, but their relationships are difficult to establish, except in the case of the laser annealing which provides an impressive change of surface morphology.

5.3 Conclusion

This chapter is dedicated to the chemically etched ZnO:Al thin films and their use in microcrystalline silicon solar cells.

The wet chemical etching process is the key step for the light confinement in the hydrogenated microcrystalline silicon solar cell. In a first part, the influence of the deposition conditions on the chemical texturation is studied. The compactness, the microstructure and the oxygen content of the film highly influenced the etching rate and resulting surface morphologies. The best compromise is the lowest thickness loss (in order to maintain rather good electrical properties) with surface morphology consisting of larger craters (for the highest haze factor). The ZnO:Al thin films deposited at the highest possible temperature (325 °C) and at the optimum working pressure (between 0.12 and 0.32 Pa) satisfy these conditions. The highest initial thickness leads to the best optical properties in terms of light trapping through the optimized surface morphology after texturation.

Finally, the ZnO:Al thin films are integrated in hydrogenated microcrystalline silicon solar cells. The ZnO:Al thin films deposited under optimized sputtering conditions exhibit the best solar cell characteristics, before and after the etching step. The influence of the surface morphology, and thus the light trapping properties of the ZnO:Al thin films, are clearly observed, especially on the short-circuit current density. The texturation time needs to be optimized depending on the deposition conditions.

The influence of the post-deposition processes is also studied. First, the thermal annealing has a beneficial influence on the series resistance through the improvement of the resistivity of the ZnO:Al thin film by the annealing process. However, the thermal annealing leads to an increase of the density of the layer. In this way, for the same etching time, non-annealed samples exhibit better surface morphology (larger craters) than the annealed ones. The time of texturation has to be increased to improve the short-circuit current density.

Laser annealed ZnO:Al thin films have been used as front electrodes in μc-Si:H, after the etching step. From the extreme surface modifications induced by the laser annealing, the wet chemical etching step emphasizes these morphologies, which further increases the light trapping effect, observed through the short-circuit current density.

Bibliography

[1] M. Berginski, J. Hüpkes, A. Gordijn, W. Reetz, T. Wätjen, B. Rech, and M. Wuttig. Experimental studies and limitations of the light trapping and optical losses in microcrystalline silicon solar cells. *Solar Energy Materials and Solar Cells*, 92(9):1037–1042, Sept. 2008. (cited page 159)

[2] M. Berginski, J. Hüpkes, W. Reetz, B. Rech, and M. Wuttig. Recent development on surface-textured ZnO:Al films prepared by sputtering for thin-film solar cell application. *Thin Solid Films*, 516(17):5836–5841, July 2008. (cited pages 112 et 148)

[3] M. Berginski, J. Hüpkes, M. Schulte, G. Schöpe, H. Stiebig, B. Rech, and M. Wuttig. The effect of front ZnO:Al surface texture and optical transparency on efficient light trapping in silicon thin-film solar cells. *Journal of Applied Physics*, 101(7):074903, 2007. (cited page 148)

[4] W. Beyer, J. Hüpkes, and H. Stiebig. Transparent conducting oxide films for thin film silicon photovoltaics. *Thin Solid Films*, 516(2-4):147–154, Dec. 2007. (cited page 159)

[5] W. Dewald, V. Sittinger, B. Szyszka, D. Wippler, J. Hüpkes, P. Obermeyer, F. Hamelmann, H. Stiebig, F. Säuberlich, D. Severin, S. Klein, M. Rhode, and U. Schmidt. Evaluation of textured TCOs for a-Si:H/mc-Si:H thin film solar cells by angular resolved light scattering measurements. In *26th European Photovoltaic Solar Energy Conference and Exhibition*, pages 2704–2708, 2011. (cited page 149)

[6] K. Ellmer and R. Mientus. Carrier transport in polycrystalline ITO and ZnO:Al II: The influence of grain barriers and boundaries. *Thin Solid Films*, 516(17):5829–5835, July 2008. (cited pages 100, 101 et 161)

[7] J. Farmer, G. Nichol, Y. Seto, N. Mcsporran, and L. Deslandes. Optical Property Measurements of High Haze TCO Coatings. In *26th European Photovoltaic Solar Energy Conference and Exhibition*, pages 2549–2553, 2011. (cited page 149)

[8] S. Flickyngerova, M. Netrvalova, L. Prusakova, I. Novotny, P. Sutta, and V. Tvarozek. Modification of AZO thin-film properties by annealing and ion etching. *Vacuum*, 84(1):215–217, Aug. 2009. (cited page 148)

[9] S. Flickyngerova, J. Skriniarova, M. Netrvalova, J. Kovac, I. Novotny, P. Sutta, and V. Tvarozek. Surface modification of doped ZnO thin films. *Applied Surface Science*, 256(18):5606–5609, July 2010. (cited page 148)

[10] A. Hongsingthong, T. Krajangsang, I. A. Yunaz, S. Miyajima, and M. Konagai. ZnO Films with Very High Haze Value for Use as Front Transparent Conductive Oxide Films in Thin-Film Silicon Solar Cells. *Applied Physics Express*, 3(5):051102, May 2010. (cited page 149)

[11] J. Hüpkes, J. I. Owen, S. E. Pust, and E. Bunte. Chemical etching of zinc oxide for thin-film silicon solar cells. *Chemphyschem : a European journal of chemical physics and physical chemistry*, 13(1):66–73, Jan. 2012. (cited pages v, 15, 16, 148 et 168)

[12] K. Ip, M. Overberg, K. Baik, R. Wilson, S. Kucheyev, J. Williams, C. Jagadish, F. Ren, Y. Heo, D. Norton, J. Zavada, and S. Pearton. ICP dry etching of ZnO and effects of hydrogen. *Solid-State Electronics*, 47(12):2289–2294, Dec. 2003. (cited page 148)

[13] O. Isabella, F. Moll, J. Krč, and M. Zeman. Modulated surface textures using zinc-oxide films for solar cells applications. *Physica Status Solidi (a)*, 207(3):642–646, Mar. 2010. (cited page 149)

[14] K. Jäger and M. Zeman. A scattering model for surface-textured thin films. *Applied Physics Letters*, 95(17):171108, 2009. (cited page 159)

[15] C. Jeong, S. Boo, H. Kim, and D. Chang. Investigation on the texture effect of RF magnetron-sputtered ZnO: Al thin films etched by using an ICP etching method for heterojunction Si solar cell applications. *Journal Of The*, 53(1):431–436, 2008. (cited page 148)

[16] S. Jeong, D.-G. Yoo, D. Kim, N.-E. Lee, and J.-H. Boo. Physical properties and etching characteristics of metal (Al, Ag, Li) doped ZnO films grown by RF magnetron sputtering. *Thin Solid Films*, 516(19):6598–6603, Aug. 2008. (cited page 148)

[17] Y. H. Kim, K. S. Lee, T. S. Lee, B.-k. Cheong, T.-Y. Seong, and W. M. Kim. Electrical, structural and etching characteristics of ZnO:Al films prepared by rf magnetron. *Current Applied Physics*, 10(2):S278–S281, Mar. 2010. (cited page 148)

[18] O. Kluth, A. Löffl, S. Wieder, C. Beneking, W. Appenzeller, L. Houben, B. Rech, H. Wagner, S. Hoffmann, R. Waser, J. A. Selvan, and H. Keppnet. Texture etched Al-doped ZnO: A new material for enhanced light trapping in thin film solar cells. In *Conference Record of the Twenty Sixth IEEE Photovoltaic Specialists Conference*, pages 715–718, 1997. (cited pages 148 et 158)

[19] O. Kluth, B. Rech, L. Houben, S. Wieder, G. Schöpe, C. Beneking, H. Wagner, A. Löffl, and H. Schock. Texture etched ZnO:Al coated glass substrates for silicon based thin film solar cells. *Thin Solid Films*, 351(1-2):247–253, Aug. 1999. (cited pages 37, 148 et 158)

[20] O. Kluth, G. Schöpe, J. Hüpkes, C. Agashe, J. Müller, and B. Rech. Modified Thornton model for magnetron sputtered zinc oxide: film structure and etching behaviour. *Thin Solid Films*, 442(1-2):80–85, Oct. 2003. (cited pages 148 et 158)

[21] M. Konagai, A. Hongsingthong, T. Krajangsang, P. Sichanugrist, and H. Fujioka. Improvement of Short-Circuit Current in Silicon-Based Thin Film Solar Cells Using ZnO Films with Very High Haze Value. In *26th European Photovoltaic Solar Energy Conference and Exhibition*, pages 2633–2636, 2011. (cited page 149)

[22] A. Krasnov. Light scattering by textured transparent electrodes for thin-film silicon solar cells. *Solar Energy Materials and Solar Cells*, 94(10):1648–1657, Oct. 2010. (cited page 149)

[23] J. Krč, M. Zeman, O. Kluth, F. Smole, and M. Topič. Effect of surface roughness of ZnO:Al films on light scattering in hydrogenated amorphous silicon solar cells. *Thin Solid Films*, 426(1-2):296–304, Feb. 2003. (cited page 159)

[24] H. J. Lee, B. S. Kwon, H. W. Kim, S. I. Kim, D.-G. Yoo, J.-H. Boo, and N.-E. Lee. Etching Characteristics of ZnO and Al-Doped ZnO in Inductively Coupled Cl 2 /CH 4 /H 2 /Ar and BCl 3 /CH 4 /H 2 /Ar Plasmas. *Japanese Journal of Applied Physics*, 47(8):6960–6964, Aug. 2008. (cited page 148)

[25] T. Moon, W. Yoon, K. S. Ji, S.-W. Ahn, S. Lee, M. Joo, H. Y. Shin, K. Park, and H.-M. Lee. Microstructure and Light-Scattering Properties of ZnO:Al Films Prepared Using a Two-Step Process through the Control of Oxygen Pressure. *Applied Physics Express*, 3(9):095801, Aug. 2010. (cited page 148)

[26] J. Müller, B. Rech, J. Springer, and M. Vanecek. TCO and light trapping in silicon thin film solar cells. *Solar Energy*, 77(6):917–930, Dec. 2004. (cited pages 37 et 159)

[27] J. Müller, G. Schöpe, O. Kluth, B. Rech, V. Sittinger, B. Szyszka, R. Geyer, P. Lechner, H. Schade, M. Ruske, G. Dittmar, and H.-P. Bochem. State-of-the-art mid-frequency sputtered ZnO films for thin film silicon solar cells and modules. *Thin Solid Films*, 442(1-2):158–162, Oct. 2003. (cited page 148)

[28] B. Rech, O. Kluth, T. Repmann, T. Roschek, J. Springer, F. Finger, H. Stiebig, and H. Wagner. New materials and deposition techniques for highly efficient silicon thin film solar cells. *Solar Energy Materials and Solar Cells*, 74:439–447, 2002. (cited page 159)

[29] B. Rech, T. Repmann, M. van den Donker, M. Berginski, T. Kilper, J. Hüpkes, S. Calnan, H. Stiebig, and S. Wieder. Challenges in microcrystalline silicon based solar cell technology. *Thin Solid Films*, 511-512:548–555, July 2006. (cited page 159)

[30] B. Rech, G. Schöpe, O. Kluth, T. Repmann, T. Roschek, J. Müller, J. Hüpkes, and H. Stiebig. Highly efficient silicon thin film solar cells with advanced light trapping. In *3rd World Conference on Photovoltaic Energy Conversion WCPEC-3*, page 1, 2003. (cited page 159)

[31] C. Rockstuhl, F. Lederer, K. Bittkau, and R. Carius. Light localization at randomly textured surfaces for solar-cell applications. *Applied Physics Letters*, 91(17):171104, 2007. (cited page 159)

[32] M. Schulte, S. Jorke, and C. Zahren. Analysis of the Scattering Properties of Textured TCO Structures for Thin Film Silicon Solar Cells. In *22nd European Photovoltaic Solar Energy Conference and Exhibition*, 2007. (cited page 148)

[33] M. Shin, M. Park, S. Jung, J. Boo, and N.-E. Lee. Effect of doping elements on ZnO etching characteristics with CH4/H2/Ar plasma. *Thin Solid Films*, 515(12):4950–4954, Apr. 2007. (cited page 148)

[34] J. Springer, B. Rech, W. Reetz, J. Müller, and M. Vanecek. Light trapping and optical losses in microcrystalline silicon pin solar cells deposited on surface-textured glass/ZnO substrates. *Solar Energy Materials and Solar Cells*, 85:1–11, Apr. 2004. (cited page 159)

[35] D. Wan, F. Huang, Y. Wang, X. Mou, and F. Xu. Highly Surface-Textured ZnO:Al Films Fabricated by Controlling the Nucleation and Growth Separately for Solar Cell Applications. *ACS Applied Materials & Interfaces*, 2(7):2147–2152, July 2010. (cited page 148)

[36] J.-C. Woo and C.-I. Kim. The Dry Etching Properties of ZnO Thin Film in Cl2/BCl3/Ar Plasma. *Transactions on Electrical and Electronic Materials*, 11(3):116–119, June 2010. (cited page 148)

[37] J. Yoo, S. K. Dhungel, M. Gowtham, J. Yi, J. Lee, S. Kim, K. Yoon, I. J. Park, and J. Song. Properties of Textured ZnO : Al Films Prepared by RF Magnetron Sputtering for Thin Film Solar Cells. *Journal of the Korean Physical Society*, 47(November):576–580, 2005. (cited page 148)

[38] J. Yoo, J. Lee, S. Kim, K. Yoon, I. Jun Park, S. K. Dhungel, B. Karunagaran, D. Mangalaraj, and J. Yi. The properties of surface textured ZnO:Al films for thin film solar cells. *Physica Status Solidi (c)*, 2(3):1228–1232, Feb. 2005. (cited page 148)

Conclusion and perspectives

Conclusion

The object of the present work was to provide a better understanding of the growth of sputtered ZnO:Al thin films and to optimize their optical, electrical and morphological properties for their integration as front electrodes in hydrogenated microcrystalline silicon thin film solar cells.

The first part of this work was dedicated to the optimization of ZnO:Al thin film. The layer properties strongly depend on the deposition parameters. The influence of the sputtering conditions was investigated, such as the argon pressure, the substrate temperature, the RF sputtering power, the oxygen partial pressure and the total thickness of the deposited film. The relationship between the sputtering parameters and the resulting thin film properties was studied and understood. In this way, an electrical and optical optimum was defined, in terms of the lowest resistivity and the highest transmittance in the visible range. The working pressure and substrate temperature are very important parameters for the growth of ZnO:Al by sputtering. The optimal pressure was found between 0.12 Pa and 0.32 Pa, where the highest texturation along the [002] orientation and the biggest vertical crystallite size were achieved. At lower pressures, the ZnO:Al growing films are damaged by ion bombardment and high energy neutral atoms, effect known as the atomic peening effect, while at high pressures, the films become highly defective due to the thermalization of sputtered particles, and their resulting lower surface mobility. The highest substrate temperature available in our reactor (325 °C) leads to the best opto-electronic properties of the ZnO:Al thin films, thanks to a higher adatoms mobility on the surface of the growing film, and thus a best crystallization. The addition of oxygen in the gas mixture slightly improves the transmittance in the visible, but strongly degrades the electrical properties due to the complete oxidation of the interstitial donors (zinc, aluminium, hydrogen) and the filling of oxygen vacancies. The influence of the deposition parameters is discussed in terms of the structure evolution during the polycrystalline film growth, nucleation and coalescence.

In the second part of this work, different post-deposition treatments have been investigated: a thermal annealing treatment, and a laser annealing treatment.

Thermal annealing treatments have been investigated under various annealing atmospheres (under vacuum, in 5% H_2 in N_2 atmosphere, or in pure N_2 atmosphere) and

annealing temperature (400, 450, or 500 °C). Different electrical behaviours are observed depending on the annealing atmospheres, and in parallel the crystalline modifications follow the annealing temperature. The thermal annealing in N_2/H_2 strongly increases the carrier concentration, while under vacuum, the concentration remains stable, and dramatically drops in pure N_2 atmosphere. A metallic conduction due to the increase of carrier density leads to the decrease of the resistivity for an annealing in N_2/H_2 compared to vacuum, but the increase of the mobility is limited by scattering from ionized impurities scattering. The best optoelectronic properties are obtained for a N_2/H_2 annealing at 400 °C with 3.5×10^{-4} Ω.cm for a Hall mobility of 39 $cm^2/V.s$, and an optical transmittance of 81.2% between 400 and 1000 nm. The degradation of electrical properties of N_2 annealed ZnO:Al films are due to the creation of acceptor centres at the grain boundaries.

The laser annealing treatments have been realized with an excimer laser at various fluences. This treatment leads to an extreme modification of the surface morphology, with a slight improvement of the opto-electronic properties. The best opto-electronic properties are obtained after the treatment on ZnO:Al thin films deposited at room temperature at 0.25 J/cm^2 of fluence, with 6.0×10^{-4} Ω.cm for a Hall mobility of 34 $cm^2/V.s$, and an optical transmittance of 79.8% between 400 and 1000 nm.

The last part of this work is dedicated to the wet chemical etching step and the use as front electrodes of the etched ZnO:Al thin films for hydrogenated microcristalline silicon solar cells. The influence of the deposition conditions on the chemical etching is studied. The compactness, the microstructure and the oxygen content of the film highly influenced the etching rate and resulting surface morphologies. The ZnO:Al thin films deposited at the highest possible temperature (325 °C) and at the optimum working pressure (between 0.12 and 0.32 Pa) give, after the etching step, the lowest thickness loss (good electrical properties) with surface morphology consisting of larger craters (the highest haze factor). The thickest films (up to 2 μm) lead to the best optical properties in terms of light trapping through the optimized surface morphology after texturation.

The integration of the ZnO:Al thin films in hydrogenated microcrystalline silicon solar cells was finally studied. The ZnO:Al thin films deposited under optimized sputtering conditions exhibit the best solar cell characteristics, with the series resistance related to the TCO resistivity, and the short-circuit current density related to the transmittance. After the chemical step, the influence of the surface morphology and thus the light trapping properties of the ZnO:Al thin films are clearly observed, and especially on the short-circuit current density. The texturation time needs to be optimized depending on the deposition conditions, especially for annealed ZnO:Al thin films. The thermal annealing decreases the series resistance and improves the short-circuit current density. The laser annealed ZnO:Al thin films have been used as front electrodes in μc-Si:H, after the etching step. From the extreme surface modifications produced by the laser annealing, the wet chemical etching step emphasizes these morphologies, which further increases the light trapping effect, observed through the short-circuit current density.

Original contributions

To achieve a better understanding of the sputtered ZnO:Al thin film physics, several characterization techniques were used and studied in detail for the first time:

* A detailed analyses of the Raman spectroscopy was realized. The A_1-LO active mode at 570 cm^{-1} was successfully linked to the (002) peak recorded by X-ray diffraction measurements, and thus to the polycrystalline and textured properties of the ZnO:Al thin films.

* For the first time, *in-situ* resistance measurements during the deposition were studied and have shown different behaviours for the nucleation, coalescence and bulk growth stages, between low and high temperature deposition.

* The optical modelling of free electrons was studied to enable the understanding of the physical conduction mechanisms, depending on the carrier concentration, for an electrical transport limited by the bulk or by the grain boundaries. The original contribution of this work is the study of three different optical characterizations and their correlation: the UV/VIS/NIR spectrophotometry, the spectroscopic ellipsometry, and the IR polarimetry which has been developed in the laboratory.

Annealing processes were rigorously studied, at various temperatures and under many atmospheres for the thermal annealing step, and depending on the fluence for the laser annealing:

* The different opto-electronic evolutions were investigated through *in-situ* Raman spectroscopy and *in-situ* XRD measurements during the annealing process.

* The modelling of temperature-dependent conductivities has enabled the understanding of the different electrical conduction in annealed ZnO:Al thin films under various atmospheres.

* For the first time on sputtered ZnO:Al thin films, an excimer laser was used to anneal the TCO layer and tune its opto-electronic properties as well as its morphological properties for the light trapping feature of the ZnO:Al front electrode.

Finally, the relationships between the deposition conditions, annealing conditions and the resulting etched ZnO:Al thin films were meticulously discussed. Solar cells were deposited on ZnO:Al thin films processed from original methods, thermally annealed or laser annealed, with success. Further optimizations are promising.

Perspectives

Even though the front electrodes for hydrogenated silicon solar cells have been studied since many decades, they still require further investigations. In the laboratory, the research on the TCO layer has been opened with this thesis, which have permitted the definition of the baseline for the daily depositions, and for further and deeper investigations.

Concerning the deposition step, opening the field of possibilities is necessary to tune the electrical properties. For example, new gas mixtures have to be investigated, such as the incorporation of hydrogen directly during the deposition step and not only through a post-deposition annealing process. The incorporation of an additional extrinsic dopant with aluminium could be tried, such as gallium or boron. The quality of the ZnO:Al thin films is directly related to the growth dynamics during the sputtering. The energy of

adatoms can be tuned by heating the substrate during the deposition and thus increase the energy transferred to the adatoms for the activation of surface and bulk diffusion, or directly by modifying the energy of the plasma particles that impinge onto the growing film transferring energy and momentum to the adatoms. New types of sputtering could be tested, classical ones such as DC sputtering, or more original ones such as High Power Pulsed Magnetron Sputtering (HPPMS) to tailor the deposited material properties. Another possibility could be to deposited ZnO:Al thin film by a two-step magnetron sputtering process to optimize the optical, the electrical and the morphological properties the more independently possible.

The post-deposition annealing step increases the global cost of the solar cells by adding an supplementary step but its gain on the opto-electronic properties is considerable. Combine the post-deposition steps could be a very interesting option to further improve the properties of the TCO layer. Indeed, while the thermal annealing improves the opto-electronic properties, the laser annealing process modifies the morphological properties. The combination of these two processes could permit to still go further into the optimization of the TCO layer, independently, while in our case and in this thesis, a compromise had always to be made. In the same way, the wet chemical etching step could be realized before the thermal annealing step in order to, first, obtain the best morphological properties without caring about the electrical properties, and in a second time, improve the electrical properties without modifying the morphology.

Finally, the use of the TCO thin film as front electrodes needs further investigation. The wet chemical etching step could be replaced by a dry etching step, or could be avoided by the deposition directly on a rough surface. Moreover, the optimization of the TCO properties requires in parallel the optimization of the p-layer.

List of publications

C. Charpentier, P. Prod'homme, E. Garcia Caurel, and P. Roca i Cabarrocas. Towards a deeper understanding of ZnO:Al electrical and optical properties. *EU PVSEC Proceedings*, 528-532, 2010, DOI: 10.4229/25thEUPVSEC2010-1DV.2.69.

E.V. Johnson, C.Charpentier, T. Emeraud, J.F. Lerat, C. Boniface, K. Huet, P. Prod'homme, and P. Roca i Cabarrocas. Room temperature fabricated ZnO:Al with elevated and unique light-trapping performance. *MRS Proceedings*, 1321:141-146, 2011, DOI: 10.1557/opl.2011.818.

C. Charpentier, P. Prod'homme, I. Maurin, M. Chaigneau, and P. Roca i Cabarrocas. X-ray diffraction and Raman spectroscopy for a better understanding of ZnO:Al growth process. *EPJ Photovoltaics*, 2(2011):25002, 2012, DOI:10.1051/epjpv/2011026.

C. Charpentier, P. Prod'homme, L. Francke, and P. Roca i Cabarrocas. Microstructural, optical and electrical properties of post-annealed sputtered ZnO:Al thin films. *MRS Proceedings*, 1394:141-146, 2011, DOI: 10.1557/opl.2012.258

A. Salomon, G. Courtois, C. Charpentier, M. Labrune, P. Prod'Homme, L. Francke and P. Roca i Cabarrocas. Effect of annealing on silicon heterojunction solar cells with textured ZnO:Al as transparent conductive oxide. *EPJ Photovoltaics*, 3(2012):35002, 2012, DOI:10.1051/epjpv/2012004.

C. Charpentier, P. Prod'homme, and P. Roca i Cabarrocas. Microstructural, optical and electrical properties of annealed ZnO:Al thin films. *Thin Solid Films*, 2012, accepted.

C. Charpentier, R. Boukhicha, P. Prod'homme, T. Emeraud, J.F. Lerat, E. Johnson, and P. Roca i Cabarrocas. Microstructural, Evolution in Optoelectronic properties of ZnO:Al thin films undergoing a laser annealing and etching process. *Solar Energy Materials and Solar cells*, 2012, under review.

C. Charpentier, F. Paumier, P. Prod'homme, L. Francke, and P. Roca i Cabarrocas. In-situ control of the structural and electrical properties of AZO thin films during annealing processes. *Thin Solid Films*, 2012, under review.

Abstract

The Transparent Conductive Oxide (TCO) thin film used as a front electrode in microcrystalline silicon solar cells is a key material for the improvement of their efficiency. A promising TCO is aluminium doped zinc oxide (ZnO:Al) deposited by RF magnetron sputtering.
A first part of the thesis is dedicated to the study of the influence of deposition conditions on microstructure, growth mechanisms, and opto-electronic properties of ZnO:Al thin films. We obtained an optimum in terms of maximal transparency in the visible range, and minimal resistivity, for films realized at a pressure of 0.12 Pa and at a temperature of 325 °C. A second part of the work is focused on the study of post-deposition annealing treatments, such as thermal or laser annealing processes, on the properties of the material deposited at room temperature. The influence of the annealing atmosphere (under vacuum, in N_2/H_2, or in pure N_2) and temperature (from 400 to 500 °C) was studied. The thermal annealing step resulted in an improvement of the optical and electrical properties of the ZnO:Al thin film up to a resistivity of 3.5×10^{-4} Ω.cm for a transmittance between 400 and 1000 nm of 81.2%. The laser annealing treatment influences particularly the morphological properties. The finale step of this thesis work is based on the study of the wet chemical etching of the TCO thin film, in order to create an optimal surface morphology for light confinement in the μc-Si:H layers without a degradation of the electrical properties. The integration of these ZnO:Al thin films as front electrodes in PIN silicon thin film solar cells was realized and investigated in depth.

Keywords : Transparent Conductive Oxide (TCO), solar cell, Aluminium doped zinc oxide, magnetron sputtering, thermal annealing, excimer laser annealing, chemical etching

Résumé

La couche mince d'Oxyde Transparent Conducteur (OTC) utilisée en tant qu'électrode avant pour les cellules photovoltaïques silicium microcristallin est un matériau déterminant pour l'amélioration de leur rendement. Un OTC prometteur est l'oxyde de zinc dopé aluminium ZnO:Al déposé par pulvérisation cathodique magnétron RF.
Une première partie du travail de thèse est dédiée à l'étude de l'influence des conditions de dépôt sur la microstructure, les mécanismes de croissance et les propriétés opto-electronique du ZnO:Al. Nous avons ainsi obtenu un optimum en terme de transparence maximale dans le domaine visible et de résistivité minimale pour un dépôt réalisé à une pression de 0.12 Pa pour une température de 325 °C. Une seconde partie du travail de thèse porte sur l'effet de traitements après-dépôt, recuit thermique ou laser excimère, sur les propriétés du ZnO:Al déposé à température ambiante. L'influence de différentes atmosphères (sous-vide, N_2/H_2, et pur N_2) et températures de recuit (de 400 à 500 °C) a été étudié. L'étape de recuit thermique a permis une amélioration notable des propriétés opto-électroniques de la couche ZnO:Al, jusqu'à une résistivité de 3.5×10^{-4} Ω.cm pour une transmittance entre 400 et 1000 nm de 81.2%. L'étape de recuit laser, quant à elle, influe notamment les propriétés morphologiques du matériau. L'étape finale de ce travail de thèse est basée sur l'étude de la texturation chimique, étape ayant pour but la formation d'une morphologie de surface optimale, c'est-à-dire permettant le piégeage optique dans les couches actives μc-Si:H et ce, sans altérer les qualités électriques de la couche. L'intégration de ces couches minces ZnO:Al en tant qu'électrode avant dans des cellules photovoltaïques PIN à base de silicium microcristallin a été réalisé et étudié en détail.

Mots-clés : Oxyde Transparent Conducteur (OTC), cellule photovoltaïque, oxyde de zinc dopé aluminium, pulvérisation cathodique magnétron, recuit thermique, recuit laser excimère, texturation chimique